THE EFFECT OF VIBRATIONS ON THE BEHAVIOUR OF LUBRICATED ELASTOHYDRODYNAMIC CONTACTS

- by -

Xingnan Zhang

A Thesis Submission for the degree of
Doctor of Philosophy

Department of Engineering and Design
School of Engineering and Informatics
University of Sussex

August 2017

Abstract

It is known that rolling element bearings are the second most extensively used machine components in various mechanisms and machines. Consequently, the demand of pursuing higher bearing performance, increased load carrying capacity and prolonged operation life is crucial. The lubrication regime in which rolling element bearings operate is called Elastohydrodynamic Lubrication (EHD). The EHD lubrication regime in steady-state conditions, where working parameters such as load, geometry or speed of the surfaces are constant, is nowadays well understood. Nevertheless, in practice EHD contacts never work in completely steady-state regimes. For example, the contacts of rolling element bearings operating in a machine, which runs at constant speed, has no shock loading from the end effector still experience variable loading when the rolling elements enter and exit the loaded zone and variable speed at the start up and shut down of the machine. Factors related to the working cycle of the machine or mechanism cannot be avoided or simply the start or stop of those will always introduce unsteadiness into the EHD contacts. Vibrations in EHD contacts cause variation of load, and implicitly pressure and contact size, fluctuations of film thickness, which in their turn cause localized fluctuations of the pressure. The vibrational behavior is directly related to noise generation, which significantly influences bearing performance.

The current research is focused on the effect of forced harmonic vibrations on oil and grease lubricated EHD contacts. Experiments were carried out using a test rig that simulates real – life EHD contacts by a steel ball on glass disc contact. The method used for measuring the lubricant film thickness was optical interferometry, adapted for the specifics of this research. Lubricant film thickness was measured in systematically – designed tests where a wide range of lubricants and working parameters was employed. The trends of EHD film behaviour under variable loading were evaluated and maps of the likelihood of film thickness perturbation occurrence were drawn for the first time. An analytical model of the lubricant film thickness variation during rapid variation of load was also devised and successfully compared to the experimental findings. The systematic study of the effect of vibrations upon EHD film recovery in limited lubricant supply conditions was also carried out and published. An experimental study on the effect of vibrations was successfully extended into grease-lubricated contacts.

The scientific information gained will be a useful tool in the hands of both, lubricants and machine elements producers, with the aim of extending the life expectancy of those elements.

- Dedicated to my parents Dexin Zhang and Xiuru Wang -

- 献给我的父母 张德新 汪秀茹 -

Acknowledgements

I would like to express my sincere gratitude to Dr. Romeo Glovnea for the continuous support and encouragement for my research, for the opportunity which allowed me to grow as a research scientist. For many years, he has been a patient lecturer, a gracious tutor, a great supervisor, and more importantly a friend for life to me.

I would like to thank my parents for their continuous financial support, immense patience and encouragement not only during this research but also throughout my life.

Declaration

I hereby declare that this thesis has not been and will not be, submitted in whole or in part to another university for the award of any other degree.

Signature: _____

August 2017

Conference presentations and journal publications

X. Zhang, K. Jablonka and R. P. Glovnea, "Experimental Rig for Measuring Lubricant Film Thickness in Rolling Bearings", Applied Mechanics and Materials, Vol. 658, 381-386, 2014. ISSN 1662-7482.

X. Zhang and R. P. Glovnea, "The Behavior of Lubricated EHD Contacts Subjected to Vibrations", IOP Conf. Ser.; Mater. Sci. Eng. 174, 012036, 2017. ISSN 1757-8981.

R. P. Glovnea, **X. Zhang** and J. Sugimura, "The Effect of Lubricant Supply and Frequency upon the Behavior of EHD Films Subjected to Vibrations", *IOP Conf. Ser.; Mater. Sci. Eng*. 174, 012033, 2017. ISSN 1757-8981.

X. Zhang and R. P. Glovnea, "EHD Film Thickness Measurement in a Ball Bearing by Electrical Capacitance", presented at *70th Annual Meeting and Exhibition of Society Tribologists and Lubrication Engineers, 17-21 May 2015, Dallas, Texas, USA,*

X. Zhang and R. P. Glovnea, "Behavior of Grease-Lubricated EHD Contact under Variable Loading", presented at *World Tribology Congress*, 17-22 September 2017, Beijing, China.

X. Zhang and R. P. Glovnea, "The Effect of Lubricant Composition upon Film Thickness in Grease Lubricated EHD contacts Subjected to Vibrations", presented at *World Tribology Congress*, 17-22 September 2017, Beijing, China.

Table of contents

Nomenclature

a	radius of the contact, $[m]$
a	major semi axis of contact ellipse, $[m]$
a_r	radius ratio
A	cross-section area of the shaft supporting the disc, $[m^2]$
b	minor semi axis of contact ellipse, $[m]$
b	radius of contact, $[m]$
c	contact ellipse semi axis constant
c	equivalent contact radius, $[m]$
c	total damping
c	physical damping parameter
c_c	damping constant of the EHD film, $[Ns/m]$
C	non-dimensional damping of the EHD contact
C	constant at atmospheric viscosity
C	total damping in system without lubricant film,
d_s	diameter of ball shaft, $[m]$
D	stiffness/damping matrix
E	Young's modulus, $[Pa]$
E^*	reduced modulus of elasticity, $[Pa]$
f	force vectors
f_c	two-degree of freedom system contact frequency, $[Hz]$
f_0	linearized contact frequency, $[Hz]$
F_f	maximum friction force in the linear bearing, $[N]$
F_0	amplitude of variable load, $[N]$
F_1	function in terms of ratio of relative curvatures
F_2	function in terms of ratio of relative curvatures
F_e	elastic restoring part of the contact force
$\bar{G}$	dimensionless material parameter
h	film thickness, $[m]$
$\bar{h}$	film thickness at the location of the maximum pressure, $[m]$
h_c	central film thickness, $[m]$
h_i	initial film thickness, $[m]$
h_{min}	minimum film thickness, $[m]$
h_o	central film thickness, $[m]$
$(h_o)_f$	central film thickness at limit lubricant supply condition, $[m]$
h_{opt}	optical thickness of film, $[m]$
h_{oil}	spatial film thickness of lubricant film, $[m]$
$h_{oil\infty}$	oil thickness at contact sides, $[m]$
h_s	steady state central film thickness, $[m]$
h_{sl}	spatial film thickness of silica layer, $[m]$
h_{st}	steady state film thickness under static load, $[m]$
$h(t)$	transient film thickness, $[m]$
h_0	gap at zero pressure gradient, m
I	ball shaft cross-section moment of inertia, $[kg \cdot m^2]$
I_1	individual intensity of reflected beam, $[W/m^2]$
I_2	individual intensity of reflected beam, $[W/m^2]$
I_R	intensity of interfered light reflected from the contact, $[W/m^2]$
k_b	stiffness of the bearings connected in series with the shaft, $[N/m]$
k_{bl}	stiffness of the bellow, $[N/m]$
k_{br}	stiffness of the bearings, $[N/m]$
k_c	stiffness of the EHD contact, $[N/m]$

k_d	stiffness of the disc, $[N/m]$
k_{EHD}	stiffness of the EHD film, $[N/m]$
k_{Hz}	stiffness of the dry Hertzian contact, $[N/m]$
k_s	stiffness of the shaft supporting the ball, $[N/m]$
K	constant
K	nonlinear spring constant
K	consistency factor
K_{eq}	linearized contact stiffness, $[N/m]$
K_L	stiffness coefficient
$\overline{K}$	dimensionless spring constant
l	length between supports, $[m]$
m	length of meniscus, $[m]$
m	combined mass of disc, shaft and bearing, $[kg]$
m	ball bass, $[kg]$
M	mass matrix
n	constant
n	flow behavior index
n_{sl}	refractive index of silica layer
n_{oil}	refractive index of lubricant film
N	load, $[N]$
N	order of interference
p	pressure, $[Pa]$
p_m	mean pressure, $[Pa]$
p_0	maximum pressure, $[Pa]$
P	applied load, $[N]$
$\bar{P}$	load factor
P_m	mean load, $[N]$
P_0	amplitude, $[N]$
q_0	equivalent pressure, $[Pa]$
q_x	flow per unit width in *x* direction, $[m^2/s]$
q_y	flow per unit width in *y* direction, $[m^2/s]$
r_{ax}	contact radius in the *x*-direction of solid a, $[m]$
r_{ay}	contact radius in the *y*-direction of solid a, $[m]$
r_{bx}	contact radius in the *x*-direction of solid b, $[m]$
r_{by}	contact radius in the *y*-direction of solid b, $[m]$
R	reduced radius of curvature, $[m]$
R_e	equivalent radius of curvature, $[m]$
R_{sh}	force generated in the shaft, $[N]$
R_x	reduced radii of curvature in *x* direction, $[m]$
R_y	reduced radii of curvature in *y* direction, $[m]$
S	whole contact area, $[m^2]$
S	contribution of lubricant film to total damping
SD	starvation degree
S_f	inlet distance to achieve a fully flooded condition, $[m]$
T	period of oscillation, $[s]$
T	absolute temperature, $[K]$
t	temperature, $[K]$
t_{av}	average lubricant transit time in the loading phase of vibration cycle, $[s]$
u	the velocity in *x* direction, $[m/s]$
$u_{bearing}$	friction coefficient in linear ball bearing
u_{EHD}	traction coefficient of the lubricant film
u_0	absolute velocity of the surfaces of the ball and disc, $[m/s]$
u_ξ	fluid velocity at upstream position, $[m/s]$

U	entrainment velocity in *x* direction, $[m/s]$
$\bar{U}$	dimensionless speed parameter
v	the velocity in *y* direction, $[m/s]$
v_a	measured absolute velocity, $[m/s]$
v_d	contact deflection between ball and disc, $[m]$
v_r	velocity of the perturbation relative to the contact, $[m/s]$
v_{tr}	transport velocity, entrainment velocity of the contact, $[m/s]$
v_s	sum of speed, $[m/s]$
$\bar{W}$	dimensionless load parameter
$\bar{W}_L$	dimensionless load parameter of line contact
x	coordinate in direction of flow
x_b	displacement of the ball, $[m]$
$\dot{x}_b$	velocity of the ball, $[m/s]$
$\dot{x}_{bc}$	velocity of the ball carriage, $[m/s]$
x_d	displacement of the disc, $[m]$
$\dot{x}_d$	velocity of the disc, $[m/s]$
x_o	coordinate of maximum pressure position, $[m]$
y	generalized displacement, $[m]$
y	coordinate perpendicular to *x*, $[m]$
z	coordinate through film, $[m]$
α	pressure-viscosity coefficient, $[m^2/N]$
δ	mutual approach of two distant points, $[m]$
δ	path difference
η	absolute viscosity, $[Pa \cdot s]$
η_0	absolute viscosity at $p = 0$ and constant temperature, $[Pa \cdot s]$
η_0	dynamic viscosity, $[Pa \cdot s]$
ν	Poisson's ratio
ρ	density, $[kg/m^3]$
$\bar{\rho}$	dimensionless density
ρ_0	density at $p = 0$, $[kg/m^3]$
τ	shear stress, $[N/\ m^2]$
τ_y	yield stress, $[N/\ m^2]$
σ_s	surface tension, $[N/m]$
κ	elliptic integrals of the first kind
ε	elliptic integrals of the second kind
$\dot{\gamma}$	shear rate, $[s^{-1}]$
ϕ	plastic viscosity
ϕ	effective net phase change occurs during reflection
λ	wavelength, $[m]$
λ_h	ratio between base oil and grease film thickness
λ_h	starvation degree parameter
λ_{min}	wavelength for destructive interference occurs, $[m]$
λ_{max}	wavelength for constructive interference occurs, $[m]$
ω	circular frequency of the load cycle, $[Hz]$
$\Delta(T)$	response for sinusoidally varying loads

List of Figures

List of Tables

Chapter 1: Introduction

1.1 Thesis scope and objectives

Machine components such as rolling element bearings or gears often experience vibrations due to geometrical inaccuracies, shock loading, unbalanced rotating masses and others. These machine elements rely on a very thin lubricant film to protect the metallic surfaces form direct contact and eventual damage. Any EHD contact can be considered as a dynamic system, which consists of springs and dampers connected in parallel. Therefore, it is obvious that any vibrations which take the system out of a steady state condition will unavoidably lead to dampened oscillations until this system reaching another equilibrium condition. This is in case of free vibrations; in case of forced vibrations the transient phase passes quickly and a steady state phase ensues where the system vibrated near one of the natural frequencies mode. The way how the lubricant film transmits or eventually dampens these vibrations affects the functionality of the whole assembly. From the daily operation of machine components point of view, research into vibrating EHD contacts is most relevant to practical applications.

A series of experiments on the effect of forced harmonic vibrations upon the behaviour of lubricated EHD contacts were carried out in this research. The influence of various parameters of the oscillatory motion upon the film thickness are presented and discussed in this thesis. Simplified theoretical analyses of the dynamics of the system and of the response of the EHD film was also performed. The overall aim was to understand the influence of vibrations of machine components on lubricating films and vice versa. The main objectives of this research were:

- To quantify the influence of frequency and amplitude of harmonic vibrations upon EHD film thickness.
- To evaluate the effect of vibrations upon track replenishment of severely starved grease lubricated EHD contacts.
- To compare the experimental results obtained with theoretical models of EHD lubricated contacts subjected to forced harmonic vibration.

1.2 Thesis outline

This thesis consists of eight chapters including the *Introduction Chapter;* the content included in these chapters is briefly summarized as follows:

Chapter 2: Lubrication of High–Pressure Contacts

Features of various types of non-conformal contacts, Hertz' theory of smooth, elastic contacts, fundamentals of EHD lubrication, EHD film features, typical film thickness formulas as well as

starvation of EHD contacts are included in this chapter.

Chapter 3: Review of Transient Phenomena in EHD Lubrication

Experimental studies carried out in past decades regarding on non-steady state EHD lubrication, including the effect of variable entrainment speed, squeeze films, transient loading and vibrating EHD contacts, monitoring rolling element bearings dynamics.

Chapter 4: Lubricants

This chapter includes the basic chemistry information and function of base oil and grease lubricants, grease behaviour in EHD condition, and the list of properties of all lubricants tested in this thesis.

Chapter 5: Experimental Methodology

Chapter 5 deals with the experimental setup employed in this research. The principles of optical interferometry are explained, the basic arrangement of the experimental setup including newly designed parts and experimental procedure are all included.

Chapter 6: EHD Films Subjected to Vibrations

In this chapter, the test program is detailed, showing working parameters and selected typical results of EHD films subjected to forced harmonic vibrations. To note that due to space limitation and similarity between various tests, not all the results are presented.

Chapter 7: Discussion

This chapter contains the theoretical analysis part of this thesis. Lubricant film thickness in EHD contacts subjected to forced harmonic vibrations was extracted from optical interferometry images of the contact shown in Chapter 6. A series of simplifying assumptions are made which allow the dynamic response of the experimental rig to be evaluated and the influence of the EHD film to be extracted. The behaviour of the EHD film under rapid variation of load is analysed analytically and compared with experimental results. Good qualitative agreement was found which gives an insight into the parameters that influence the behaviour of the EHD film subjected to forced vibrations.

Chapter 8: Conclusions and Suggestions for Future Work

This chapter summarizes the most important conclusions and achievements of this thesis, together with suggestions for future work.

Chapter 2: Lubrication of High–pressure Contacts

2.1 Non-conformal contacts

Two bodies with different radii of curvature, approaching each other, will initially make contact at either a point or along a line. The problem of the effect of the geometry and load upon the deformation of surfaces under loading was analysed intensely in the 19th century by many scientists who brought great contributions to the field of theory of elasticity (e.g. Lame, Cauchy, Boussinesq, Cerruti) however it was a very young, at the time, Heinrich Hertz who in 1881 published an acceptable solution to the problem [1]. Hertz came from the field of electromagnetism and was interested on the effect upon light, of the contact between lenses. He used the potential theory to find the pressure field and the shape of the contact area. A number of simplifying assumptions had to be made as follows:

- The materials are homogeneous and the yield stress is not exceeded;
- No tangential forces are induced between the solids;
- The contact is limited to a small portion of the surface, such that the dimensions of the contact region are small in comparison with the radii of curvature of the contacting bodies;
- The solids are at rest and in equilibrium.

2.1.1 Elliptical point contact

Two elastic solids with convex surfaces make contact at a single point in zero loading conditions; such contact is called a “point contact”. The geometry of a point contact is showed in figure 2.1. It has to be noted that the radii of curvature of convex surfaces are considered positive and radii of curvatures of concave surfaces negative. The shape and dimensions of the contact area, contact stress and deformation are strongly dependent on the sum of the radii of curvature.

The reduced radii of curvature in *x* and *y* directions are expressed by:

$$\frac{1}{R_x} = \frac{1}{r_{ax}} + \frac{1}{r_{bx}} \tag{2.1}$$

$$\frac{1}{R_y} = \frac{1}{r_{ay}} + \frac{1}{r_{by}} \tag{2.2}$$

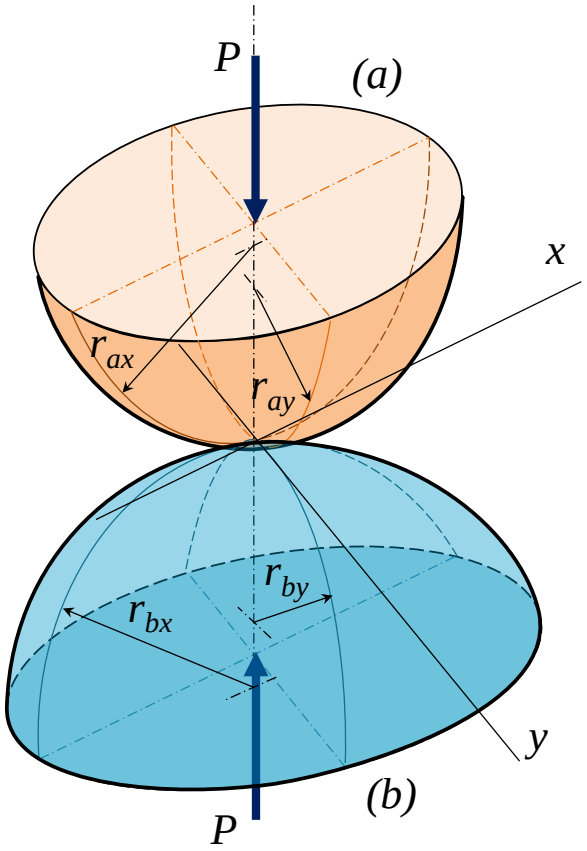

Figure 2.1: Geometry of contacting elastic solids

The radius ratio a_r can be defined as:

$$a_r = \frac{R_y}{R_x} \tag{2.3}$$

There are plenty of machine components with reduced radii of curvature not equal in the two principal planes, i.e. $a_r \neq 1$, such as rolling element bearings and hypoid gears, in which cases the contact area is elliptical. According to Hertz's theory the pressure distribution over the contact area is an elliptical paraboloid, as shown in figure 2.2.

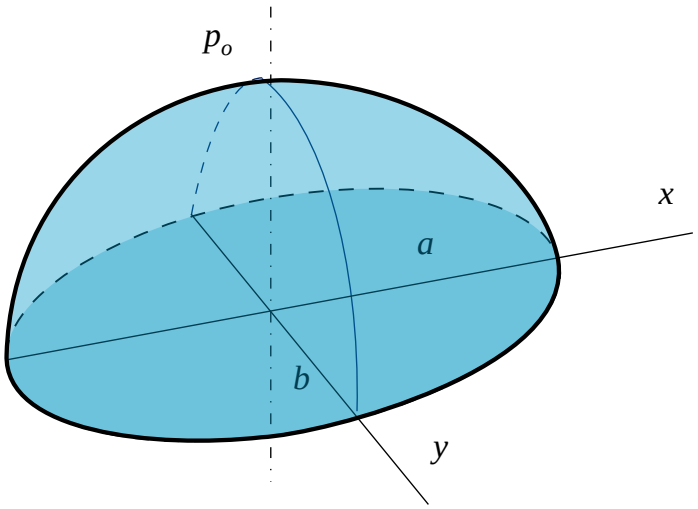

Figure 2.2: Pressure distribution in ellipsoidal contacts

The equation of this pressure distribution is:

$$p = p_0\left[1-\left(\frac{x}{a}\right)^2-\left(\frac{y}{b}\right)^2\right]^{1/2} \tag{2.4}$$

Where

$a =$ semi axis of contact ellipse in x direction,

$b =$ semi axis of contact ellipse in y direction

If the equivalent radius of curvature is defined as:

$$R_e = \sqrt{R_x R_y} \tag{2.5}$$

Then the semi – axes of the contact ellipse are found from the relationships:

$$\frac{a}{b} \approx \left(\frac{R_x}{R_y}\right)^{2/3} \tag{2.6}$$

$$c = (ab)^{1/2} = \left(\frac{3PR_e}{E^*}\right)^{1/3} F_1\left(R_x / R_y\right) \tag{2.7}$$

The maximum pressure is further given by:

$$p_0 = \left(\frac{6PE^{*2}}{\pi^3 R_e^2}\right)^{1/3}\left[F_1\left(R_x / R_y\right)\right]^{-2/3} \tag{2.8}$$

The approach of the bodies also depends of the ratio of the reduced radii by the relationship:

$$\delta = \left(\frac{9P^2}{16R_e E^{*2}} \right)^{1/3} F_2\left(R_x / R_y\right) \tag{2.9}$$

Functions F_1 and F_2 can be, at first approximation taken as unity, if not, they can be extracted from graphs for example *figure 4.4* in [2] or calculated as functions of the ratio R_x/R_y.

2.1.2 Circular point contact

For the case when $r_{ax} = r_{ay}, r_{bx} = r_{by}$, the contact shape is circular rather than elliptical; this type of contact is called circular contact. This is the case of for example a ball contacting with a plane, or two contacting spheres, as seen in figure 2.3.

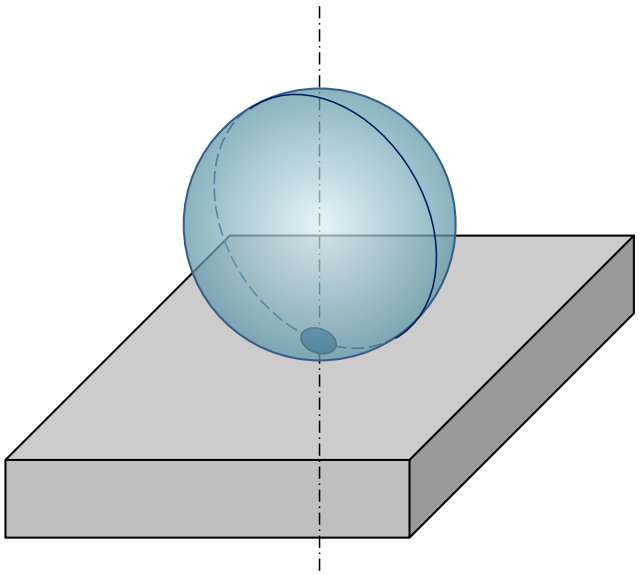

Figure 2.3: Ball on plane contact

Hertz's solution of smooth elastic contacts gives the dimensions of the contact area, maximum pressure and the approach of the bodies, as shown by the expressions below, for a circular contact [2]:

$$a = \left(\frac{3RP}{4E^*} \right)^{1/3} \tag{2.10}$$

$$p_0 = \left(\frac{6PE^{*2}}{\pi^3 R^2} \right)^{1/3} \tag{2.11}$$

$$p_m = \frac{2}{3} p_0 \tag{2.12}$$

$$\delta = \left(\frac{9P^2}{16E^{*2}R} \right)^{1/3} \tag{2.13}$$

Where a denotes the radius of the contact, δ denotes the mutual approach of two distant points, p_0 and p_m are the maximum pressure and mean pressure respectively. E^* is the reduced modulus of elasticity given by:

$$\frac{1}{E^*} = \frac{1-\nu_a^2}{E_a} + \frac{1-\nu_b^2}{E_b} \tag{2.14}$$

P is the applied load, and R is the reduced radius of curvature.

$$\frac{1}{R} = \frac{1}{R_a} + \frac{1}{R_b} \tag{2.15}$$

2.1.3 Linear contact

When two elastic cylinders are brought into contact with axes parallel and are loaded by a load P per unit length, as shown in the figure 2.4, their theoretical contact area is a strip of semi – width a. The characteristic parameters of the contact can be calculated as followed:

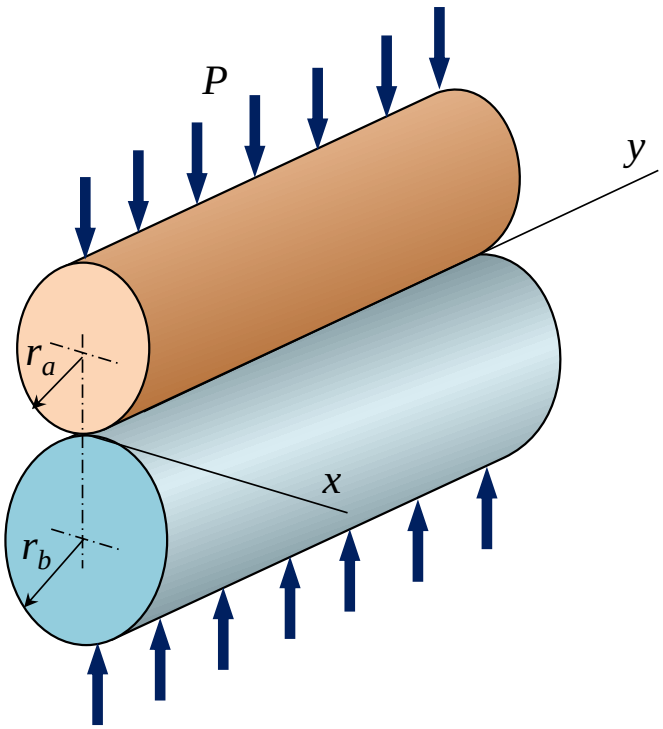

Figure 2.4: Contact of two cylinders with parallel axes

$$a = \left(\frac{4RP}{\pi E^*} \right)^{1/2} \tag{2.16}$$

The contact pressure is in this case a parabolic cylinder with the maximum contact pressure given by:

$$p_0 = \left(\frac{PE^*}{\pi R} \right)^{1/2} \tag{2.17}$$

The mean contact pressure is then:

$$p_m = \frac{\pi p_0}{4} \tag{2.18}$$

The solution for the mutual approach of distant points is not as straight forward as in the case of point contacts, but analytical solutions do exist.

These relationships for two cylinders with parallel axes are also proved to be valid for the case of cylinder loading on a plane and cylinder loading in a cylindrical groove.

2.2 Elastohydrodynamic lubrication

2.2.1 Fluid film lubrication regimes

Machine components which work with Hertzian contacts would not be able to survive the operating conditions in the absence of a lubricant film to separate the solid surfaces. As it is known between clean metallic surfaces, strong adhesive forces are generated which increase friction and eventually lead to failure by wear. The lubricant film has thus the main roles to not allow direct contact between asperities of the solid surfaces, even the pressure distribution and to convect away some of the heat generated. Ideally the lubricant film should separate completely the metallic surfaces, in which case a full-film condition is achieved. When this is not the case, mixed or boundary conditions are formed. In the present thesis, only full film conditions are considered.

The regime of lubrication of Hertzian contacts is called ElastoHydroDynamic (EHD), to distinguish it from the hydrodynamic regime characteristic to sliding bearings. There are several well-defined regimes within the range of conditions of fluid-film, elastohydrodynamic lubrication. The type of lubrication characteristic to each regime is influenced by the elastic deformation between contacting solids under loads and the variation of fluid viscosity with pressure. Johnson [3] defined four main regimes of fluid-film lubrication in high-pressure contacts. A reproduction of a chart from reference [3] is shown in figure 2.5.

Isoviscous-rigid Regime

In this regime, the viscosity of the fluid does not change and the magnitude of the elastic deformation of the surfaces is an insignificant part of the fluid film which separates the contacting surfaces, thus it can be neglected. Low contact pressure makes the lubricant viscosity almost constant. This type of lubrication is typically encountered in circular-arc thrust bearing pads.

Piezo-viscous-rigid Regime

In this regime, the contact pressure is sufficiently high to increase the fluid viscosity within the conjunction significantly, however the contacting solids remain rigid; that is the deformations of the surfaces are insignificant in comparison to the fluid film thickness. This form of lubrication may be encountered in moderately loaded cylindrical tapered roller bearings at the contacts between rollers' end and guide flanges, and in contacts between piston rings and cylinder liners.

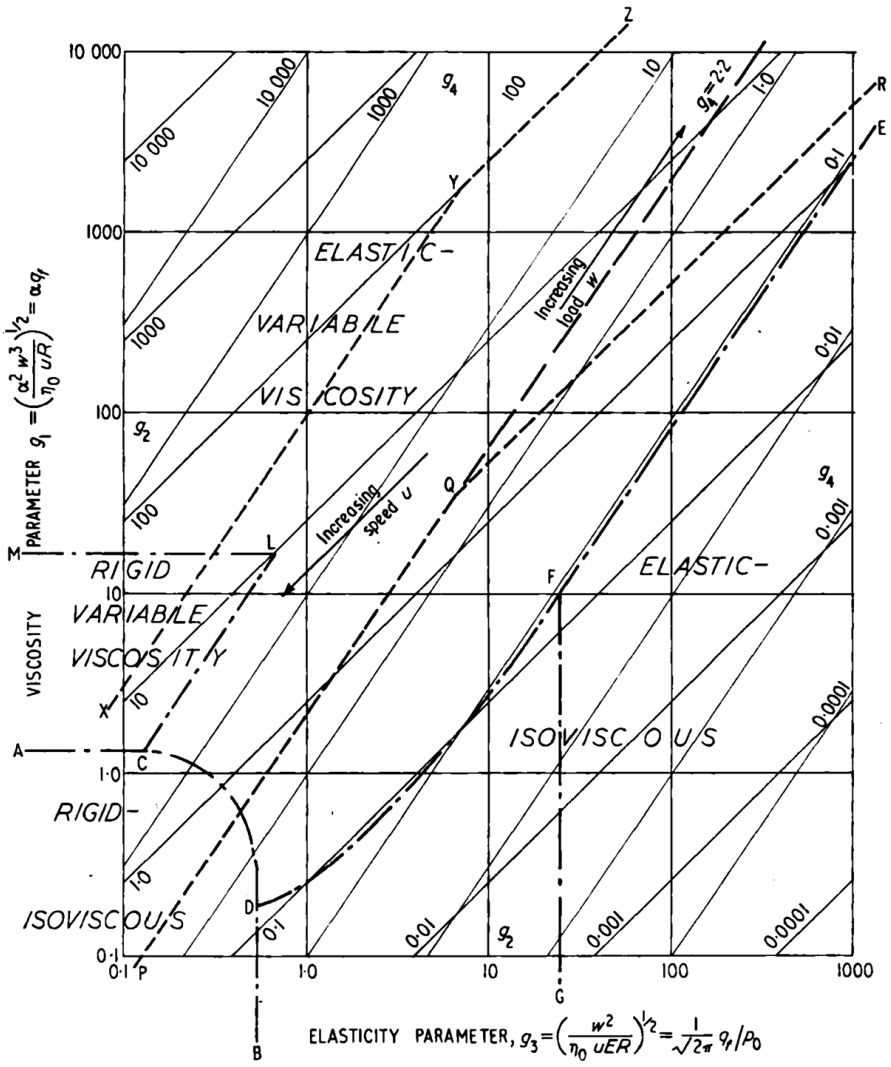

Figure 2.5: Regimes of elastohydrodynamic lubrication [3]

Isoviscous-elastic Regime

Comparing with the previous two regimes, the elastic deformation of the solids is comparable with the thickness of the fluid film in isoviscous-elastic regime, however the viscosity of the fluid does not change substantially due to the low contact pressure due to low pressure-viscosity coefficient. This form of lubrication may be encountered in seals, human joints, tires and elastomeric material machine elements. It can be treated as soft elastohydrodynamic lubrication.

Piezo-viscous-elastic Regime

In fully developed elastohydrodynamic lubrication, the elastic deformation of the solids is always a significant proportion of the thickness of the fluid film thickness, and the contact pressure is high enough to generate a significant increase in the viscosity of the fluid. This form of lubrication is typically encountered in ball and roller bearings, gears and cams. It can be treated as hard elastohydrodynamic lubrication.

In the current research, only hard elastohydrodynamic lubrication is considered due to the properties of the contacting materials studied. This lubrication regime will be simply called EHD from now on.

2.2.2 Constituent equations of EHD lubrication

As mentioned previously, the elastic deformation of the contacting surfaces and the increase of the viscosity of the lubricant with pressure play important roles in the lubrication of Hertzian contacts, however, without the entraining action of the lubricant, no film can be formed. Thus, the other mechanism, crucial for the formation of the EHD film, is the hydrodynamic action as the lubricant is forced to enter the converging gap in the inlet of the contact. From practical point of view the lubricant film thickness is what it is important, thus historically there have been efforts to develop equations to quantitatively describe the film thickness as function of working and material parameters. In this section, the equations used for solving the EHD film thickness are presented.

2.2.2.1 Reynolds equation

The history of lubrication can be traced back to 19th century, when Reynolds [4] described the flow of Newtonian fluids in converging gaps. Generally, the equation that describes the motion of a Newtonian fluid is the well-known Navier-Stokes equation. In the case of lubrication, the lubricant film has some characteristics which simplifies the treatment of the fluid flow. These simplifying assumptions, as stated by Reynolds, are:

1. The body forces are negligible,
2. The pressure is constant through the film thickness,

3. No slips at boundaries,
4. Lubricant is Newtonian,
5. The flow is laminar,
6. The density of the fluid is constant,
7. Inertia and surface tension forces are negligible,
8. The viscosity is constant through the film thickness.

Reynolds equation, for steady state flow, can be derived from the equilibrium of an element of fluid, similarly to the derivation of Navier-Stokes equations.

Equilibrium of an element of fluid volume

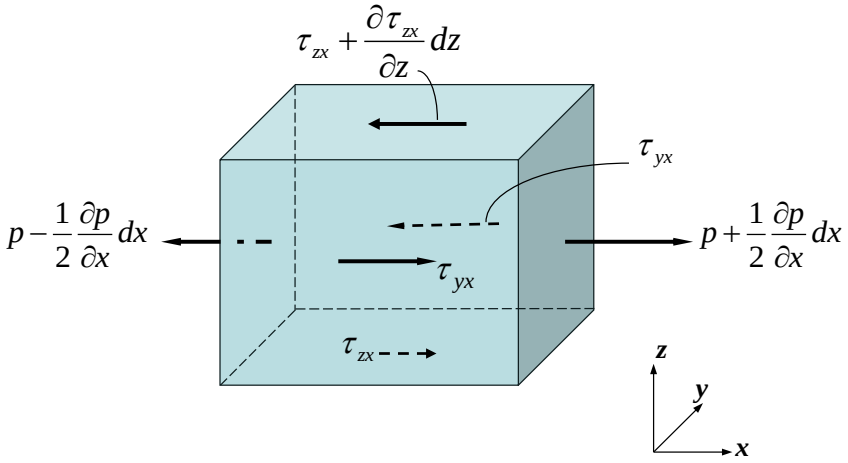

Figure 2.6: Equilibrium of an element of fluid

Consider the flow of a fluid taking place in x direction only and an elementary volume of sides *dx, dy, dz*. This element is subjected to forces derived from stresses and pressure, in the x direction as shown in figure 2.6. The variation of pressure between the left and right surfaces is divided in equal parts. On the top and bottom faces of the element, there are shear stresses which we assume that also have variations along the corresponding directions. Finally, the shear stresses acting on faces perpendicular to y axis do not change because there is no flow in that direction. As the flow is laminar and there are no inertia forces, the above forces must form a balanced system.

$$\left(p + \frac{1}{2}\frac{\partial p}{\partial x} dx\right) dydz + \tau_{zx} dxdy + \tau_{yx} dxdz - \\ - \left(p - \frac{1}{2}\frac{\partial p}{\partial x} dx\right) dydz - \left(\tau_{zx} + \frac{\partial \tau_{zx}}{\partial z} dz\right) dxdy - \tau_{yx} dxdz = 0 \tag{2.19}$$

After expanding the brackets and cancelling the like terms, this becomes:

$$\frac{\partial p}{\partial x} dxdydz = \frac{\partial \tau_{zx}}{\partial z} dxdydz \tag{2.20}$$

Since $dxdydz$ is an arbitrary, non-zero, volume it can be cancelled out so:

$$\frac{\partial p}{\partial x} = \frac{\partial \tau_{zx}}{\partial z} \tag{2.21}$$

Upon the hypothesis that the fluid is Newtonian the shear stress is proportional to the shear rate:

$$\tau_{zx} = \eta \frac{\partial u}{\partial z} \tag{2.22}$$

with η the viscosity and u the velocity in x direction. Replacing this into the force equation yields:

$$\frac{\partial p}{\partial x} = \eta \frac{\partial^2 u}{\partial z^2} \tag{2.23}$$

Similar in y direction:

$$\frac{\partial p}{\partial y} = \eta \frac{\partial^2 v}{\partial z^2} \tag{2.24}$$

In this case v is the velocity in y direction. According to the second assumption, pressure is constant through the film thickness thus the pressure gradient in the z direction is zero:

$$\frac{\partial p}{\partial z} = 0 \tag{2.25}$$

The equations in x and y directions can be integrated twice, with respect to variable z to get the velocity profiles across film thickness. If the velocities of the surfaces are U_1, V_1, respectively U_2, and V_2, and the local film thickness is denoted by h, the boundary conditions for velocities are:

$z = 0$, $u = U_1$, $v = V_1$;

$z = h,\ u = U_2,\ v = V_2.$

The velocities in x and y directions become:

$$u=\frac{1}{2\eta}\frac{\partial p}{\partial x}.\left(z^2-zh\right)+\left(U_2-U_1\right)\frac{z}{h}+U_1 \tag{2.26}$$

$$v=\frac{1}{2\eta}\frac{\partial p}{\partial y}.\left(z^2-zh\right)+\left(V_2-V_1\right)\frac{z}{h}+V_1 \tag{2.27}$$

Flow through a column of fluid

A column of lubricant between the solid surfaces it is now considered. Flow per unit width in the x and y directions respectively can be written as:

$$q_x = \int_0^h u dz \tag{2.28}$$

$$q_y = \int_0^h v dz \tag{2.29}$$

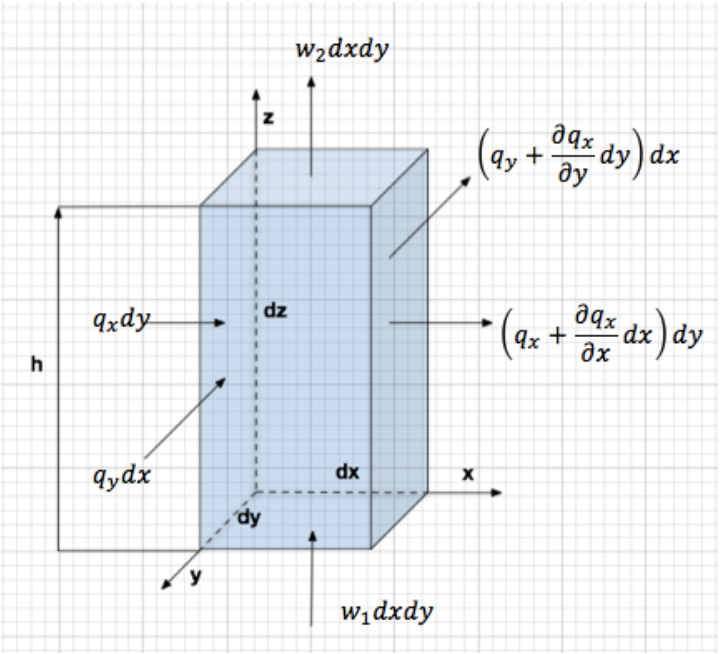

Figure 2.7: Flow through a column of fluid

Replacing the expressions of u and v and integrating these equations gives:

$$q_x=-\frac{h^3}{12\eta}\frac{\partial p}{\partial x}+\left(U_2+U_1\right)\frac{h}{2} \tag{2.30}$$

$$q_y=-\frac{h^3}{12\eta}\frac{\partial p}{\partial y}+\left(V_2+V_1\right)\frac{h}{2} \tag{2.31}$$

Reynolds equation

The fluid must obey the law of continuity of flow in each direction, thus using figure 2.7, the flow entering the column is equal to the flow exiting it.

$$q_x dy + q_y dx + w_1 dx dy = \left(q_x + \frac{\partial q_x}{\partial x} dx \right) dy + \left(q_y + \frac{\partial q_y}{\partial y} dy \right) dx + w_2 dx dy \tag{2.32}$$

After simplifying the like terms this equation becomes:

$$\frac{\partial q_x}{\partial x} + \frac{\partial q_y}{\partial y} + (w_2 - w_1) = 0 \tag{2.33}$$

Substituting the expressions of the flow in both *x* and *y* directions and making the notations $U = (U_1 + U_2)/2$ and $V = (V_1 + V_2)/2$, the full 2-dimensions Reynolds equation is obtained:

$$\frac{\partial}{\partial x}\left\{ \frac{h^3}{\eta} \frac{\partial p}{\partial x} \right\} + \frac{\partial}{\partial y}\left\{ \frac{h^3}{\eta} \frac{\partial p}{\partial y} \right\} = 12\left\{ U \frac{\partial h}{\partial x} + V \frac{\partial h}{\partial y} + w_2 - w_1 \right\} \tag{2.34}$$

2.2.2.2 Equations of elastic deformation of surfaces

In Hertz's theory of smooth contacts, the surfaces are approximated with paraboloids near the point of initial contact, since the contact dimensions are much smaller than the radii of curvature. Further on the deflection of the surfaces, outside of the contact, in EHD conditions are considered equal to those for dry contact. The displacement of a surface, due to a point load, according to Boussinesq [2] is:

$$u(x, y) = \frac{1 - \nu^2}{\pi E} \frac{P}{\sqrt{x^2 - y^2}} \tag{2.35}$$

Where *u* is the displacement of the surface in direction perpendicular to it, at point (x, y), *P* is the applied point load, ν is the Poisson's ratio and E is the Young's modulus of the semi – infinite body. Subsequently, the deformation caused by a surface distributed load $p(x, y)$ can be found by summation (integration) over the whole contact area, S, of point loads due to local application of pressure:

$$u(x,y)=\frac{1-\nu^2}{\pi E}\iint_S \frac{p(x',y')dx'dy'}{\sqrt{(x-x')^2+(y-y')^2}} \tag{2.36}$$

It follows that the actual gap outside the contact area $h(x,y)$ is obtained by mutual approach δ, from the sum between the elastic deformation and the parabolic approximation of the undeformed gap between the two solids:

$$h(x,y)=-\delta+\frac{x^2}{2R_x}+\frac{y^2}{2R_y}\frac{2}{\pi E^*}\iint_S \frac{p(x',y')dx'dy'}{\sqrt{(x-x')^2+(y-y')^2}} \tag{2.37}$$

2.2.2.3 Force balance equation

In EHD contacts the pressure distribution is caused by the applied load on the lubricating film therefore the integral of this pressure distribution should equal the applied force.

$$\iint_S p(x,y)dxdy=P \tag{2.38}$$

2.2.2.4 Viscosity and density variation with pressure

In EHD lubrication, viscosity and density of the lubricant are dependent on the high pressure generated within the contact. One of the most used pressure-viscosity equations, due to its simplicity and convenience for mathematical manipulations, was proposed by Barus [5] as early as in 1893.

$$\eta=\eta_0 e^{\alpha p} \tag{2.39}$$

where:

- η is the absolute viscosity of the lubricant at a given pressure p
- η_0 is absolute viscosity at atmospheric pressure and constant temperature
- α is pressure-viscosity coefficient of the lubricant

Barus's equation is widely applied to calculate the viscosity of lubricants at a given pressure, however, it only provides reasonable prediction at moderate pressures, that is < 0.1GPa.

In 1966, Roelands [6] developed an approach to evaluate the effect of a wide-range pressures on lubricant viscosity.

$$\eta = \eta_o \exp\left(\frac{P_o \alpha_o}{z} \left\{ \left(1 + \frac{p}{P_o} \right)^z - 1 \right\} \right) \tag{2.40}$$

α_0 is the pressure – viscosity coefficient given by $\alpha_o = 5.1e^{-9} z\left(\ln(\eta_o) + 9.67\right)$ while z and P_0 are constants depending on the type of oil. For example, suitable values for these constants for mineral oils are $z = 0.68$ and $P_o = 1.98 \times 10^8$.

Due to the high pressure generated in EHD films, it is also necessary, in numerical calculations, to consider the dependence of density on pressure. According to Dowson and Higginson [7], the expression for the dimensionless density for mineral oils can be written as:

$$\bar{\rho} = \frac{\rho}{\rho_0} = 1 + \frac{0.6p}{1 + 1.7p} \tag{2.41}$$

Where ρ_0 is density at atmospheric pressure and p is gage pressure [GPa].

2.2.2.5 Viscosity variation with temperature

In the current research the temperature of the lubricating fluid was kept constant, however it is worth mentioning that the viscosity depends strongly of temperature. There are many models describing this variation [8], Some of these equation, together with their author are shown in Table 2.1.

Table 2.1: Various equations for the variation of viscosity with temperature

Equation	Author
$\eta = \mathrm{Re}^{-\alpha t}$	Reynolds
$\eta = \dfrac{S}{(a+t)^m}$	Slotte
$\eta = Ke^{b/(t+\theta)}$	Vogel
$\eta + \gamma = \beta D^{1/T^c}$	Walter (ASTM)
T – absolute temperature, t – temperature	

2.2.3 Ertel – Grubin solution for line contacts

Efforts to find an analytical solution to the problem of lubrication of gears were intense at the beginning of the 20th century, however only in 1949 Grubin and Vinogradova in [8] published a semi – analytical solution which gives an excellent insight into the phenomena which govern the EHD lubrication regime. Cameron [9] claimed that the solution belonged to Ertel, Grubin's

professor, but who did not have a courage to publish the work, so it was due to his assistant to do it after his death. For this reason, the solution, which was developed for linear contacts, is often known as the Ertel – Grubin solution. Ertel – Grubin realised two important phenomena: the lubricant is dragged within the converging gap between the contacting cylinders thus the Reynolds equation for lubrication of sliding bearings must apply. In two dimensions, this equation is [8]:

$$\frac{\mathrm{d}p}{\mathrm{d}x} = 6U\eta\left(\frac{h-\bar{h}}{h^3}\right) \tag{2.42}$$

In equation 2.42, p is the pressure, U the entrainment velocity in direction x, η is the lubricant viscosity, h the separation between solid surfaces, in other words the lubricant film thickness, and $\bar{h}$ is the film thickness at the location of the maximum pressure, where the pressure gradient is zero.

Secondly, they appreciated that the pressure inside the EHD contact cannot be very different from the Hertzian pressure of the dry contact. This means that the geometry of the deformed surfaces, in front of the contact is the same as that given by Hertz theory for dry contacts. As it was shown previously the distribution of the pressure in a linear contact is a parabolic cylinder, so in two dimensions this distribution is parabolic, as shown in figure 2.8. This distribution made Ertel and Grubin realise that the pressure increases very rapidly just inside the contact boundary and then changes very little over most of the contact area. Thus, they defined an equivalent pressure, denoted by q_0 and defined as:

$$q_0 = \frac{1}{\alpha}\left(1 - e^{-\alpha p}\right) \tag{2.43}$$

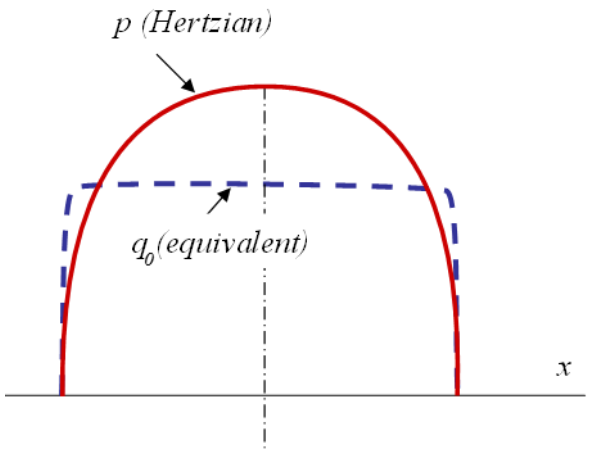

Figure 2.8: Hertzian and equivalent pressure distributions

In equation 2.43, α is the pressure – viscosity coefficient, thus as the pressure for most over the contact area is very large, the second term in the bracket becomes negligible in comparison to unity and the equivalent pressure is constant over the contact area and equal to $1/\alpha$.
The Reynolds equation now changes to:

$$\frac{dq_0}{dx} = 6U\eta_0\left(\frac{h-\bar{h}}{h^3}\right) \tag{2.44}$$

Two important observations can be drawn from this equation:

- Because q_0 is constant with respect to x and its derivative is zero. this in turn means that the lubricant film thickness must be constant and equal to $\bar{h}$, that is the thickness at the point where the pressure is maximum (over the whole contact area);
- The second observation is that the viscosity of the lubricant which determines the film thickness is that at ambient pressure, η_0. This is the viscosity in front of the contact, where the pressure has not increased yet significantly.

The two sides in equation 2.44 are multiplied by dx and integrated between $-\infty$ and the edge of the contact ($x = -a$) yielding:

$$q_0 = 6U\eta_0\int_{-\infty}^{-a}\left(\frac{h-\bar{h}}{h^3}\right)dx = \frac{1}{\alpha} \tag{2.45}$$

This equation can be further written as:

$$\int_{-\infty}^{-a}\left(\frac{h-\bar{h}}{h^3}\right)dx = \frac{1}{6U\eta_0\alpha} \tag{2.46}$$

If the lubricant film thickness is constant over the whole contact area, then the separation between the solid surfaces, in the inlet is given by this thickness plus the gap resulted from Hertz theory. Denoting the constant thickness gap by h_c we get:

$$h(x) = h_c + \frac{a}{2R}\left[\frac{x}{a}\sqrt{\frac{x^2}{a^2}-1} - \ln\left(\frac{x}{a}+\sqrt{\frac{x^2}{a^2}-1}\right)\right] \tag{2.47}$$

Introducing $h(x)$ in equation 2.48, it results into an integral which can be solved numerically to give the constant thickness of the lubricant film inside the contact. Further on by writing the

semi-width of the contact in terms of the load and elastic properties as given by Hertz theory, the central film thickness results as [8]:

$$\frac{h_c}{R} = 1.19\left(\frac{U\eta_0\alpha}{R}\right)^{8/11}\left(\frac{W}{ELR}\right)^{-1/11} \qquad (2.48)$$

This equation is for the case when materials of both surfaces are the same, with elastic modulus E.

The Ertel – Grubin equation is approximate and makes use of many simplifying assumptions, however it is better in explaining the mechanisms of the formation of the EHD film thickness than the more accurate, numerically derived formulae.

2.2.4 EHD film features

As explained above, when two non-conformal contacting surfaces are in relative motion, the lubricant in front of the contact is dragged within the convergent constriction to generate the hydrodynamic action which allows the completed separation between surfaces by a thin lubricant film. Once the lubricant enters the contact, it travels almost unchanged until it reaches the outlet area of the contact, where the pressure drops rapidly to ambient values. The rapid decrease of pressure means that the pressure gradient is negative. According to Reynolds equation, equation 2.42, negative pressure is obtained if the film thickness h, is smaller than the central film thickness $h < h_c = \bar{h}$. It follows that at the exit from the contact, the pressure drop is accompanied by a constriction in the film thickness, as shown in figure 2.9. This feature is not included in Ertel – Grubin equation, although they were aware of the phenomenon and discussed it.

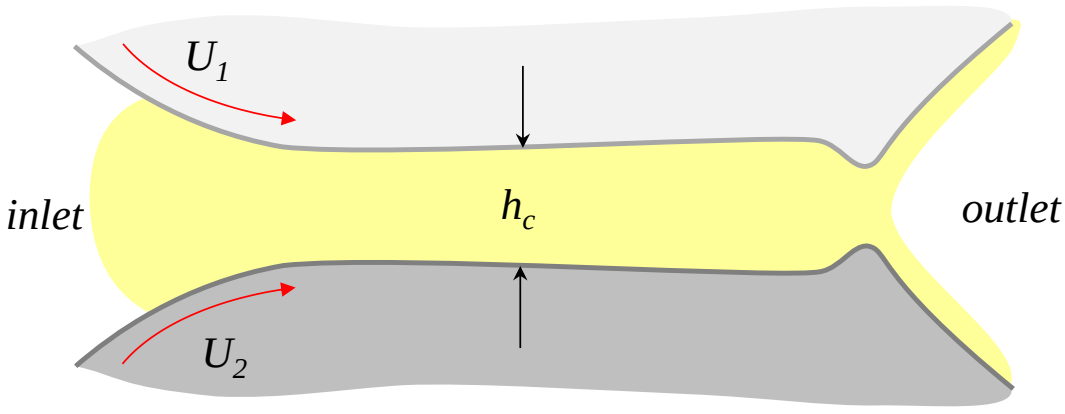

Figure 2.9: Surface separation by a thin lubricant film

Greenwood [10] derived the exit constriction theoretically by moving the parallel region of the film off centre.

Detailed features of EHD film captured by optical interferometry for PAO 40 (poly–alpha–

olefin) at an entrainment speed of 0.126 m/s, under 20 N normal contact load and at ambient temperature is shown in figure 2.10. Newton's rings and the distinctive horseshoe shape of the contact can be seen clearly, alongside the constricted regions at the side lobes and the exit region of the contact. Film thickness is constant in the central region of the contact.

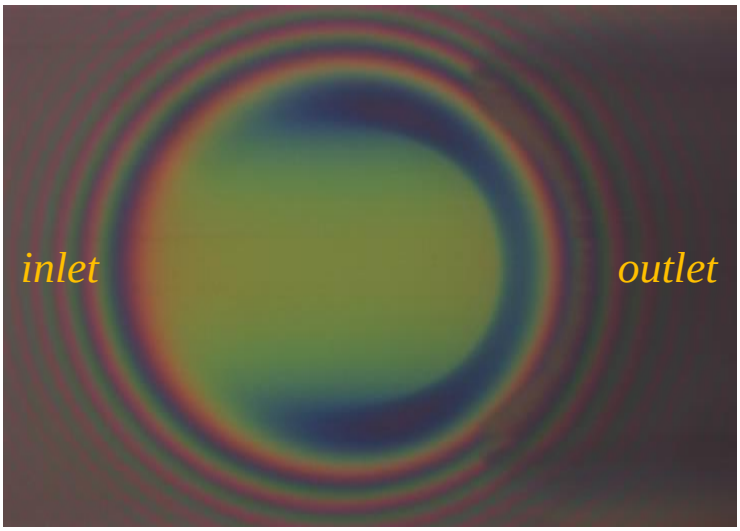

Figure 2.10: Example of contact image by optical interferometry

The film thickness profiles longitudinal and transversal to the rolling direction are presented in figure 2.11.

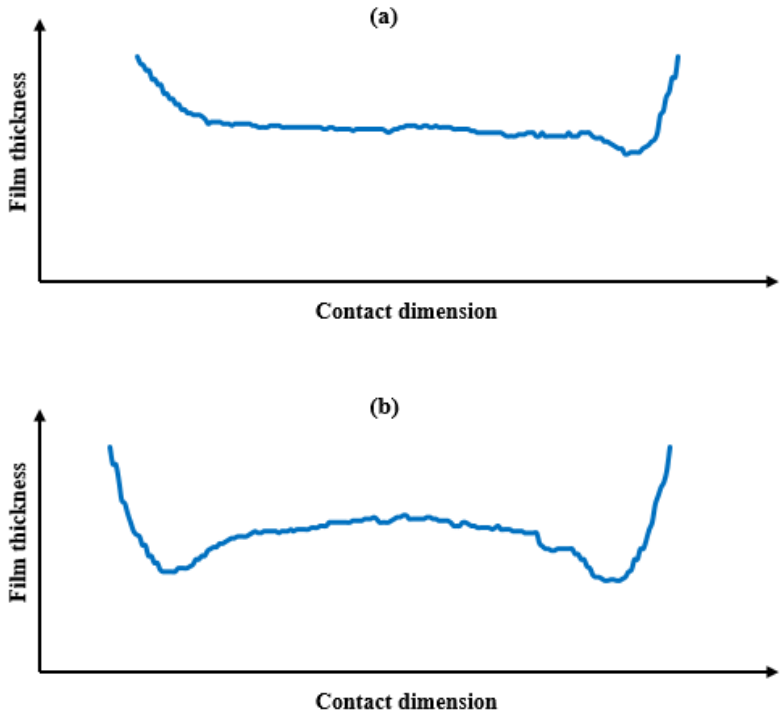

Figure 2.11: Film thickness profiles in the contact (a) film thickness profile longitudinal to the rolling direction; (b) film thickness profile transversal to the rolling direction

From both theoretical and experimental point of investigations, it is well understood that steady state condition EHD film is mainly influenced by the following factors [99-101]:

- Lubricant viscosity strongly affects both central and minimum film thickness in the contact
- Load applied to the contact only slightly affect both central and minimum film thickness
- Entrainment speed strongly affects both central and minimum film thickness in the contact.

2.2.5 EHD film thickness equations

After the earlier semi-analytical solution of Ertel and Grubin, Dowson and Higginson [7] have developed a full numerical solution to the line contact EHD film thickness.

$$\frac{h_{\min}}{R_x}=2.65\overline{U}^{0.7}\overline{G}^{0.54}\overline{W}_L^{-0.13} \tag{2.49}$$

As seen the film thickness can be written in terms of three non-dimensional parameters. These are called dimensionless groups of EHD lubrication.

$\overline{U}=\frac{U\eta_o}{E^*R_x}$ - speed parameter;

$\overline{G}=\alpha E^*$ - materials parameter;

$\overline{W}_L=\frac{W}{E^*R_xL}$ - load parameter;

The good agreement of Ertel – Grubin equation with experimental results have prompted researchers in the field to try to extend it to point contacts. Archard and Kirk [11] suggested a formula for central film thickness, based on a derivation which was not shown in the paper, but which the authors said was very similar to that of Grubin. They claimed good agreement with experimental results based on electrical capacitance.

$$h=0.84\left(\alpha\eta_0V\right)^{0.741}R^{0.407}\left(E/W\right)^{0.074} \tag{2.50}$$

Gohar and Cameron have also tried a solution for point contacts [12] in which they use a power law for the variation of the viscosity with pressure.

$$\eta = \eta_0 (1 + Cp)^n \tag{2.51}$$

Using two-dimensional Reynolds equation, the central film thickness becomes:

$$\frac{h_c}{R} = -\frac{1}{10}\left(\frac{W}{ER^2}\right)^{2/3}\left[\frac{1}{28}\left(\frac{W}{ER^2}\right)^{4/3} + 1.09\left(\frac{W}{ER^2}\right)^{1/3}\left(\frac{\alpha\eta_0 U}{R}\right)^{4/3}\right] \tag{2.52}$$

Dowson and his co-workers have later extended their analysis to point contacts publishing a number of formulae widely used currently to predict both central film thickness and minimum film thickness in circular and elliptical geometries respectively.

Hamrock and Dowson [13]

$$\frac{h_c}{R_x} = 2.69\overline{U}^{0.67}\overline{G}^{0.53}\overline{W}^{-0.067}\left(1 - 0.61e^{-0.73\left(R_y/R_x\right)^{0.64}}\right) \tag{2.53}$$

$$\frac{h_{\min}}{R_x} = 3.63\overline{U}^{0.68}\overline{G}^{0.49}\overline{W}^{-0.073}\left(1 - e^{-0.68\left(R_y/R_x\right)^{0.64}}\right) \tag{2.54}$$

The load parameter is in this case: $\overline{W} = \frac{W}{E^* R_x^2}$

Chittenden and co-workers also developed equations for the lubrication of elliptical contacts, distinguishing the cases of the entrainment along the short and long axes of the contact ellipse [14].

$R_x \geq R_y$ (long ellipse axis is along rolling/entrainment direction)

$$\frac{h_{\min}}{R_x} = 3.00\overline{U}^{0.68}\overline{G}^{0.49}\overline{W}^{-0.073}\left(1 - e^{-0..96\left(R_y/R_x\right)}\right) \tag{2.55}$$

$$\frac{h_c}{R_x} = 3.06\overline{U}^{0.68}\overline{G}^{0.49}\overline{W}^{-0.073}\left(1 - e^{-3.36\left(R_y/R_x\right)}\right) \tag{2.56}$$

$R_x \leq R_y$ (Long ellipse axis is transverse to rolling/entrainment direction)

$$\frac{h_{\min}}{R_x} = 3.63\overline{U}^{0.68}\overline{G}^{0.49}\overline{W}^{-0.073}\left(1 - e^{-0.67\left(R_y/R_x\right)^{2/3}}\right) \tag{2.57}$$

$$\frac{h_c}{R_x} = 4.30\overline{U}^{0.68}\overline{G}^{0.49}\overline{W}^{-0.073}\left(1 - e^{-1.30\left(R_y/R_x\right)^{2/3}}\right) \tag{2.58}$$

2.3 Starvation of EHD contacts

The theoretical analyses mentioned in previous sections were all carried out in the hypothesis that there is plenty of lubricant in the inlet of the contact, that is the so–called fully flooded conditions are met. Very often though there is not enough lubricant in the inlet to ensure fully flooded conditions, in which case the contact is called to be "starved". The most typical machine element working in starved EHD conditions is the rolling element bearing. The repetitive pass of the rolling elements over the same spot on the raceways continuously pushes the lubricant to the sides of rolling track. At large speed, or in case of viscous lubricant, there is no time for the fluid to flow back onto the track and feed the contact of the next rolling element. After certain period of time, this can lead to severe starvation and even contact failure. The film thickness in starved EHD contacts is invariably smaller than that of fully flooded EHD contacts, and it is not only determined by contact geometry, velocity, slide-rolling ratio, load, as well as lubricant properties, but also by the lubricant supply to the contact. Given the importance of rolling element bearings for the correct operation of mechanisms and machines, a great deal of work has been dedicated to the analysis of the starved EHD and the prediction of lubricant film thickness.

In fully flooded conditions, the pressure build-up starts relatively far from contact area as seen in figure 2.12.

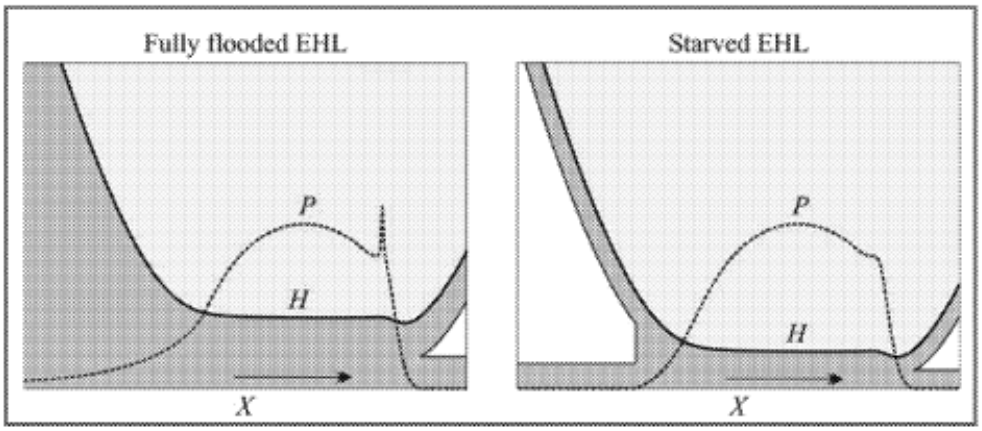

Figure 2.12: Pressure profile in a fully flooded and starved EHD contacts [15]

In the absence of large amount of oil in the inlet of the contact, a very thin layer of lubricant normally adheres to the moving surfaces. As these moving towards the converging gap, these layers merge forming a meniscus in the inlet of the contact. The pressure build-up can only start at this point, meaning that it does not have time to increase significantly before the lubricant enters the Hertzian area. Consequently, the reduced pressure leads to decreased lubricant film thickness within the contact. In severe starved conditions, the film thickness can decrease close to the magnitude of the thickness of oil layers supplied to the contact.

Starved conditions and the effect upon film thickness within the contact can be conveniently observed by optical interferometry.

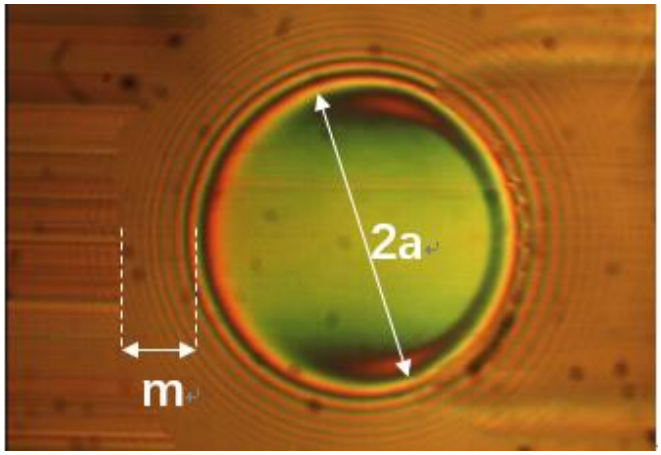

Figure 2.13: Optical interferometry image showing inlet meniscus position

Figure 2.13 shows a circular EHD contact formed by a steel ball rolling against a glass disc coated with a silica spacer layer. The lubricant is PAO 40 and entrainment speed is 0.1 m/s. A simple quantification of starvation can be done by dividing the length of meniscus (*m* in the figure) over the contact diameter (*2a* in the figure); the start of starvation is normally considered when the position of meniscus is closer than two times of contact diameter [16].

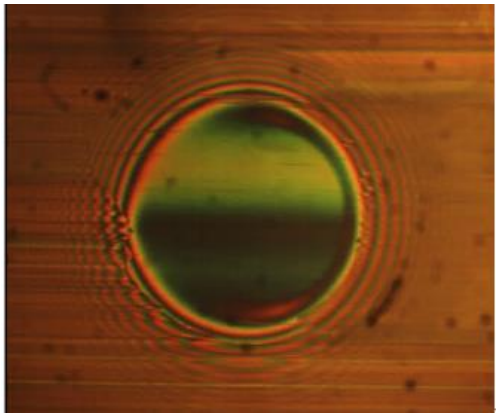

Figure 2.14: Example of starved EHD contact

For quantifying starvation with optical interferometry, the method of meniscus position is only suitable for mild starvation. When the position of meniscus approaches the high – pressure zone (figure 2.14), which means the contact is under severe starvation, the method of meniscus position cannot be used for quantifying starvation and the film thickness cannot be predicted by various equations.

If optical interferometry is available, there is a versatile approach to quantify starvation, which is to calculate film thickness reduction parameter, defined as starved film thickness divided

by its fully flooded film thickness [16,17]. The advantage of this parameter is that it can be used in all range of starvation degrees, and the disadvantage is that fully flooded results must be obtained in the same conditions as the starved results.

Back as earlier as in 1971, Wedeven et al. [18] carried out one of the first detailed, experimental studies of starvation, focusing on rolling point contact. They used optical interferometry to measure the lubricant film thickness in contacts under various degrees of starvation and compared the results with theoretical predictions. Results showed that the film thickness decreases close to zero value when the inlet meniscus approaches the Hertzian contact region. Wedeven's approach will be discussed in more detail in Chapter 7.

Chiu [19] proposed a method for theoretically predicting inlet meniscus position and the degree of starvation by considering the replenishment in the inlet contact oil reservoir. It showed that the theoretically predicted speed at which starvation occurred was in good agreement to the experimental results.

Kingsbury [20] built a cross flow model of a starved EHD contact. He suggested that film thickness in a starved EHD contact was dependent on the rate at which lubricant was forced from the Hertzian contact area normal to the entraining direction.

A few years later, Hamrock and Dowson [21] proposed a starvation formula describing the relation between the inlet boundary (inlet meniscus distance) and film thickness in EHD point contact however, this formula was not practicable for realistic engineering solutions due to the unknown dimensionless inlet meniscus distance.

Cann et al. [22] also employed an optical ball-on-disc based rig to study and monitor the transition between fully flooded and starved regimes in EHD by controlling the lubricant supply volume, contact dimensions, oil viscosity and speed. The test lubricant was a high viscosity poly-alpha-olefin and the test speed range was controlled between 0.01 m/s and 0.5 m/s.

Table 2.2: Test conditions and base oil properties [22]

Load [N]	10, 20, 30
Temperature $°C$	30, 40, 58
Oil volume (μl)	20, 30, 50
Speed (m/s)	0.01-0.5
Lubrication viscosity (Pa s)	0.59 at 30 $°C$ 0.34 at 40 $°C$ 0.16 at 58 $°C$

A dimensionless starvation parameter called "starvation degree" (*SD*), based on operating

parameters was established within this study. The starvation parameter was defined as followed:

$$SD = \frac{\eta_0 ua}{h_{oil\infty}\sigma_s} \tag{2.59}$$

Where $h_{oil\infty}$ denotes oil thickness at contact sides, η_0 is base oil viscosity, σ_s denotes surface tension effects, u is the entrainment speed and a is the radius of contact. Results showed that film thickness was proportional to $u^{0.67}$ when the contact was fully flooded and under relatively low speed. Starvation was found to start at $u = 0.06\, m/s$ and film thickness was proportional to u^{-1} beyond this critical speed. The influence of load upon film thickness in fully flood regime was small, namely film thickness was nearly independent of load changes, however results showed that the film thickness was proportional to $w^{-0.333}$ in the starved regime. Combining the film thickness as a function of speed, viscosity, load and volume of lubricant, the relative film thickness as a function of starvation parameter was plotted as shown in figure 2.15. It was concluded the transition between fully flooded and starved regimes happens at *SD = 1*.

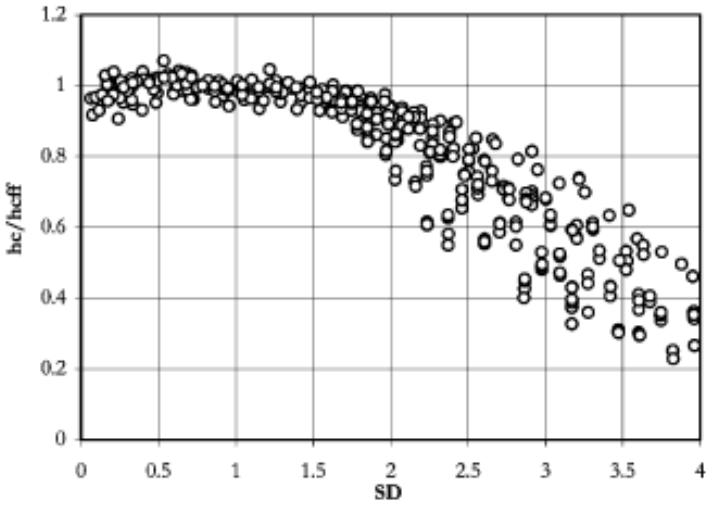

Figure 2.15: Relative film thickness as a function of the SD parameter [22]

Nagata et al. [23] applied lateral vibrations (up to 50 Hz) to a ball-on-flat configuration to study the effect of lateral vibrations upon track replenishment. They used optical interferometry to measure lubricant film thickness on a severely starved grease lubricated EHD contact. They found the lubricant film thickness recovered nearly to the fully flooded value as long as the lateral vibrations were applied and the film thickness level remained unchanged over long periods of time.

More recently, Svoboda et al. [24] employed a two contacts EHD test rig to develop a new experimental method which was able to provide film thickness in starved EHD contacts as a function of film thickness of the inlet oil layer. A schematic of the test rig is shown in figure 2.16.

Two contacts were formed by steel ball/glass disc and spherical roller/glass disc respectively. The principle of this experimental approach was based on the presumption that the residual lubricant film thickness on the glass disc at outlet area of first contact was equal to half of the central film thickness of the first contact, the other half would adhere to the spherical roller surface.

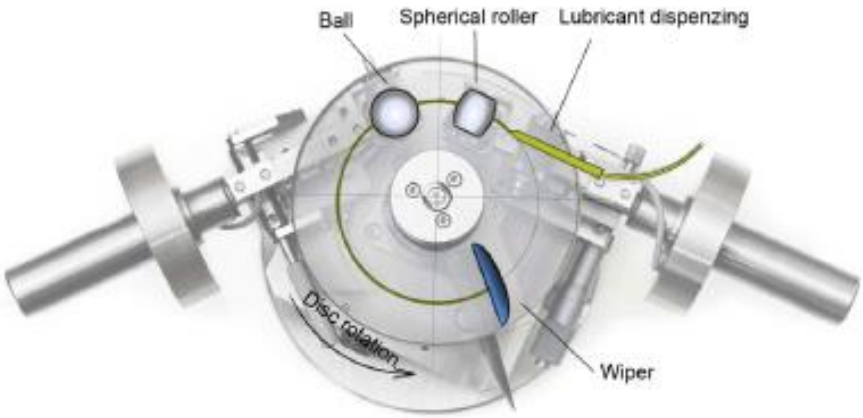

Figure 2.16: The position of rolling elements [24]

In this way, they were able to quantify lubricant supply to the second contact formed between steel ball and glass disc. The film thickness evaluation was done by the Thin Film Colorimetric Interferometry method. An example of contact image is shown in figure 2.17.

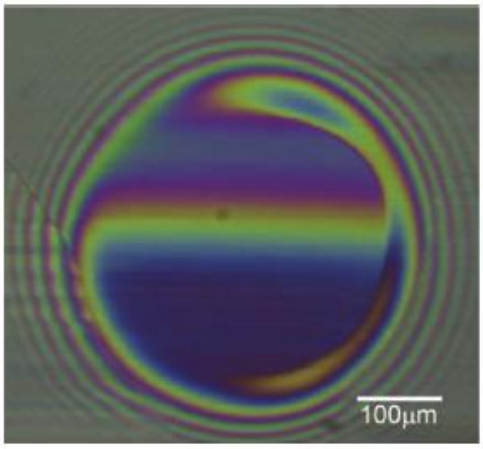

Figure 2.17: Example of image of starved EHD contact [24]

The results showed that this multiple contact rig was capable to simulate starved conditions of rolling bearings. They also compared well with theoretical prediction showed in [17].

Kostal et al. [16] published the results of a study dedicated to controlling and measuring starvation severity in EHD contacts by using a ball on disc machine with lubricant dispenser. This paper summarised the main aspects of starvation and showed experimentally a comparison with fully flooded regime. The process of transition between fully flooded regime to severe starved

regime was monitored by a high-speed camera. Colorimetric interferometry was applied to evaluated captured interferometry images of the EHD contact, as seen in figure 2.18. Measured central film thickness were found in good agreement with Hamrock-Downson formula.

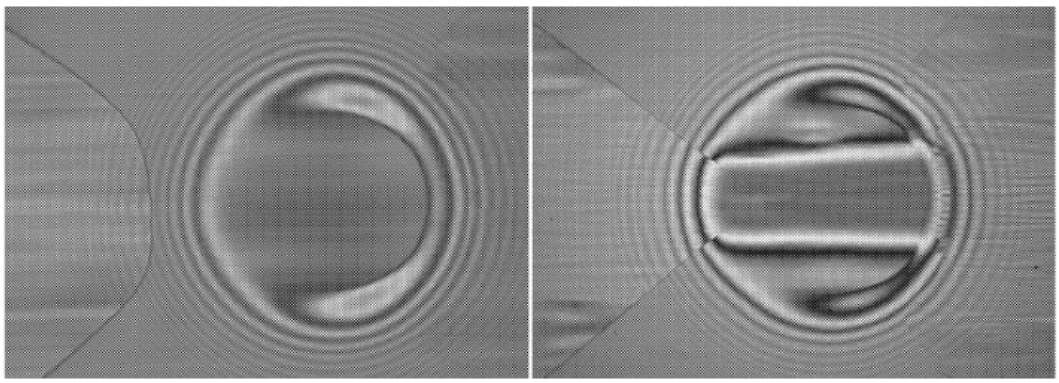

Figure 2.18: Mild and severely starved contacts [16]

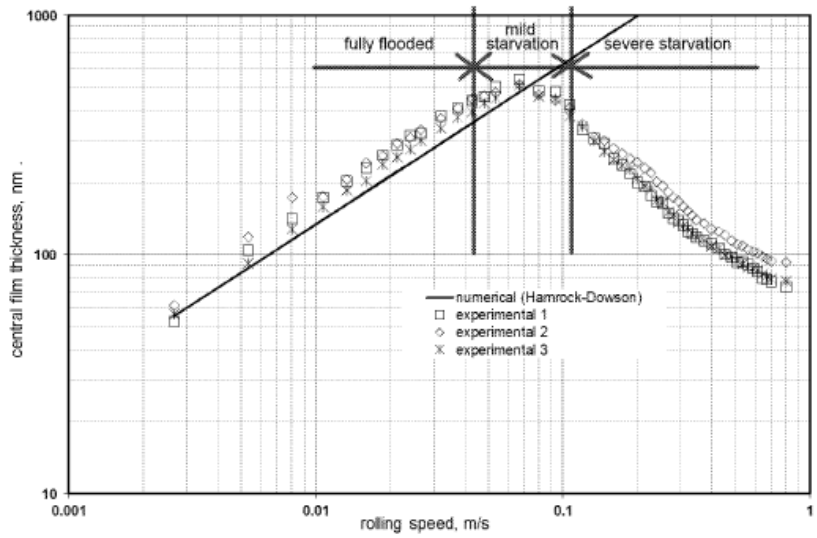

Figure 2.19: Transition between fully flooded and starved regimes [16]

Fully flooded and starved results are showed in the figure 2.19; the film thickness in fully flooded regime were found to be identical to theoretical prediction, however in severe starved conditions it was continuously decreasing (approaching zero) with increasing the rolling speed. The regime of mild starvation indicated that this was the area where starvation normally starts to occur and there was a balance between starvation and replenishment effects.

Liang et al. [25] employed the so - called optical relative intensity technique (ROII) to study lubrication film starvation at higher speeds. The newly designed test rig was able to observe starvation at high speeds of up to 30 m/s. The test lubricant was poly-alpha-olefin (PAO8) and working temperature was maintained at $25°C$. Test load was 25N and the contact was in pure rolling conditions throughout the whole experiments. The amount of oil supply was 255 ml/min and 51 ml/min for fully flooded and starvation tests respectively.

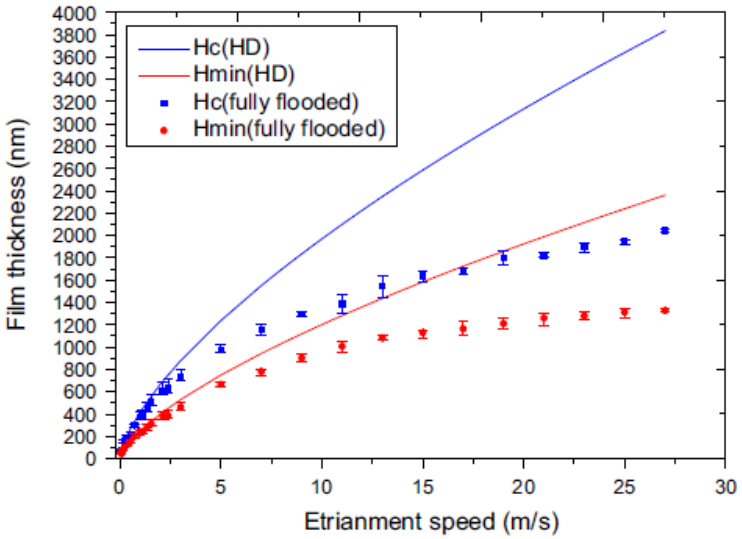

Figure 2.20: Fully flooded central film thickness and minimum film thickness [25]

The figure above shows the measured central film thickness and minimum film thickness compared with Hamrock-Dowson prediction throughout the experimental speed range. The measured central film thickness and minimum film thickness followed the theoretical prediction until rolling speeds of up to 4m/s. After this speed both central film thickness and minimum film thickness started to depart from theoretical predictions. The authors claimed that the deviation between measured film thickness and theoretical prediction after 4m/s was due to thermal heating effect in the inlet of the contact.

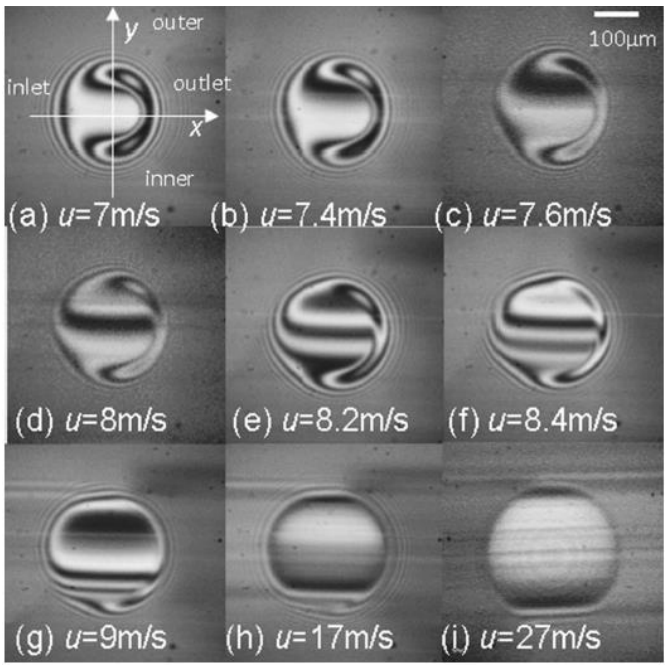

Figure 2.21: Starved interference images at different rolling speeds [25]

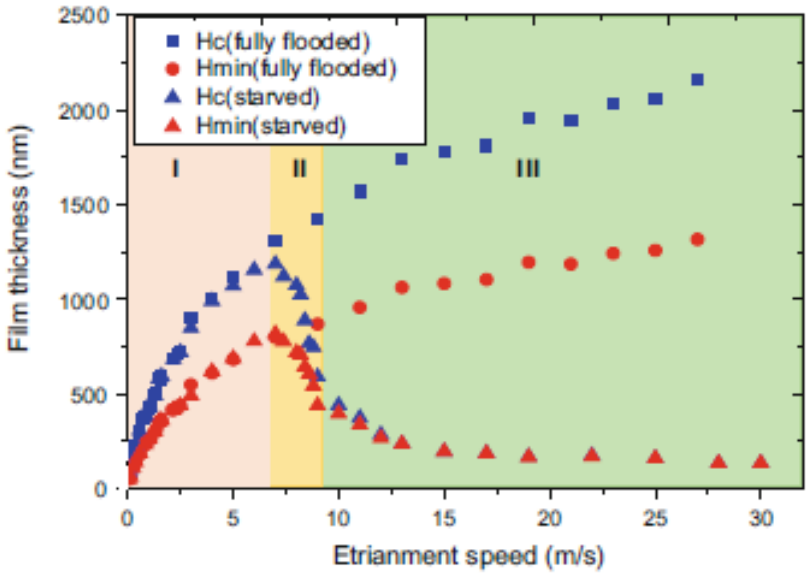

Figure 2.22: Starved film thickness compared with the fully flooded film thickness [25]

Figure 2.22 shows that the central film thickness under starved condition extracted from images in figure 2.21 was proportional to $u^{-1.6}$ after a critical speed of 7 m/s. The conclusions of these results can be summarised as:

- Centrifugal forces played an important role in the oil reservoir, thus it could indirectly determine the degree of starvation.
- Film thickness distribution in the contact zone was dependent on the amount of oil in the side reservoirs.
-

2.4 Conclusions

The elastohydrodynamic film formations mechanisms are well understood in steady state regime due to extensive experimental and theoretical work. The thickness of the EHD films can be predicted with formulas derived from numerical analysis and proved by experiments.

Often the conditions of operation of machine components make the EHD contacts work with limited supply of lubricant, condition known as starved regime. Contacts lubricated by greases are typical examples of this regime. Starvation of EHD contacts is controlled by the amount of lubricant in the inlet of the contact and by the mechanisms by which the inlet is replenished. Various criteria for evaluating the conditions of the occurrence of starved lubrication have been proposed. In this case the film thickness formulas mentioned above do not hold.

Chapter 3: Review of Transient Phenomena in EHD Lubrication

The behaviour of machine components' contacts lubricated in the elastohydrodynamic (EHD) regime is well understood for smooth surfaces, steady-state conditions. However, EHD contacts of real applications frequently experience variation of speed, load, geometry, and vibrations generated within the contacts or transmitted from the environment. Therefore, the effect of transient phenomena in EHD lubrication has drawn particular attention from both a theoretical and experimental point of view during the last couple of decades. Transient events in EHD lubrication can be divided into three main categories [26]:

- Variation of surface velocity, including squeeze, entrainment, and a combination of the two;
- Variation of load, including impact loading;
- Variation of contacting surfaces geometry, including surface roughness;

The variation of load is the subject of this research thus it will be reviewed in this chapter. The variation of speed in the direction normal to the contact surfaces is also similar to the phenomena analysed in this thesis thus it will also be included. The variation of entrainment speed maybe surprisingly has the same effect upon the lubricant film thickness as the variation of load [26]. This is because an EHD contact running in steady state conditions is a dynamic system in equilibrium; sudden variation of speed or load takes this system out from the equilibrium state, and it responds by gradually adjusting the film thickness until equilibrium is again reached. The behaviour of EHD films in the presence of surface features (dimples, ridges, depressions, etc.), although it is an important aspect of transient EHD lubrication, it will not be treated in this chapter as the phenomena which accompanies it are different in nature from those induced by rapid variation of speed or load.

3.1 EHD contacts subjected to variation of speed

3.1.1 The effect of variable entrainment speed

Rapid variation of the entrainment speed causes the collapse of the film such that in this situation the film formation is governed by both entrainment and squeeze. The combination of these phenomena makes the film thickness very different from the steady state conditions. At the same time, any change of the conditions in the inlet of the contact will result in the variation of the film thickness, travels through the gap at the entrainment velocity, which adds a temporal dimension to the phenomena. Both experimental and theoretical studies upon this aspect of EHD lubrication have been carried out by many researchers, such as Scales et al. [27], Ren et al. [28],

Rutlin et al. [29] and Nishikawa et al. [30] as well as many others. It can be concluded that the research focusing on the effect of entrainment speed variation addresses five particular types of situations [26]:

- Start form rest or step of entrainment speed;
- Start-stop of motion;
- Unidirectional variation of entrainment speed;
- Repetitive start-stop;
- Reversal of entrainment.

Following on experimental research in which the entrainment speed of a ball – on – disc apparatus was varied cyclically, Sugimura et al. [31] proposed an equation based on continuity of flow to evaluate the EHD film thickness under acceleration. The film thickness approximation was supported by experimental film thickness results from ultra-thin film interferometry technique.

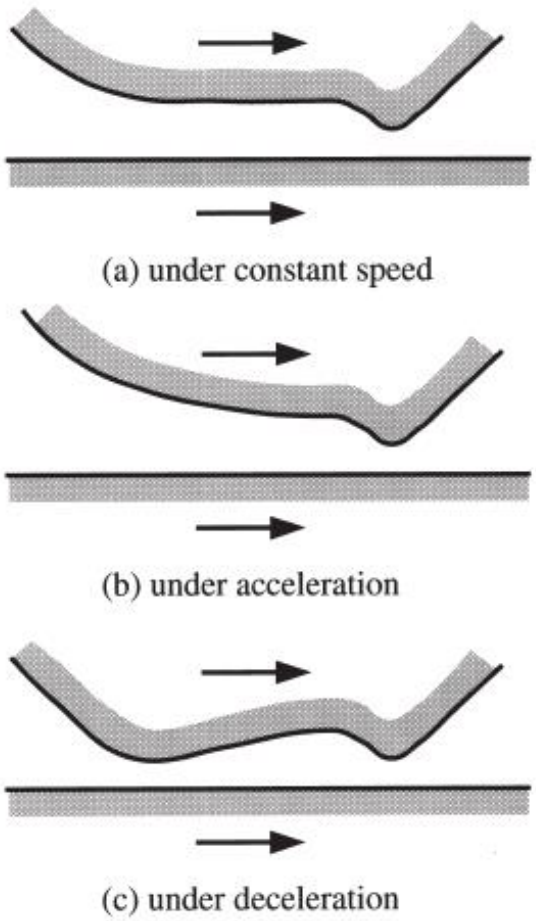

Figure 3.1: EHD film profiles under different speed variations [31]

The proposed equation was based on two assumptions; firstly, the central film thickness was related to the velocity of the upstream boundaries of the Hertzian contact when the fluid flowed into the conjunction, and secondly, the film thickness can be approximated by the conventional steady-state EHD formula with upstream velocity.

The central film thickness at the velocity u under acceleration a was then written as:

$$h(u,a) = h_s\left(u_\xi\right) \tag{3.1}$$

Where h_s is the steady state central film thickness, u_ξ is the velocity that fluid at upstream position $-\xi b$, with ξ the non – dimensional distance. The film thickness, according to Hamrock and Dowson equation was written as:

$$h(u) = Ku^{0.67} \tag{3.2}$$

For constant acceleration the relationship between the velocity at a certain location ξb and that at the inlet can be written as $u_\xi^2 = u^2 - 2a\xi b = u^2\left(1 - \frac{2a\xi b}{u^2}\right)$. Introducing this in (3.2) the relationship of the film thickness becomes:

$$h(u) = Ku^{0.67}\left(1 - \frac{2a\xi b}{u^2}\right)^{0.67/2} \tag{3.3}$$

In equation 3.3, b is Hertzian radius, K is constant. Neglecting the higher order terms, the film thickness becomes:

$$h(u) = Ku^{0.67}\left(1 - \frac{0.67a\xi b}{u^2}\right) \tag{3.4}$$

Figure 3.1 illustrates film thickness profiles along the direction of entraining motion calculated by using this simple formula. It indicated that film between inlet and centre of contact has a converging shape under acceleration, but a diverging shape during deceleration.

Chang [32] changed the Reynolds equation to a simplified, transient form which practically accounts for the passage of the lubricant through the contact. This equation was subsequently solved numerically for the transient film thickness. Glovnea and Spikes [33] described an experimental investigation into EHD film thickness response to rapid halting of motion. Four types of oils such as Poly-alpha-olefin (PAO), Mineral oil (HVI 650), Alkylated Cyclopentane (MACP) and Polyphenyl Ether (5P4E), were tested to find the influence of lubricant properties upon the changes in film thickness and film profile. They emphasized that there were two distinct stages for EHD film collapse. During the first stage of film collapse which according to their

experimental conditions, lasted up to 5 milliseconds, the lubricant behaviour was dominated by entrainment and squeeze. They concluded that during this stage, the pressure over the contact area did not change significantly. The second stage started when the motion had completely ceased, and the film was under pure squeeze. In the second stage, the film thickness and film profile characteristics were strongly dependent on fluid's viscosity and pressure viscosity coefficient.

Glovnea and Spikes [34,35] continued the studies of EHD film collapse during rapid deceleration (up to 75 ms^{-2}) from both experimental and theoretical point of view. Their experiment setup was based on ultra-thin film interferometry coupled with a high-speed camera to measure the change in film thickness and film profile during controlled deceleration in both pure sliding and pure rolling conditions.

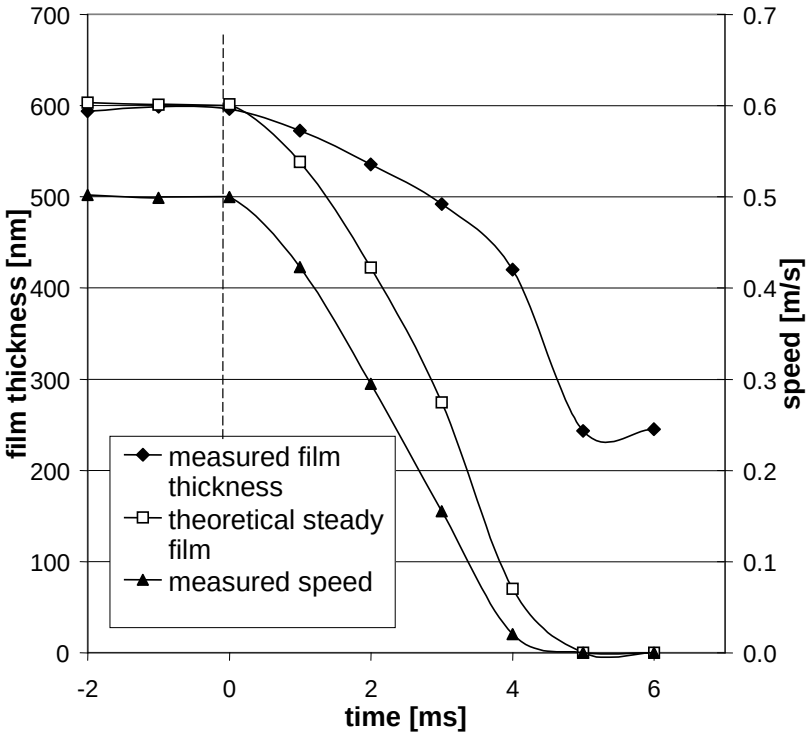

Figure 3.2: Comparison of measured and theoretical steady state film thickness [34]

In pure sliding conditions, the disc was fixed and only the ball moved, to make it easier to control during sudden halting due to the low inertia of the ball. In pure rolling conditions, both the ball and the disc were separately driven by same speed and halted synchronously. The oil employed in these experiments was poly-alpha-olefin (PAO) at the temperature of 50°C in pure sliding conditions and at the temperature of 70°C in pure rolling conditions. During the first stage of film collapse, their experimental results showed that the film geometry remained almost unchanged while film thickness decreasing rate, derived from measured values, was smaller than that predicted by steady-state theory. Figure 3.2 compares the steady state (eq. 2.53) and transient central film thickness during rapid deceleration at 75 ms^{-2}. They also showed that the transient film thickness deviated less from steady state predictions at lower decelerations, as illustrated in

figure 3.3.

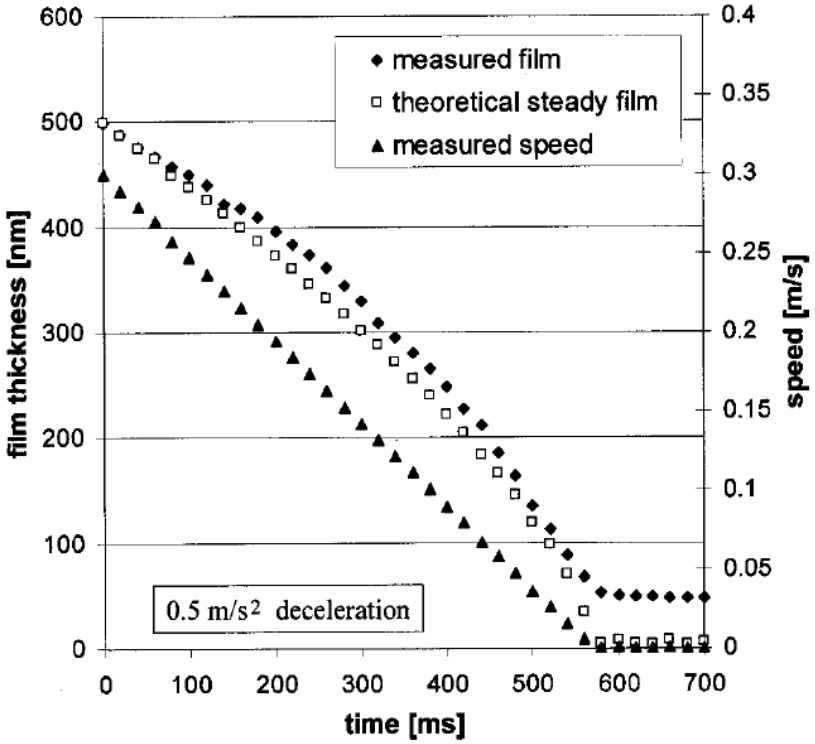

Figure 3.3: Comparison of measured and transient film thickness (1 ms^{-2}) [34]

In the second stage of film collapse, their experimental results showed that a dimple was formed inside the contact area and the central film thickness remained almost constant for long periods of time.

Based on those experimental results the same authors developed a theoretical model [35] following Ertel-Grubin analytical solution [8] for EHD lubrication to compare with the experimental results. The analytical solution used time-dependent Reynolds equation combined with Ertel-Grubin approach according to which gap geometry in the inlet region was that corresponding to dry contacts. Based on experimental observation that the film thickness profile does not change significantly during the first stage, the pressure gradient can be written as:

$$\frac{\partial p}{\partial x} = 6\eta U \frac{h - h_o}{h^3} + 12\eta \dot{h}_o \frac{x - x_o}{h^3} \tag{3.5}$$

From this point forward, they followed Grubin's semi-analytical method and derived the transient, central film thickness:

$$h_o = h_s \left(1 - 8.968 \frac{b}{h_o} \frac{\dot{h}_o}{U}\right)^{8/11} \tag{3.6}$$

This equation was simplified further by expanding in series, neglecting higher order terms and arranging it into a Bernoulli-type differential equation.

$$\dot{h}_o - \frac{U}{6.522b} h_o = -\frac{U}{6.522bh_s} h_o^2 \tag{3.7}$$

This differential equation, with the unknown h_0, was solved to give transient film thickness with variable entrainment speed:

$$h_o(t) = \frac{h_s}{e^{\left(-\frac{1}{6.522\,b}\int_0^t U\,dt\right)}\left\{\frac{h_s}{h_i} + \frac{U^{8/11}}{6.522\,b}\int_0^t\left[U^{3/11}e^{\left(\frac{1}{6.522\,b}\int_0^t U\,dt\right)}\right]dt\right\}} \tag{3.8}$$

where h_i is the value at time, t=0.

The theoretical model seen above showed good agreement over 80-85 percent of deceleration time in pure rolling and pure sliding conditions, as illustrated in figure 3.4.

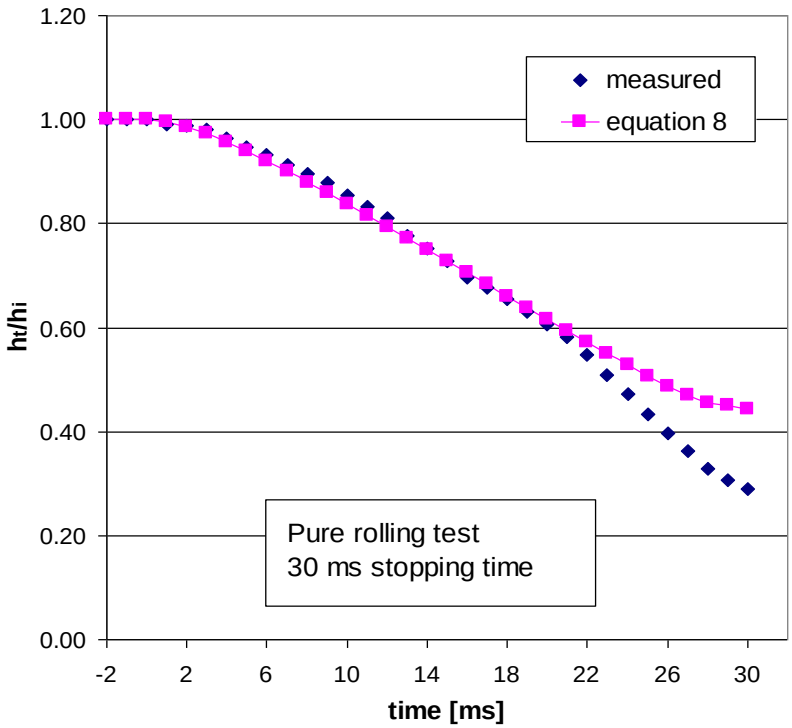

Figure 3.4: Comparison of theoretical and measured film thickness [35]

The sudden start motion is obviously the reverse of the halting of motion. It was also studied in many papers. Glovnea and Spikes [36] carried out a detailed study of the EHD films at the sudden start of the motion. The finding most relevant to this thesis is that, at the brusque change of the entrainment speed, the film thickness experiences fluctuations similar to the damped

amplitude of a mass, spring and damper system, when taken from the position of equilibrium. This can be seen in figure 3.5.

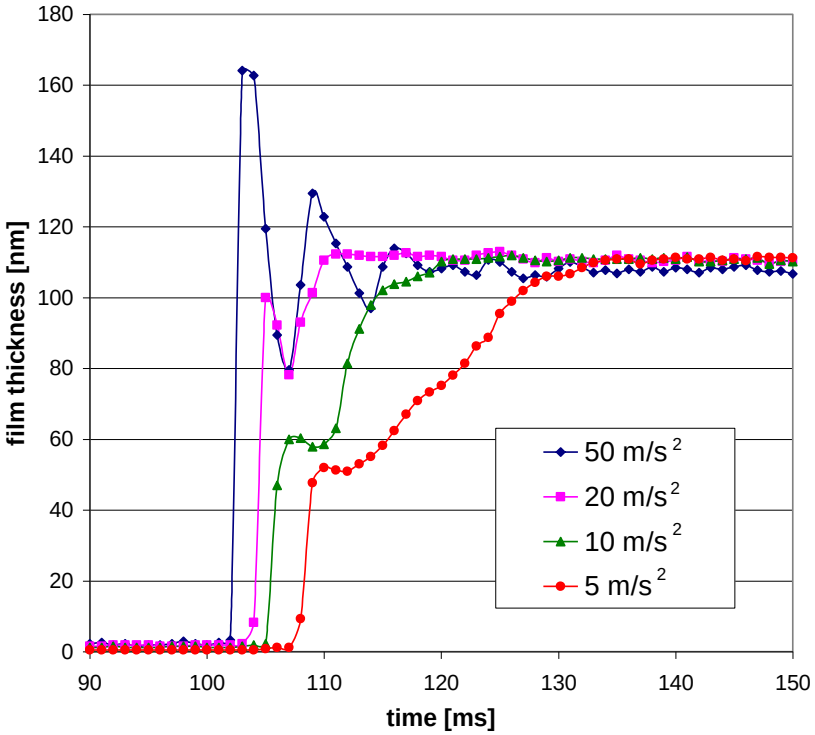

Figure 3.5: Central film thickness during sudden start of motion [36]

The behaviour of EHD films during sudden halting and staring of motion observed experimentally by Glovnea and Spikes was replicated numerically by Holmes et al, showing excellent agreement between the two approaches [37, 38].

Popovici et al. [39] validated the influence of inertia and stiffness related to the configuration of the loading system upon EHD film thickness and mutual approach for a ball-on-disc experimental rig during start up. More importantly, validation of the vibrational behaviour of EHD contacts was achieved by numerically replacing the force balance equation with an equation of motion assuming Hertzian dry contact in the start-up of a single contact model.

The central film thickness and elastic displacement, plotted versus time are shown in figure 3.6. These clearly showed that the loading systems induced oscillations in the film thickness. Moreover, results showed that the period of these oscillations was dependent on the dimensionless natural frequency Ω and a dimensionless spring constant $\overline{K}$. The smaller the natural frequency, the larger the amplitude of the oscillations would be.

Hooke [40] made a detailed theoretical investigation of the minimum film thickness during reversal of entrainment. He predicted that the minimum film thickness for the elastic-isoviscous regime was written as:

$$H^* = 10.2G_3^{0.875} \tag{3.9}$$

For the elastic-piezoviscous regime the minimum film thickness becomes:

$$H^* = 2.66G_1G_3^{-0.5} \tag{3.10}$$

Where $H^* = \frac{h_{min}}{R}[\frac{w^2}{\eta_0^2 aR}]^{2/3}$, $G_1 = [\frac{a^3W^5}{\eta_0^2 aR^4}]^{1/3}$, $G_2 = [\frac{W^7}{E^3\eta_0^3 a^2R^5}]^{1/6}$

In the equations above, a represents the entrainment acceleration, w is the load, η_0 and α is the dynamic viscosity and pressure/viscosity coefficient respectively, R is the reduced radius of curvature in rolling/sliding direction.

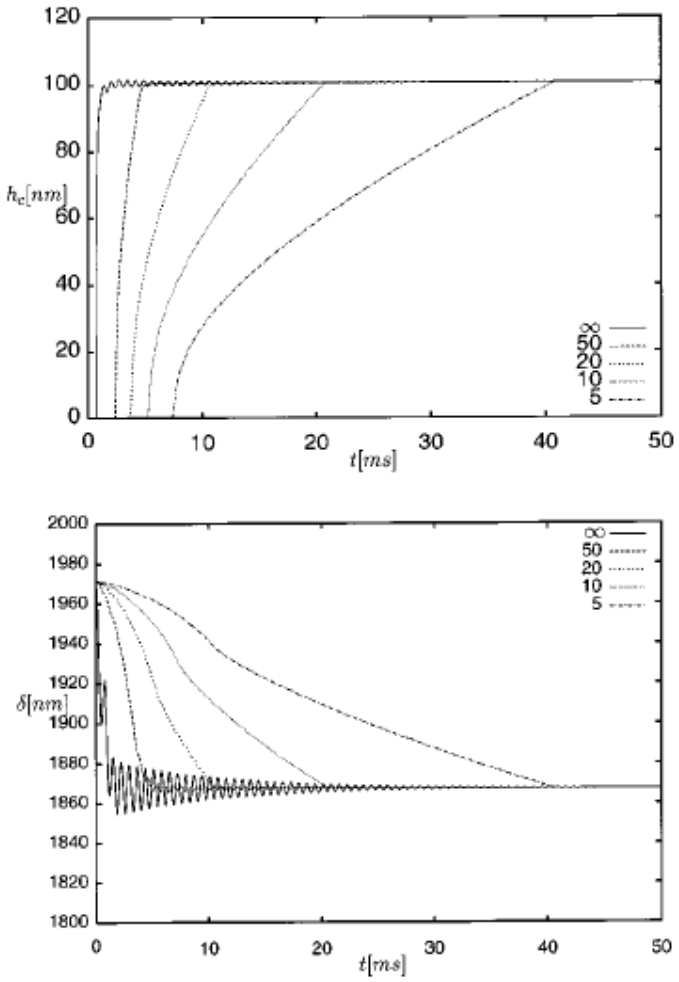

Figure 3.6: Central film thickness (top) and mutual approach (bottom) as functions of time for different accelerations [39]

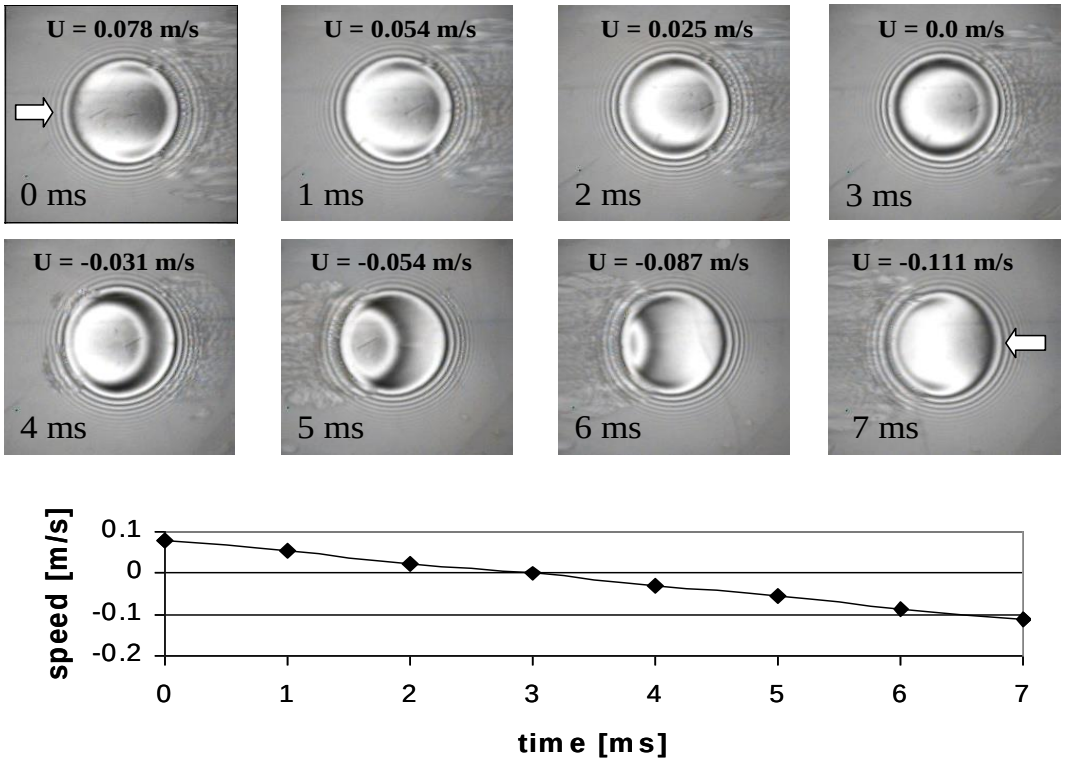

Figure 3.7: Images of the contact during reversal of entrainment [41]

Experimental studies by ultra-thin film interferometry of the behaviour of EHD films subjected to reversal of entrainment were carried out by Glovnea and Spikes [41]. Figure 3.7 shows images of the contact during the reversal of entrainment cycle. As the entrainment speed rapidly decreases the film thickness in the inlet region of the contact drops, however it takes a finite time for this thinner film to pass through the contact. In this way a fluid entrapment is formed over the whole central area of the contact at zero entrainment speed, which prevents the EHD film from complete collapsing. As the velocity changes direction and picks up the minimum film at the right-side of the contact, which has now become the new inlet, travels through the contact as a crescent-shaped film perturbation. It was concluded that, during reversal of entrainment, film perturbations travelling through the contact create large pressure fluctuations.

Figure 3.8 shows measured and theoretical, central and minimum film thickness over one cycle of speed oscillation. The minimum film thickness in the direction of rolling and in transverse direction is also shown.

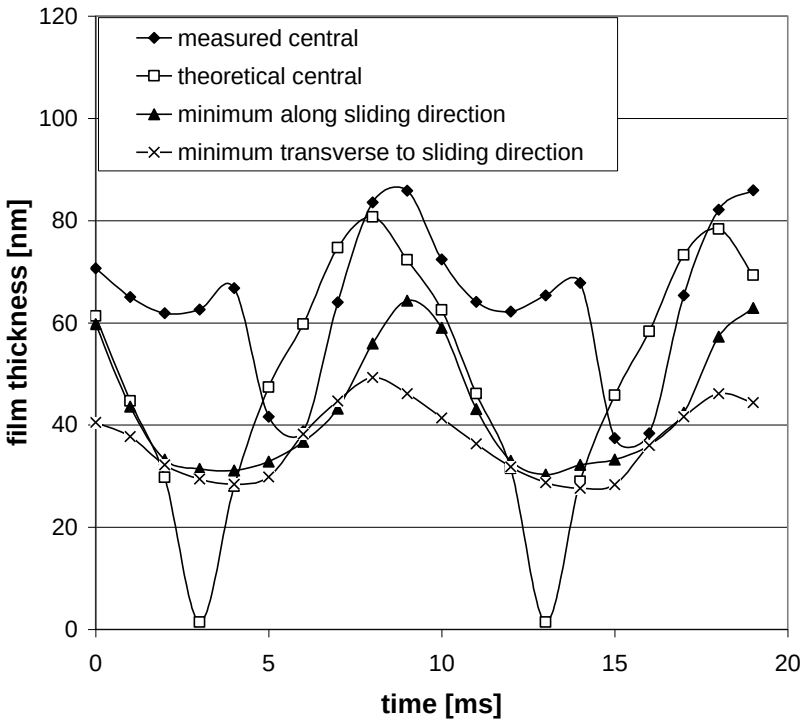

Figure 3.8: Central and minimum film variation during one cycle (50Hz) [41]

Their results showed that transient effects can be neglected at the rates of change of entrainment speed below $\pm 10\, m/s^2$. The measured minimum film thickness value at the side of contact was found to be higher than predicted by Hooke's theory.

3.1.2 Pure squeeze films

The squeeze effect occurs when one solid body drops or rebounds on a lubricated surface, or when the two solid surfaces approach or separate rapidly due to a variation of the entrainment speed. In 1970's, Christensen [42-43] seems to be the pioneer of the theoretical studies in this field of lubrication research. He theoretically combined Reynold's equation with the elastic deformations of the solid bodies during normal approach to obtain pressure distributions and load carrying capacity. He found that the high pressure generated in the central region of the contact could significantly exceed the maximum Hertzian pressure. Herrebrugh [44] proposed a subsequent pure squeeze solution for low elastic modulus materials for the isoviscous point contact. Vichard [45] carried out extended theoretical and experimental studies into the effect of load variation upon EHD film thickness. A capacitive method was used to measure the film thickness in the contact formed between a cam and a follower, the results were compared with theoretical calculations. He found that the squeeze effect contributed to the stability of lubricating thin films.

Lee and Cheng [46] developed a numerical method to solve pure squeeze EHD problems lubricated by a compressible fluid with viscosity varying arbitrarily with pressure. They investigated the effects of surface velocities due to local deformation, the lubricant compressibility and the effect of a lubricant with composite viscosity-pressure coefficients. They found that some lubricant was entrapped in the central part of the conjunction and a dimple was formed when two cylinders impacting each other. Their theoretical results were in good agreement with the experimental findings as found in [47-48].

With the development of more accurate numerical models, it was possible to have detailed solutions to impact EHD lubrication problems (impact and rebound process of a steel ball dropped onto an oily plate) in early 1990's. The problems were analysed by Yang and Wen [49-50] who solved the equation of motion of the ball to determine its position during impact, and Larsson and Hoglund [51] who used a multigrid method to find maximum pressure in the lubricant film. All these theoretical works confirmed the observation of a pressure spike from Safa and Gohar's experimental work [52].

In the middle of 1990's, the prevailing experimental technique of optical interferometry was used in search of more experimental findings on transient phenomenon of EHD lubrication which included squeeze films. Larsson and Lundberg [53] carried out an experimental study of lubricated impact using optical interferometry and a monochromatic light source. PAO type lubricant with the viscosity range from 27 to 2600 mm^2s^{-1} was placed onto a glass disc, which was then impacted with a $\emptyset 70mm$ ball mounted on a pendulum. The impact velocity was kept between 0.08 and 0.29 ms^{-1} throughout their experiments. Black and white recorded interference fringes can be seen in figure 3.9.

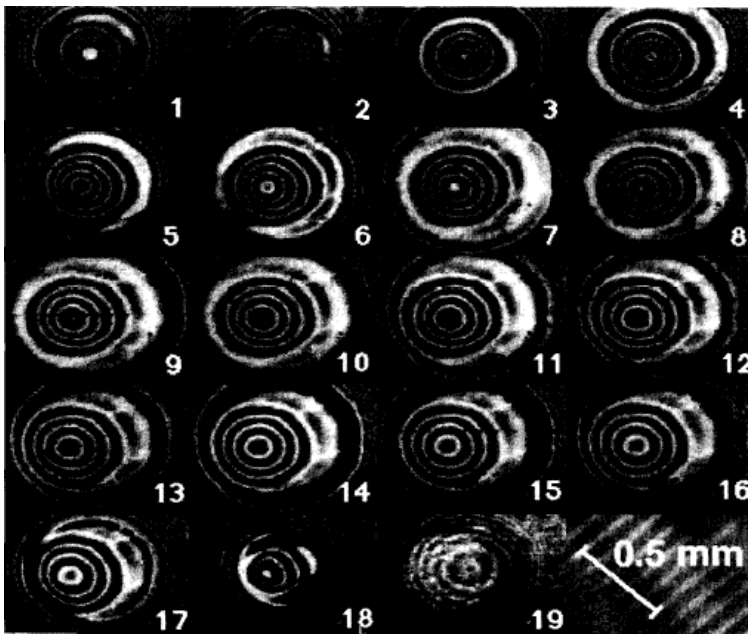

Figure 3.9: High-speed video recordings of interference fringe [53]

Their experimental results can be summarized as follows:

1. For low viscosity lubricants, the deepest dimple was formed at the beginning of the impact time, and after a while it would decrease to a constant level.
2. For high viscosity lubricants, the dimple depth increased slower than low viscosity lubricants
3. The higher the viscosity was, the deeper the dimple would be.
4. Cavitation occurred at the end of the impact time and took place just outside the edges of the dimple.

3.2 Vibrating EHD contacts and transient loading

Over the past few decades of research on EHD contacts, it has been well established that the change of load has little influence on steady-state EHD film thickness. Thus, the experimental studies on the field of dynamic variation of load upon the behaviour of EHD films are less numerous in comparison to those on speed or micro-geometry. Vibrations caused by a variation of the load or entrainment velocity have been reported in a few studies. Both previous experimental and theoretical works on vibrations and transient loading upon the behaviour of EHD films will be discussed in this section.

Carson and Johnson [54] developed a flexible, rolling contact disc experimental rig to investigate the effect of normal vibrations generated by surface corrugations on cylinder-cylinder contacts. They found that vibrations, caused by irregularities of the contacting surfaces in rolling motion, can be sufficiently severe to cause the bodies to bounce apart. This implies that no friction forces can be transmitted by the contact and thus no motion between the bodies. At the same time, the maximum values of the dynamic forces in the contact can exceed the elastic limit of one or both of the bodies and lead to permanent deformations to the contacting surfaces. One of their conclusions was that corrugations of the surfaces due to plastic deformations occur even if a lubricant film was present in the contact.

One year later, Nayak [55] carried out some theoretical works based on sphere – on – plane contact model to discuss and to qualitatively support Carson and Johnson's experimental results in vibratory point contacts. Three areas had been considered, such as loss of contact, plastic information and the formation of corrugations.

In 1975, Dareing and Johnson [56] experimentally studied the fluid film damping of rolling contact vibrations generated by a lubrication film with the aim to find out whether the damping of the film contributes to the total damping. They used a disc machine where the rolling mating discs were subjected to periodic excitations caused by surface corrugations.

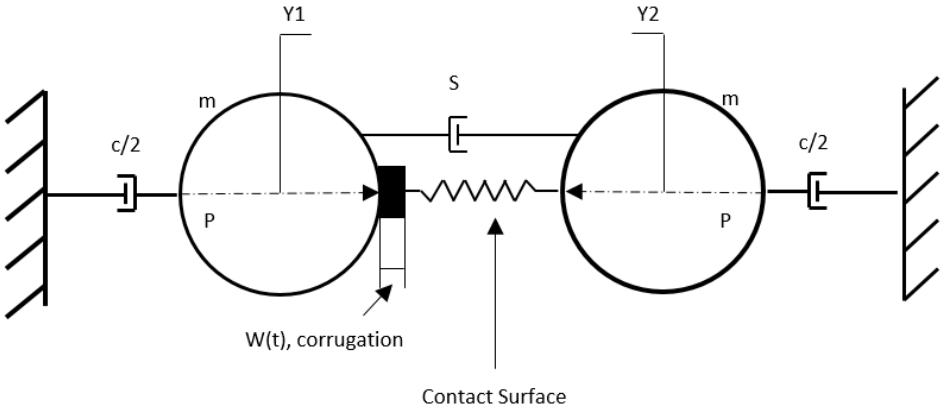

Figure 3.10: Simplified model of test apparatus [56]

Their theoretical model approximated the EHD lubricant film to a linear spring and damper arrangement as shown in figure 3.10. The equation of motion was written as:

$$m\frac{d^2y}{dt^2} + c\frac{dy}{dt} + 2\left[K\left(y + \Delta\sin\omega t\right)\right]^{3/2} = 2P \tag{3.11}$$

where $y = (y_1 + y_2 + \delta)$, and the third term is zero if $(y + \Delta sinwt) < 0$, δ is static Hertz compression, *S* means the contribution of lubricant film to the total damping, C denotes the total damping in system without lubricant film, *c* denotes the total damping in system (*c=S+C)*, and K is the nonlinear spring constant, determined with the load related to the body displacements by:

$$P = \left(K\delta\right)^{3/2} \tag{3.12}$$

The slope of the load-deflection curve was becoming:

$$\frac{dP}{d\delta} = \frac{3}{2}K\left(K\delta\right)^{1/2} = \frac{3}{2}KP^{1/3} \tag{3.13}$$

The two-degree of freedom system's contact frequency was thus derived as:

$$f_c = \frac{1}{2\pi}\left[\frac{3K}{m}P^{1/3}\right]^{1/2} \tag{3.14}$$

Ultimately, they showed that the fluid film damping generated by the squeeze film mechanism contributed enormously to the total damping of the system, and the maximum damping of the fluid film occurred at the load of 75 lbf.

The work done by Smith and Cameron [57] revealed that EHD contacts subjected to vibrations show unexpected and dramatic phenomena. They used a two-disc machine with the disc attached to shafts supported by hydrostatic bearings. Even though that work is now thirty years old no explanations to the questions raised there have been found yet. The two phenomena observed and presented in [57] are:

- An important reduction of the scuffing load at a frequency of about 15 Hz, accompanied by an increase of friction.
- A reduction of fatigue life (due to pitting) 26 times the life under steady conditions.

Rahnejat and Gohar [58] presented a theoretical work regarding the vibration response of a rotating shaft supported by two radial deep-groove oil lubricated ball bearings. They investigated the influence of radial interference on the damping factor, the influence of the ball complement on the natural frequency as well as the influence of the ball complement on the damping coefficient. Moreover, they found that the contribution of squeeze film damping played a key role in the thick film region.

At the beginning of 1990's, Mehdigoli et al. [59] developed a numerical model to simulate the experiments performed in [56]. They investigated the influence of EHD lubricant film damping and preloading, in the concentrated non-conforming contacts of rolling discs. According to their simulation results, it can be concluded that increasing the preload would increase the natural frequency of the system which was expected as the stiffness of Hertzian contacts increase with the increasing load. Even with higher viscosity lubricant, the modelled EHD film had very low damping characteristics. Unfortunately, some other factors which also contributed to higher damping were not able to be modelled in that paper.

Sabot et al. [60] built a symmetrical plane-sphere-plane contact device (one-degree-of-freedom non-linear oscillator) to study non-linear vibrations of Hertzian contacts, as shown in figure 3.11.

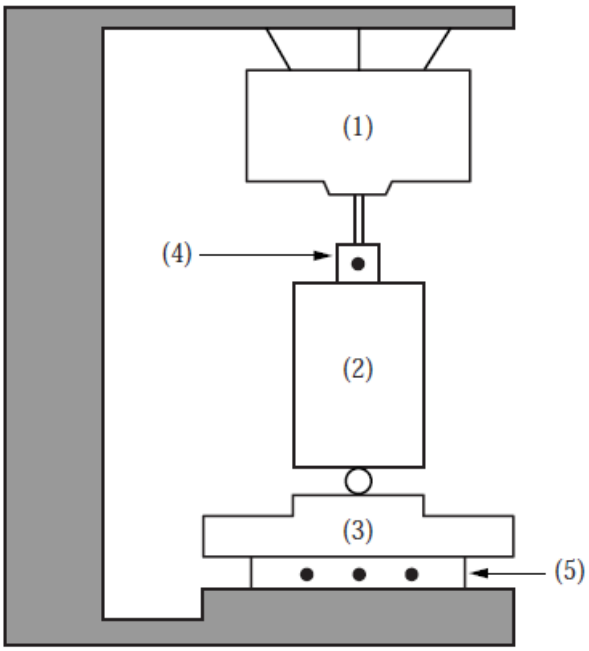

Figure 3.11: Experimental device: (1) vibration exciter; (2) moving cylinder; (3) fixed plane; (4) impedance head; (5) three components force transducer [60]

During free vibration tests, the difference between experimental results of contact natural frequency and theoretically predicting results was only 2.5%. Damping ratio was in good agreement with the proposed equation as illustrated in figure 3.12.

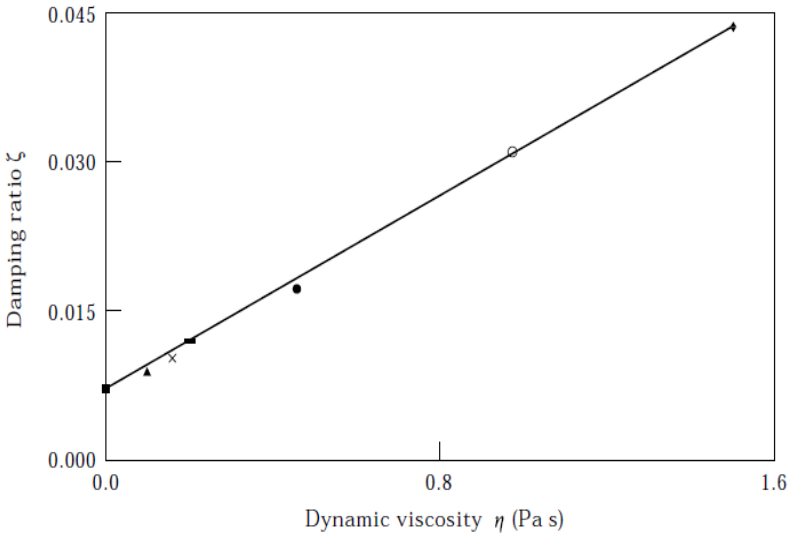

Figure 3.12: Damping factor for lubricated contacts [60]

The damping was small and can be expressed by an equivalent viscous damping in dry contacts, while in lubricated contacts, the fluid itself could add a noticeable amount of damping. During forced contact vibrations experiments, they clearly showed that softening of primary resonance when no loss of contact occurred, as shown in figure 3.13.

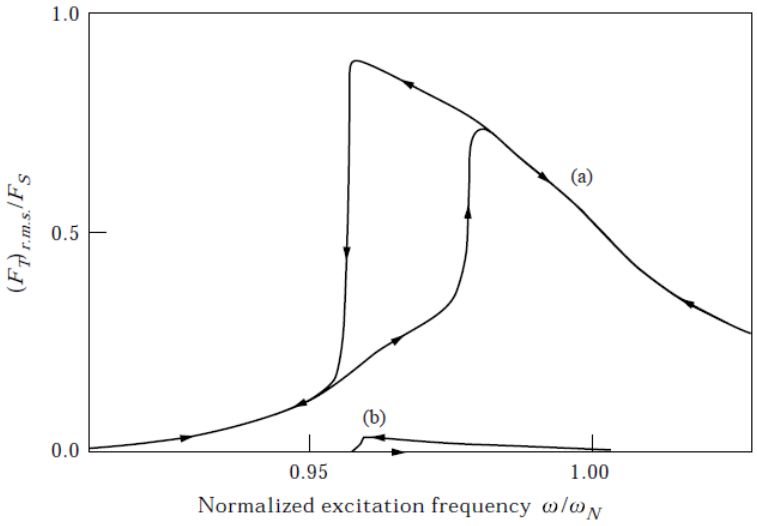

Figure 3.13: Measured contact load versus excitation frequency ω/ω_N (a) normal component; (b) ten times the tangential component [60]

Wijnant et al. [61] performed experiments using optical interferometry on a ball-on-disc apparatus to investigate the effects of structural vibrations on the EHD film thickness. Experimental results of film thickness were qualitatively compared with theoretical contact predictions obtained by numerical simulations. In the experimental part of the investigation, the lubricant was poly-alpha-olefin (PAO) oil of viscosity grade VG46 and its temperature was held at 23℃. The applied initial load was 45N and it was suddenly increased to 165N. The entraining velocity was 0.37 m/s.

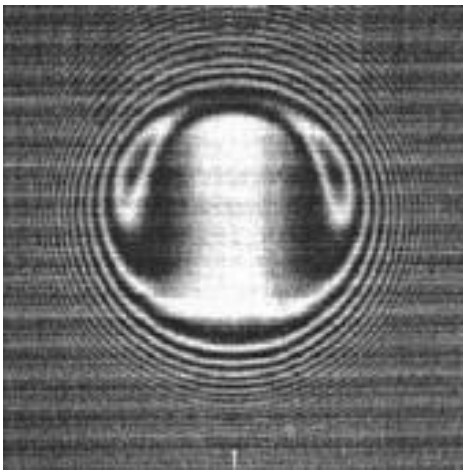

Figure 3.14: Interferogram of the contact at the initial load (t=0) [61]

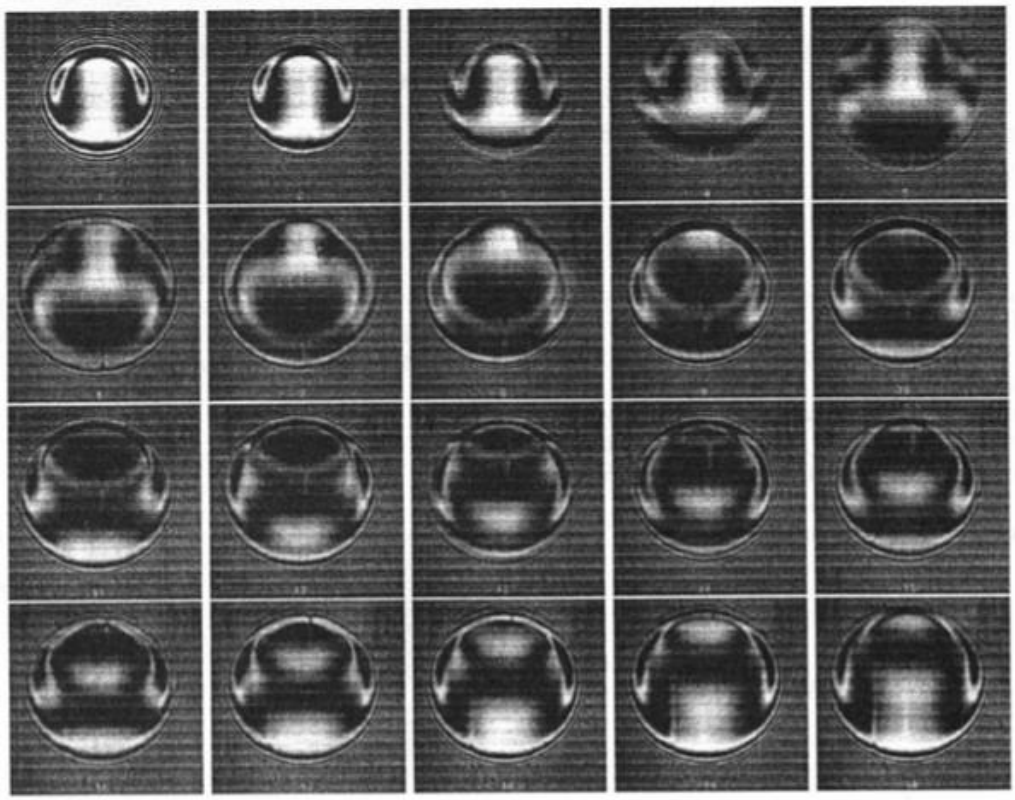

Figure 3.15: Interferograms of film thickness for $0 \leq t \leq 4.22ms$ [61]

The recorded interferograms of the film thickness at the initial load is illustrated in figure 3.14. For the initial load case, the measured central film thickness was $h_c = 0.34\mu m$, and the minimum film thickness was $h_m = 0.15\mu m$. Figure 3.15 shows interference images of the contact after the sudden increase of the load. It could be seen that the sudden increase of the load lead to an expansion in the Hertzian contact circle, consequently inducing film thickness changes propagated along the entraining direction. The main changes of film thickness happened just outside the initial Hertzian contact circle due to squeeze motion. After suddenly increasing the applying load, the film thickness did not immediately reach the new steady-state value with the higher load due to inertia effects, the ball and disc started to carry out an oscillatory motion.

In the numerical part of their investigation, an EHL contact model incorporated both squeeze and entraining motion. This model assumed that the only "vibrating mass" was the ball. The authors directly compared experimental results with the calculated film thickness in the form of pseudo interferograms.

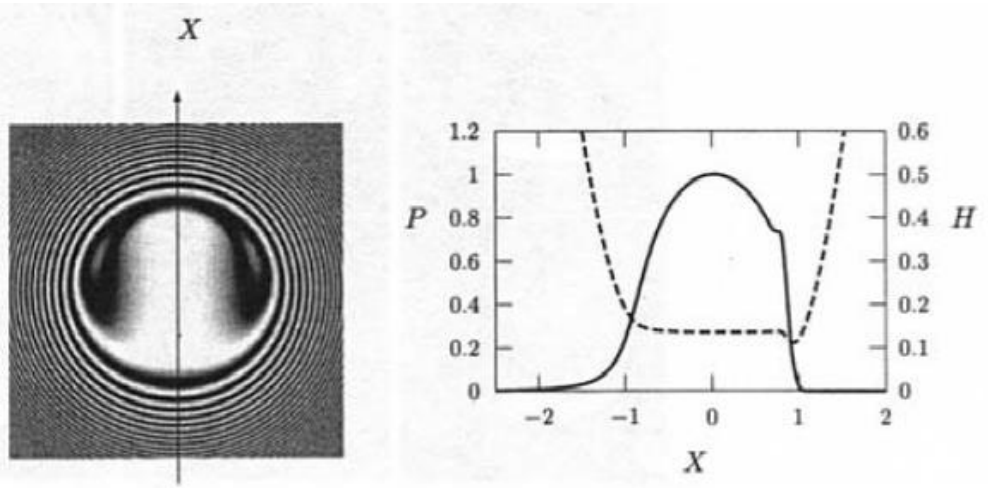

Figure 3.16: Computed pseudo interferogram of film thickness and pressure and film thickness at t=0 [61]

The computed interferogram of the film thickness at the initial load together with the dimensionless pressure and film thickness are illustrated in figure 3.16. The calculated central film thickness was $h_c = 0.32\mu m$, differing 5.9% from the experimental value. The calculated minimum film thickness was $h_m = 0.18\mu m$, differing 20% from the experimental value.

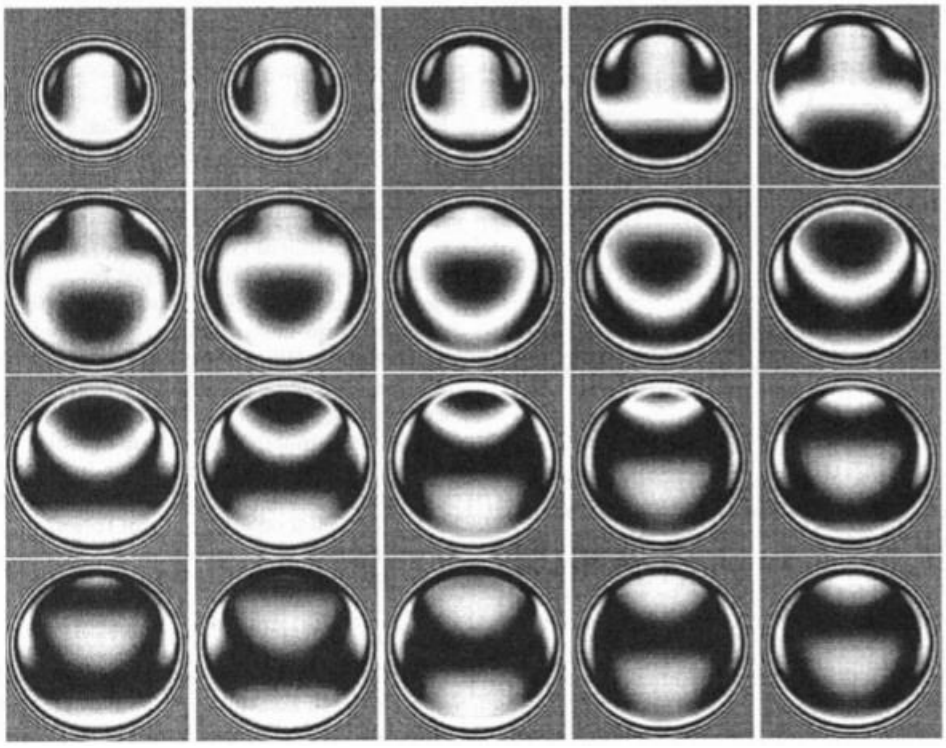

Figure 3.17: Computed pseudo interferograms of film thickness for $0 \leq t \leq 4.22ms$ [61]

For the sudden increasing load case, the computed pseudo interferograms of film thickness are presented in figure 3.17. The film thickness change behaviour in numerical simulation results was found in good agreement with the experimental case.

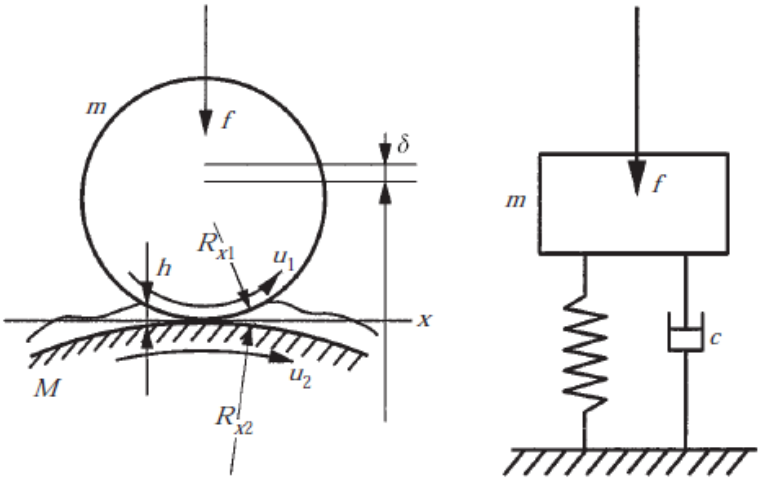

Figure 3.18: Rolling element on raceway and the approximated spring-damper model [62]

In the same year, a paper dedicated to stiffness and damping of EHD contacts was published by Wijnant et al. [62]. Stiffness was accurately determined by steady state numerical solutions for both dry circular and elliptical contacts. A simplified spring-damper model is shown in figure 3.18 where the stiffness was referred to as the EHD stiffness or EHD spring. In this simulation, the rolling element was slighted lifted from its equilibrium position and subsequently released to start a damped oscillatory motion. They concluded that fluid film built up between the rolling elements and raceway influenced the stiffness and the eigenfrequencies of bearings. This influence was moderate for medium load and speed but increased for low loads and higher speeds in comparison to dry contact case.

In the beginning of 2000's, Ramamurthy et al. [63] built a dynamic apparatus to evaluate the axial vibration in grease lubricated bearing systems as well as the damping characteristic of different types of greases. They have combined threshold, kurtosis and mean square methods to compare and rank grease vibration based on the bearing vibration. Their results indicated that ultra-filtered greases showed the lowest bearing vibration in the mid-frequency band among all greases tested. The damping factor and damping coefficient of greases based on the bearing vibration system have not been quantified though because of uncertainties in grease behaviour.

Cann and Lubrecht [64] applied optical interferometry to study the effect of transient loading on replenishment of contacts lubricated with greases. The period of cyclic loading/unloading was two seconds and the authors did not carry out result into any oscillatory motion but they could still see the beneficial effect of cyclic loading/unloading on track replenishment of the contact and fluid film recovery. They concluded that cyclic loading/unloading can be a mechanism which can practically help lubrication mechanisms of rolling element bearings lubricated with grease, which enhanced EHD contact replenishment in the starved lubrication regime.

Rigaud and Liaudet [65] developed an experimental rig to investigate the dynamic responses of a preloaded vibro-impacting Hertzian dry contact under purely harmonic input force.

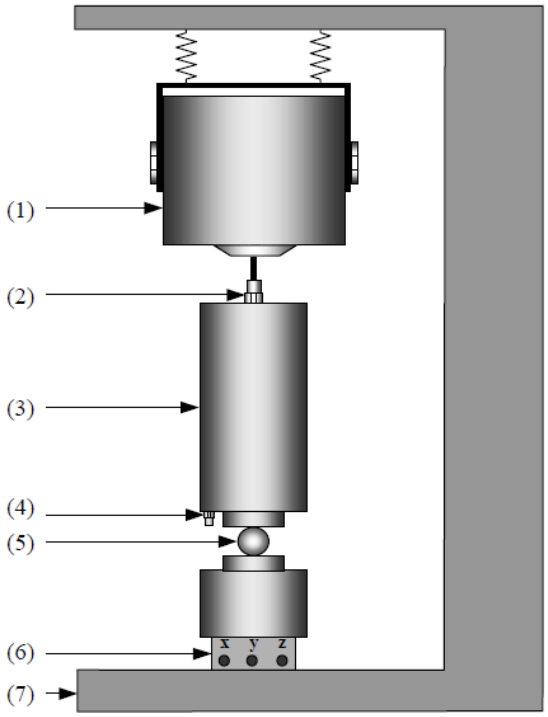

Figure 3.19: Test rig: (1) Vibration exciter, (2) force transducer, (3) moving cylinder, (4) accelerometer, (5) ball, (6) tri-axis force transducer, (7) rigid frame [65]

The experimental system, shown in figure 3.19, could be modelled by a two degrees-of freedom nonlinear dynamic system. Experimental results showed that the loss of contact did not occur when the input amplitude was lower than 1% of the static load and verified the softening behaviour of Hertzian contacts. Unfortunately, the priority of this research was to focus on resonance response of Hertzian contacts so the study of damping mechanisms in vibro-impact conditions was not reported explicitly.

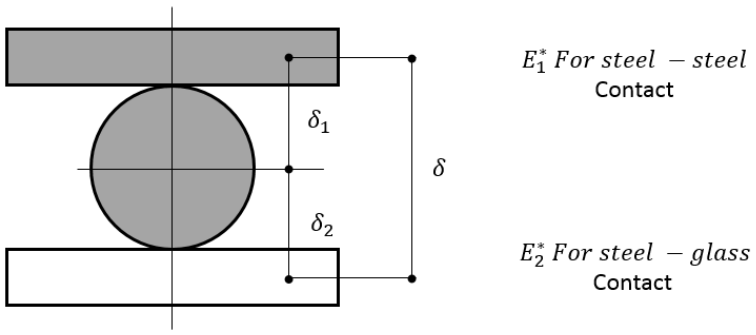

Figure 3.20: Static contact compression at both contact points [66]

Kilali et al. [66] built an optical-based rig combined with a system which superimposed the normal load excitation on the static one to measure the fluid film thickness and the dynamic

response of the contact subjected to a harmonic loading. There were two kinds of contact in this rig, steel-steel contact and steel- glass contact as seen in figure 3.20.

According to the Hertzian theory for non-conformal contacts, the total displacement of the surfaces can be expressed by following equation:

$$\delta = \delta_1 + \delta_2 = \left[\frac{9}{16}\frac{N^2}{R}\right]^{1/3} . \left[\frac{1}{E_1^{*2/3}} + \frac{1}{E_2^{*2/3}}\right] \tag{3.15}$$

Then the applied load can be rewritten:

$$\mathrm{N} = \left[\frac{4}{3}\left[\frac{1}{E_1^{*2/3}} + \frac{1}{E_2^{*2/3}}\right] . R^{1/2}\right] . \delta^{3/2} = \left[\frac{4}{3} E_{eq} . R^{1/2}\right] . \delta^{3/2} \tag{3.16}$$

The equivalent stiffness was then defined as:

$$K_{eq} = \frac{4}{3} E_{eq} . R^{1/2} \tag{3.17}$$

Finally, the applied load becomes:

$$N = K_{eq} . \delta^{3/2} \tag{3.18}$$

A linearized stiffness of the contact has been introduced to theoretically discuss the dynamic point of view.

$$K_L = K_{eq} . \delta^{1/2} \tag{3.19}$$

Then the linearized contact frequency can be written as:

$$f_0 = \frac{1}{2\pi}\sqrt{\frac{K_L}{m}} \tag{3.20}$$

A numerical dynamic model based on the finite element analysis was built. Fluid film thickness was measured by the interferometry technique with semi-reflective chromium layer. The tested lubricant was a 400 NS mineral oil (viscosity = 153mPa.s at $26.8^{\circ}C$, pressure viscosity coefficient = $22GPa^{-1}$). Results were presented into two sections which included lubricated static contact and pure rolling contact.

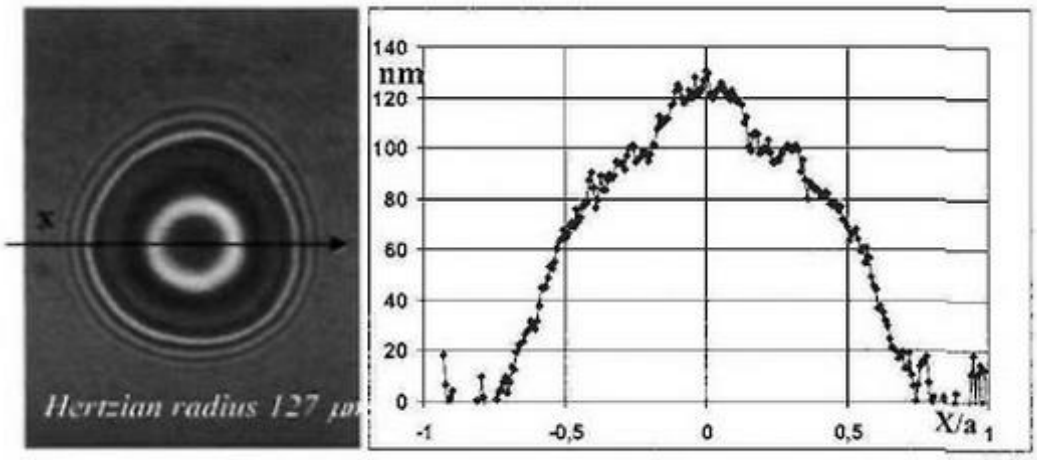

Figure 3.21: Interference fringe patterns and the relative film thickness [66]

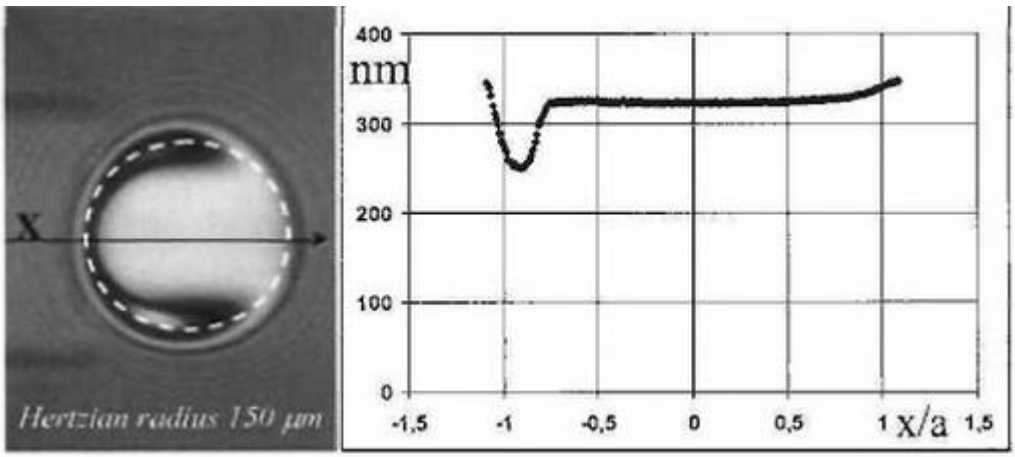

Figure 3.22: The lubricant film thickness along the rolling direction inside the contact [66]

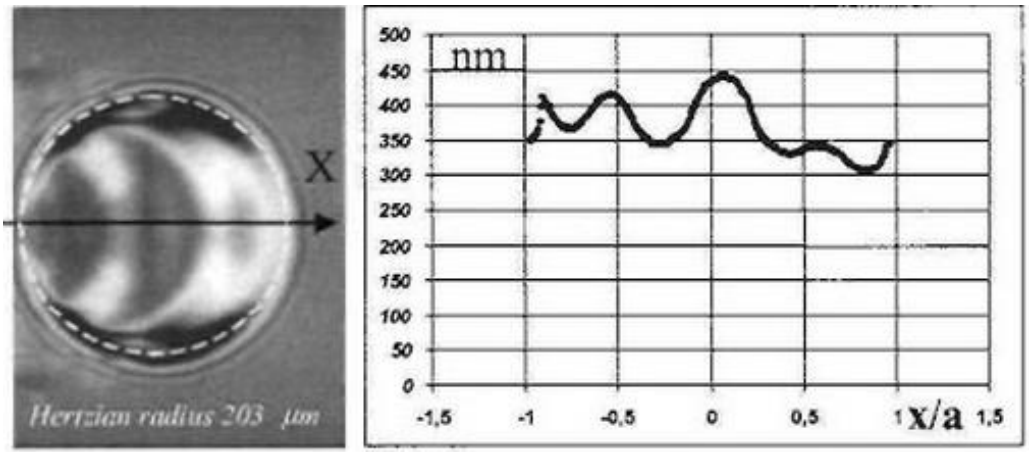

Figure 3.23: Free dynamic response of film thickness along the rolling direction [66]

Figure 3.21 shows an example of lubricated static contact subjected to an impact load by a hammer. The lubricant was squeezed out from the contact region in this case. The authors could not determine the minimum film thickness because of the unknown order of interference fringe. A dimple was formed in the centre of the contact, which indicated the location of lubricant entrapment. They concluded that the lubricant flowed out of the contact zone more easily in the case of low viscosity lubricant, and the dimple size decreased quicker than for the high viscosity lubricant.

For pure rolling contact conditions, with a rolling speed of 0.3m/s, the steady state rolling contact is shown in figure 3.22. The observed central film thickness was $h_c = 324nm$ and the minimum film thickness is $h_m = 250nm$. In free dynamic condition, after a load shock, the measured interferogram of the rolling contact along the rolling direction is shown in figure 3.23. The maximum and minimum film thickness were $h_{max} = 440nm \; and \; h_{min} = 308nm$. The disturbance of film thickness travelled along the direction of rolling. Forced harmonic vibration tests were not included in this work.

Sakamoto et al. [67] also applied the optical interferometry technique to directly observe the effects of cyclic pulsating and impact load on EHD point contact under static and rolling/sliding conditions. The cyclic pulsating and impact loads were applied by a direct-current solenoid. BS, ST100 and TN320 with different viscosity and viscosity-pressure coefficient were chosen as the test lubricants.

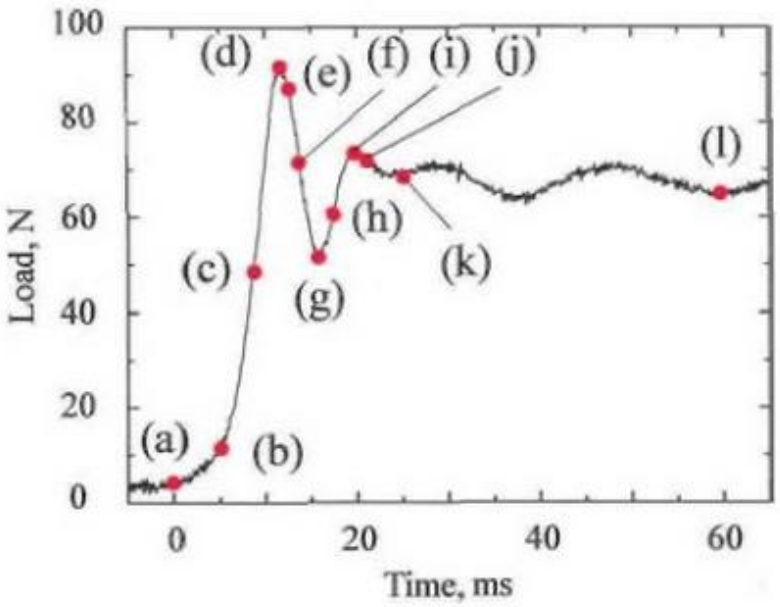

Figure 3.24: Load curve in loading phase (BS) [67]

Figure 3.24 indicates that the load applied to a static point contact suddenly increased from minimum load of 4N, overshooting to a maximum load of 90N within a period of 11.5ms and then kept fluctuating until it approached a constant value of 66N.

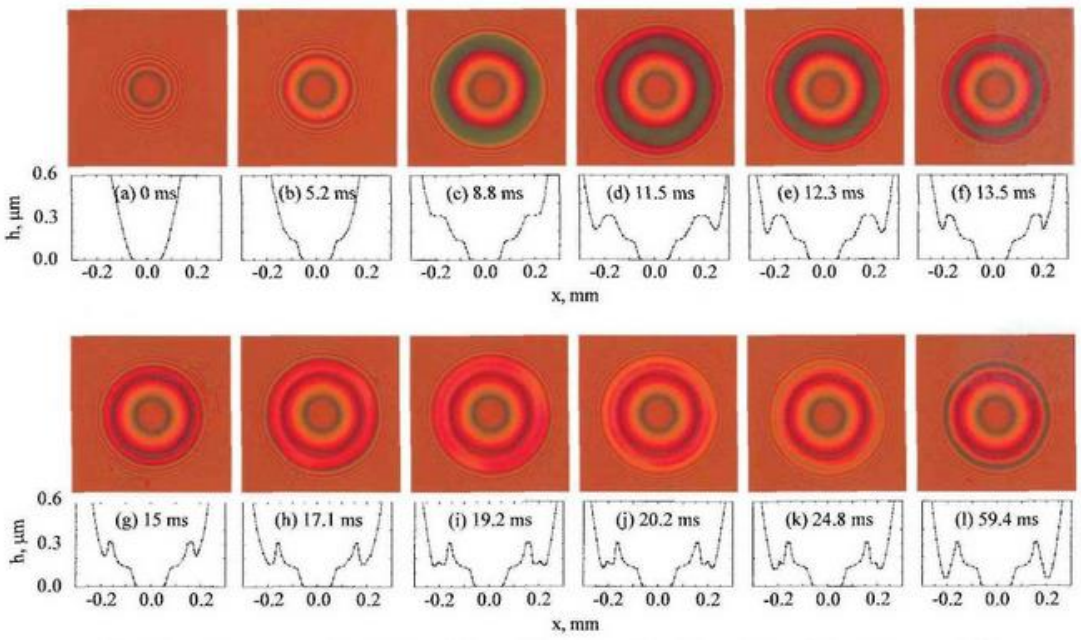

Figure 3.25: Interferograms and midplane film profiles in loading phase (No rolling, BS, $w_{min} = 4N$) [67]

Figure 3.25 shows representative interferograms corresponding to the red points in figure 3.24. A thick film was formed at the periphery of the initial Hertzian contact due to the sudden increase of the load leading to a sudden expansion in the contact region. The author pointed out that the amount of oil being entrapped between surfaces was mainly depending on the applied load, loading speed, viscosity of the lubricant at ambient pressure and viscosity-pressure coefficient.

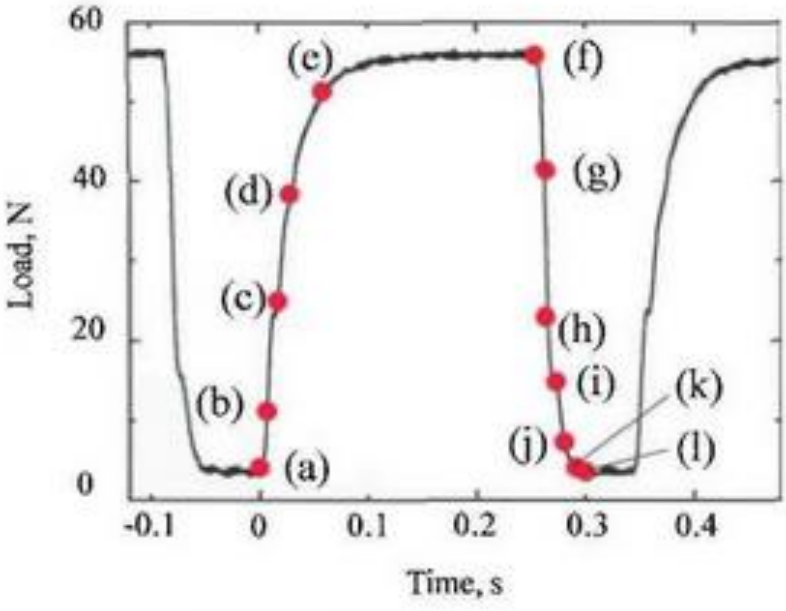

Figure 3.26: Pulsating load curve [67]

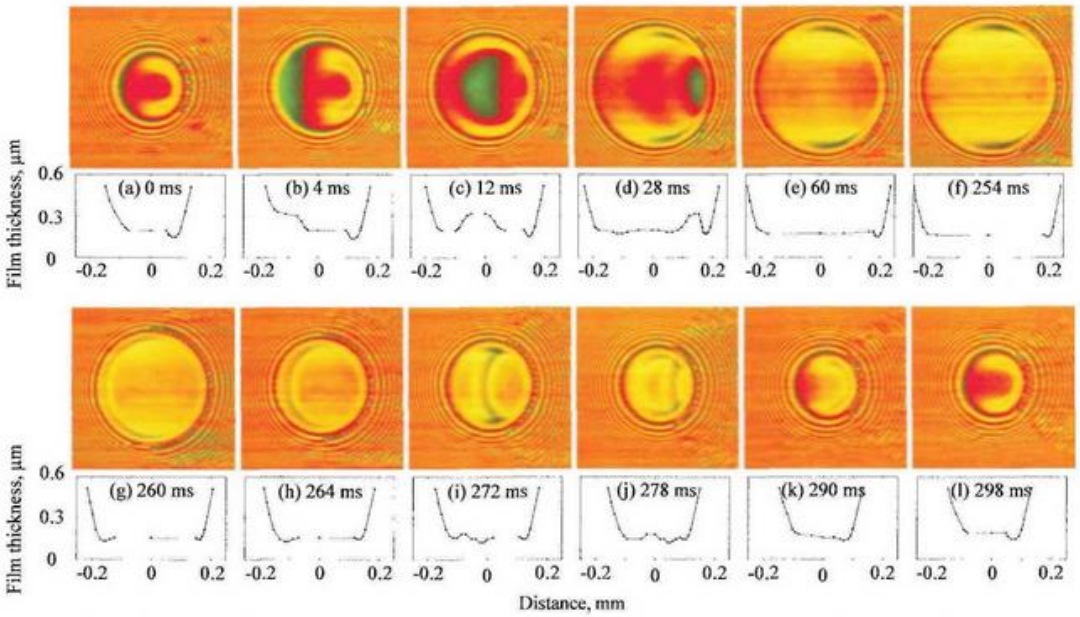

Figure 3.27: Interferograms and mid-plane film profiles [67]

After comparing tests for three different lubricants, the authors found that ST100 which had smaller viscosity and larger viscosity-pressure coefficient would escape easily from the contact area before the surfaces outside the initial Hertzian contact approaching each other when the applied load and loading speed were not large enough.

Figure 3.26 indicates the cyclic pulsating load increased from a minimum load value of 5N to a maximum load value of 55N within a period of 336ms. Figure 3.27 shows a series of interferograms corresponding to the points in the pulsating load curve in figure 3.26 taken under pure rolling condition with an entrainment speed of 12 mm/s. The authors observed that the behaviour of the EHD film was similar to that in the test under pure squeeze motion, sudden increase of load brought an expansion in the contact region, subsequently an entrapped crescent shaped film was formed and moved through the EHD conjunction at nearly the entrainment speed. During the unloading phase, the sudden decrease of the load caused the starvation, due to air bubbles at the entrance of the contact, so that film thickness at the inlet periphery was reduced. The authors compared verified experimental minimum and central film thickness under oil entrapment with theoretical simulations. It was found that the effect of pulsating load on EHD films diminished as the entrainment velocity increased due to the fact that the effect of squeeze motion was reduced by the large overall film thickness.

Guo et al. [68] carried out a numerical study of the EHD films subjected to entrainment and cyclically squeeze. They defined a so – called squeezing coefficient, although it was not clear how this was derived from their theoretical analysis or how it was related to the lubricant film thickness. They found that the central film thickness increased with frequency following a power function, which was in a logarithmic graph appears a straight line. Their simulation also showed

that the central film thickness was constant during the load – increasing phase of the cycle.

Felix-Quinonez and Morales-Espejel [69] proposed an improved semi-analytical method for film thickness fluctuations in the normal-approach of EHD contacts. The method was based on squeeze film effects as well as the variation of lubricant entrainment speed caused by the oscillating load and change of the conditions in the inlet region of the EHD contact. Film thickness results predicted by the semi – analytical method was compared with full numerical simulations. It was concluded that film thickness perturbations could be ascribed to two effects; squeeze film phenomenon caused by vertical rigid body motion of the surfaces and variation in effective entrainment velocity due to fluctuations of contact width.

Nonato and Cavalca [70] introduced a nonlinear contact model based on multi-level method for EHD lubricated point contact to discuss the nonlinear dynamic response of EHD contact. After obtaining the EHD contact transient response and verifying the nonlinear contact model conditions, they suggested that the proposed contact model is applicable to any lubricated contact system with one degree of freedom.

More recently, research focusing on the behaviour of EHD films subjected to lateral vibrations was carried out by Kalogiannis [71]. An optical based experimental rig was successfully built and modified to mainly study the effect of various parameters including the frequency, Hertzian pressure, rolling speed as well as the properties of base oils upon the behaviour of the EHD film under lateral vibrations.

One of the most important conclusions showed that EHD film perturbations only existed at the inlet of the contact under largest lateral frequency and lower entrainment speeds. It was also found that the contact pressure did not influence the behaviour of EHD film under lateral oscillations.

3.3 Monitoring rolling element bearings dynamics

Rolling element bearings are simple systems that include inner and outer races rolling elements and a cage to separate the later from touching. They are the second most numerous machine elements in use nowadays. The working condition of rolling element bearings is the EHD lubrication regime. Every single machinery or piece of equipment which involves rotating parts needs bearings to support them. If one thinks only in terms of road vehicles, there are about 600 million running every year. This amounts to over 2.4 billion bearings only for the wheels. Vibrations and noise in rolling element bearings are common and are transmitted from the machinery they are part of, or are due to the rotation of lubricated contacts and geometrical imperfections (roughness, damage and waviness). A better understanding and investigation of rolling element bearing dynamic behaviour requires experimental techniques, employment of kinematics, kinetics, theory of elasticity and EHD lubrication. Experimental work based on the

principles of optical interferometry applied to the study of EHD contacts has been published extensively during the past fifty years. The results obtained in these works are nevertheless idealisations, and simplifications of the EHD contacts in rolling element bearings. In order to overcome the restrictions of experimental techniques for studying the dynamic behaviour in real rolling bearings, a great amount of theoretical and modelling works on vibration in rolling element bearing with regarding of EHD phenomenon must be carried out. Research in this area was published by many authors including Sunnersjo [72] and Gupta [73-76].

One of the most typical numerical research focusing on contact dynamics in rolling element bearings aiming to answer the question how do EHD contacts behave under dynamic loads or vibrations was carried out by Wijnant [77]. After obtaining the steady state Hertzian solution using the multilevel, multigrid technique, the author firstly discussed the dynamic behaviour of two contacting elastic solids where no lubricant was present in the gap between two solids (dry contact model). A quasi-static solution for sinusoidally varying loads and a solution for inertia of rolling elements were derived. Figure 3.28 shows the displacement Δ during cyclically variation of the force applied to the contact.

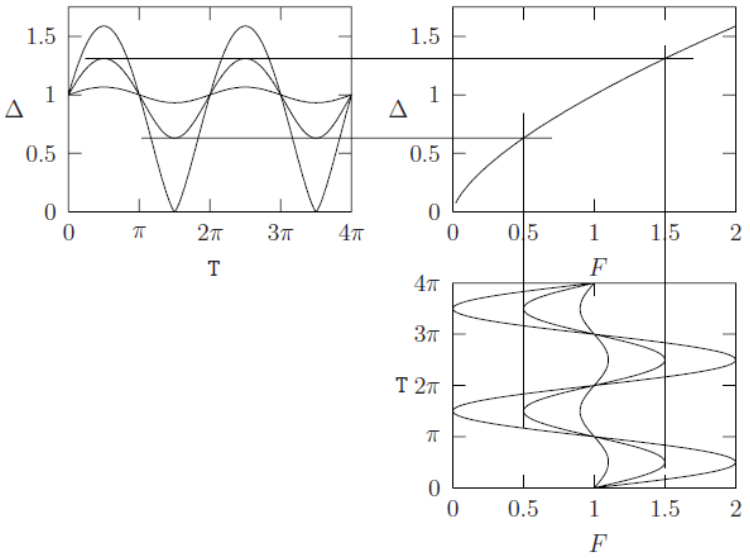

Figure 3.28: Response $\Delta(T)$ for sinusoidally varying loads [77]

The author then extended the isothermal dry contact model to lubricated contacts assuming Newtonian behaviour of the lubricant. A modified Reynolds equation was presented both in fully flooded and staved conditions. Subsequently, multigrid method and the multilevel multi-integration method were used to study the effect of the ellipticity and starved lubrication conditions. The study of the influence of vibrations upon film thickness and the pressure distribution were divided into circular and elliptical contacts.

For circular EHD contacts, an analytical curve-fit function was used to predict flexibility of

the steady state solution, which included a wide range of governing parameters. Damping studies was obtained by using free vibrations in numerical experiments considering the time-dependent EHD model in the solution. The author showed that the nature of damping was indeed viscous according to simulated sinusoidally varying loads, thus it could be modelled as a viscous damper. Damping values were presented as a function of load parameter, lubricant parameter and frequency. It was concluded that small oscillations were damped by the viscous forces in the lubricant film. For elliptical EHD contacts, the stiffness was derived from the steady state solution. The effect of ellipticity upon damping was deduced from the simulated sinusoidally varying loads. Results showed that the pressure and film thickness of ellipitical contacts could be easily solved by applying the Hertzian solution. Additionally, the results of elliptical contacts could be obtained by replacing the dimensionless load parameter in the results of circular EHD contacts.

Another typical modelling work aim to investigate the influence of dynamic behaviour of ball bearings was carried out by Wensing [78]. A three-dimensional ball bearing model including geometrical imperfections was built throughout this study. The shaft, bearing housing and the outer ring were modelled using the finite element method (FEM).

The bearing model built in this study was experimentally validated by vibration tests of a bearing fitted to a spindle. For the implementation of the EHD contact model, the author described stiffness as a nonlinear spring and damping as a linear viscous damper as seen in figure 3.29.

Figure 3.29: Dynamic models of the lubricated contacts in a ball bearing [78]

Wensing used a relationship for non-dimensional damping of the EHD contact derived by Wijnant [77] which was written as:

$$C = c\frac{av_s}{4F_eR}\frac{\kappa}{\varepsilon} \tag{3.21}$$

Where c is the physical damping parameter (Ns/m), a is the Hertzian half contact length, v_s is the sum speed, R is the reduced radius of curvature, F_e is the elastic restoring part of the

contact force, κ and ε are the elliptic integrals of the first and second kind. Based on the above equation he calculates and plots the damping constant as a function of the viscosity of the lubricant as shown in figure 3.30.

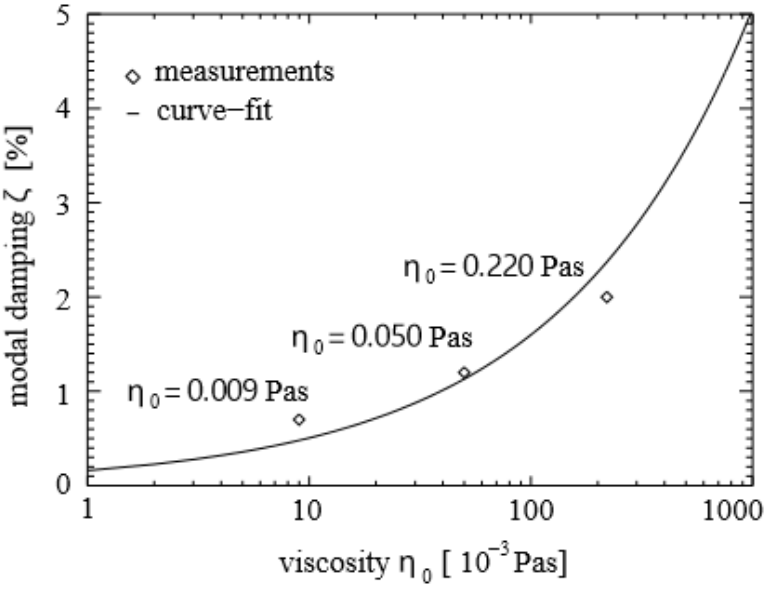

Figure 3.30: Damping of EHD contacts variation with lubricant's viscosity [78]

3.4 Conclusions

Elastohydrodynamic contacts rarely work in steady state conditions. Most often they are subjected to transient variation of entrainment speed, geometry and load. A good number of studies, both experimental and numerical, focus on the behaviour of the EHD films under rapid variation of entrainment velocity. It was shown that in this case film perturbations are formed in the inlet which, then travel through the contact creating large fluctuation of the thickness of the lubricant film over the contact area.

Studies on the response of the EHD films to variation of load are less numerous and are focused on a shock application of load. It was found that the EHD films respond to a sudden increase of load under steady entrainment speed, in a similar manner they respond to a sudden variation of speed under constant load.

This literature search revealed that no systematic study on the response of the EHD films to harmonic loads has been published thus far. Very few studies approached the effect of vibrations upon the film thickness in EHD contacts. Moreover, the effect of cyclic variation of load upon the inlet replenishment was tackled in one paper only, however the frequency of variation of load in that study, 0.5 Hz, was too low to be representative to real applications.

Chapter 4: Lubricants

4.1 Introduction

The primary purpose of applying lubricants to machine components is to reduce friction and wear between surfaces in relative motion. Machine manufacturers generally designate the lubricants with low shear strength, good corrosion protection ability, good thermal conductivity, good oxidation strength, which are suitable for their particular requirements. In order to make sure the lubricant works effectively, theoretically it must be viscous enough to form a film separating the surfaces between machine components at working conditions, but it also should be as fluid as possible to remove the heat generating within the contact. For EHD contacts, lubricant is travelling through within the small non-conformal contact area at extremely high velocity during which is subjected to a pressure pulse of about one giga Pascal or more. Such conditions can lead to variations in temperature and subsequently alter the characteristics of the lubricant. Thereby, there is always a challenge to characterize lubricant behaviour from chemical, physical, rheological and tribological point of view.

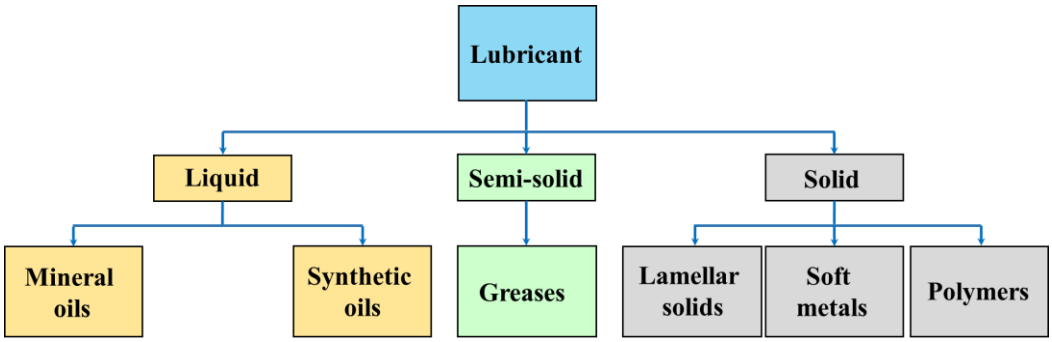

Figure 4.1: Structure of lubricant groups

Lubricants can be mainly divided into three groups, liquid, semi-solid and solid as showed in figure 4.1. Generally, in oil lubrication, the oil has also the role of a coolant to minimize the temperature rise in the contact, thus maintaining a sufficient high viscosity and constant film thickness. In case of grease and obviously solid lubricants convection of heat through the lubricant is not possible, so other means of cooling the surfaces are needed.

Excepting the solid lubricants, liquid lubricant and greases are formed by a base oil to which additives and for greases a thickener are added. The base fluid will give general properties to the lubricant, such as viscosity, pressure-viscosity coefficient, density, thermal conductivity, while additives will confer specific properties to the lubricant, for example low friction, good wear resistance, enhanced viscosity at high temperature, good anti oxidation, etc. In this chapter, a brief description of properties and behaviour of lubricants will be discussed as a background for later

experimental research description. Solid lubricants will not be discussed as they are not within the scope of this thesis.

4.2 Base oils

4.2.1 Mineral oils

In general, a mineral oil is defined as a liquid by-product of the distillation of petroleum to produce gasoline and other petroleum-based products from crude oil. Mineral oils always containing a large variety of chemical components, such as hydrocarbons in their composition. There are three basic classes of refined mineral oils; paraffinic, naphthenic and aromatic.

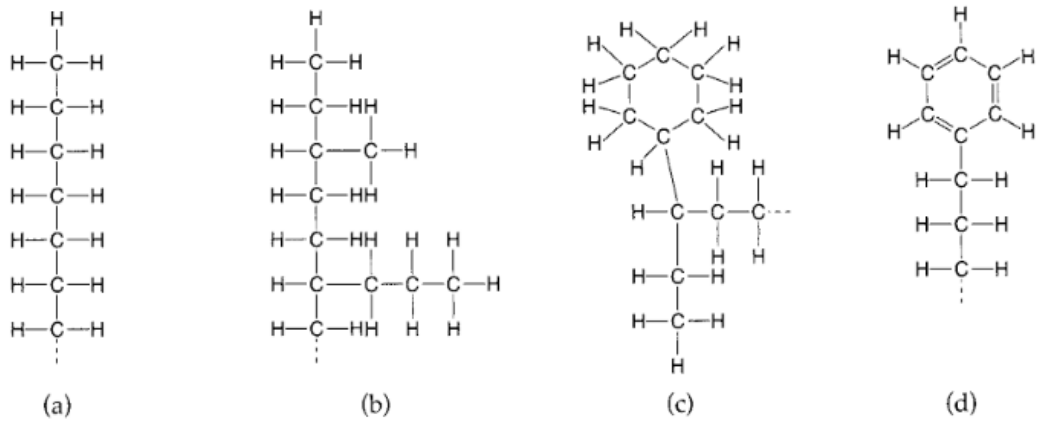

Figure 4.2: Types of mineral oils: a) straight paraffin, b) branched paraffin, c) naphthene, d) aromatic [79]

As shown in figure 4.2, paraffinic implies straight chain hydrocarbons with some wax. The rating of octane number of branched paraffin is higher than straight chain paraffin, therefore it is the desirable constituents of gasoline. The advantage of paraffinic oils is their high viscosity index and good oxidative stability. Naphthenic oils have cyclic carbon molecules with no unsaturated bonds. They have excellent low temperature properties. Finally, aromatic molecules are ring structures with alternative double bonds which are both chemically and physically totally different from paraffinic and naphthenic oils.

4.2.2 Synthetic oils

A synthetic lubricant contains more highly refined base oils than those found in conventional mineral oils, offering the machine components superior protection and performance, such as excellent low temperature flow performance, higher viscosity index, lower internal friction, improved oxidation and thermal stability [80]. Synthetic hydrocarbons are compounds containing only carbon and hydrogen.

Poly – Alpha – Olefins (PAO)

The most widely used commercial synthetic hydrocarbon oils are based on poly-alpha-olefins (PAO).

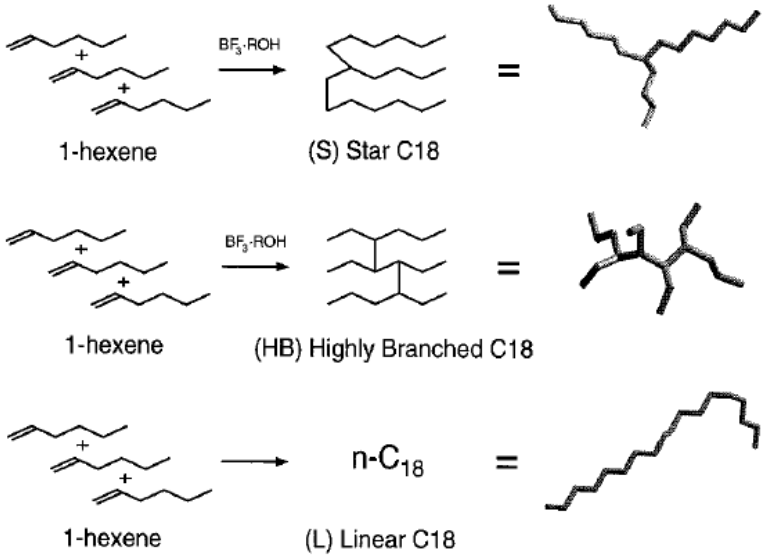

Figure 4.3: Three different molecular structures of PAO lubricants [81]

Poly–alpha–olefins have a great number of outstanding properties, such as low pour points, low volatility and good natural lubricity. Due to their totally paraffinic structure, it can also meet various requirements by changing the structure of the molecule, as shown in figure 4.3. A wide range of lubricant viscosities can be obtained with basically the same chemical composition by changing the length of the molecular chain. Nowadays, PAOs are used in the application of aerospace, internal combustion engines, gears, rolling bearings and refrigeration compressors.

Organic Esters (Diesters and Polyolesters)

Diesters and polyolesters (POE) are also popular for many industrial applications. Both can be combined with other synthetic oils to provide flexibility in formulating lubricants. POEs have improved properties over diesters, especially high temperature properties which goes up to 750 °C. The manufacturing cost of organic esters is four to five times higher than that of mineral base oils.

4.3 Lubricating greases

Probably animal fats were first greases used for lubrication purposed before the 19th century. A specialized definition of grease is: “a solid to semi-fluid product or dispersion of a thickening agent in a liquid lubricant. Other ingredients imparting special properties may also be included” by National Grease Lubricating Institute (NLGI) [82]. This means that greases contain a thickener and a type of liquid lubricant, plus other ingredients which are additives and co-thickeners. Its

unique structure and composition makes it work as an 'oil in a sponge', where oil is released during rolling and shearing. In rolling element bearings greases offer a series of advantages over liquid lubricants. A precise amount of lubricant can be applied; bearings are then sealed for life thus no maintenance is needed. Due to its simple structure of oil storage, an expensive and complex circulation system like the one needed for oil lubricants is not required. Moreover, because of its consistency, grease acts as a sealant to prevent lubricant leakage and to prevent entrance of corrosive contaminants

There are three main challenges to be addressed with regard to grease lubrication [80]:

- Developing greases that give longer life or are able to operate under more severe conditions (extreme low and high temperature and speed);
- The development of predictive tools, such as numerical models or expert systems;
- To design bearing systems that would increase grease life by optimizing grease flow.

90% of all rolling element bearings, the second most numerous machine components, are lubricated with grease [80]. It is thus crucial that the behaviour of grease – lubricated EHD contacts is well understood.

4.3.1 Grease Structure

Lubricating greases are, as mentioned previously, semi – solid materials that is they have their own shape but shear easily under tangential forces. The composition of greases is schematized in figure 4.4. The physical grease matrix contains approximately 80-90% base oil, 10-15% thickener and 5-10% additives. The base oil is kept inside the thickener structure by a combination of Van der Waals and capillary forces [83]. The composition of grease is schematized in figure 2.

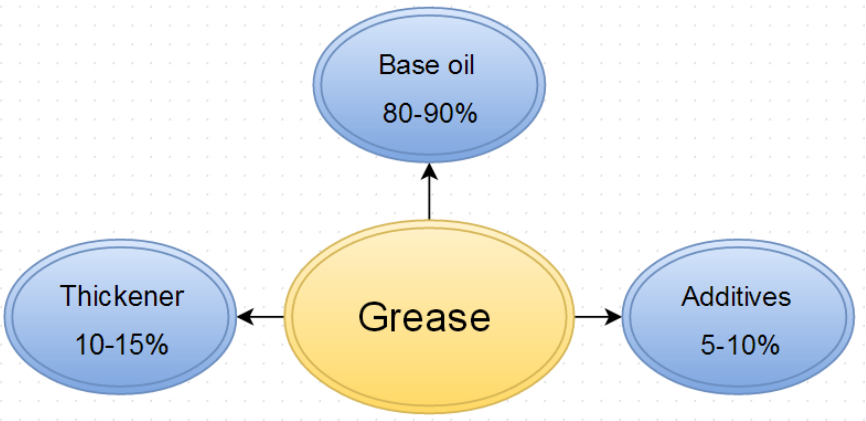

Figure 4.4: Grease composition layout

The thickener system is similar to a sponge holding water. The thickener in greases lubricating EHD contacts holds the base oil until the rolling elements roll it over, when the oil is released. The intrinsic properties of the thickener play a crucial role in the lubrication performance and decide properties like water resistance, running temperature, dropping point, mechanical stability and lubricity.

Figure 4.5 shows the structure of the thickener of various greases with the base oil washed away by a non-polar solvent.

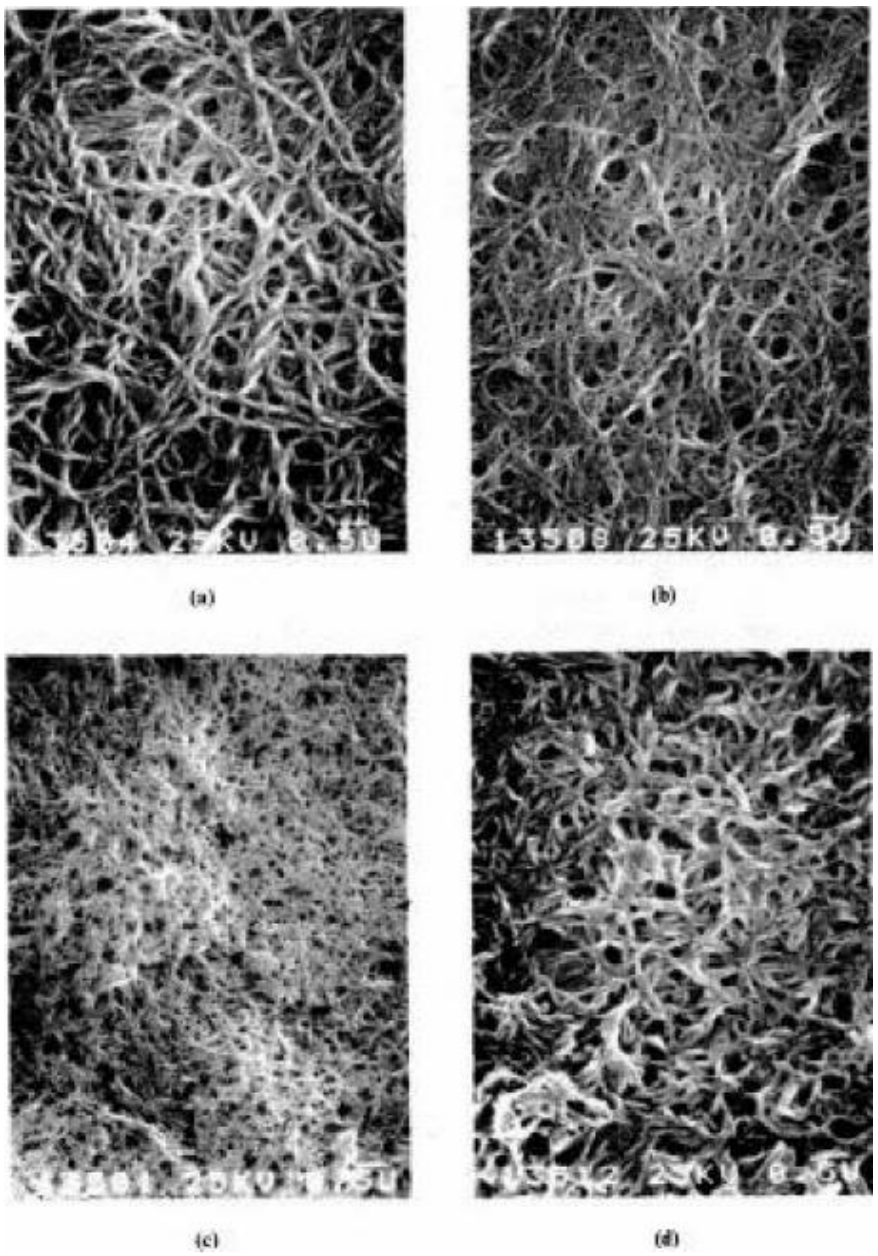

Figure 4.5: SEM photographs of different grease soap structures: (a) lithium-12-hydroxy stearate in mineral oil, coarse structure; (b) lithium-12-hydroxy stearate in mineral oil, fine structure; (c) lithium-12-hydroxy stearate in ester oil, very fine structure; (d) modified lithium-12-hydroxy stearate in mineral oil [84]

Greases can be distinguished by their type of thickener. Grease thickener types can be divided into two major groups, metal soaps and non-soap based thickener, as shown in the figure below.

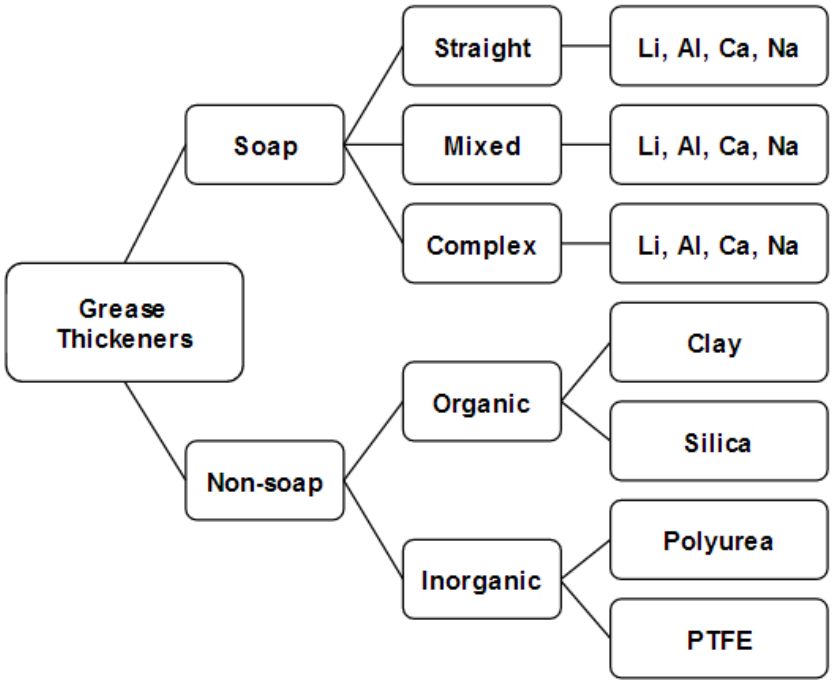

Figure 4.6: Classification of thickener types

Polyurea thickener

Polyureas are made with ashless inorganic thickeners and different types of iso-cyanates and amines, which have an outstanding resistance to oxidation. High temperature performance keeps its consistency constant to avoid potential leakage in rolling element bearings. In many industrial applications, this type of grease has become a choice as filled-for-life.

Lithium 12-hydroxy stearate thickener

Catalysed mainly by developments in the aircraft industry during the late 1930s, the introduction of lithium based greases came as a very significant step forward, (with patents issued to Clarence Earle in 1942-43) [85]. For the first time, lubrication engineers had access to a grease which could be classified as truly "multipurpose". Early lithium soaps were made from simple stearic acid, derived mainly from beef tallow. Good mechanical stability, water resistance and high temperature performance up to 120 ℃ are the capabilities of lithium thickened greases. Today, almost all lithium greases are based on castor oil derivatives and 12-hydroxy stearic acid [86].

Lithium complex thickener

Lithium complex thickeners have been popular during last two decades due to their good

thermal performance with dropping points over 300 ℃ and operating temperature which goes up to 240 ℃. The structure of this thickener is formed by dense fibre, where small polar fibres strongly bind the base lubricant providing good resistance to oxidation.

4.3.2 Grease behaviour in EHD conditions; Film thickness models

The behaviour of liquid lubricants in EHD conditions has been largely understood for several decades. This is not the case for lubricating greases, although important progress has been made due to intense research effort. As opposed to oil lubricants, greases have roughly two main operating conditions in rolling element bearings; first phase is churning phase where the lubricant film thickness is under fully flooded conditions and grease reservoir is formed; second phase is the oil – bleeding phase where the contact is supplied by oil released from the reservoirs formed at the side of the track. In the latter case starvation, film thickness breakdown and track replenishment phenomena happen. The difficulty of predicting the behaviour of greases in elastohydrodynamic conditions arises from its dual phase composition.

Analysis of grease lubrication must take into account the fact that the grease has non – Newtonian shear behaviour thus the shear stress is not directly proportional to the shear rate. In 1972 Kauzlarich and Greenwood [87] derived a theory to predict two-dimensional grease elastohydrodynamic film thickness using a Herschel-Bulkley model [88] for the shear behaviour of the grease.

$$\tau = \tau_y + K\dot{\gamma}^n \tag{4.1}$$

Here τ is shear stress, τ_y is the yield stress, K is the consistency factor, $\dot{\gamma}$ is the shear rate and n is the flow behaviour index.

$$h_0^{n+1/3} = 2.373\left(\frac{E^*}{w}\right)^{1/6} R^{1/2}\alpha\phi_0 U^n\left[\left(4+\frac{2}{n}\right)^n \frac{(n-1/3)!(n-2/3)!)}{2(n!)}\right] \tag{4.2}$$

The film thickness equation includes the yield stress of grease although the authors conclude that this parameter has little effect upon the film thickness.

Later in 1979, Jonkisz and Krzeminski-Freda [89] presented pressure distribution and the shape of a grease film and its base oil. Using the same Herschel-Bulkley model, their analytical solution was slightly more accurate than that in [87]. In many applications, it is assumed that fully flooded film thickness can be directly calculated using the base oil viscosity. This is going to be the way of theoretically predicting lubricant film thickness for later experiments.

Later on, the same authors investigated the effects of grease structure breakdown and of starvation conditions on the film thickness [90]. Theoretical results were verified by optical interferometry technique. They found that the film thickness of fresh grease was about 1.5 times greater than that calculated for base oil in fully flooded conditions. They analysed the starvation in terms of the ratio between base oil and grease film thickness.

$$\lambda_h = \frac{grease\ filmthickness}{base\,oil\ filmthickness} \tag{4.3}$$

They concluded in starved conditions this ratio was about 0.5 to 0.7. Moreover, they pointed out that the yield stress of grease had a negligible effect on the film thickness.

Accinelli [91] built a bearing rig to study grease effect on the performance of rolling contact bearings. This rig could fit 20 and 25mm ball bearing and to operate at speeds up to 100000rpm. Several grease variables were considered during experiments such as grease consistency, viscosity of base oil in the grease, oil type and gelling agents. Three types of grease with different soap composition and different consistency level were used as testing lubricant. The work came with a series of valuable conclusions: vibrations had more influence upon bearing performance than grease variables, high bleeding in grease would help diminishing the centrifugal force effect that results in inadequate lubrication, the period of grease lubrication was possible over 100 hours under ideal conditions. The limitation of this study was that the process of quantifying grease film thickness was not provided.

Wilson [92] used electrical capacitance of the contact to investigate comparatively the film thickness in rolling bearings lubricated by grease and by their base oils. He treated the bearing under test as an electric circuit formed by a number of capacitors in series and in parallel. The capacitances of the balls were treated as connected in parallel; each ball had two capacitors (one for the inner ring contact and one for the outer ring contact) connected in series; each contact between one ball and one of the raceways was thus treated as three capacitors in parallel – the capacitance of the Hertzian contact, the capacitance of the inlet zone and that of the outlet zone. The dielectric constant of the lubricant inside the contact was adjusted to account for the larger pressure while the dielectric constant of the outlet region was estimated by considering that the lubricant film splits in two halves which stay attached to the solid surfaces, and the gap in between was filled with air. He found that at the beginning of the test grease formed a film with thickness corresponding to a base oil with viscosity 30–35 percent larger than the actual base oil of the tested grease. As the time of running increased, the film thickness of the grease lubricated bearing decreased to less than half the initial thickness.

A similar study was conducted by Muenich and Gloeckner [93], who used a capacitive type displacement probe to measure the film thickness of a cylindrical roller thrust bearing under both

grease and oil lubricated condition. Test results of grease lubricated contacts in the fully flooded and starved lubrication regime were evaluated and compared. They concluded that the thickener type and base oil viscosity played a major role in grease film thickness. They also showed that the dependence of grease film thickness on speed was proportional to the 0.7 power of the rotational speed in the flooded condition and the film thickness of the grease was always higher than that of the base oil. The transition point from fully flooded to starved conditions varied with the type of grease.

Palacios et al. [94] applied optical interferometry to study and monitor the film thickness of nine kinds of greases, and soap suspensions and of their base oils in point and line contacts. Boundary of lubricant inlet meniscus was kept three times the Hertz width to ensure all experiments were carried out under fully flooded conditions. They found that film thickness reducing with the increasing entrainment speed was due to temperature rise rather than shear degradation. The soap had little influence on grease film thickness and grease formed thicker film than its base oil in all experiments.

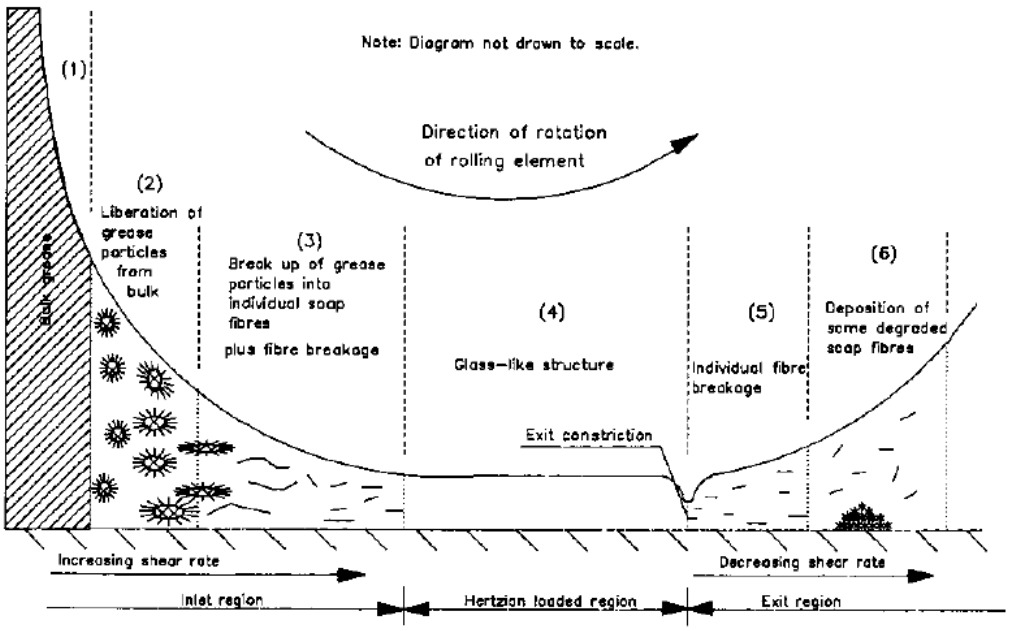

Figure 4.7: Schematic diagram of an operating EHD contact showing main elements of the proposed grease model [95]

EHD film thickness of a range of greases was measured by optical interferometry by Cann et al. [95]. The work was combined with reflection-absorption infrared spectroscopy to monitor the grease structural changes in the inlet of EHD contacts. The tested greases were divided into three groups depending of grease composition and structure in order to evaluate the effect of base oil viscosity, the effect of soap concentration and the effect of thickener type. Optical results indicated that EHD film performance depended upon both base oil viscosity and soap

concentration under fully flooded conditions. Increasing base oil viscosity and soap concentration would linearly increase film thickness. Based on both optical interferometry and spectroscopy results, a schematic of grease rheology in the inlet of the contact was proposed as illustrated in figure 4.7. As the shear rate continuously increased in the inlet region, greases started to breakdown into individual soap fibres. Due to the structure of soap fibres, soap gellants could survive inside the Hertzian loaded region so that it contributed to EHD film thickness.

Later on, Cann [17] continued the research of grease lubrication into the starved regime. Starved film thickness was compared with fully flooded conditions films, using an optical interferometry based apparatus. A group of six grease samples and three different types of thickener concentration were chosen as tested lubricants.

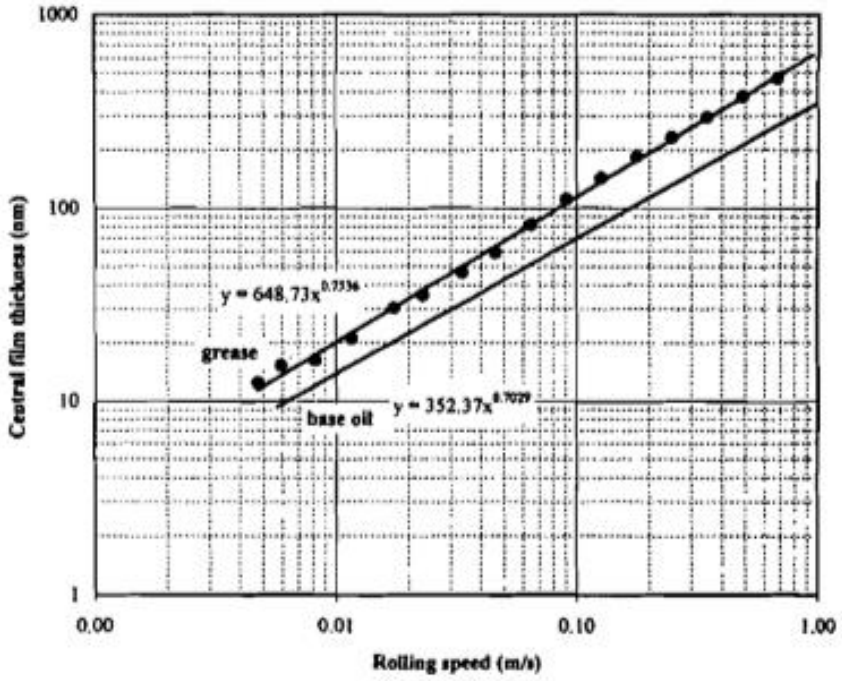

Figure 4.8: Curve fitted film thickness results for 9% 200 cSt grease and base oil at 60℃ [17]

As seen in figure 4.8, for the fully flooded condition the results showed that the power law of film thickness versus entrainment speed was 0.75 for greases and 0.7 for the base oil. Film thickness was found to increase with thickener content and base oil viscosity. However, thickener lumps would distort EHD film formation when passing through the contact region at low speed. It was also found that the film thickness in starved regime significantly depends on the amount of lubricant reflowing to the track, and this, on its turn would depend on the oil release properties and shear stability of the grease.

A starvation degree parameter was suggested based on these results:

$$\lambda_h = \frac{starved\ filmthickness}{fully\ flooded\ filmthickness} \tag{4.4}$$

It was shown that this parameter decreased with increasing temperature, but increased with increasing the base oil viscosity, thickener content and rolling speed.

Kaneta et al. [96] applied the optical interferometry technique to study the effect of the thickener content on the grease film formation by testing three different types of diurea grease without additives in an EHD point contact. From directly observing the thickener lumps in the EHD conjunction, the authors found that the behaviour of EHD film strongly depends on the thickener structure. The thickener lumps behaved as a solid-like material and would repeat attaching to and detaching from the surfaces when traveling through the EHD contact.

By studying the effect of grease composition and structure upon film thickness of rolling contact EHD films, Couronne et al. [97] showed that greases forming thick film in rolling contact was mainly dependent on the soap-base oil interaction, however the microstructure of grease was not the determining parameter.

Cann and Lubrecht [98] further experimented the relationships between film thickness in rolling element bearings and some lubricant parameters, such as grease shear stability and base oil viscosity, as well as bearing parameters and operating parameters. Various grease shear stability was measured in a rotational viscometer.

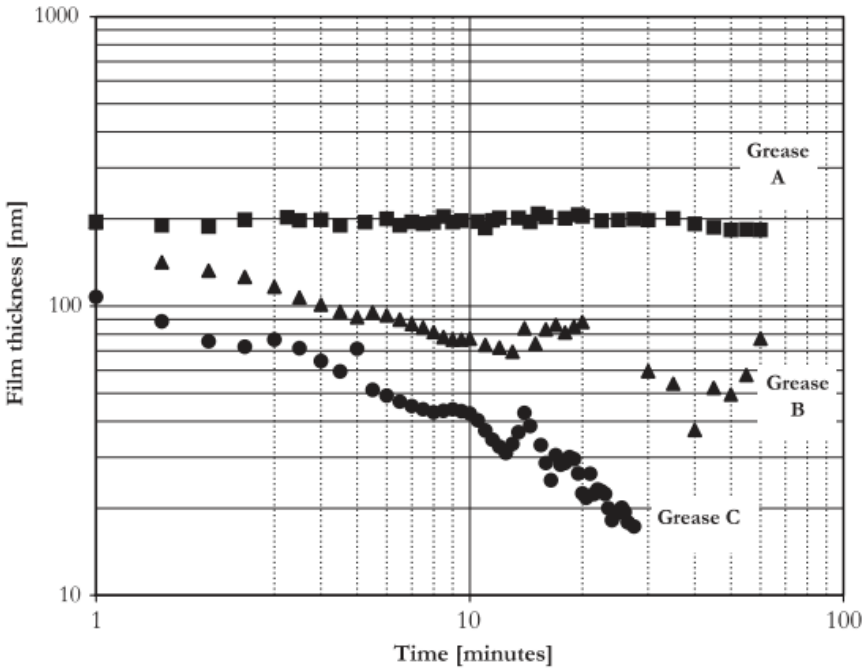

Figure 4.9: Starved film thickness as a function of shear stability;
$Grease\ A < Grease\ B < Grease\ C$ [98]

According to the results shown in figure 4.9, shear stability was a determining parameter on starvation because it affected the availability of free oil for replenishment of the rolling track. It

suggests increasing shear stability of the lubricant would thus lead to starvation. Grease with poor shear stability would release free oil quickly, which would strongly help to diminish starvation.

Summarizing the research into the behaviour of EHD contacts lubricated by grease the following conclusions can be drawn:

General

- The micro-structure of grease is not a determining parameter of grease film thickness;
- Self-healing ability of grease film may happen during the film breakdown process in metal-to-metal contact;
- Thickener adhering to surfaces behaves as a sold-like material.

Fully flooded regime

- In the stage of low rolling speed, grease forms thicker film than base oil; As the speed increases the grease film thickness markedly decreases;
- In the stage of low rolling speed, thickener lumps sometimes pass through the contact thereby contributing film formation;
- Increasing base oil viscosity and thickener concentration increases the film thickness;

Starved regime

- Grease film thickness depends on its thickener type and its ability of releasing oil;
- The degree of starvation increases with increasing base oil viscosity and thickener content, but decreases with increasing temperature;
- Grease with poor shear stability will quickly release oil to the track, which helps prevent starvation.

4.4 Tested lubricants in this research

To study of the effect of forced vibrations upon the behaviour of EHD films, three oil lubricants and three greases and their base oils were studied and compared.

4.4.1 Liquid lubricants

1. **PAO 4** is made and provided by INEOS Europe Limited in Belgium. This synthetic based oil is used for industrial applications. Its flash point and pour point are $224\ ℃$ and $-65\ ℃$ respectively, kinematic viscosity is $17\ mm^2/s$ (17 cSt) at $40\ ℃$ and $4.1.mm^2/s$ (4.1 cSt) at $100\ ℃$. Density is 0.81 g/cm^3.
2. **PAO 40** is supplied by Chemtura Corporation in USA. Its flash point and pour point are $266\ ℃$ and $-30\ ℃$ respectively, kinematic viscosity is between $339.8\ mm^2/s$ (339.8 cSt)

at 40 ℃. and $35.8\ mm^2/s$ (35.8 cSt) at 100 ℃. Density is 0.84 g/cm^3.

3. **HVI 650** is a petroleum hydrocarbon based oil produced by Shell Global Solutions and provided by Belgian Shell Corporation. Its flash point is 500 ℃. Its kinematic viscosity is between $484.2\ mm^2/s$ (484.2 cSt) at 40 ℃ and $31.4\ mm^2/s$ (31.4 cSt) at 100 ℃. Density is 0.89 g/cm^3.

Poly-alpha-olefins are lubricants with stable chemical composition, which come in a wide range of viscosity depending on the length of the polymeric chain. They are widely used in many applications because their high viscosity index.

The mineral oil HVI650 was chosen for many reasons: a comparison between synthetic and mineral oils was envisaged; one of the greases employed in this work has a mineral oil as its base lubricant, thus another mineral oil, with different viscosity was needed; finally HVI650 has a viscosity larger than PAO40 thus a wide range of film thickness can be obtained, even at low entrainment speeds.

Base oil of tested greases

4. **SBM grease**'s base oil is a synthetic hydrocarbon oil supplied by Dr. Shinya Kondo from Kyodo Yushi Corporation in Japan. Its flash point is 240 ℃. Density is 0.83 g/cm^3.
5. **SRL grease**'s base oil is a synthetic ester oil also supplied by Dr. Shinya Kondo from Kyodo Yushi Corporation in Japan. Its flash point is 254 ℃. Density is 0.97 g/cm^3.
6. **HIV 160S** is a 100% mineral oil commercially produced by Shell Global Solutions and provided by Belgian Shell Corporation. Its flash point is 280 ℃. This is the base oil of the RL2 grease. Density is 0.87 g/cm^3.

4.4.2 Greases

1. **SBM grease** contains (75%-80%) synthetic hydrocarbon base oil, (10%-20%) Urea derivatives thickener, ($< 10\%$) zinc and barium compound additives. It was supplied by Dr. Shinya Kondo from Kyodo Yushi Corporation in Japan. Flash point and dropping point (melting) are 210 ℃ and 260 ℃ respectively.
2. **SRL grease** contains (80%-90%) synthetic ester base oil, (5%-15%) Lithium soap thickener, ($< 5\%$) barium compound additives. It was supplied by Dr. Shinya Kondo from Kyodo Yushi Corporation in Japan. Flash point and dropping point (melting) are 225 ℃ and 190 ℃ respectively.
3. **Stamina RL 2** is a kind of automotive and industrial greases. It contains (80%-100%) highly -refined mineral oil, diurea thickener, (1%-15%) additives. It was supplied by Belgian Shell Corporation. Flash point and dropping point (melting) are 200 ℃ and 180 ℃ respectively.

Table 4.1: Properties of tested greases and the corresponding base oils

Grease	Base oil	Base oil viscosity	Thickener	Additives
SBM	Synthetic hydrocarbon oil	45 $mm^2/s\ at$ 40°C 7.7 $mm^2/s\ at$ 100°C	Urea (10%-20%)	zinc and barium compound ($< 10\%$)
SRL	Synthetic ester oil	23 $mm^2/s\ at$ 40°C 4.7 $mm^2/s\ at$ 100°C	LiSt (5%-15%)	barium compound ($< 5\%$)
RL 2	HVI 160S	107 $mm^2/s\ at$ 40°C 12 $mm^2/s\ at$ 100°C	Diurea	not applicable

4.5 Conclusions

A wide range of lubricant types is used in practice. Their primary role is to protect metallic surfaces from wear and to reduce friction, thus improving the efficiency of systems. Liquid lubricants come as a large variety of lubricating oils, which can be mineral or synthetic. They are best suited to large speed applications and require a pumping and recirculating system. Lubricating greases are semi-solid substances formed by the mixture of a liquid lubricant with a soap or other solid chemical. This gives them some advantages in comparison to liquid oils such as, easier application, no need of recirculating systems, no leakage, protection from contaminant.

Three oils and three greases were chosen for this research, such that a wide range of film thickness and working conditions can be obtained.

Chapter 5: Experimental Methodology

5.1 Optical interferometry technique in EHD

The methodology chosen for the measurement of the EHD film thickness and the evaluation of EHD film behaviour is optical interferometry. Over the years, in its many variants, this technique proved to be the most accurate in measuring lubricant film thickness in EHD contacts.

The application of optical interferometry to the measurement of lubricant film thickness in EHD contacts was pioneered by the lubrication laboratory at Imperial College London. In 1966, Cameron and Gohar [12] carried out a theoretical analysis of the EHD point contacts deriving a formula for predicting the lubricant film thickness. They backed up their analysis with an experimental investigation which resulted in detailed maps of the film thickness over the contact area. The contact consisted of a steel ball sliding against a glass plate, the used white light source resulted in coloured images of the contact, which were captured by camera. These results revealed for the first time what it is now the familiar horse-shoe shape of EHD film distribution as it can be seen in figure 5.1.

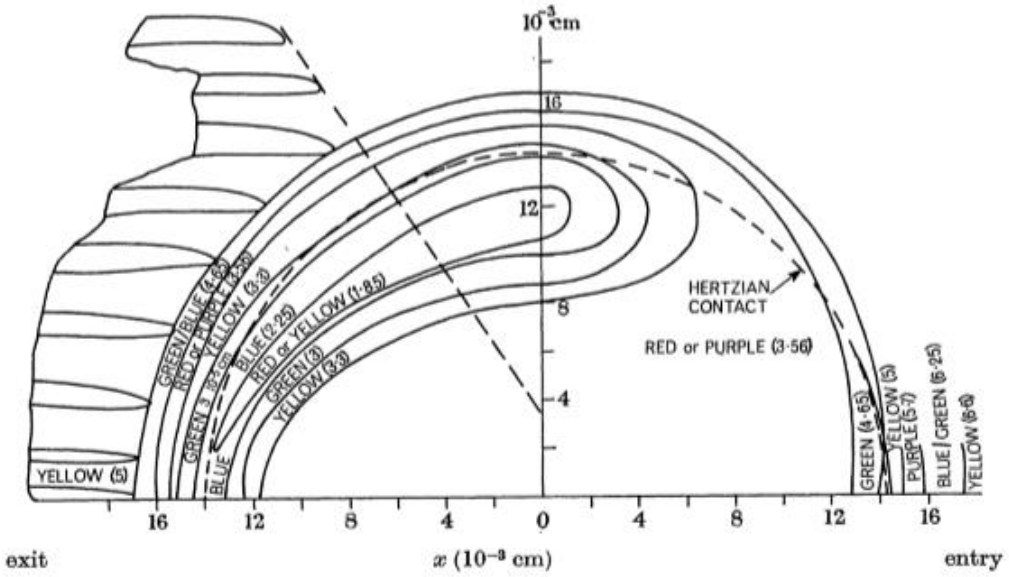

Figure 5.1: Oil contour map [12]

One year later, Gohar and Cameron [99] extended this interferometric method to determine the shape and thickness of EHD films. The EHD point contact was formed between a rotating ball and diamond, sapphire and glass discs respectively, which allowed higher contact pressure to be obtained. Their results showed that the film shape for point and line contacts depends strongly on the load and speed.

In 1968, Foord et al. [100] used the same optical experimental set-up to study the effects of

fluids of different structure on the thickness and topography of the lubricant film. A semi-reflective chromium layer, which reflected only 20 percent of incident light, was coated on the contacting surface of the disc to overcome the problem of similar refractive indexes between lubricant and glass. The evaluation of the results revealed that fluid structure influenced the lubricants film by its viscosity and pressure viscosity coefficient.

The work done by Cameron and his group enlightened the understanding and knowledge of lubricant behaviour in EHD contacts. It made it possible to predict lubricant film thickness when the contact was fully flooded and perfectly smooth. Before 1990's, optical interferometry had also been applied to other lubrication conditions, in situations which lubricant film thickness cannot be simply predicted, such as the study of starvation [101], grease-lubricated contacts [102] and contact in rough surface [103].

In 1970s, Westlake [104] firstly proposed the use of a spacer layer to overcome the limitation of conventional optical interferometry that is it cannot measure films less than one quarter the wavelength of the light used in experiments. In 1991, Johnston et al. [105] combined a silica space layer with conventional optical interferometry technique and a spectrometer, which allowed accurate measurement of lubricant film thickness in rolling point contacts below 100nm and even down to 5nm. Their results also showed that standard circular contact EHD film thickness equations can be used with a great number of fluids to predict central film thickness down to 15nm. Their contribution has made it possible to study the lubricant film in thin film lubrication regime thus this technique is known as Ultra – Thin Film Interferometry (UTFI).

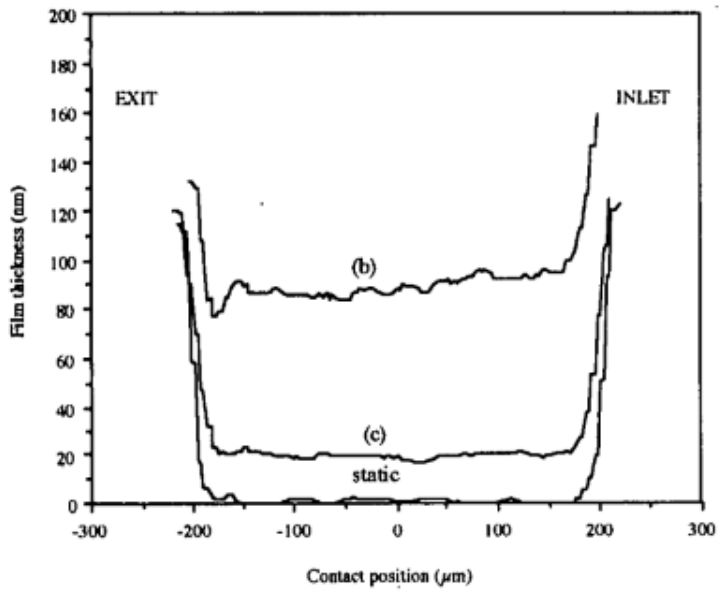

Figure 5.2: Comparison of fully flooded and starved film thickness profiles [106]

In 1996, Cann et al. [106] developed a contact mapping imaging technique (Spacer layer imaging technique (SLIM)) to visualize and measure lubricant film thickness in concentrated

contacts. A colour CCD camera was employed to capture images of the contact, then the images were translated into a colour bit map which can be converted into an absolute film thickness map by using the HSI (Hue, Saturation, Intensity) calibration method. Regardless of the calibration curve error and intensity changes within measurements, this technique could measure and map thin EHD films down to 10nm, as seen from the film thickness profiles shown in figure 5.2.

In 2001, Marklund and Gustafsson [107] used a ball-and-disc apparatus and computer-based analysis of the obtained interferograms to extract EHD film thickness. They discussed a calibration look-up procedure based on intensity methods, which transferred 3-tuple [red-green-blue (RGB)] into the hue-saturation-intensity system.

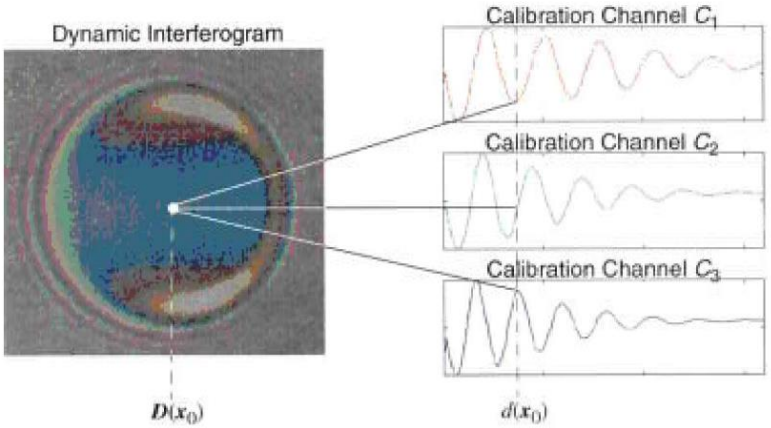

Figure 5.3: Marklund and Gustafsson calibration look-up procedure [107]

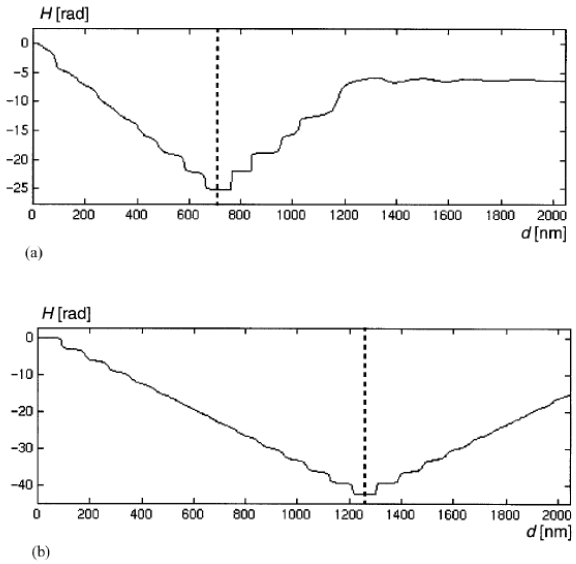

Figure 5.4: (a) Unwrapped Hue calibration table (white light); (b) Unwrapped Hue calibration table (trichomatic light) [107]

Figure 5.3 is a dynamic colour interferogram recorded from a ball-on-disc apparatus with white light source. In order to facilitate one to one mapping, a calibration table must be built.

As shown in figure 5.4, the effective film thickness measurement range is 80-750nm when white light is used; if a spacer layer was added the effective film thickness measurement range extends to about 1300nm.

In 2003, Glovnea et al. [108] refined the technique of ultra-thin film interferometry by replacing the two-beam interference analysis with a multiple-beam one. The improved technique was tested with three different fluids and it successfully measured film thickness down to 0.3nm with a standard deviation 0.15nm. There are also other techniques based on optical interferometry to study the behaviour of EHD films, for instance relative optical interferometry intensity (ROII) by [109-110] and thin film colorimetric interferometry [111-112].

5.1.1 Setup of optical interferometry technique

It is known that light consists of electromagnetic wavetrains emitted by atoms of any material. The finite length of these wavetrains makes the light emitted, for example by a thermal source, form a frequency spectrum, which we perceive as white light. When emitted from a single thermal source, the light waves are coherent thus if a phase difference occurs between various rays they can interfere [113]. This property is exploited in optical interferometers and it was firstly successfully used by Cameron and his team at Imperial College London.

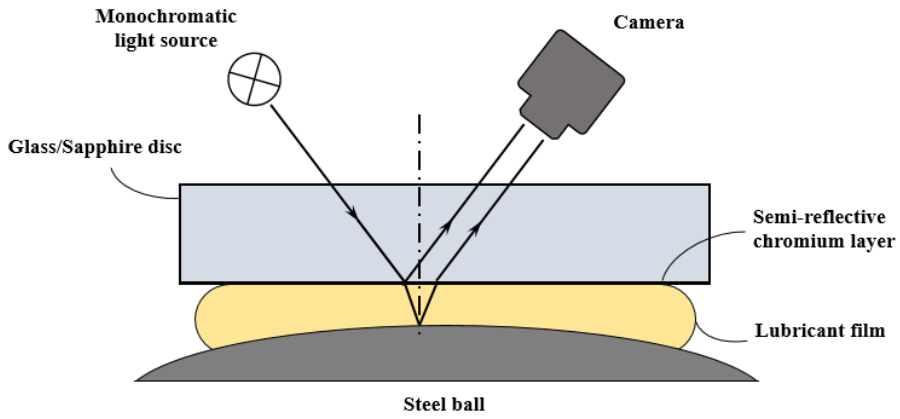

Figure 5.5: Schematic diagram of the optical interferometry principle

As shown in figure 5.5, a transparent glass or sapphire disc is loaded against a super polished steel ball or roller. The contacting side of the transparent disc is coated with about 10-20 nm semi-reflective chromium layer. When an incoming monochromatic light beam is incident on the transparent disc, it is partly transmitted and partly reflected by the chromium layer and passes through the lubricant film. Due to the phenomena known as multiple reflection, internal reflection can take place several times within the film, however it should be noted that the amplitudes of the reflected rays become negligible after the second internal reflection. The rays reflected by the chromium layer and by the steel surface will then undergo optical interference because of the path

difference, which will result in either constructive or destructive interference.

For two-beam interferometry, the fringe visibility is governed by the intensity distribution within the fringe pattern [108].

$$I_R = I_1 + I_2 + 2\sqrt{I_1 I_2}\cos\left(\frac{2\pi\delta}{\lambda}\right) \tag{5.1}$$

Where I_1 and I_2 are the individual intensities of the two reflected beams, λ is the wavelength and δ is the path difference due to the beam twice passing the optical thickness of the film and ϕ is an effective phase change at the reflection at the steel surface.

$$\delta = 2h_{opt} + \lambda\phi, \tag{5.2}$$

Where N is the order of interference, λ_{max} the wavelength for which complete constructive interference occurs and λ_{min} the wavelength for complete destructive interference, then the optical film thickness can be extracted from the relationships:

Constructive interference: $(N-\phi)\lambda_{max} = 2h_{opt}$ $N = 1,2,3..$ (5.3)

Destructive interference: $\left(N-\frac{1}{2}-\phi\right)\lambda_{min} = 2h_{opt}$ $N = 1,2,3..$ (5.4)

5.1.1 The development of optical interferometry in EHD

There are two main limitations in conventional optical interferometry described above: firstly, it cannot distinguish between films thinner than approximately one quarter of the wavelength of the light used. Secondly, only certain, discrete thicknesses, spaced at least 50nm apart can be determined [105]. These two limitations of optical interference technique have been eliminated by Ultra-thin film interferometry (UTFI).

As shown in figure 5.6, white light source is incident onto the contact through a specially - built microscope which includes a beam splitter. A thin strip of the resultant coloured interference image across the contact centre is passed into the slit of a spectrometer, where it is dispersed by wavelength. The dispersed image is captured by a black and white CCD camera. In the image, intensity of the contact is measured by brightness, so the dispersed image gives information of the wavelengths undergoing constructive or destructive interference across the contact. From the wavelength and knowledge of the order of interference and taking the phase shift at the steel surface as π, the optical film thickness can be extracted.

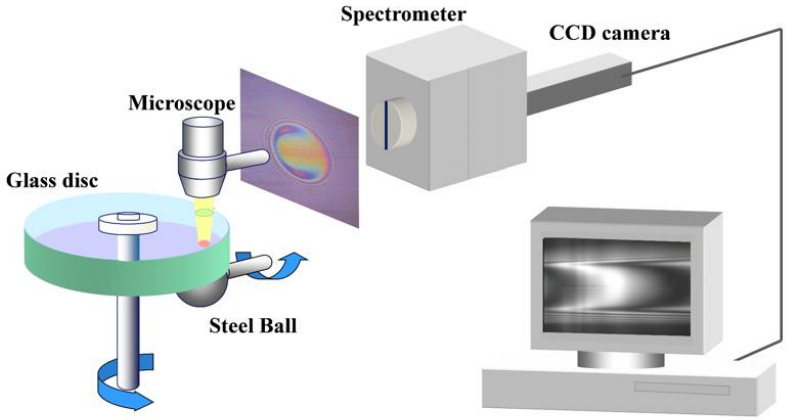

Figure 5.6: Schematic diagram of ultra-thin film interferometry setup [108]

From this the lubricant film thickness is derived as follows:

$$h_{opt} = n_{sl}h_{sl} + n_{oil}h_{oil} \tag{5.5}$$

Where n_{sl} and n_{oil} are the refractive indexes of silica layer and lubricant film respectively while, h_{sl} and h_{oil} are spatial film thickness of silica layer and lubricant film.

Ultra-thin film optical interferometry technique (UTFI) is currently one of the most accurate technique for determining lubricant film thickness of EHD contacts therefore, the construction of lubricant film thickness calibration curve in the current experiments relies on it.

5.2 Experimental Rig

An optical interferometry based experimental rig was built and modified with the aim of investigating the effect of vibrations upon the behaviour of base oil and grease lubricated EHD contacts. Elliptical contact in real rolling element bearings was simplified by a circular point contact between a super polished steel ball and a flat disc, which was so-called ball-on-disk apparatus. Spacer layer imaging technique (SLIM) was applied to evaluate EHD film thickness during vibration motion. Detailed description and schematic of the experimental rigs as well as the working and controlling principle will be presented in the following context.

A EHD contact was formed between a 20 mm diameter AISI 52100 precision steel ball (figure 5.7(4)) and a glass disc, double coated with a thin layer of chromium and another of silica on top about 130 nanometres thick (figure 5.7(13)) loaded against each other. The disc was driven by a DC motor, not shown in the figure, through a special designed gear box and a shaft, and the ball was driven by friction forces generated in the EHD contact.

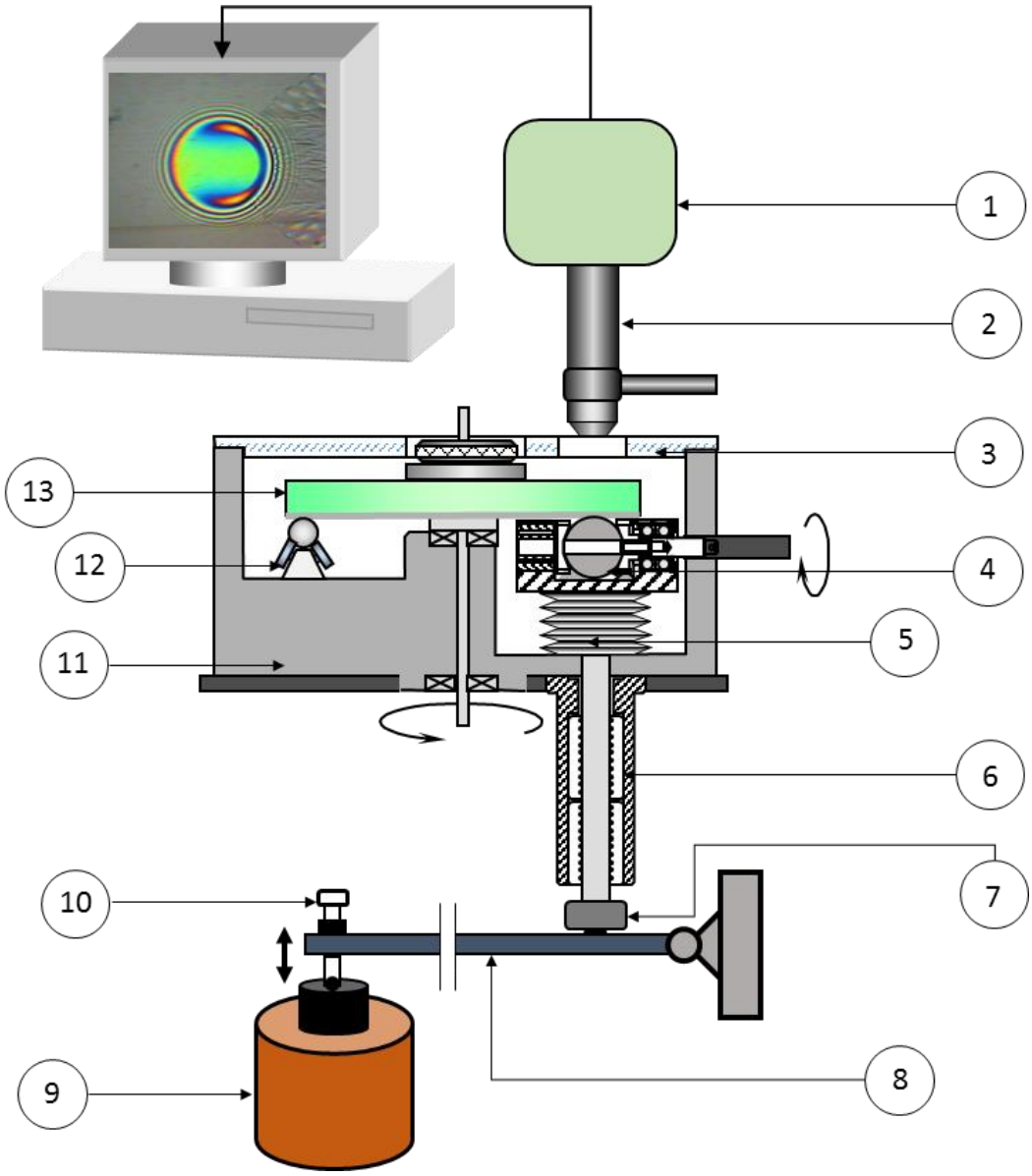

Figure 5.7: Schematic diagram of the experimental rig of vertical vibration

The contact was thus in nominal pure rolling (slide roll ratio, defined as ratio of sliding and rolling speeds is nominally zero) kinematic condition in all the tests. The ball was half immersed in a lubricant chamber (figure 5.7(11)) while rolling with the disc achieved fully flooded conditions throughout most of the experiments. Vertical vibrations were generated by an electro-dynamic shaker (figure 5.7(9)), which was placed underneath a cantilever arm (figure 5.7(8)) and connected by an adjustable screw (figure 5.7(10)), which enabled bringing the ball into contact with the disc and achieving any desired preload level. An additional ball carriage was placed under the disc on the opposite side to prevent the deflection of the disc under loading, as shown in figure 5.7(12). A transparent lid (figure 5.7(3)) was placed on top of the lubricant pot to avoid lubricant splashing. A 250N tension & compression load cell (figure 5.7(7)) was mounted between the cantilever and the loading plunger (figure 5.7(6)). The loading plunger was guided by two

linear bearings enclosed in a precision rolling bush to minimize friction. A stainless-steel bellow (figure 5.7(5)) with spring rate of $8.17\ N/mm$ was precisely manufactured and mounted between the ball carriage holder and the loading plunger, allowing an axial movement of 10 mm. Contact images were captured and recorded by a high-speed camera (figure 5.7(1)) through a microscope (figure 5.7(2)). A PC was used to analyse the contact images and to evaluate lubricant film thickness.

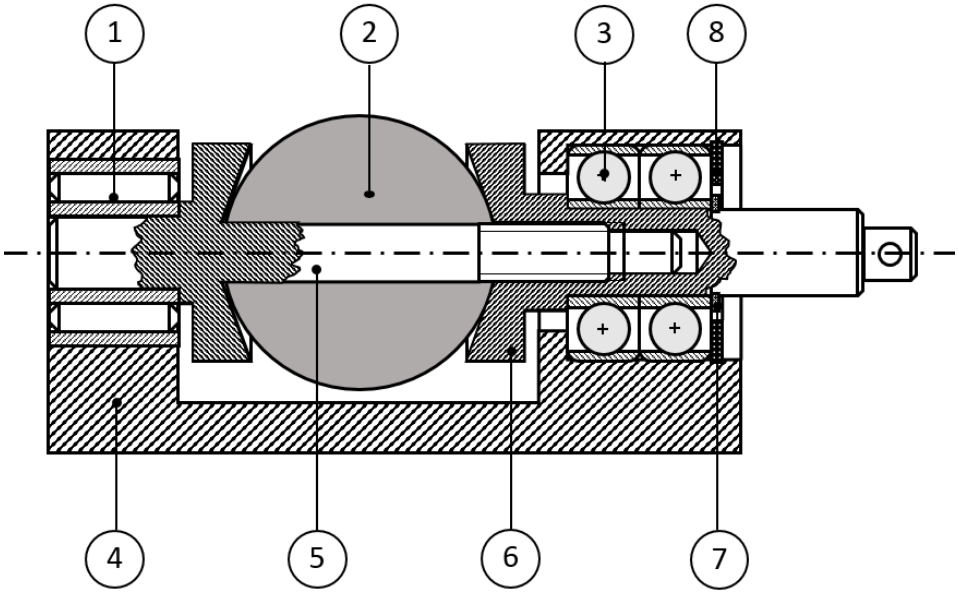

Figure 5.8: Schematic of ball carriage holder

A detailed schematic of the ball carriage holder is presented in the figure above. The super polished steel ball (figure 5.8(2)) was fitted to a shaft (figure 5.8(5) and (6)) supported by a needle bearing (figure 5.8(1)). Lateral oscillations and movements were cancelled by two miniature angular contact bearings (figure 5.8(3)) preloaded with both internal (figure 5.8(7)) and external circlips (figure 5.8(8)). Figure 5.9 shows photos of the ball carriage, bellow, plunger and linear bearing holder. Figure 5.10 shows photo of the experimental rig.

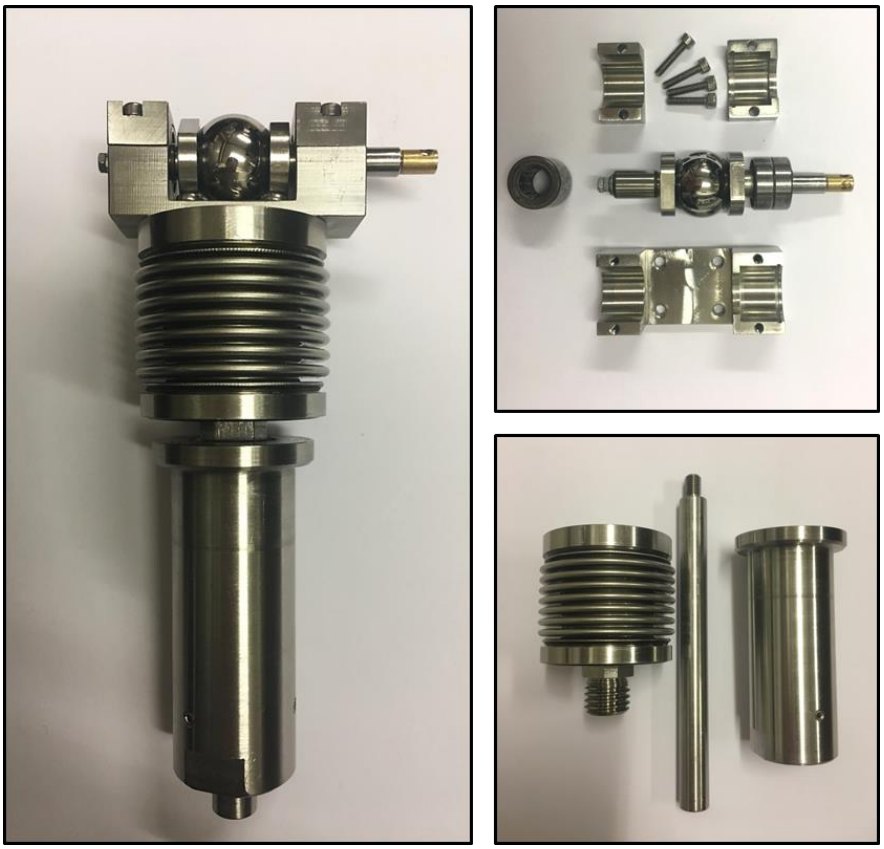

Figure 5.9 Photo of ball carriage and bellow assembly

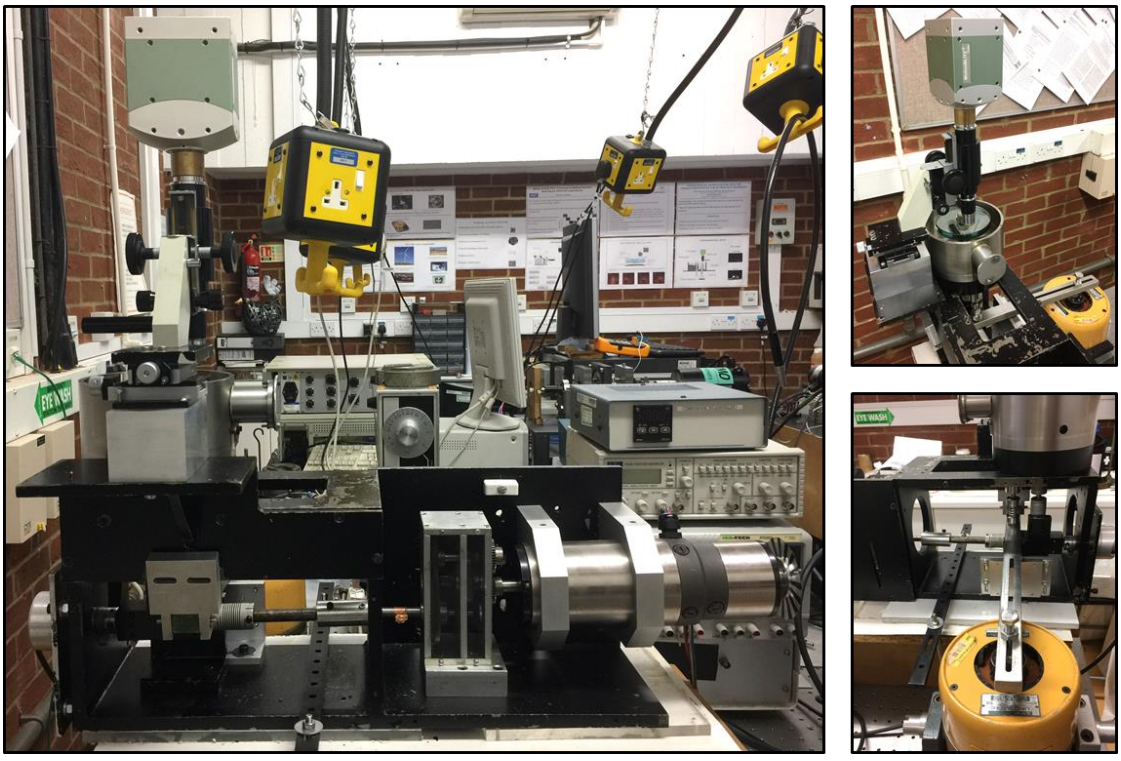

Figure 5.10: Photo of experimental rig

5.2.1 Test equipment

Function Generator

A TG330 series function generator (Aim & Thurlby Thandar Instruments) was employed for producing a variety of precision waveforms over a capable range of frequencies from mHz to MHz. It provided a wide range of controlled amplitudes from a low-impedance source, maintaining a constant amplitude as the frequency was varied. The signal generated was sent to the dynamic shaker with amplification.

Dynamic shaker

Vertical oscillatory motion was applied to the lever by a Ling Dynamic Systems model 406 series dynamic shaker. The dynamic shaker provides a frequency range from 1.5 Hz to 9 kHz with a TPO 100 amplifier. The maximum thrust force generated (with forced cooling) is 196 N and the maximum amplitude is 9 mm. The actual displacement required at the contact between the ball and disc was of the order of magnitude of micrometres. Therefore, to accommodate this displacement a suitable stiffness spring was placed between the cantilever arm and the load cell.

Miniature Load Cell

A 250 N tension & compression stainless steel miniature load cell with environmental sealing IP67 was mounted underneath the plunger for direct measurement of load variation. Maximum excitation of the load cell is between 5 and 15 V and the input resistance is 353 ohms. The full load output of the load cell is 1.9457 mV/V according to the manufacturer.

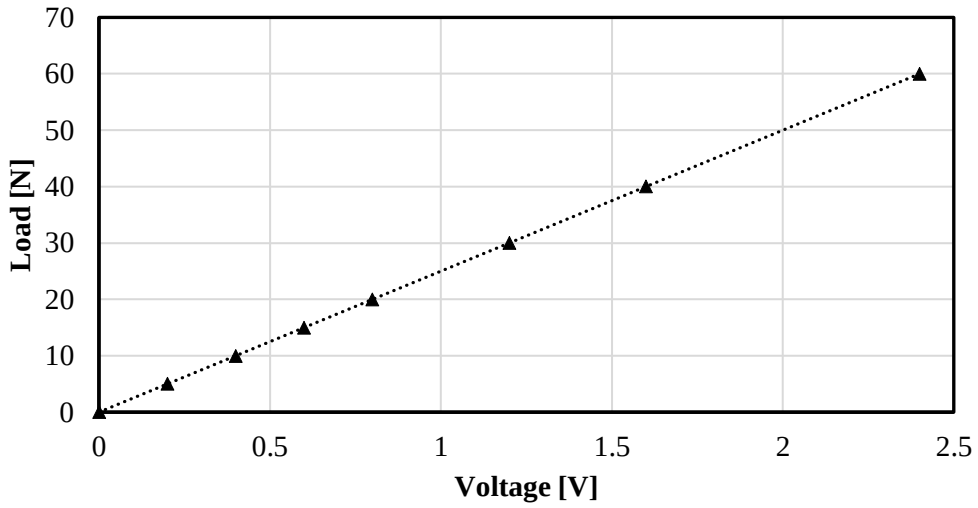

Figure 5.11: Load cell calibration curve

To filter inevitable electrical noise and to achieve high resolution output signal, an IP66 enclosed, high stability load cell amplifier was used. The signal of the load cell, after amplifying reached a level up to ± 10 V. The maximum frequency of the signal that can be processed is 1 KHz bandwidth. This is well higher than the frequency of the vibrations intended to be studied in this research.

The load cell was calibrated by placing calibrated masses on it and recording the voltage variation. The calibration curve seen in figure 5.11 shows very good linearity within the load range used.

Digital Oscilloscope

The load variation applied to the EHD contact was recorded by a G-Tech GDS-2064 digital storage oscilloscope featuring a bandwidth of 60 MHz. The four channels delivered a sample rate of 1 G Samples/s and a maximum record length 25 K Samples. There are four types of advance triggering modes available, *Auto-Level Trigger* (digital oscilloscope generates an internal trigger if there is no trigger event), *Normal Trigger* (it acquires waveforms in a trigger event), *Single Trigger* (it acquires waveform only once in a trigger event), *Line Trigger* (it uses the internal source as the trigger source). Only two channels of the digital oscilloscope had been used during this study, a maximum record length of 12.5 k samples was fixed and normal trigger mode was selected for acquiring load distribution waveform.

High-speed camera

A coloured MotionBlitz Cube Z3 digital high-speed camera was employed for capturing and recording EHD contact images during rapid variation of load. The camera has a maximum resolution of 512×512 pixels and a maximum framerate of 120000 fps (at reduced resolution). In the presented study, the framerate was set at 2000 fps, which provided 20 frames in a vibration cycle when the EHD contact was subject to a load with 100 Hz cycle. The objective lens fitted to the camera through a microscope has $\times 10$ magnification. A white light source was used resulting in coloured interference images of the EHD contact.

Trigger control of the camera

To be able to correlate the recorded images with a certain value of the load during vibration cycle, triggering procedure of both camera and oscilloscope must be achieved. This was done by starting the system and using a switch to send a low-to-high signal to both the camera trigger port and to the oscilloscope. This is illustrated in figure 5.12.

When the external trigger switch was switched on, a trigger signal would activate the normal trigger mode in the oscilloscope to acquire the load variation waveform, while the camera would stop recording contact images. Thus, the stop recording time of the camera and the stop acquiring

waveform time was at identical point.

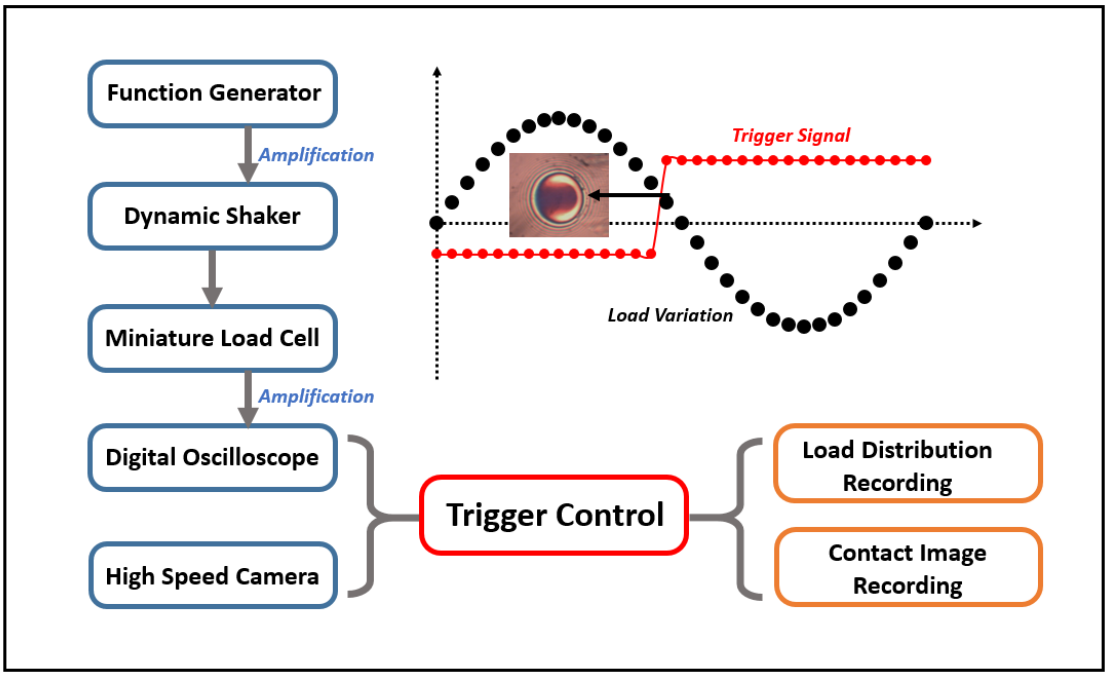

Figure 5.12: Synchronised trigger control procedure

5.3 Film thickness calibration procedure

The actual values of the film thickness over the EHD contact area were extracted by a custom – written code following a calibration curve which relates the RGB content at each pixel of the image with a value of film thickness. Calibration procedures for each different test lubricant were carried out before vibration experiments. The first step was to find the dependency of steady state EHD film thickness on entrainment speed in pure rolling conditions, by using UTFI (ultra-thin-film-inteferometry). Due to different refractive index of the lubricants used, a total of five groups of calibration tests were performed.

The graphs in figure 5.13 show the variation of film thickness as a function of entrainment speed, as recorded by a PCS Instruments EHD2 ultra-thin film measurement system. Because the dependence of EHD film thickness on the entrainment speed follows a power law, a linear relationship between film thickness and entrainment speed is seen in log-log format.

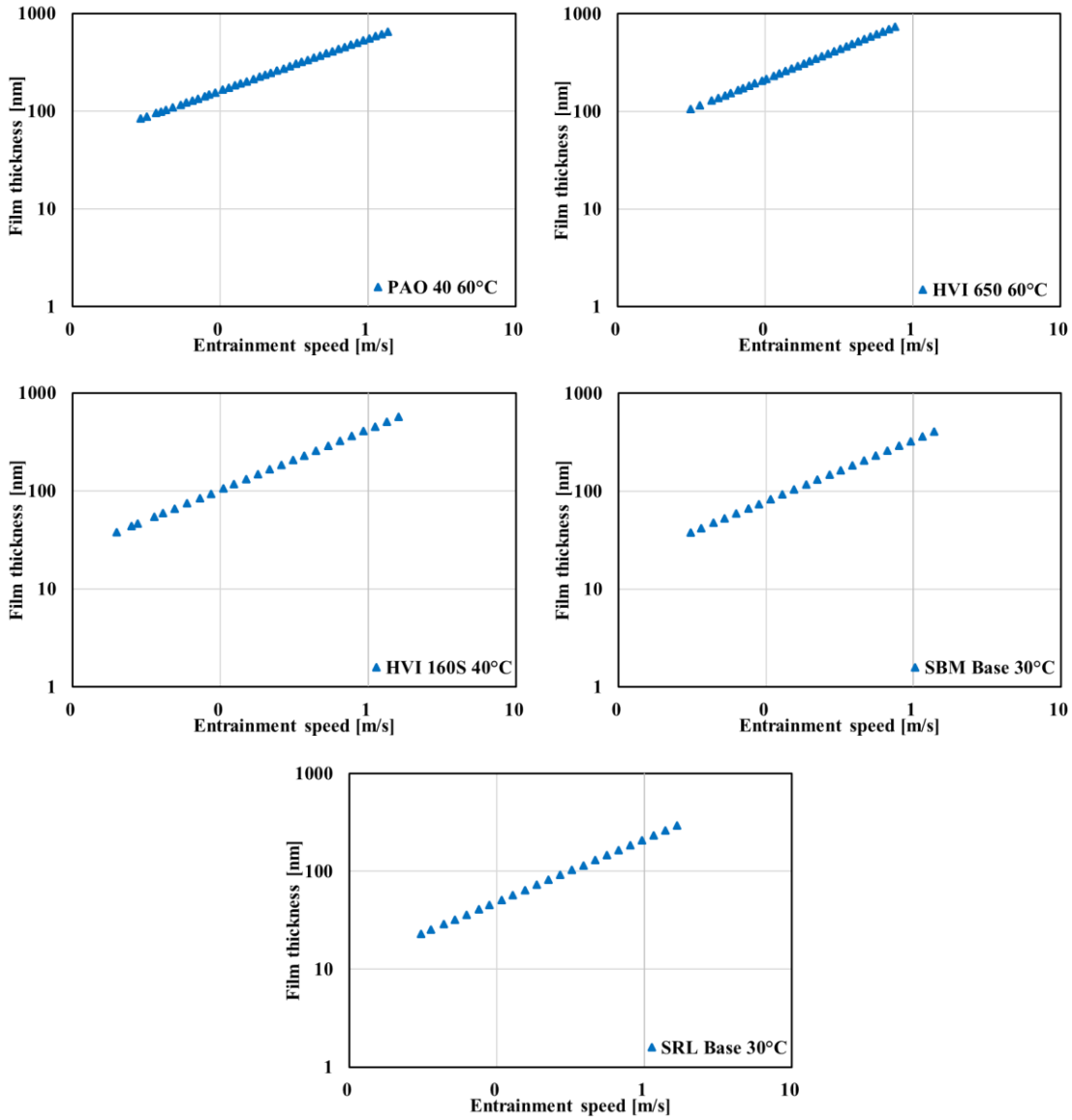

Figure 5.13: Relationships between EHD film thickness of five lubricants and increasing entrainment speed under pure rolling condition

5.3.1 RGB Values

In order to get the correlation between RGB content of the images and film thickness, the former as a function of entrainment speed has to be obtained first. Thus, in the second step of the calibration procedure, the silica layer disc was replaced with a disc coated with only a semi-transparent chromium layer. Images of the contact were then recorded at exactly same entrainment velocity and temperature conditions as in the UTFI tests. As the central film thickness is almost constant over the central contact area, averaged RGB values of each pixel within a rectangular region located in the central region of every image were extracted.

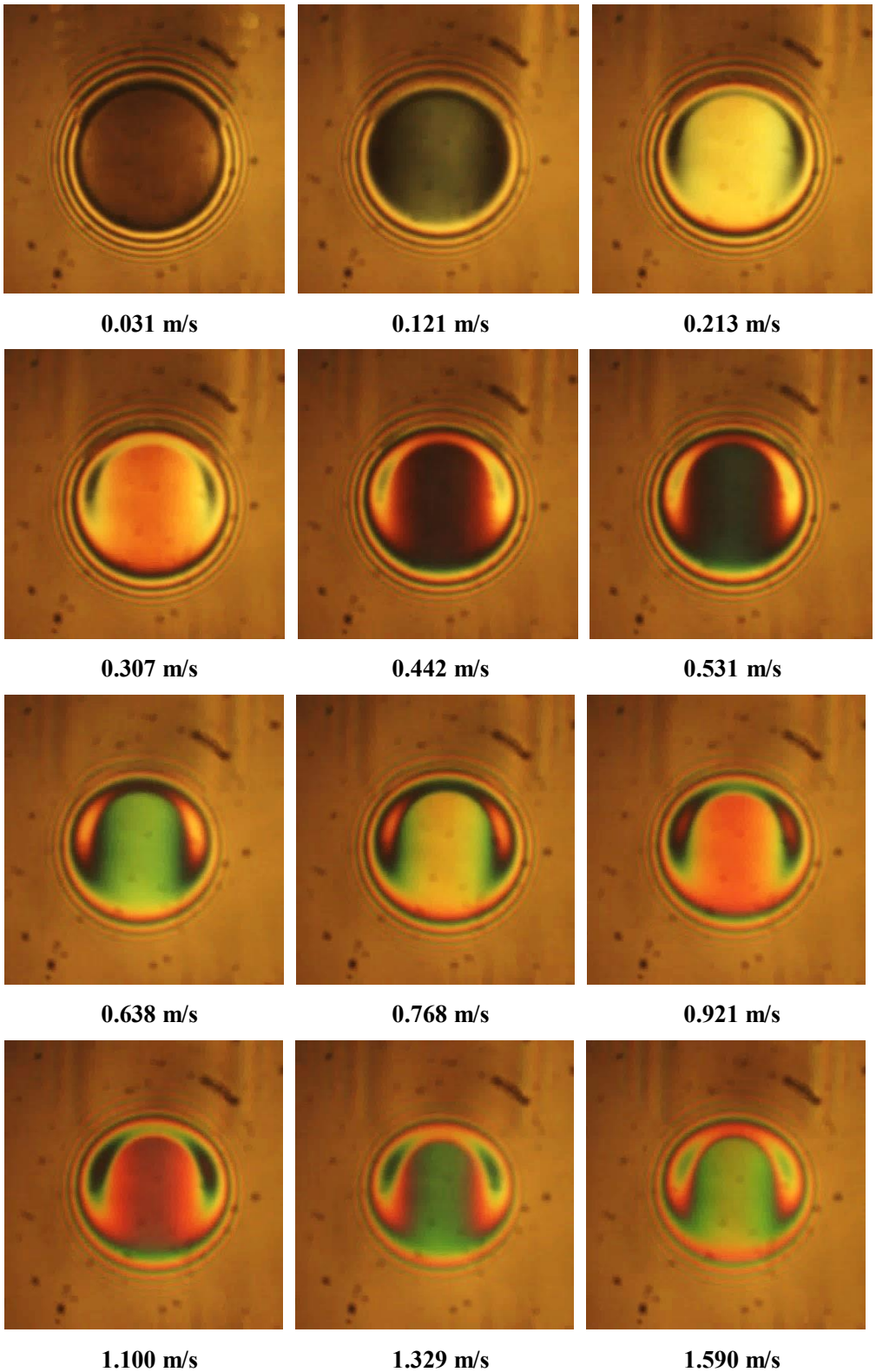

Figure 5.14: Selected interference fringe patterns, ***HVI 160S Base oil*** at 40℃

Images of the contact for HVI 160S oil at 40°C are shown in figures 5.14. The change of the colour of the contact with increasing the entrainment speed can be observed. This is because the film thickness changes with entrainment speed and when it becomes equal to integer values of half-wavelength of ta ray the latter interferes constructively stronger than other wavelengths.

In this way the central film thickness from (UTFI) and the averaged RGB content from the interferograms, both as functions of the entrainment were obtained. Eliminating the speed between these two sets of values, the RGB versus film thickness is obtained. These variations, for five oils tested are shown in figures 5.15.

These graphs are actually used not in the form of analytical functions, but that of tables of values of R, G, and B for various thicknesses of the lubricant film. After the experimental interference images of the contact, under variable load conditions, were obtained, the R, G, B information was read from the desired area of the contact by a purposely built computer programme, and converted into film thickness values based on the calibration tables.

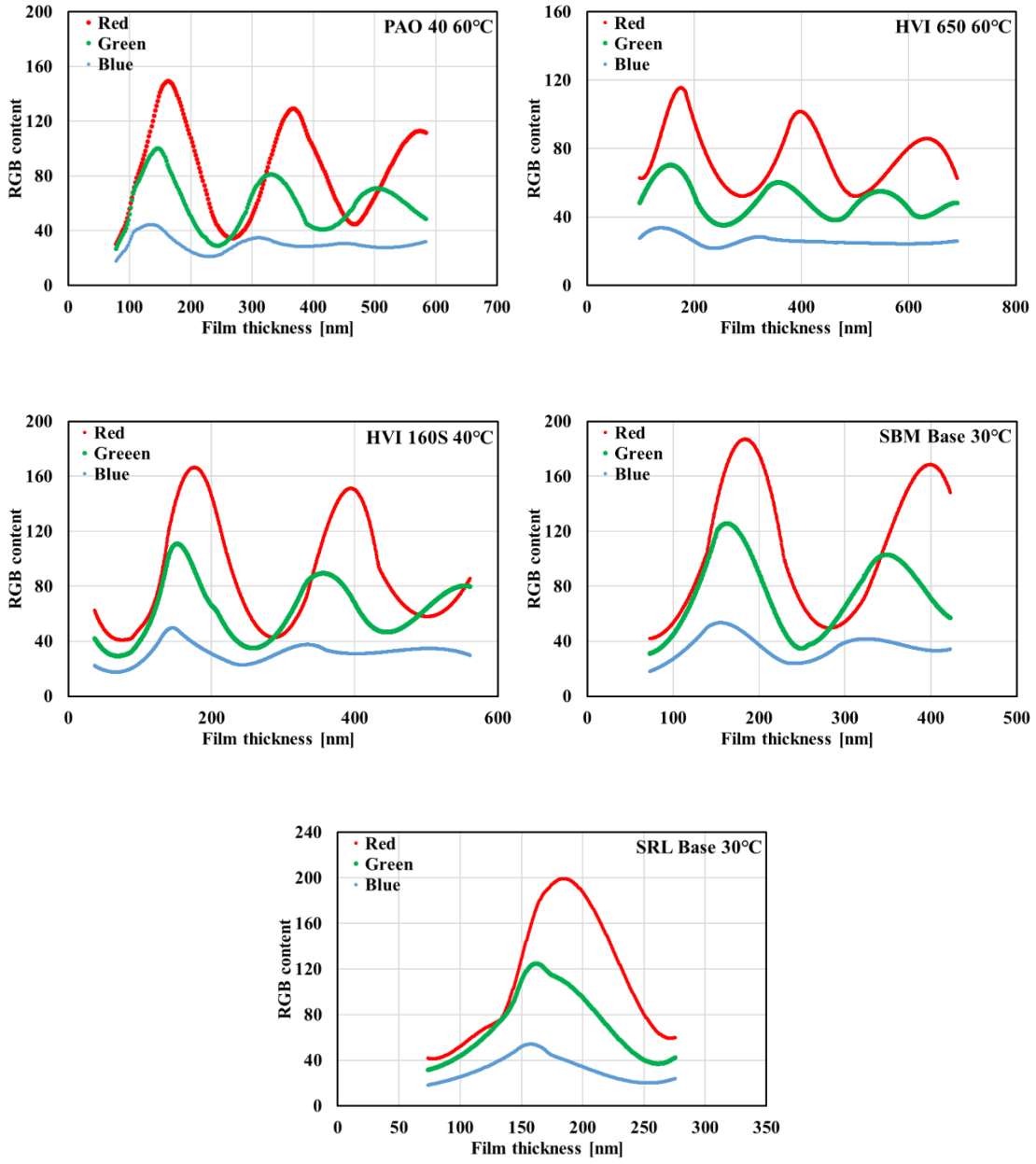

Figure 5.15: Relationships between EHD film thickness of five lubricants and their **RGB** content under pure rolling condition

5.3.2 Accuracy of film thickness calibration procedure

Figure 5.16 shows film thickness results extracted from 100 image samples of PAO 40 60°C at 0.126 m/s used in the calibration process. These are compared with the value of the film thickness from the UTFI method. The results obtained with this procedure varied ±5 percent about the average which on its turn was within 3.8 percent of the values obtained by UTFI method.

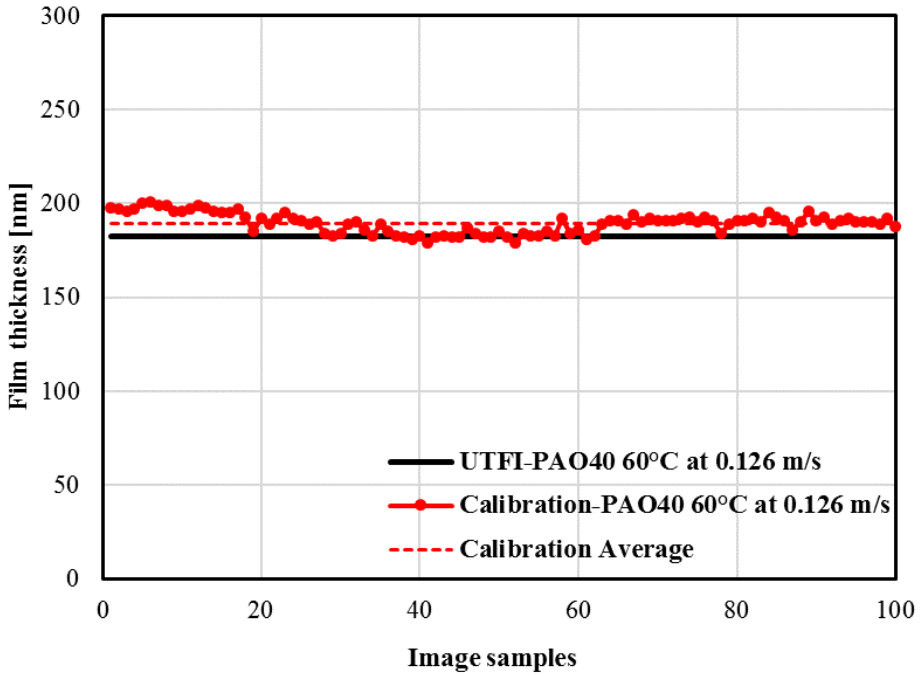

Figure 5.16: Accuracy of film thickness calibration procedure

The deviations from the UTFI values are attributed to fact that the sputtering process used to graft the chromium coating onto the disc used for the calibration procedure, does not guarantee a perfect uniform thickness of chromium layer around the circumference of the disc. Variation as small as 1-2 nm of the chromium layer thickness leads to variations in the transmissibility and reflectivity of chromium, thus the way the light beams interfered was influenced by the position of the disc when the images were captured.

5.4 Analysis of dry contact dimensions during vibration

To make sure that the experimental contact dimension is identical to theoretical calculations, a detailed vibrational contact dimension analysis of static EHD dry contact was completed prior to base oil lubricated experiments. As shown in figure 5.17 (left), a small pin hole with a contact diameter of 200 µm was mapped on the ball-on-disc apparatus without loading. The diameter of the pin hole expands in the horizontal direction 133 pixels, which gives the relationship between pixel and contact area, $\mathbf{1}\ \boldsymbol{pixel} \approx \mathbf{1.5}\ \boldsymbol{\mu m}$.

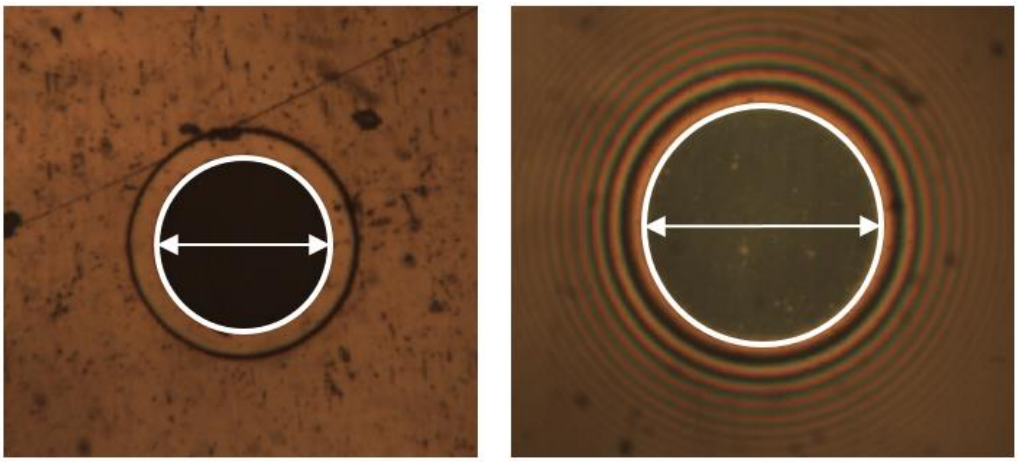

Figure 5.17: Dimension of pin hole (left) and contact dimension (right)

A static contact was also mapped as shown in the figure 5.17 (right). The diameter of the Hertzian contact area in horizontal direction is 188 pixels, thus the diameter of the contact is 280 μm. The theoretical contact diameter is 286 μm, which is only 2 percent difference from the experimental one.

Table 5.1: Hertzian dry contact parameters

Elastic modulus of disc	[Pa]	6.9×10^9
Poisson's ratio of disc material		0.29
Elastic modulus of ball	[Pa]	2.06×10^{11}
Poisson's ratio of ball material		0.3
Radius of ball	[m]	0.009525
Applied load	[N]	23

A series of coloured inteferograms of the dry EHD contact subjected to load variation at 5 Hz, were recorded as seen in figure 5.18. The images of the contact correspond to typical loading points within one loading – unloading cycle of vibration at static condition are shown together with load variation over one cycle.

As shown in figure 5.22, the difference between measured and theoretical diameter of the contact was between 0.18 percent and 5.35 percent.

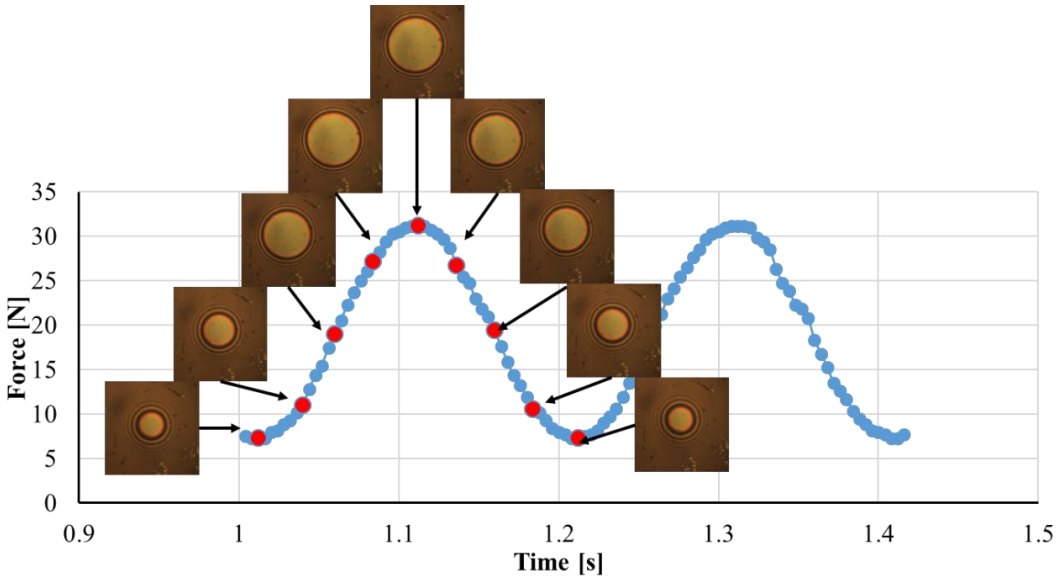

Figure 5.18: Typical behaviour of EHD contact in one loading-unloading cycle

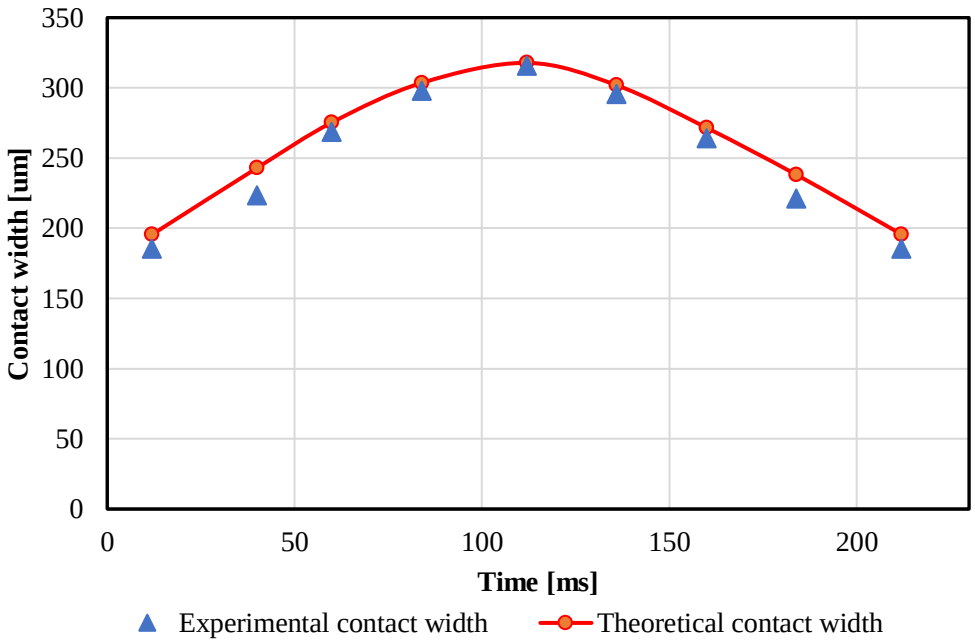

Figure 5.19: Variation of Hertzian contact width during one loading-unloading cycle

5.5 Conclusions

Due to its accuracy and possibility of obtaining maps of the film thickness over the whole contact area, optical interferometry was chosen as the method for study of the film thickness under harmonic loading. The test rig which incorporates this method allows controlled application of load, entrainment speed and working temperature. The calibration procedure employed resulted in an accuracy of ±5 percent and a precision of 3.8 percent when compared to values obtained with the established ultra-thin-film interferometry technique.

Chapter 6: EHD Films Subjected to Vibrations

In this chapter, the results of EHD films subjected to vibrations, with variable lubricant viscosities, different rolling speeds as well as frequencies will be presented.

Table 6.1: Selected completed experiments of EHD oil film subjected to vertical vibrations

Oil Lubricant	*Temp*	*Speed*	*10 Hz*	*20 Hz*	*25 Hz*	*40 Hz*	*50 Hz*	*60 Hz*	*100 Hz*
PAO 40	Ambient	0.05 m/s	•		•		•		•
		0.1 m/s	•		•		•		•
		0.2 m/s	•		•		•		•
		0.3 m/s	•		•		•		•
		0.5 m/s	•		•		•		•
HVI 650	40°C	0.05 m/s	•		•		•		•
		0.1 m/s	•		•		•		•
		0.2 m/s	•		•		•		•
		0.3 m/s	•		•		•		•
		0.5 m/s	•		•		•		•
PAO 40	40°C	0.05 m/s	•		•		•		•
		0.1 m/s	•		•		•		•
		0.2 m/s	•		•		•		•
		0.3 m/s	•		•		•		•
PAO 40	60°C	0.05 m/s	•		•		•		•
		0.1 m/s	•		•		•		•
		0.2 m/s	•		•		•		•
		0.3 m/s	•		•		•		•
PAO 40	75°C	0.05 m/s	•		•		•		•
		0.1 m/s	•		•		•		•
		0.2 m/s	•		•		•		•
		0.3 m/s	•		•		•		•
SBM base	40°C	0.1 m/s	•	•		•		•	
		0.3 m/s	•	•		•		•	
		0.5 m/s	•	•		•		•	
		0.7 m/s	•	•		•		•	
		0.9 m/s	•	•		•		•	
PAO 4	40°C	0.1 m/s	•		•		•		•
		0.2 m/s	•		•		•		•
		0.3 m/s	•		•		•		•
		0.5 m/s	•		•		•		•

PAO 40 at the test temperatures used, and PAO 4 gave a wide range of viscosities, which allowed the evaluation of this parameter upon the behaviour of the EHD film. The highly refined mineral oil HVI 650 was used in order to see the effect of the lubricant composition, especially because the base oil of one of the greases tested (RL2) is also a mineral oil of the same group. All the experiments carried out in this chapter were under pure rolling condition. The EHD film generated within the contact was subjected to sinusoidal load variation on a direction

perpendicular to the contact to obtain a forced harmonic vibrations system. The results are grouped in two sections: base oil tests and grease tests. Table 6.1 shows the selected number of tests carried out with base oil as lubricant together with the working conditions employed.

Table 6.2: Completed experiments of EHD grease film subjected to vertical vibrations

Grease Lubricant	*Temperature*	*Speed*	*Vibration Period*	*10 Hz*	*20 Hz*	*40 Hz*	*60 Hz*
SRL	40°C	0.38 m/s	5 minutes	•	•	•	•
			10 minutes	•	•	•	•
			15 minutes	•	•	•	•
			20 minutes	•	•	•	•
SBM	40°C	0.55 m/s	5 minutes	•	•	•	•
			10 minutes	•	•	•	•
			15 minutes	•	•	•	•
			20 minutes	•	•	•	•
RL2	40°C	0.77 m/s	5 minutes	•	•	•	•
			10 minutes	•	•	•	•
			15 minutes	•	•	•	•
			20 minutes	•	•	•	•

Three different greases (with one of their base oil included in table 6.1) were also tested as shown in table 6.2. Details of test conditions for each performed test and the selected, typical, captured EHD film images are presented in the rest of this chapter.

6.1 Results for oil-lubricated EHD films subjected to vibrations

6.1.1 PAO 40 at ambient temperature

The experiments were performed at four different frequencies, 10 Hz, 25Hz, 50 Hz and 100 Hz. The general properties of this lubricant can be found in Chapter 4. The lubricant was kept at ambient temperature of 20 ± 1℃ by two thermocouples fitted near the contact inside the lubricant chamber. Tests were carried out at entrainment speed with values between 0.05 m/s to 0.5 m/s. The maximum applied load and the minimum applied load were between about 0 N to 55 N, which led (for steel on glass) to the Hertzian pressure varying between 0 GPa and around 0.7 GPa.

Due to the presence of the silica spacer layer which practically enhances the separation between the chromium layer and the steel ball surface, the thickness of the spacer layer must be

known. This was done by taking an image of the static, un-lubricated contact prior to every test. Subsequently the spacer thickness was derived using the corresponding film thickness calibration curves showed in Chapter 5. In order to have a base of comparison for film behaviour under vibrations, the lubricant film thickness in steady state conditions at different test speeds was firstly recorded. Figure 6.1 shows images of the contact at various entrainment speed (a-e) and the static, dry image of the contact (f). The yellow arrow indicates the lubricant entrainment direction.

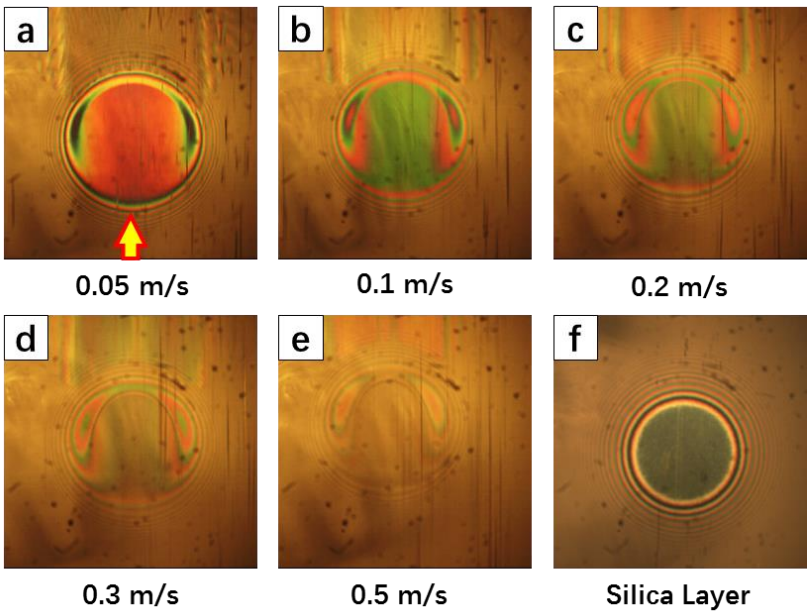

Figure 6.1: Steady state EHD contact lubricated with PAO 40 at different entrainment speeds, ambient temperature(a-e), and dry static contact (f).

A constant load of 47 N was applied to the EHD contact in these steady states rolling conditions. In figure 6.1 (a-e), it can be obviously seen that after the lubricant entering the Hertzian contact area, the thickness of the film is unchanged in the central region of the contact and only drops at the exit and the sides of the contact, showing the well-known horse-shoe feature. As the entrainment speed increases, the interference order of the central film thickness also increases. Because of the thick film, the objective lens of the microscope comes out of focus, make the images blurry as seen in pictures (d) and (e). The focus of the experimental work will thus be in the region of thinner films, bellow around 400 nm, which are more relevant to practical applications such as rolling bearings and gears.

After steady state contact images were recorded, the load was started to vary in a sinusoidal fashion resulting in harmonic forced vibrations. Because PAO 40 is a very viscous lubricant, especially at room temperature, only images for velocities bellow 0.2 m/s are presented and analyzed.

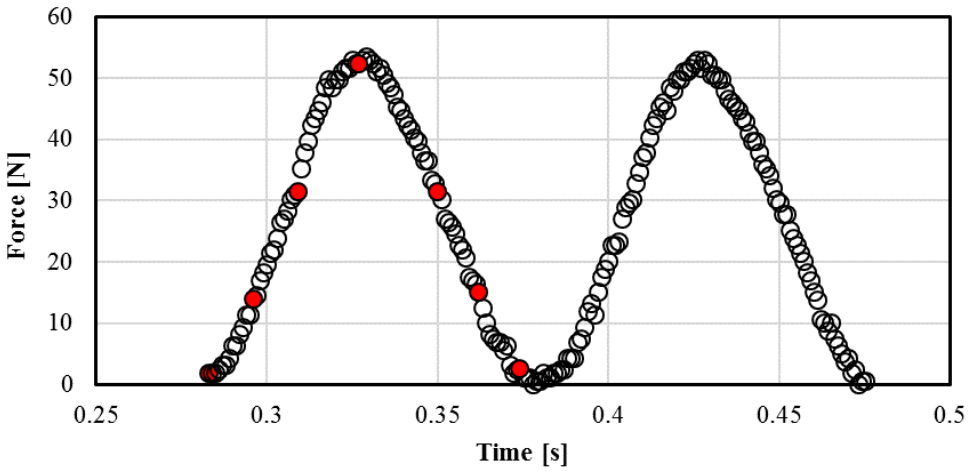

Figure 6.2a: Example of load variation, **10 Hz**, PAO 40 at ambient temperature vibration test.

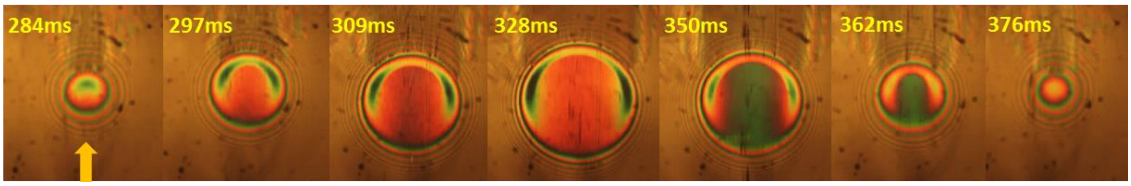

Figure 6.2b: Interferograms of the PAO 40 at ambient temperature, captured at 10 Hz, **0.05 m/s**

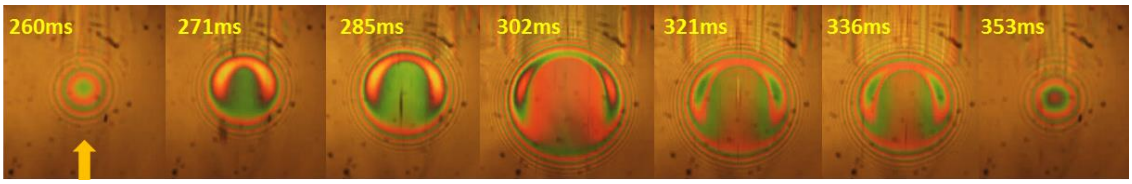

Figure 6.2c: Interferograms of the PAO 40 at ambient temperature, captured at 10 Hz, **0.1 m/s**

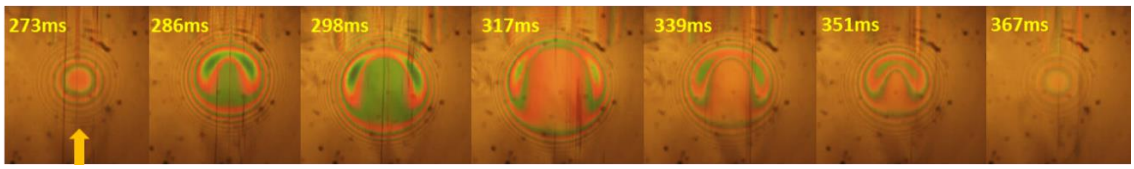

Figure 6.2d: Interferograms of the PAO 40 at ambient temperature, captured at 10 Hz, **0.2 m/s**

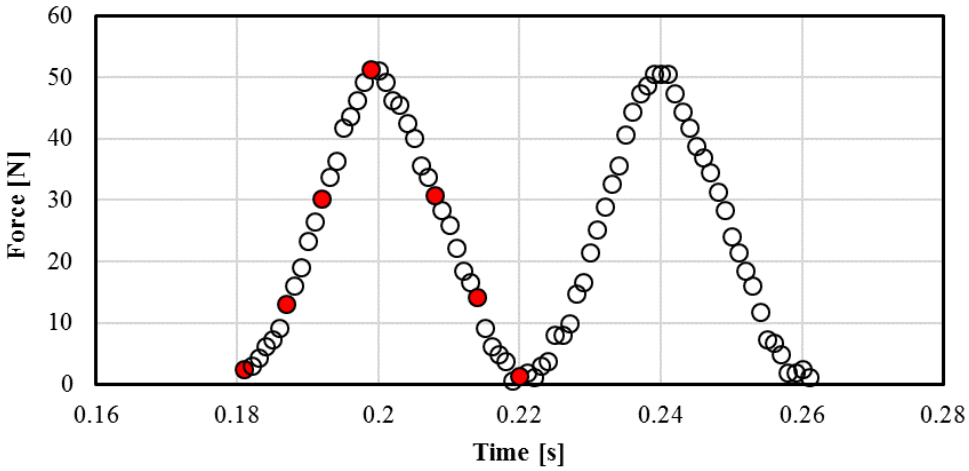

Figure 6.3a: Example of load variation, **25 Hz**, PAO 40 at ambient temperature vibration test.

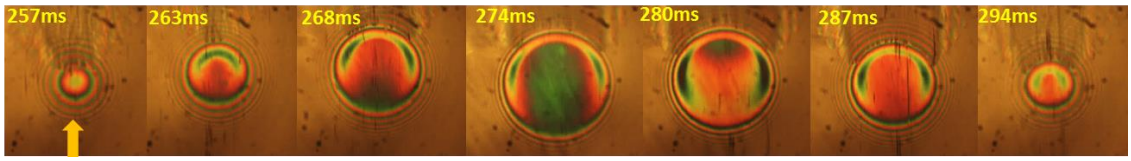

Figure 6.3b: Interferograms of the PAO 40 at ambient temperature, captured at 25 Hz, **0.05 m/s**

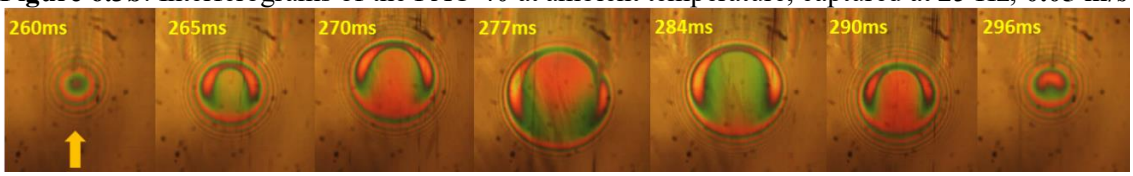

Figure 6.3c: Interferograms of the PAO 40 at ambient temperature, captured at 25 Hz, **0.1 m/s**

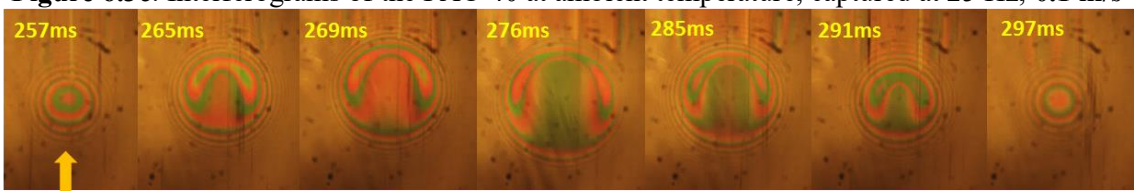

Figure 6.3d: Interferograms of the PAO 40 at ambient temperature, captured at 25 Hz, **0.2 m/s**

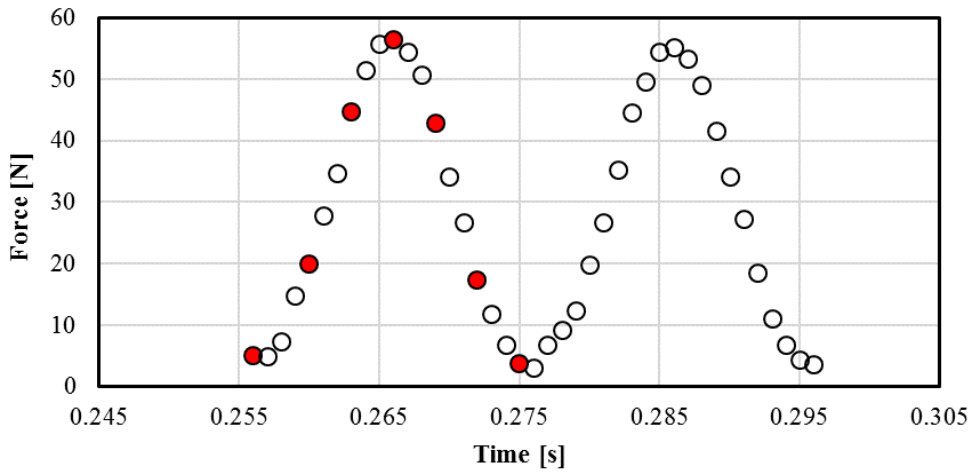

Figure 6.4a: Example of load variation, **50 Hz**, PAO 40 at ambient temperature vibration test.

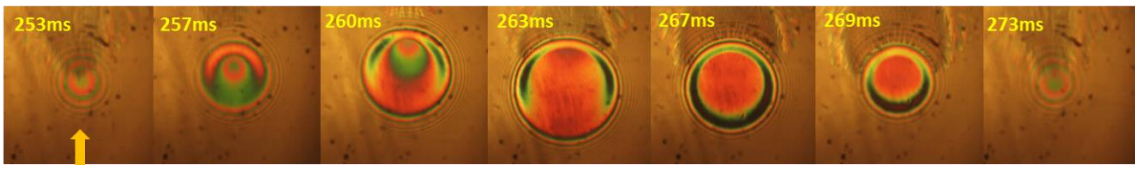

Figure 6.4b: Interferograms of the PAO 40 at ambient temperature, captured at 50 Hz, **0.05 m/s**

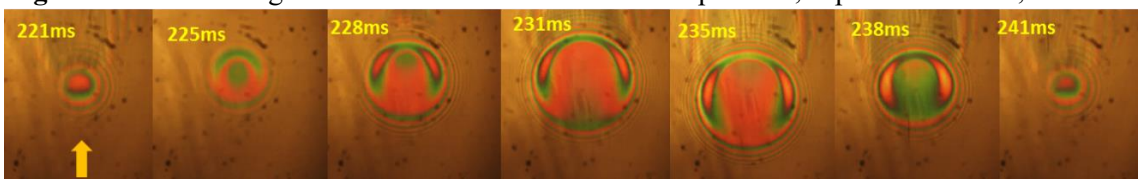

Figure 6.4c: Interferograms of the PAO 40 at ambient temperature, captured at 50 Hz, **0.1 m/s**

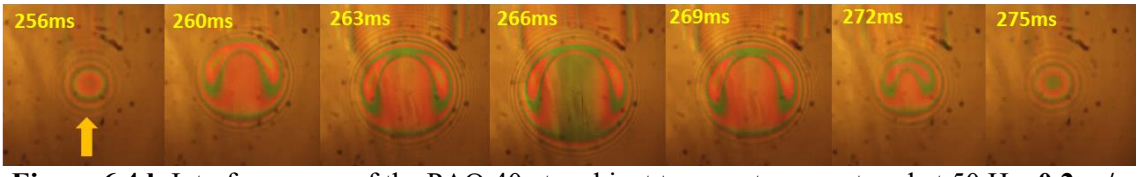

Figure 6.4d: Interferograms of the PAO 40 at ambient temperature, captured at 50 Hz, **0.2 m/s**

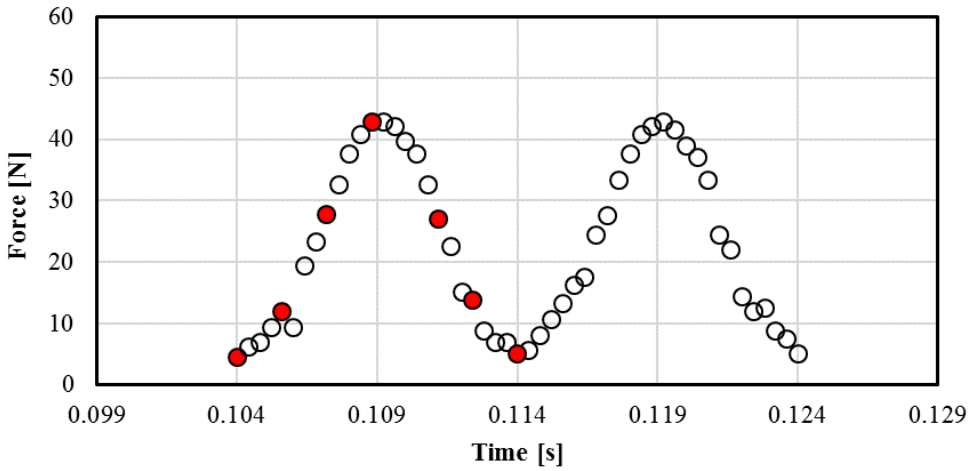

Figure 6.5a: Example of load variation, **100 Hz**, PAO 40 at ambient temperature vibration test.

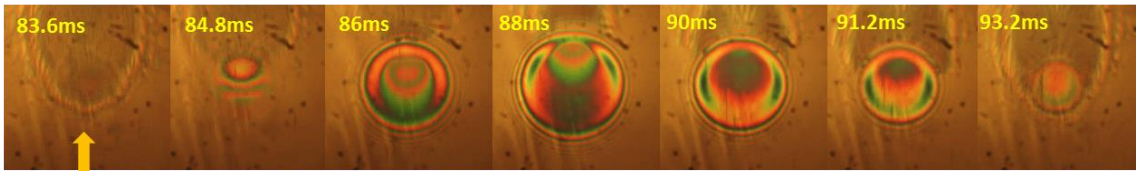

Figure 6.5b: Interferograms of the PAO 40 at ambient temperature, captured at 100 Hz, **0.05 m/s**

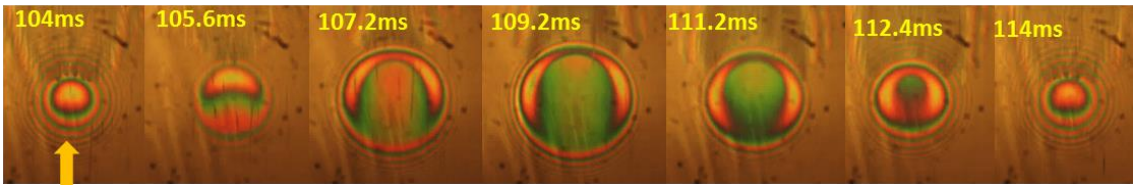

Figure 6.5c: Interferograms of the PAO 40 at ambient temperature, captured at 100 Hz, **0.1 m/s**

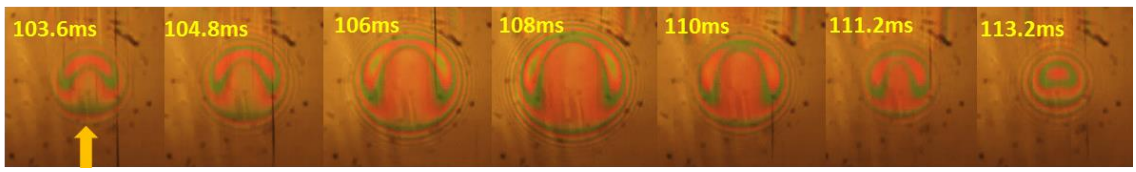

Figure 6.5d: Interferograms of the PAO 40 at ambient temperature, captured at 100 Hz, **0.2 m/s**

Figures 6.2 to 6.5 present the typical behaviour of EHD contact with entrainment speed of 0.05m/s, 0.1m/s, 0.2m/s and subjected to vertical vibration at 10 Hz, 25 Hz, 50 Hz and 100 Hz. A typical example of load variation for each frequency is presented in figures 6.2a to 6.5a. Seven captured images out of the whole number of captured images for one vibration cycle (loading-unloading phase) are selected. The variable load corresponding to these selected images are marked by the red dots in the load variation curve from left to right.

An overall view of the recorded EHD contact images in figures 6.2 and 6.3, show that there are no special features in the film, this follows the steady state behaviour explained earlier. A clear deviation from the classic film behaviour can be observed in figure 6.4b and 6.5b for the two largest frequencies of 50 Hz and 100 Hz respectively. It is noted, however, that this deviation

only occurs for entrainment speed not exceeding 0.1 m/s. It is seen in the first three selected images for both cases, the contact diameter increases nearly four times in as time interval of milliseconds. This sudden increase of contact area implies a sudden expansion in the convergent region of the contact inlet, which is equivalent to a sudden increase of entrainment speed. As the EHD film thickness is established by conditions in the inlet, and because entrainment speed has one of largest influence upon the film thickness, this means that a film thicker than that in the centre of the contact is formed at the inlet region. This enhanced film can be regarded as a film perturbation which, once formed, passes through the whole EHD contact area along the direction of entraining motion. It can also be observed that the phenomenon of film perturbation is diminishing with the increasing entrainment speed. A better insight into the film perturbation phenomena seen above will be given in the discussion chapter.

6.1.2 HVI 650 at **40**℃

In this section, the experiments performed with the mineral oil HVI 650 with properties shown in Chapter 4, at four frequencies, 10 Hz, 25Hz, 50 Hz and 100 Hz are presented. The lubricant was kept at temperature of 40 ± 1℃. Tests were carried out at entrainment speeds with values between 0.05 m/s to 0.5 m/s. The load varied between a minimum value of 0 and a maximum value of 62 N, which led to corresponding Hertzian pressure variation between 0 GPa and 0.74 GPa.

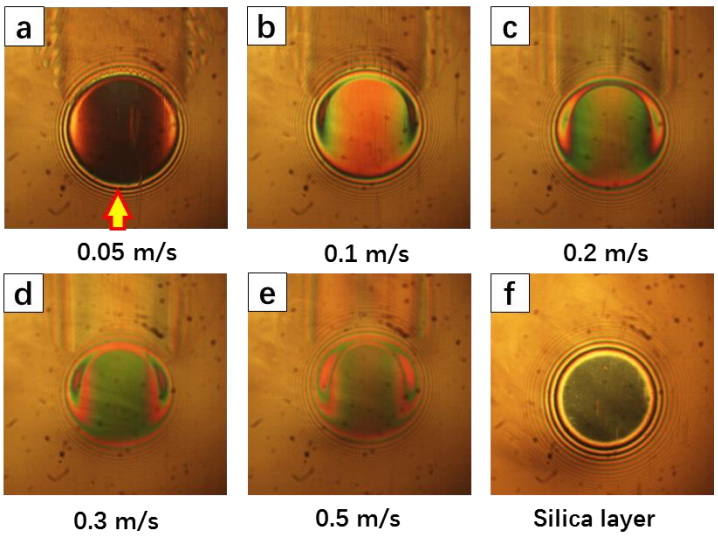

Figure 6.6: Images of EHD contact lubricated with HVI 650 at different entrainment speed (a-e), 40℃ and dry, static contact (f).

The steady state interferometric images of the EHD contact lubricated with HVI 650 at 40℃ with various entrainment speeds are shown in figure 6.6 (a-e), while in figure 6.6 (f) was the silica layer contact image. A constant load of 44.7 N was applied to the EHD contact under these steady states rolling conditions. The test was continued by applying a vertical forced sinusoidal vibration

to the EHD contact. Load variation and selected images of the contact during the cycle are shown in figures 6.7 to 6.10.

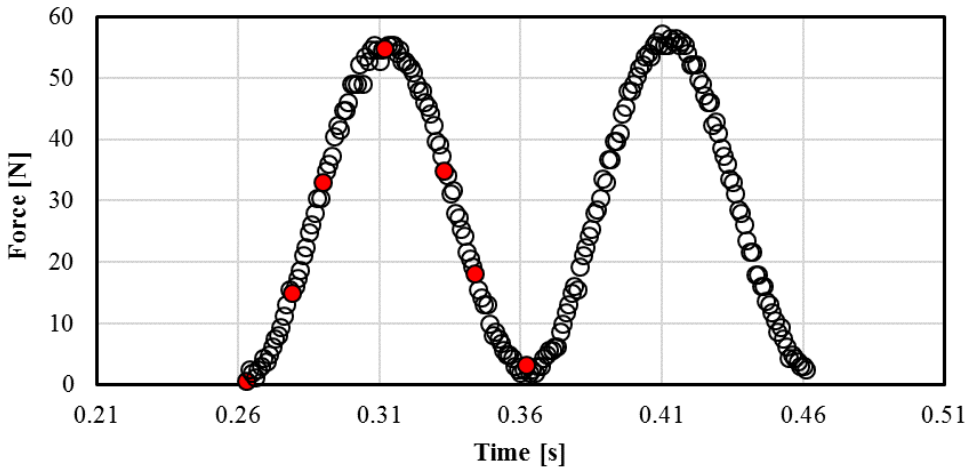

Figure 6.7 (a): Example of load variation, **10 Hz**, HVI 650 at $40^{\circ}C$ vibration test.

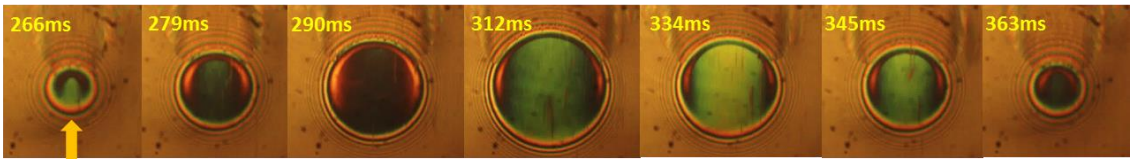

Figure 6.7 (b): Interferograms of the HVI 650 at $40^{\circ}C$, captured at 10 Hz, **0.05 m/s.**

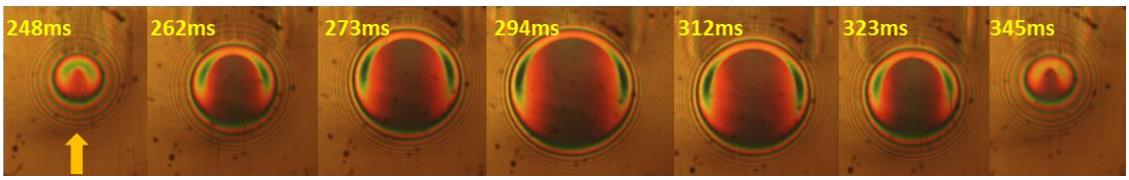

Figure 6.7 (c): Interferograms of the HVI 650 at $40^{\circ}C$, captured at 10 Hz, **0.1 m/s**.

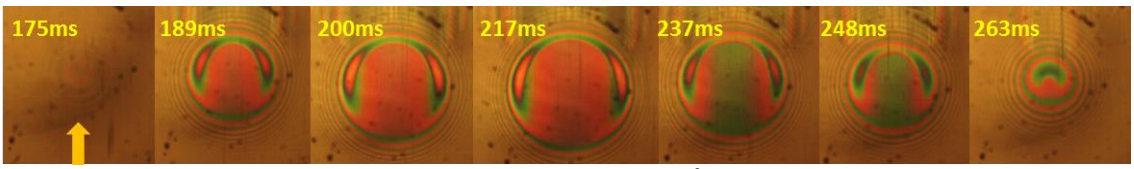

Figure 6.7 (d): Interferograms of the HVI 650 at $40^{\circ}C$, captured at 10 Hz, **0.2 m/s.**

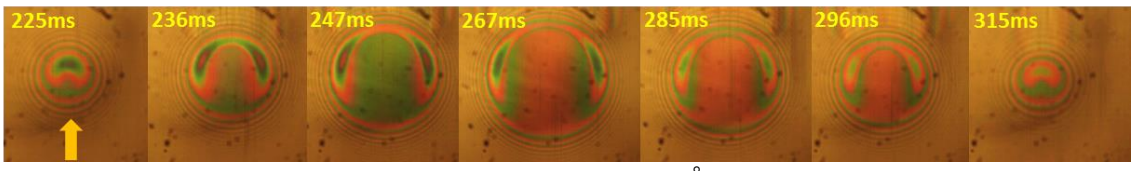

Figure 6.7 (e): Interferograms of the HVI 650 at $40^{\circ}C$, captured at 10 Hz, **0.3 m/s.**

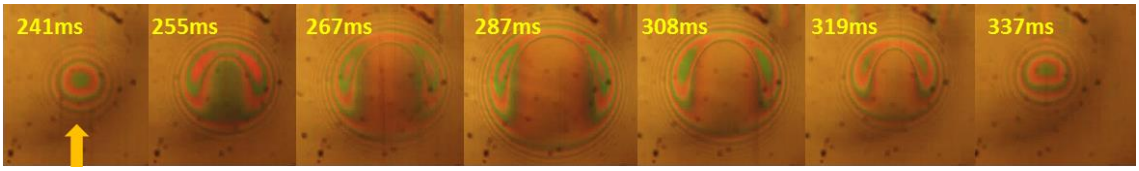

Figure 6.7 (f): Interferograms of the HVI 650 at $40^{\circ}C$, captured at 10 Hz, **0.5 m/s**.

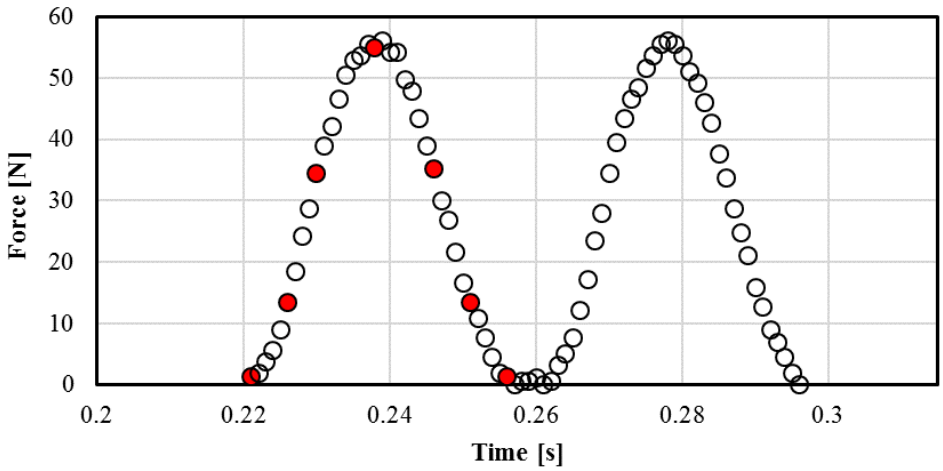

Figure 6.8 (a): Example of load variation, **25 Hz**, HVI 650 at $40^{\circ}C$ vibration test.

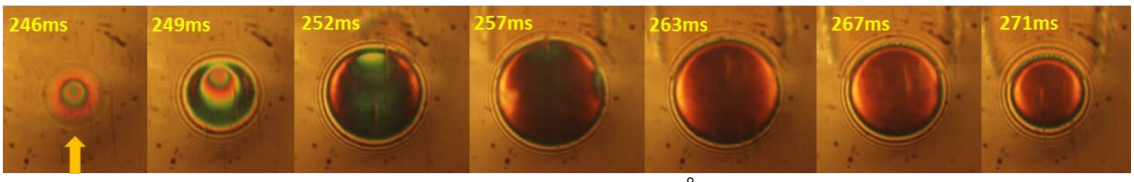

Figure 6.8 (b): Interferograms of the HVI 650 at $40^{\circ}C$, captured at 25 Hz, **0.05 m/s.**

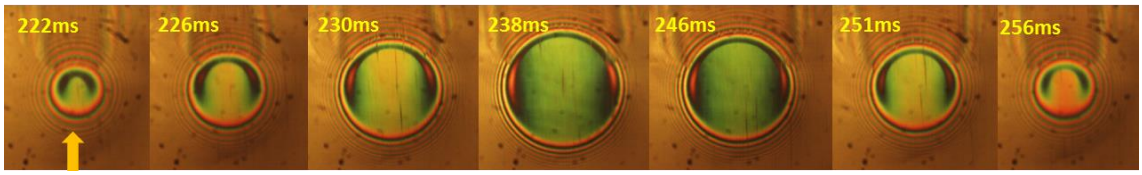

Figure 6.8 (c): Interferograms of the HVI 650 at $40^{\circ}C$, captured at 25 Hz, **0.1 m/s.**

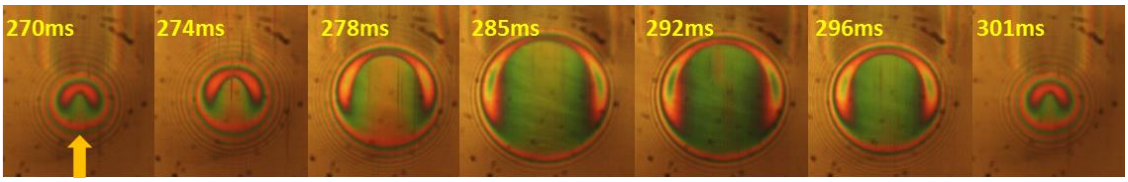

Figure 6.8 (d): Interferograms of the HVI 650 at $40^{\circ}C$, captured at 25 Hz, **0.2 m/s.**

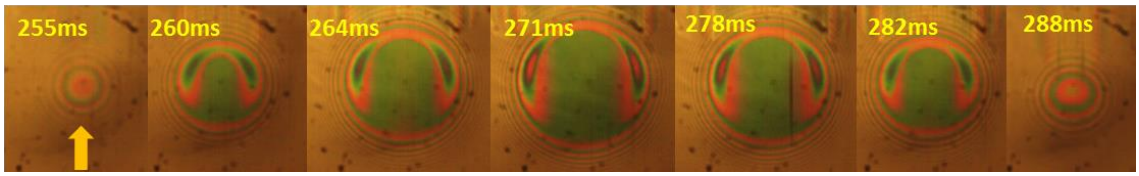

Figure 6.8 (e): Interferograms of the HVI 650 at $40^{\circ}C$, captured at 25 Hz, **0.3 m/s.**

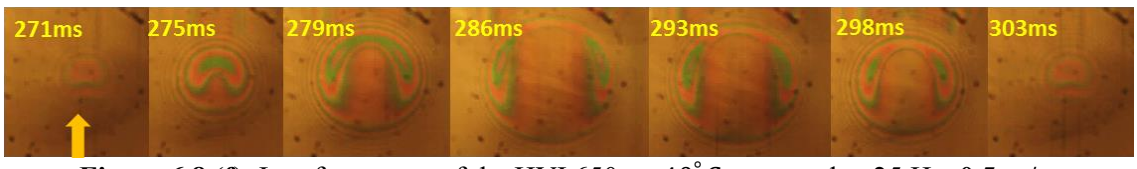

Figure 6.8 (f): Interferograms of the HVI 650 at $40^{\circ}C$, captured at 25 Hz, **0.5 m/s**.

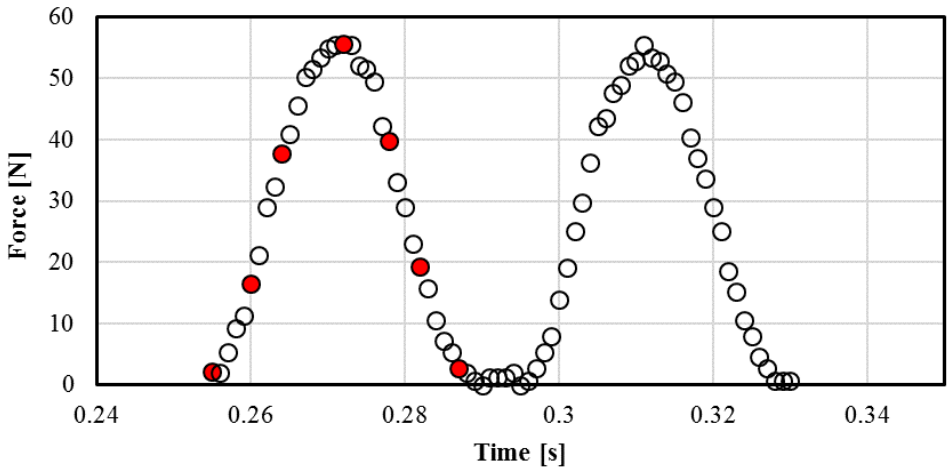

Figure 6.9 (a): Example of load variation, **50 Hz**, HVI 650 at $40^{\circ}C$ vibration test.

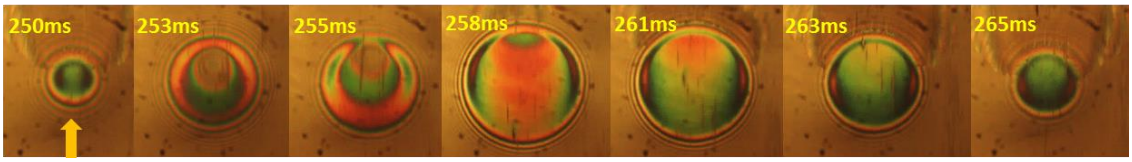

Figure 6.9 (b): Interferograms of the HVI 650 at $40^{\circ}C$, captured at 50 Hz, **0.05 m/s.**

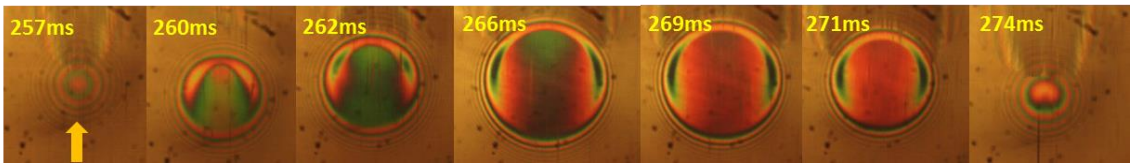

Figure 6.9 (c): Interferograms of the HVI 650 at $40^{\circ}C$, captured at 50 Hz, **0.1 m/s**.

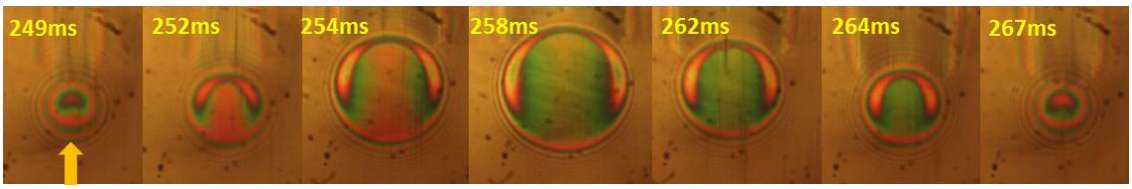

Figure 6.9 (d): Interferograms of the HVI 650 at $40^{\circ}C$, captured at 50 Hz, **0.2 m/s.**

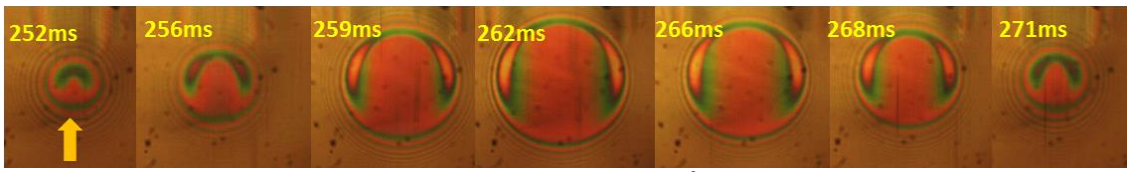

Figure 6.9 (e): Interferograms of the HVI 650 at $40^{\circ}C$, captured at 50 Hz, **0.3 m/s**.

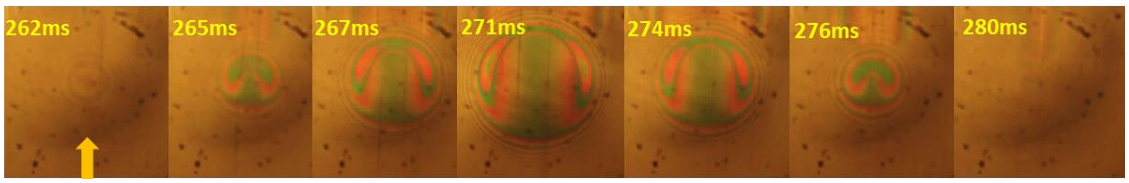

Figure 6.9 (f): Interferograms of the HVI 650 at $40^{\circ}C$, captured at 50 Hz, **0.5 m/s**.

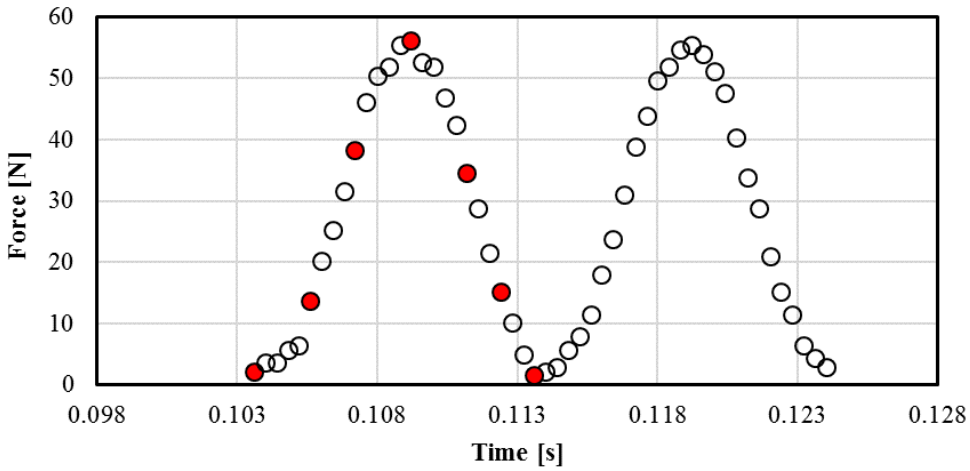

Figure 6.10 (a): Example of load variation, **100 Hz**, HVI 650 at $40^{\circ}C$ vibration test.

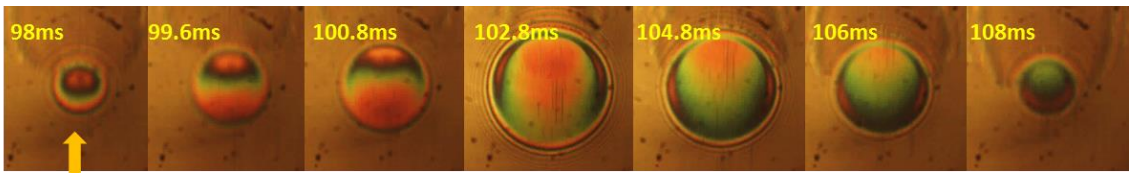

Figure 6.10 (b): Interferograms of the HVI 650 at $40^{\circ}C$, captured at 100 Hz, **0.05 m/s.**

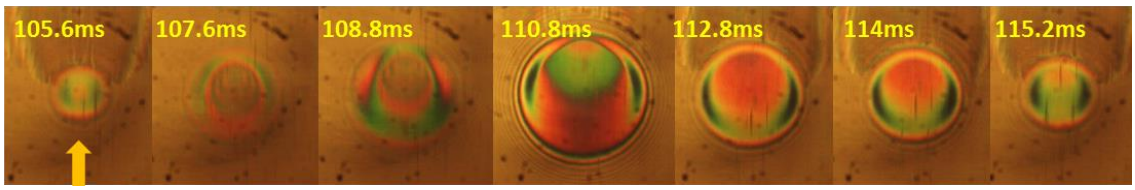

Figure 6.10 (c): Interferograms of the HVI 650 at $40^{\circ}C$, captured at 100 Hz, **0.1 m/s.**

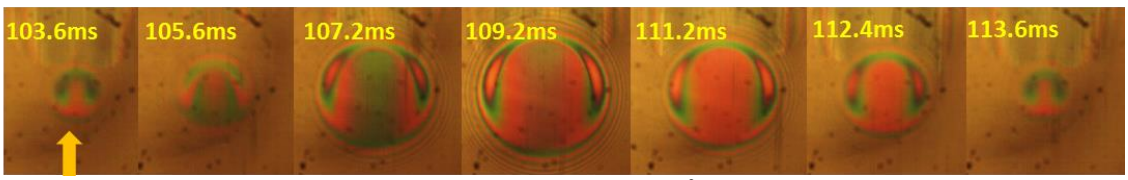

Figure 6.10 (d): Interferograms of the HVI 650 at $40^{\circ}C$, captured at 100 Hz, **0.2 m/s.**

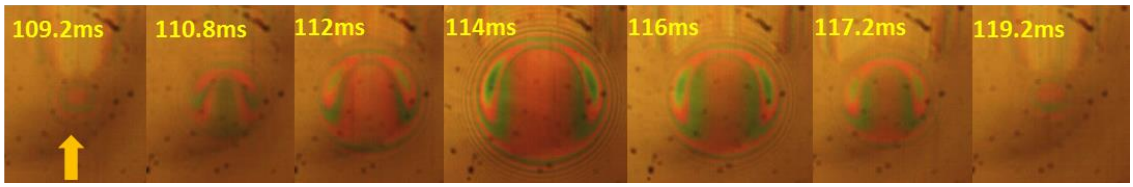

Figure 6.10 (e): Interferograms of the HVI 650 at $40^{\circ}C$, captured at 100 Hz, **0.3 m/s.**

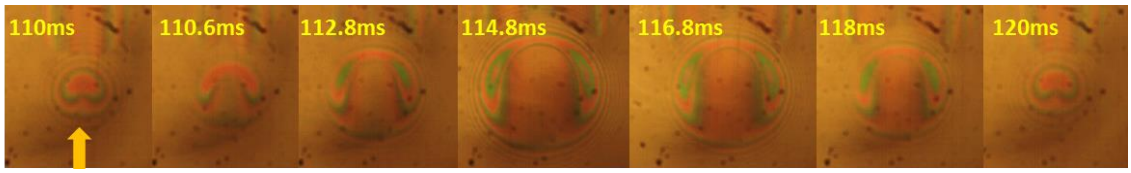

Figure 6.10 (f): Interferograms of the HVI 650 at $40^{\circ}C$, captured at 100 Hz, **0.5 m/s.**

The working parameters for the experiments carried out in this section were kept almost exactly same as the ones for the tests in section 6.1.1, however the lubricant viscosity was reduced. Deviation from the classic flat film region under steady state condition can be observed at higher frequency but not at higher entrainment speed.

6.1.3 PAO 40 at 40℃

Tests were carried out at entrainment speed with values between 0.05 m/s to 0.3 m/s. For the pair of material used in the experiments, the maximum and minimum applied load were between about 5 N to 64 N, which led to the corresponding Hertzian pressure variation between 0.32 GPa and around 0.75 GPa.

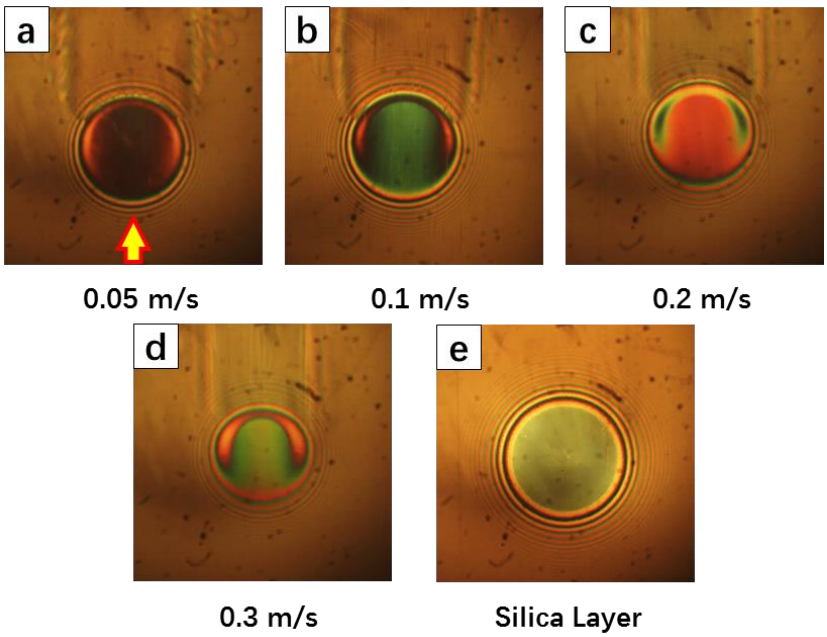

Figure 6.11: EHD contact lubricated with PAO 40 at different entrainment speed (a-d), 40℃ and dry, static contact (e).

The steady state film thickness of the EHD contact lubricated with PAO 40 40℃ at tested entrainment speed was evaluated from images recorded as shown in figure 6.11 (a-d). A constant load of 30 N was applied to the EHD contact under these steady states rolling conditions. To note that PAO 40 at 40℃ is less viscous than HVI 650 oil at 40℃.

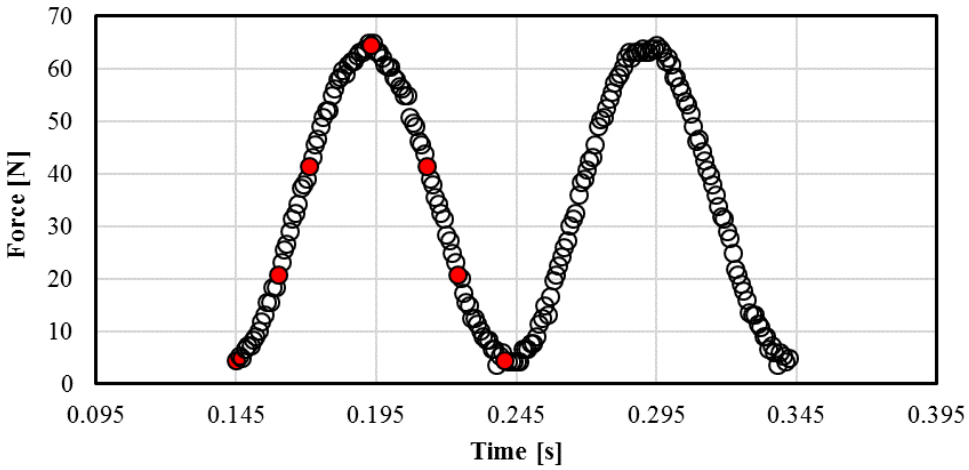

Figure 6.12 (a): Example of load variation, **10 Hz**, PAO 40 at $40^{\circ}C$ vibration test.

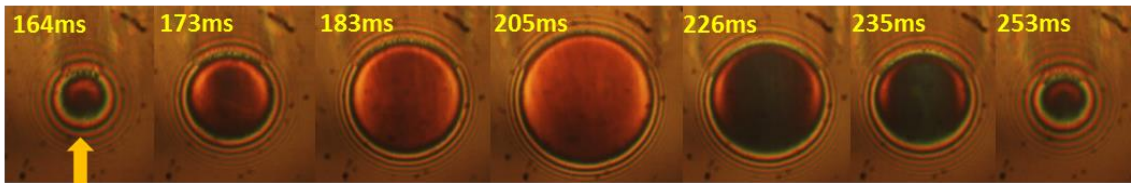

Figure 6.12 (b): Interferograms of the PAO 40 at $40^{\circ}C$, captured at 10 Hz, **0.05 m/s**.

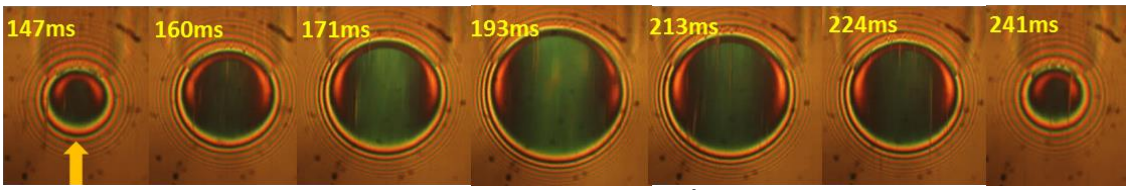

Figure 6.12 (c): Interferograms of the PAO 40 at $40^{\circ}C$, captured at 10 Hz, **0.1 m/s**.

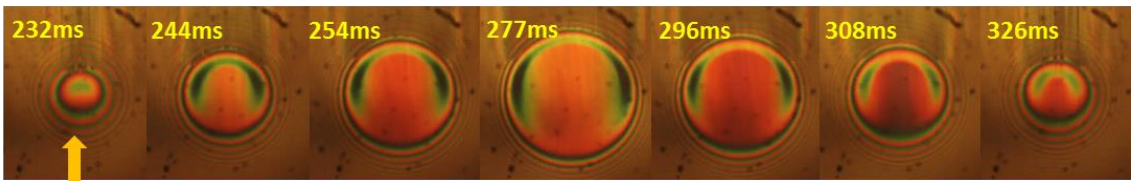

Figure 6.12 (d): Interferograms of the PAO 40 at $40^{\circ}C$, captured at 10 Hz, **0.2 m/s**.

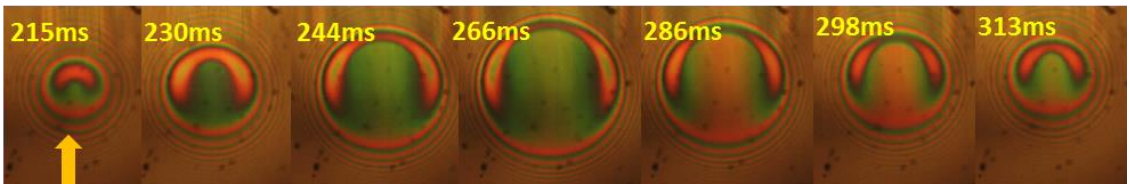

Figure 6.12 (e): Interferograms of the PAO 40 at $40^{\circ}C$, captured at 10 Hz, **0.3 m/s**.

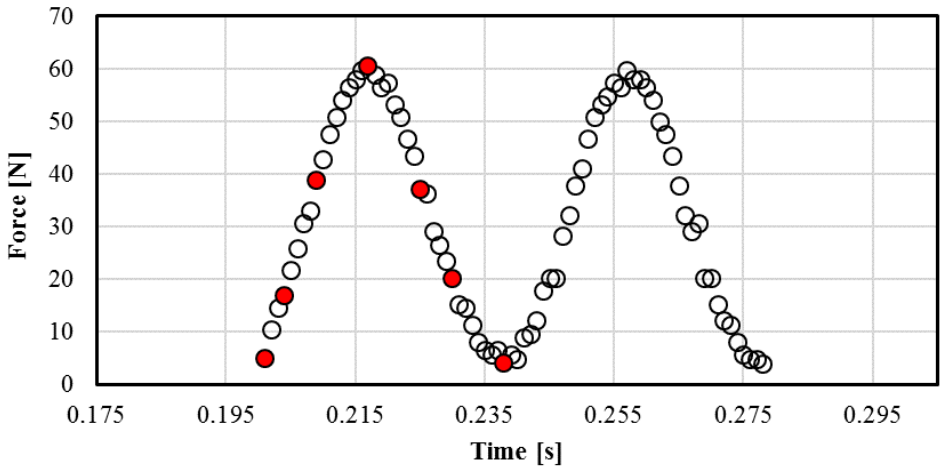

Figure 6.13 (a): Example of load variation, **25 Hz**, PAO 40 at $40^{\circ}C$ vibration test.

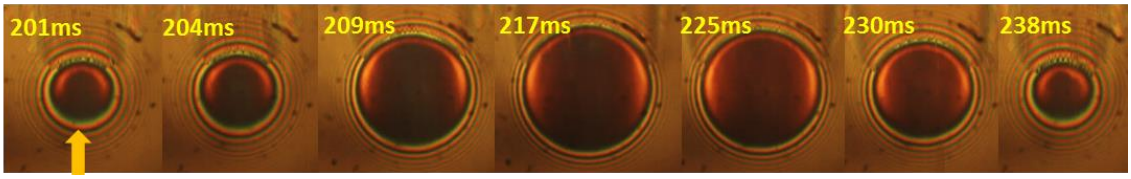

Figure 6.13 (b): Interferograms of the PAO 40 at $40^{\circ}C$, captured at 25 Hz, **0.05 m/s**.

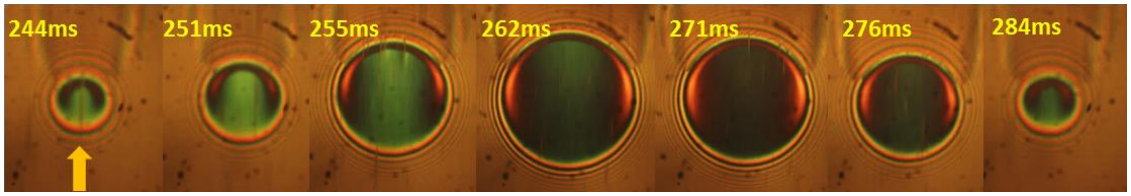

Figure 6.13 (c): Interferograms of the PAO 40 at $40^{\circ}C$, captured at 25 Hz, **0.1 m/s**.

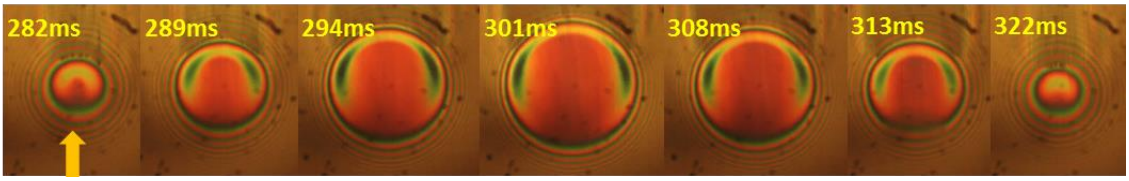

Figure 6.13 (d): Interferograms of the PAO 40 at $40^{\circ}C$, captured at 25 Hz, **0.2 m/s**.

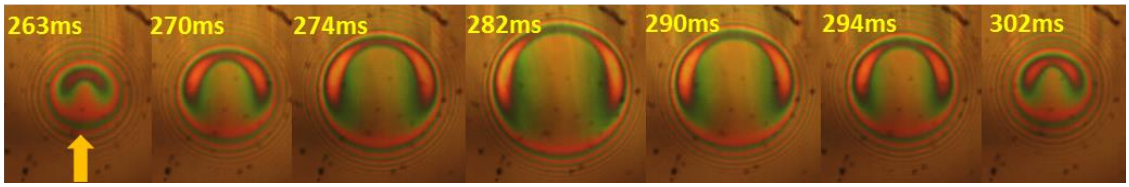

Figure 6.13(e): Interferograms of the PAO 40 at $40^{\circ}C$, captured at 25 Hz, **0.3 m/s**.

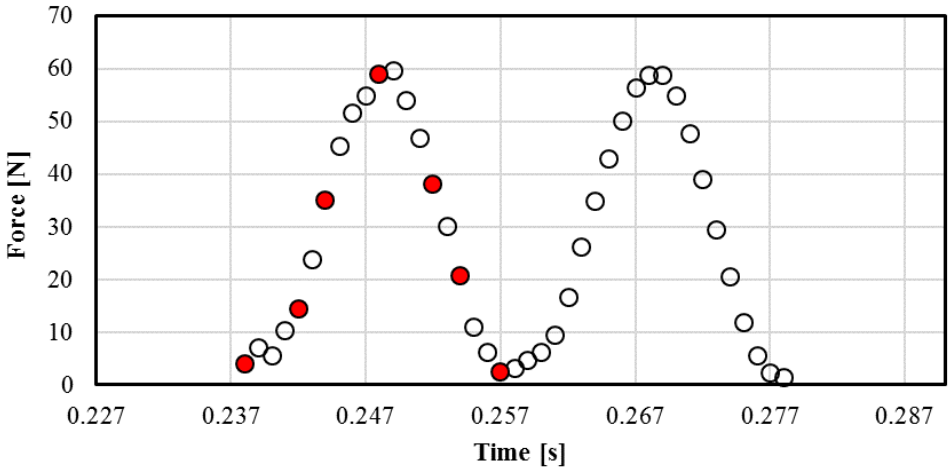

Figure 6.14 (a): Example of load variation, **50 Hz**, PAO 40 at $40^{\circ}C$ vibration test.

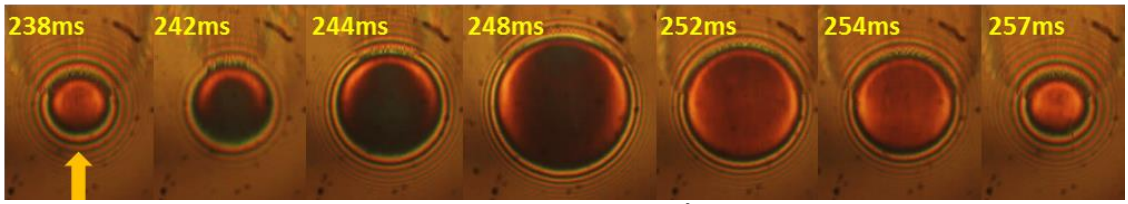

Figure 6.14 (b): Interferograms of the PAO 40 at $40^{\circ}C$, captured at 50 Hz, **0.05 m/s**.

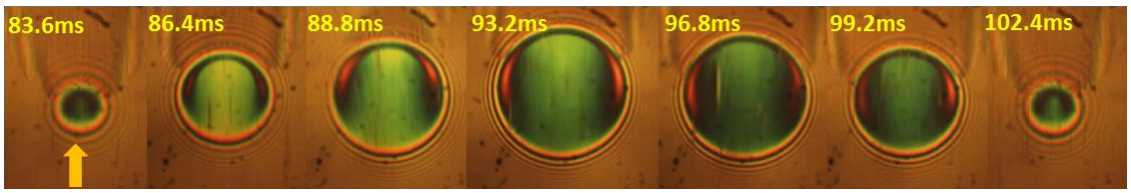

Figure 6.14 (c): Interferograms of the PAO 40 at $40^{\circ}C$, captured at 50 Hz, **0.1 m/s**.

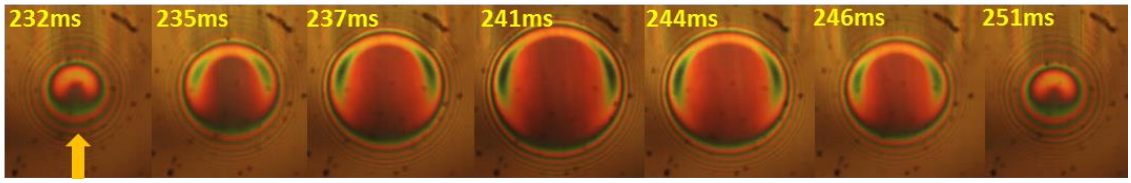

Figure 6.14 (d): Interferograms of the PAO 40 at $40^{\circ}C$, captured at 50 Hz, **0.2 m/s**.

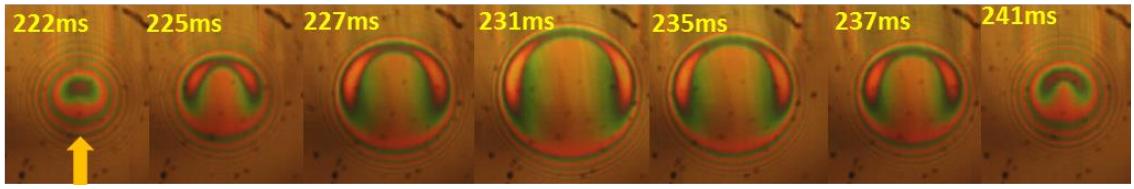

Figure 6.14 (e): Interferograms of the PAO 40 at $40^{\circ}C$, captured at 50 Hz, **0.3 m/s**.

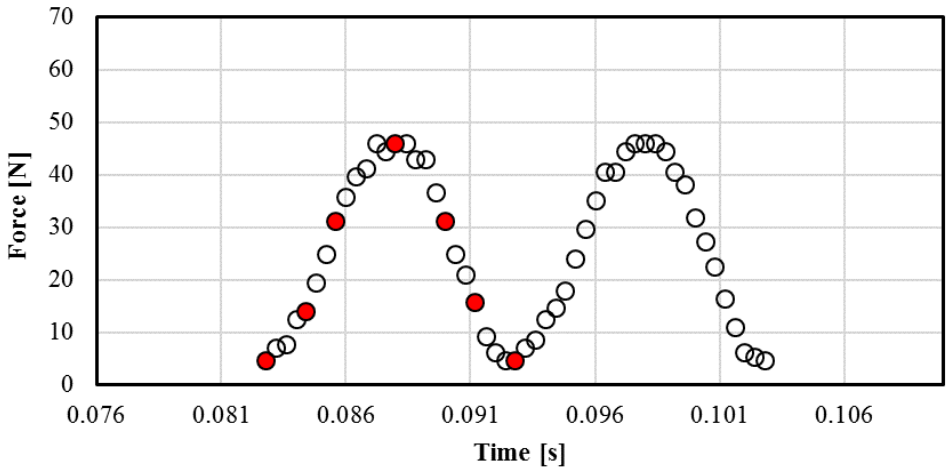

Figure 6.15 (a): Example of load variation, **100 Hz**, PAO 40 at $40^{\circ}C$ vibration test.

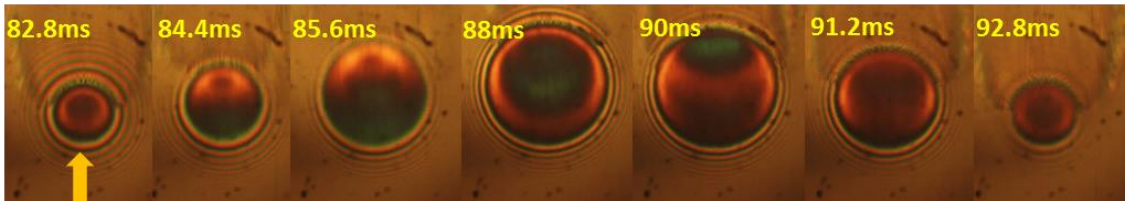

Figure 6.15 (b): Interferograms of the PAO 40 at $40^{\circ}C$, captured at 100 Hz, **0.05 m/s**.

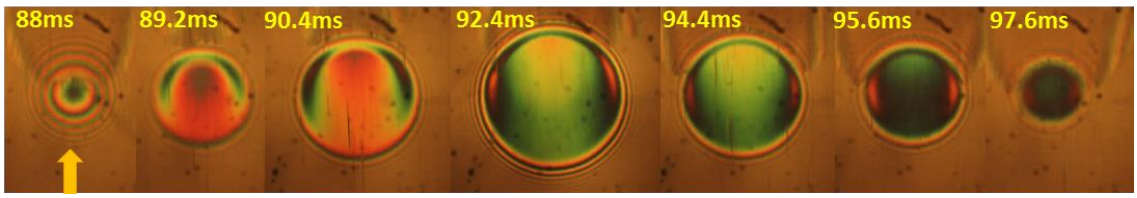

Figure 6.15 (c): Interferograms of the PAO 40 at $40^{\circ}C$, captured at 100 Hz, **0.1 m/s**.

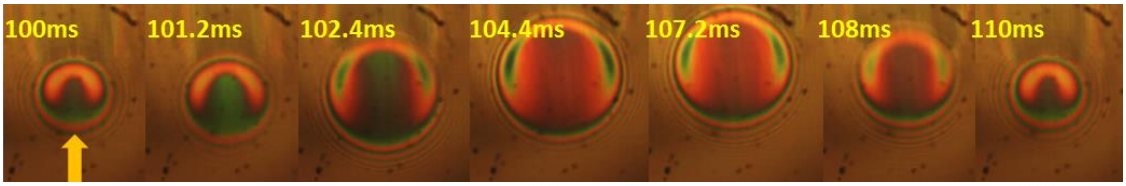

Figure 6.15 (d): Interferograms of the PAO 40 at $40^{\circ}C$, captured at 100 Hz, **0.2 m/s**.

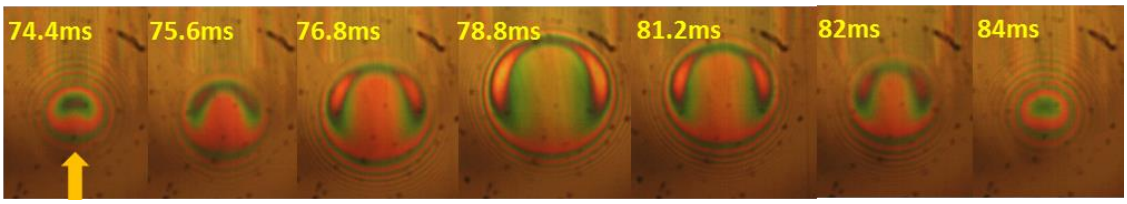

Figure 6.15 (e): Interferograms of the PAO 40 at $40^{\circ}C$, captured at 100 Hz, **0.3 m/s.**

It can be seen from the captured images that the EHD film tested at lower frequencies, i.e. 10 Hz, 25 Hz and 50 Hz, behaves similarly to the film in steady state condition, that is showing insignificant film fluctuation phenomenon during the full vibration cycle (loading-unloading phase) at all entrainment speed range applied. Nevertheless, the deviation from the classic flat film region can be seen at the maximum applied frequency that is 100 Hz, with the contact rolling at relatively lower entrainment speed. This phenomenon can be clearly observed in figures 6.15 (b) and in a lesser extent in figure 6.15(c). As the entrainment speed is increased, figures 6.15(d) and 6.15(e), this film perturbation phenomenon becomes insignificant.

6.1.4 PAO 40 at **60**℃

In this section, the experiments performed at the same frequencies, 10 Hz, 25 Hz, 50 Hz and 100 Hz for PAO 40 at temperature of 60 ± 1℃ are shown. Tests were carried out at entrainment speed with values between 0.05 m/s to 0.3 m/s. The maximum and minimum applied load were between about 3.7 N to 65 N, which led to the corresponding Hertzian pressure variation between 0.29 GPa and around 0.75 GPa.

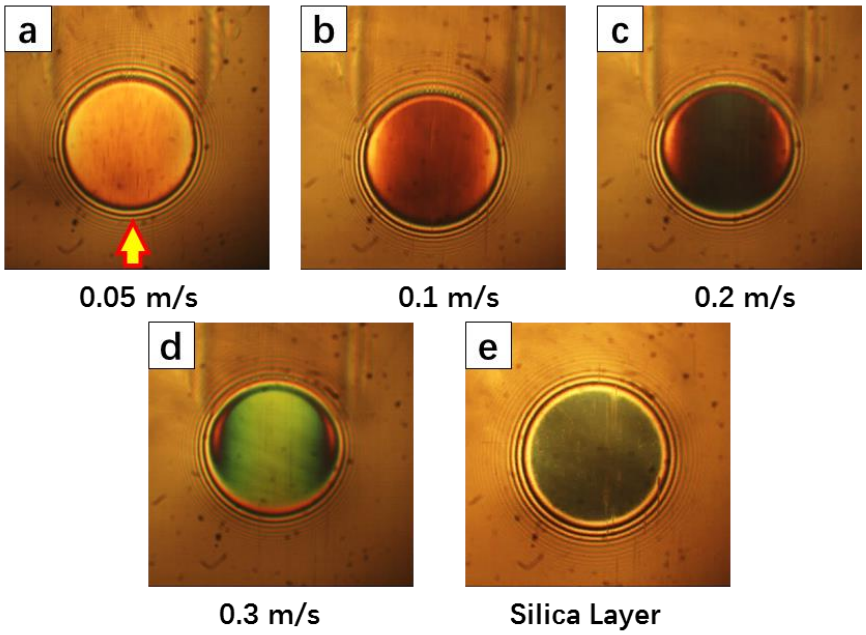

Figure 6.16: EHD contact lubricated with PAO 40 at different entrainment speed (a-d), 60℃, and dry static contact (e).

Steady state interferometric images of the EHD contact lubricated with PAO 40 60℃ at tested entrainment speed are shown in figures 6.16 (a-d), while 6.16 (e) shows the spacer layer contact image. A constant load of 35 N was applied to the EHD contact under these steady states rolling conditions. Representative images of the contact under vibrations are shown in figure 6.17 to 6.20.

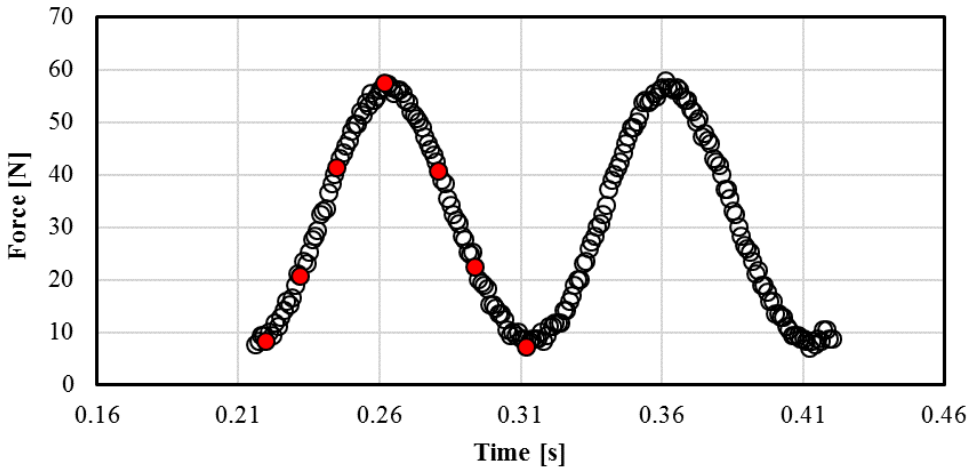

Figure 6.17 (a): Example of load variation, **10 Hz**, PAO 40 at $60^{\circ}C$ vibration test.

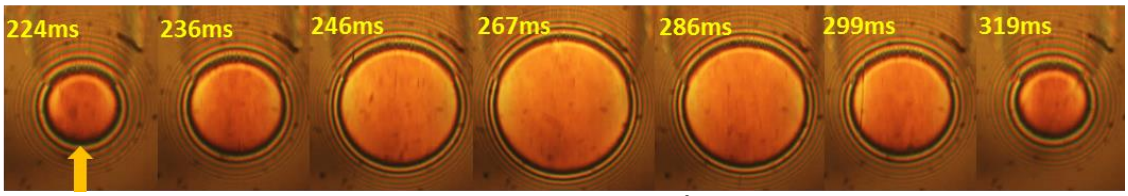

Figure 6.17 (b): Interferograms of the PAO 40 at $60^{\circ}C$, captured at 10 Hz, **0.05 m/s.**

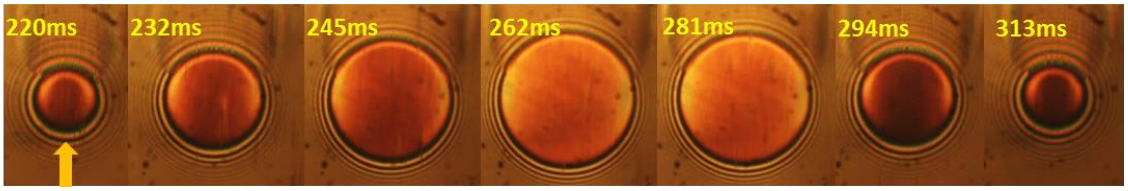

Figure 6.17 (c): Interferograms of the PAO 40 at $60^{\circ}C$, captured at 10 Hz, **0.1 m/s.**

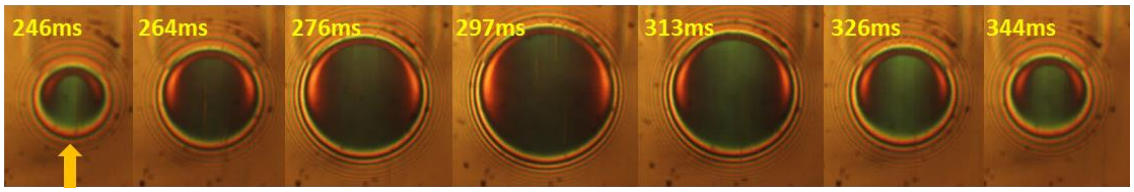

Figure 6.17 (d): Interferograms of the PAO 40 at $60^{\circ}C$, captured at 10 Hz, **0.2 m/s.**

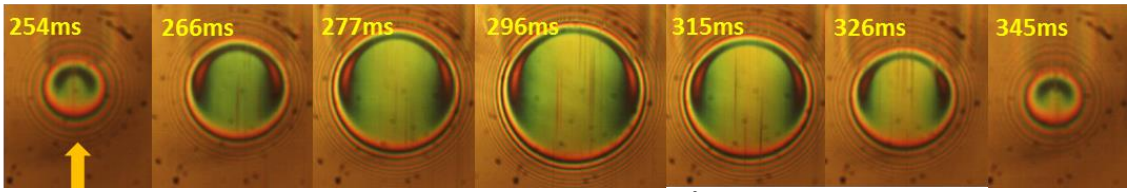

Figure 6.17 (e): Interferograms of the PAO 40 at $60^{\circ}C$, captured at 10 Hz, **0.3 m/s**.

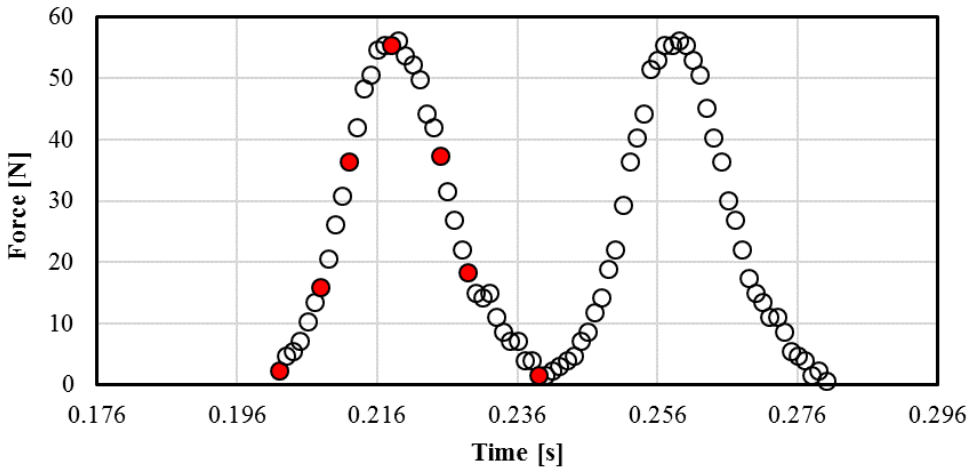

Figure 6.18 (a): Example of load variation, **25 Hz**, PAO 40 at $60^{\circ}C$ vibration test.

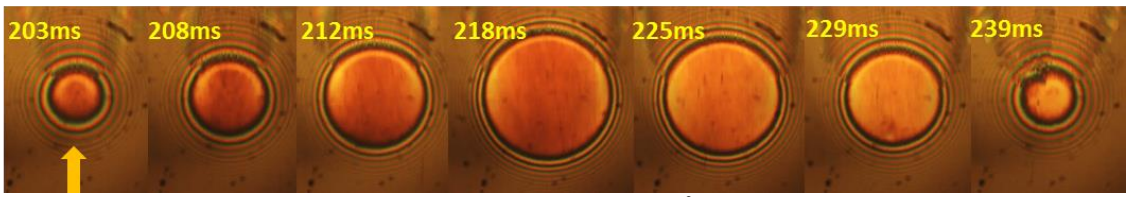

Figure 6.18 (b): Interferograms of the PAO 40 at $60^{\circ}C$, captured at 25 Hz, **0.05 m/s**.

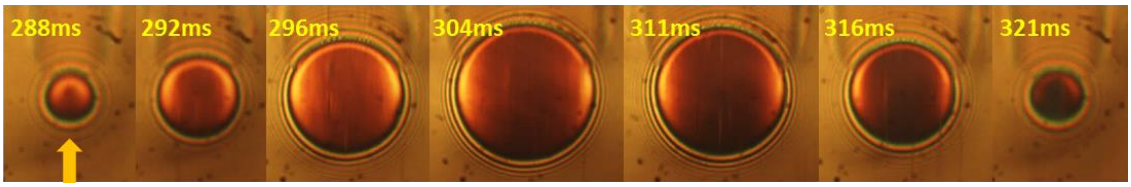

Figure 6.18 (c): Interferograms of the PAO 40 at $60^{\circ}C$, captured at 25 Hz, **0.1 m/s**.

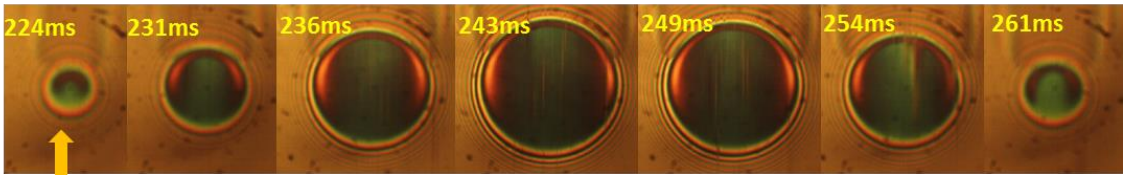

Figure 6.18 (d): Interferograms of the PAO 40 at $60^{\circ}C$, captured at 25 Hz, **0.2 m/s**.

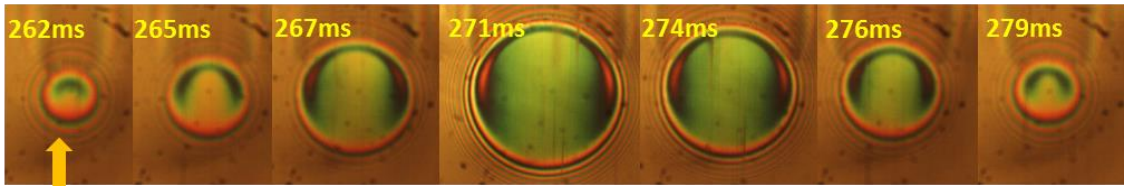

Figure 6.18 (e): Interferograms of the PAO 40 at $60^{\circ}C$, captured at 25 Hz, **0.3 m/s**.

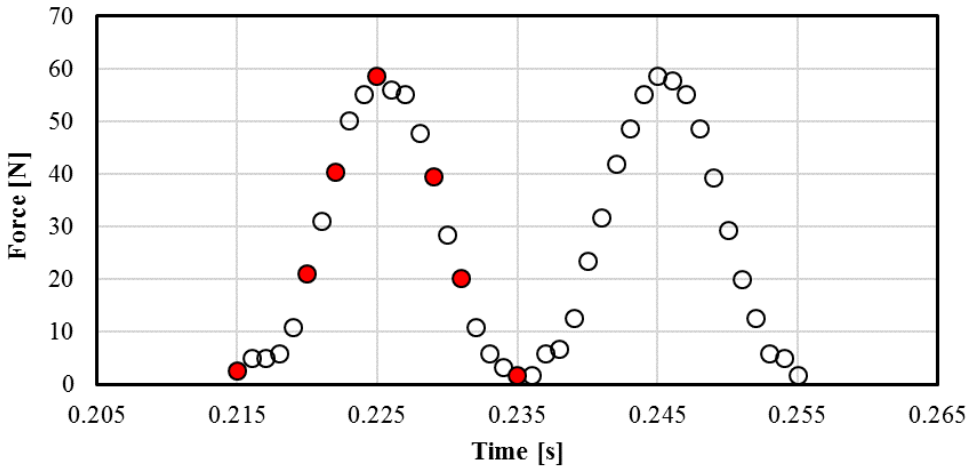

Figure 6.19 (a): Example of load variation, **50 Hz**, PAO 40 at $60^{\circ}C$ vibration test.

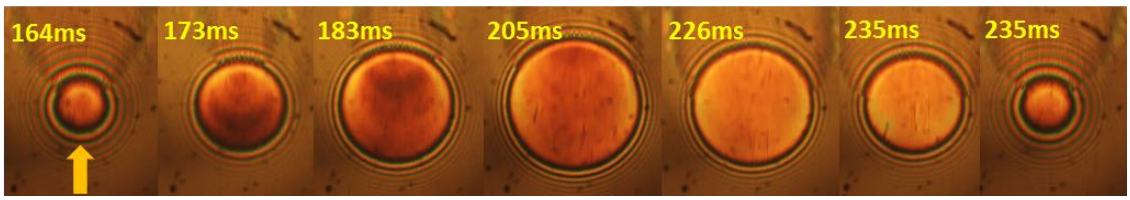

Figure 6.19 (b): Interferograms of the PAO 40 at $60^{\circ}C$, captured at 50 Hz, **0.05 m/s**.

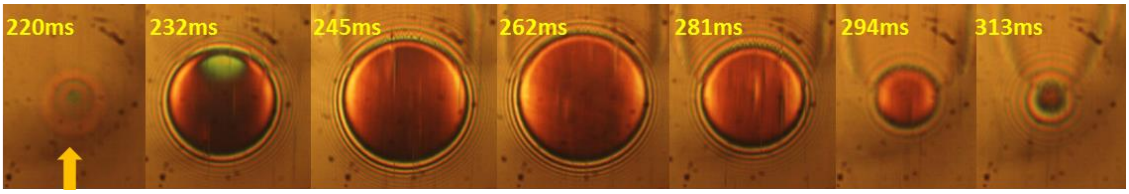

Figure 6.19 (c): Interferograms of the PAO 40 at $60^{\circ}C$, captured at 50 Hz, **0.1 m/s**.

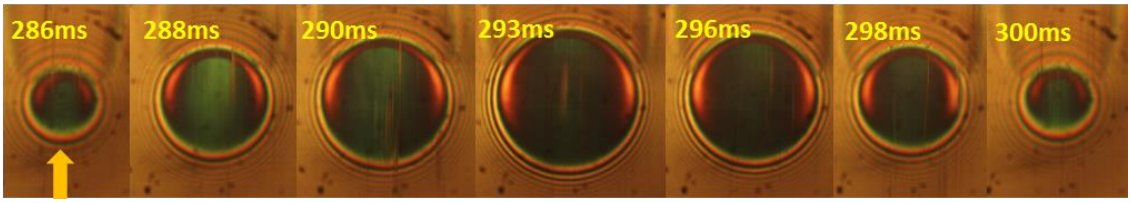

Figure 6.19 (d): Interferograms of the PAO 40 at $60^{\circ}C$, captured at 50 Hz, **0.2 m/s**.

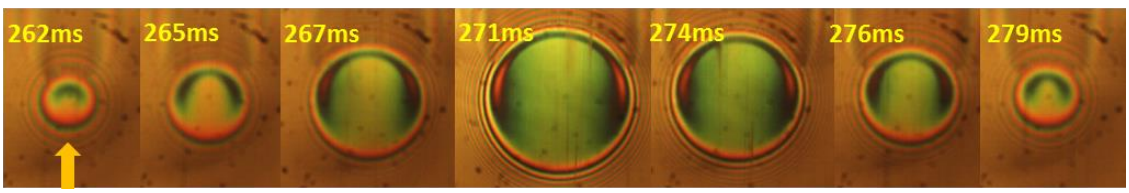

Figure 6.19 (e): Interferograms of the PAO 40 at $60^{\circ}C$, captured at 50 Hz, **0.3 m/s**.

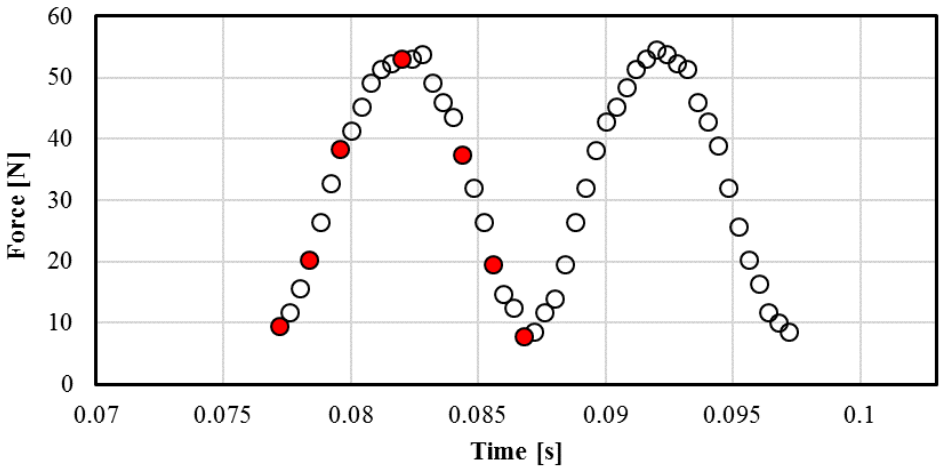

Figure 6.20 (a): Example of load variation, **100 Hz**, PAO 40 at $60^{\circ}C$ vibration test.

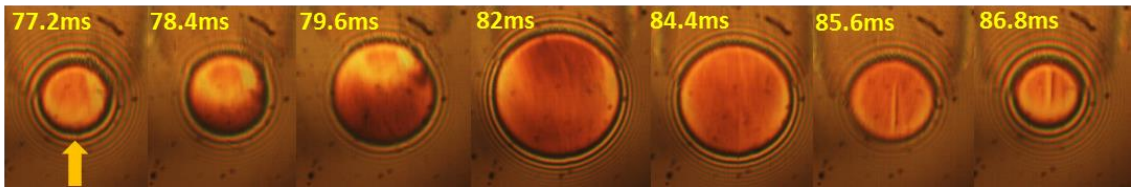

Figure 6.20 (b): Interferograms of the PAO 40 at $60^{\circ}C$, captured at 100 Hz, **0.05 m/s**.

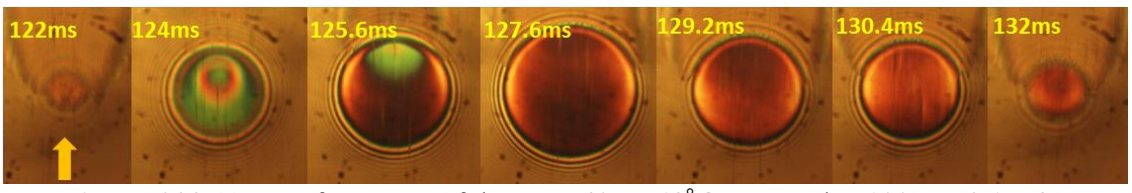

Figure 6.20 (c): Interferograms of the PAO 40 at $60^{\circ}C$, captured at 100 Hz, **0.1 m/s**.

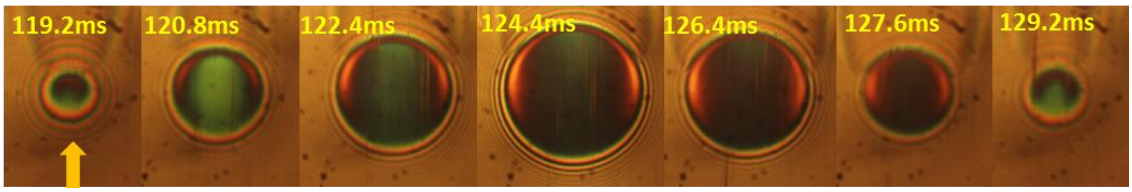

Figure 6.20 (d): Interferograms of the PAO 40 at $60^{\circ}C$, captured at 100 Hz, **0.2 m/s**.

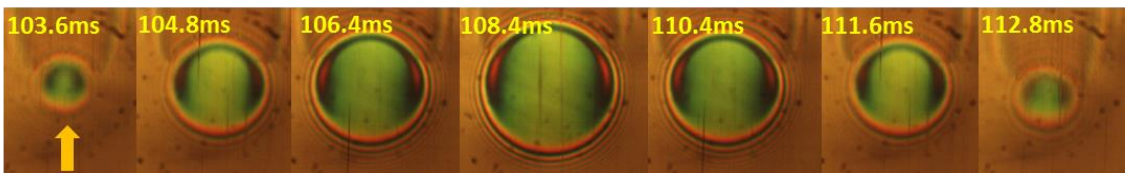

Figure 6.20 (e): Interferograms of the PAO 40 at $60^{\circ}C$, captured at 100 Hz, **0.3 m/s**.

As seen in the images in figures 6.17 and figure 6.18 at lower frequencies of vibration, which implies relatively small variation of load, the film behaviour does not show any special features

comparing with the steady state film behaviour.

At 50 Hz, and especially at 100 Hz similar pronounced deviations from the classic flat film thickness central region can be clearly seen. The deviations are larger during the load increasing phase of the vibration cycle. With increasing the entrainment speed, again this effect seems to become insignificant.

6.1.5 Results of PAO 40 subjected to vertical vibration at 75℃

As in previous tests, these experiments in this section were also carried out at entrainment speed with values between 0.05 m/s to 0.3 m/s. The maximum applied load and the minimum applied load were between about 1.7 N to 57 N, which led to a corresponding Hertzian pressure variation between 0.22 GPa and around 0.72 GPa.

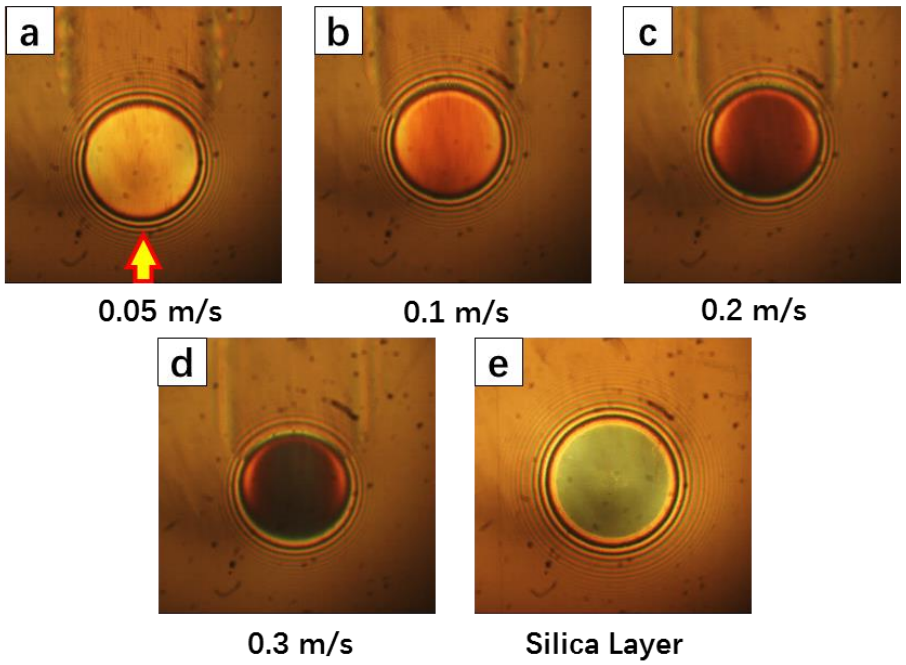

Figure 6.21: EHD contact lubricated with PAO 40 at different entrainment speed (a-d), 75℃ and dry static contact (e).

The evaluation of the steady state film thickness for the EHD contact lubricated with PAO 40 at 75℃ was done from images showed in figure 6.21 (a-d) and compared to UTFI EHD results. In image 6.21 (e), the dry static image of the contact is seen, from which the thickness of the silica layer was extracted. A constant load of 30 N was applied to the EHD contact under these conditions.

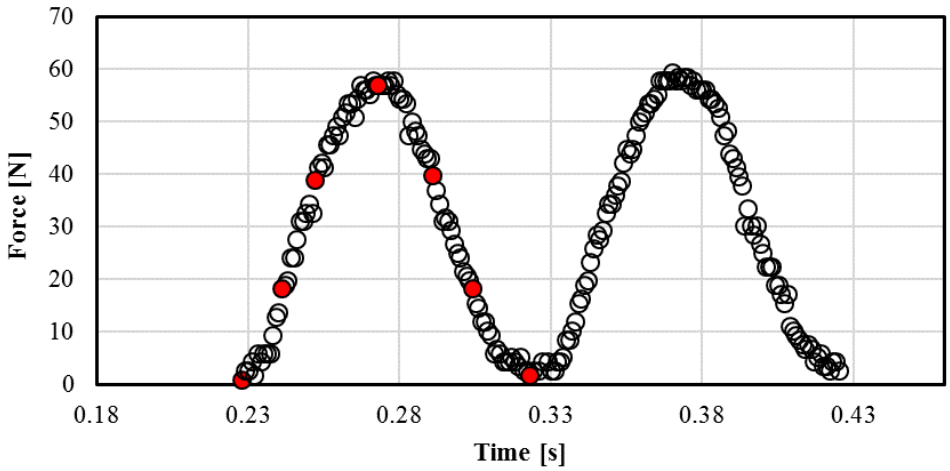

Figure 6.22 (a): Example of load variation, **10 Hz**, PAO 40 at $75^{\circ}C$ vibration test.

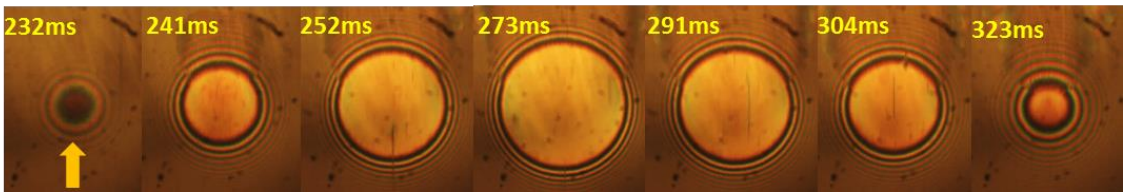

Figure 6.22 (b): Interferograms of the PAO 40 at $75^{\circ}C$, captured at 10 Hz, **0.05 m/s**.

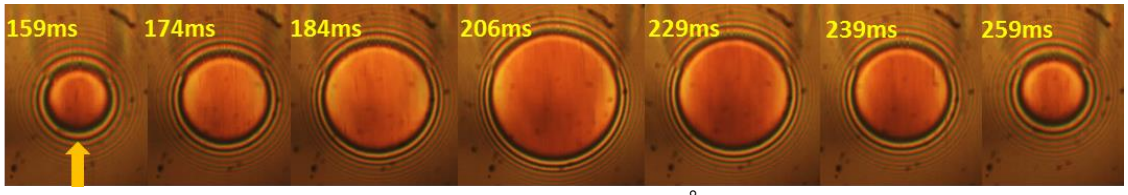

Figure 6.22 (c): Interferograms of the PAO 40 at $75^{\circ}C$, captured at 10 Hz, **0.1 m/s**.

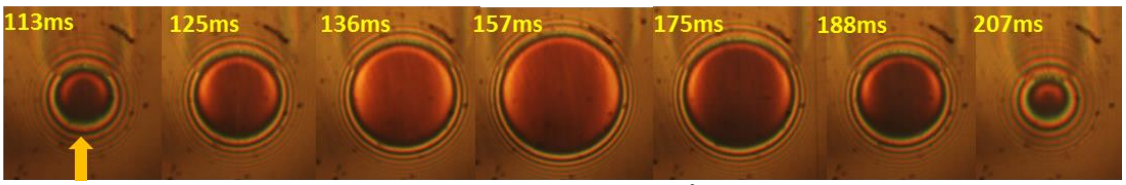

Figure 6.22 (d): Interferograms of the PAO 40 at $75^{\circ}C$, captured at 10 Hz, **0.2 m/s**.

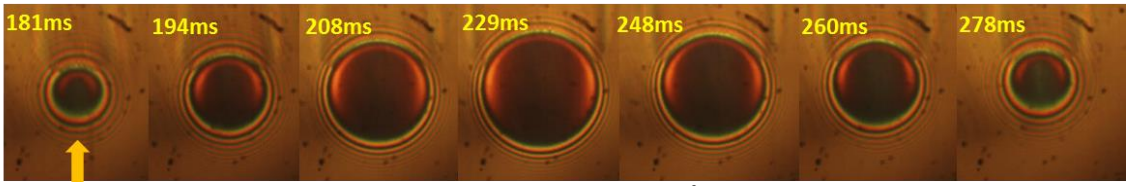

Figure 6.22 (e): Interferograms of the PAO 40 at $75^{\circ}C$, captured at 10 Hz, **0.3 m/s**.

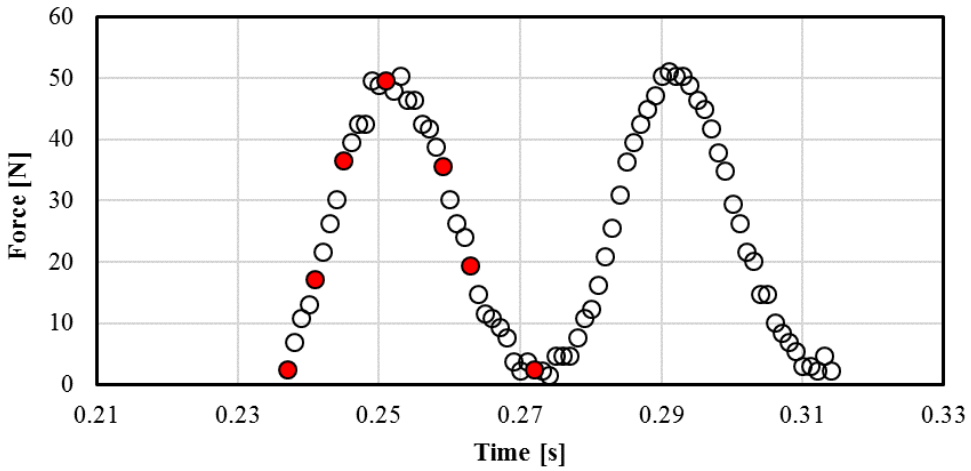

Figure 6.23 (a): Example of load variation, **25 Hz**, PAO 40 at $75^{\circ}C$ vibration test.

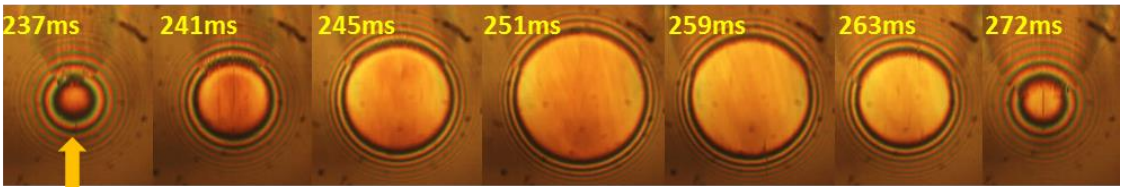

Figure 6.23 (b): Interferograms of the PAO 40 at $75^{\circ}C$, captured at 25 Hz, **0.05 m/s**.

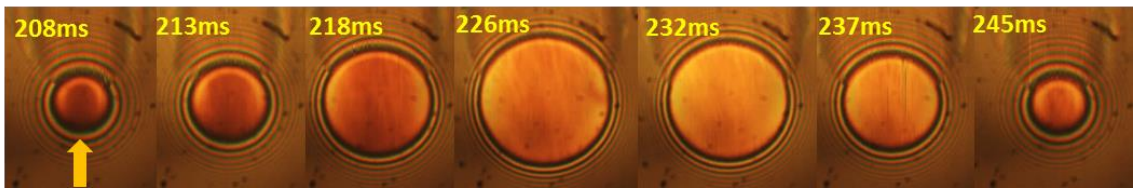

Figure 6.23 (c): Interferograms of the PAO 40 at $75^{\circ}C$, captured at 25 Hz, **0.1 m/s**.

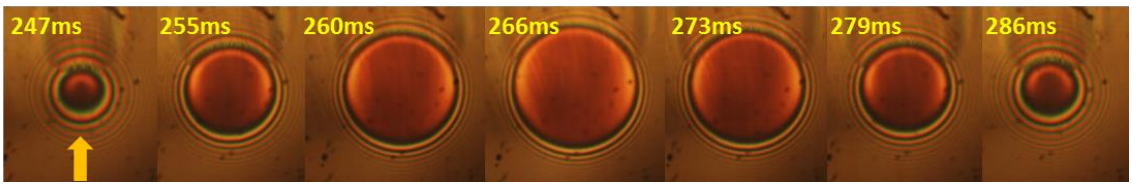

Figure 6.23 (d): Interferograms of the PAO 40 at $75^{\circ}C$, captured at 25 Hz, **0.2 m/s**.

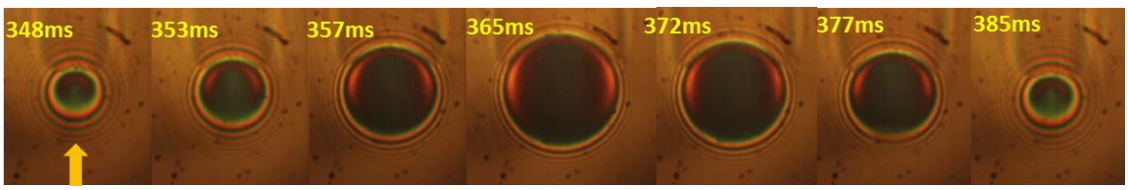

Figure 6.23 (e): Interferograms of the PAO 40 at $75^{\circ}C$, captured at 25 Hz, **0.3 m/s**.

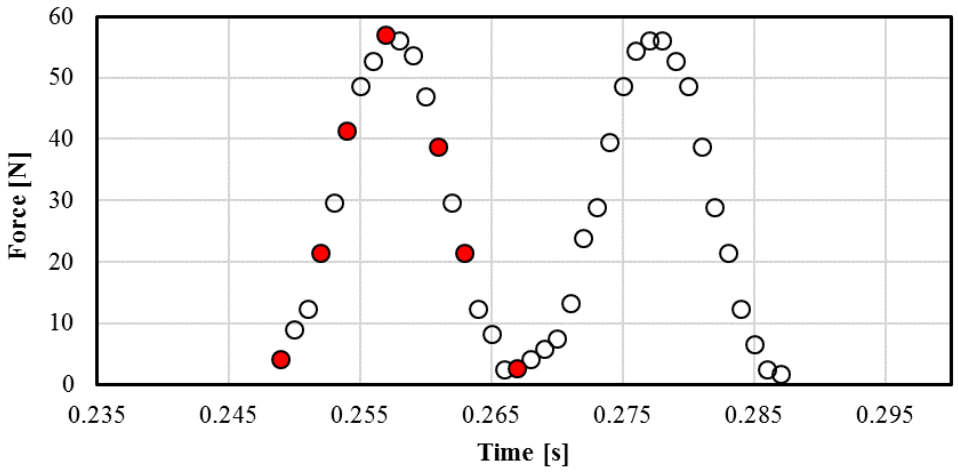

Figure 6.24 (a): Example of load variation, **50 Hz**, PAO 40 at $75^{\circ}C$ vibration test.

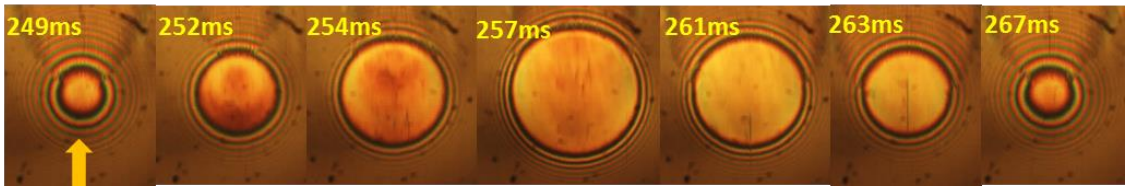

Figure 6.24 (b): Interferograms of the PAO 40 at $75^{\circ}C$, captured at 50 Hz, **0.05 m/s**.

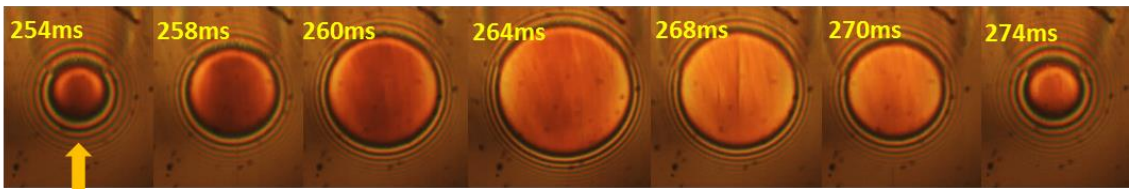

Figure 6.24 (c): Interferograms of the PAO 40 at $75^{\circ}C$, captured at 50 Hz, **0.1 m/s**.

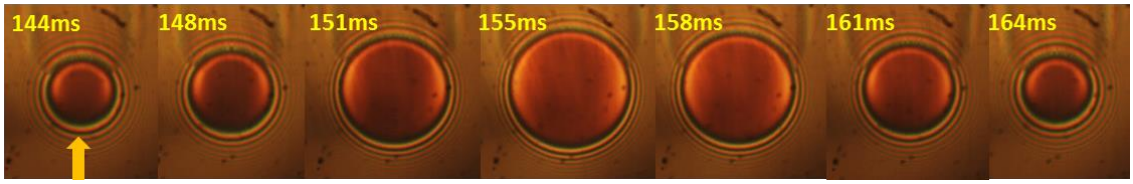

Figure 6.24 (d): Interferograms of the PAO 40 at $75^{\circ}C$, captured at 50 Hz, **0.2 m/s**.

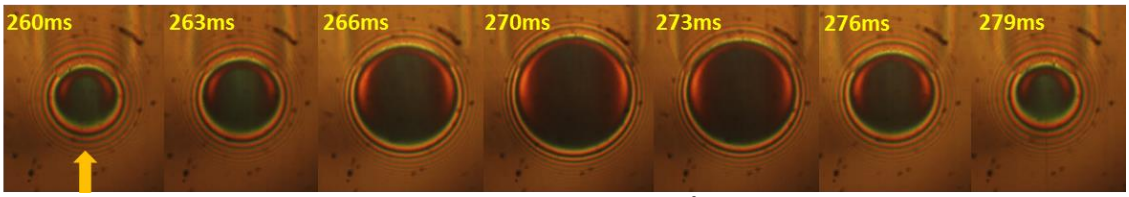

Figure 6.24 (e): Interferograms of the PAO 40 at $75^{\circ}C$, captured at 50 Hz, **0.3 m/s**.

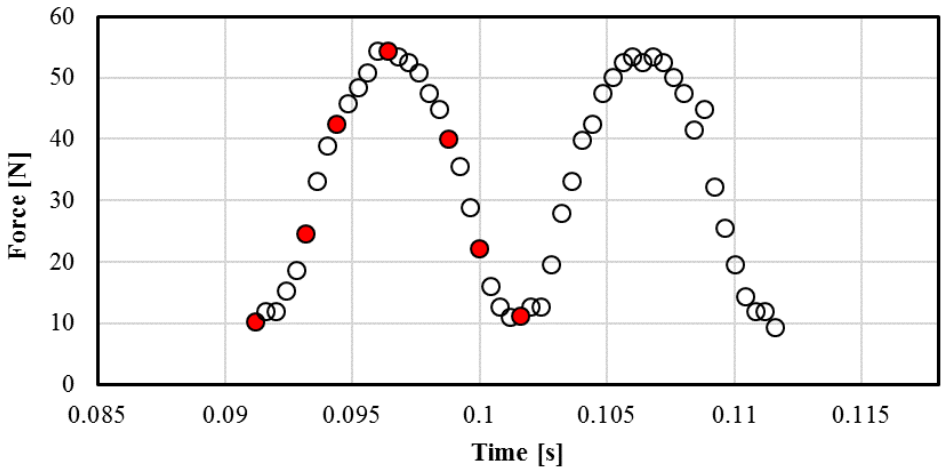

Figure 6.25 (a): Example of load variation, **100 Hz**, PAO 40 at $75^{\circ}C$ vibration test.

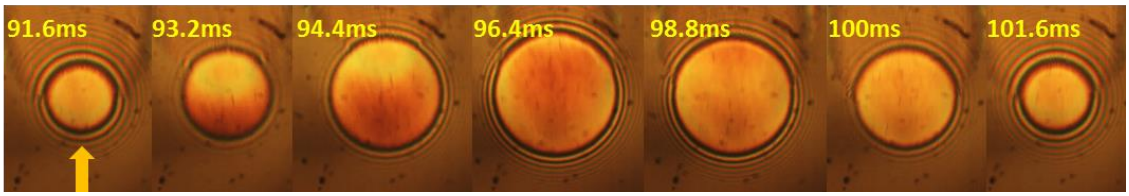

Figure 6.25 (b): Interferograms of the PAO 40 at $75^{\circ}C$, captured at 100 Hz, **0.05 m/s**.

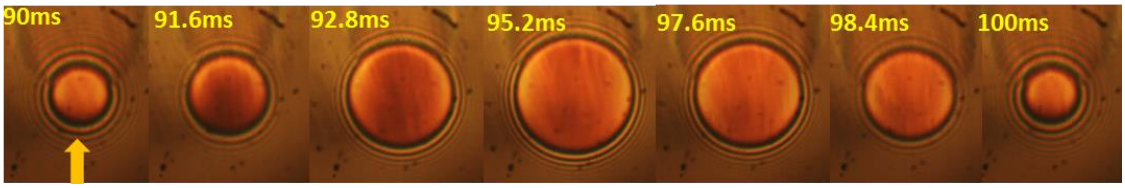

Figure 6.25 (c): Interferograms of the PAO 40 at $75^{\circ}C$, captured at 100 Hz, **0.1 m/s**.

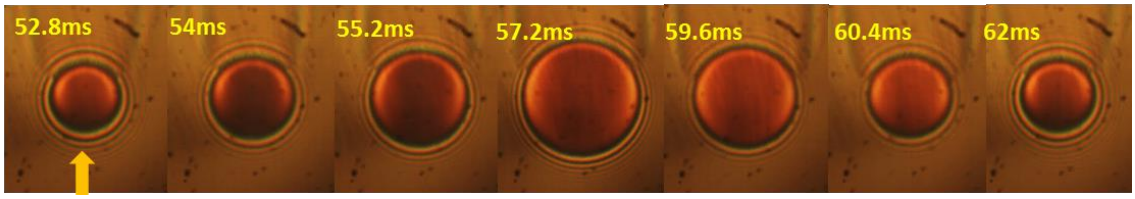

Figure 6.25 (d): Interferograms of the PAO 40 at $75^{\circ}C$, captured at 100 Hz, **0.2 m/s**.

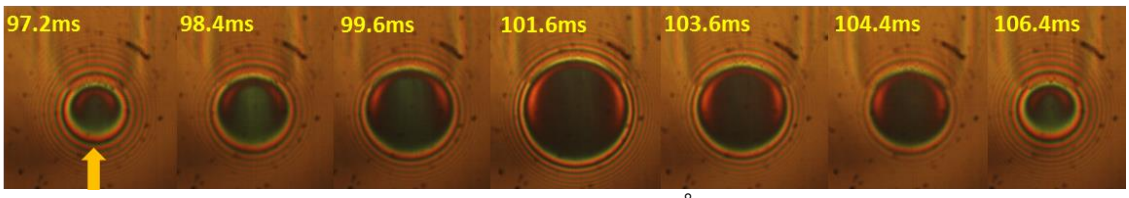

Figure 6.25 (e): Interferograms of the PAO 40 at $75^{\circ}C$, captured at 100 Hz, **0.3 m/s**.

In these experiments, deviations from the classic flat film region are almost invisible. Most of the recorded EHD contact images in vibration cycles are more or less following the film thickness under steady state condition. Even at the highest frequency magnitude of 100 Hz, it can be seen that vibrations do not generate any strong film thickness fluctuations across the whole contact area, however a slightly film thickness perturbation phenomenon can be observed, which shows a crescent shape travelling through the EHD contact.

6.1.6 SBM base oil at **40**℃

These tests were carried out at entrainment speed with values between 0.1 m/s to 0.9 m/s to match those of the grease tests. The maximum and minimum applied load were about 1.7 N to 57 N, which led to the corresponding Hertzian pressure variation between 0.22 GPa and around 0.72 GPa.

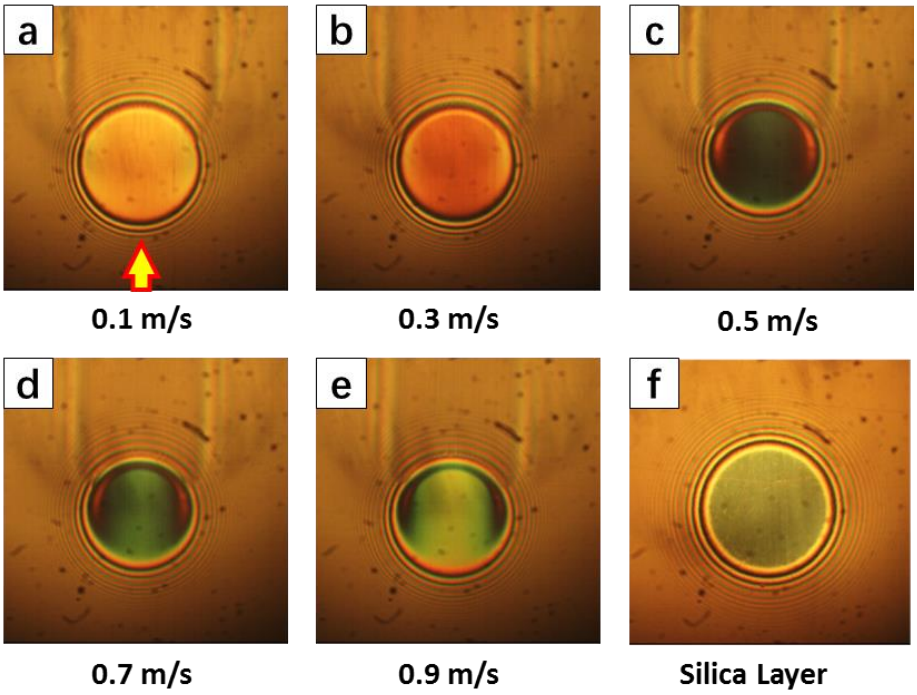

Figure 6.26: EHD contact lubricated with SBM Base oil at different entrainment speed (a-e), 40℃ and dry static contact (f).

Figures 6.26 (a-e) and 6.26 (f) for the spacer layer were used to measure the film thickness in steady state, under pure rolling conditions. Tests carried out with UTFI EHD measurement showed similar values. A constant load of 29 N was applied to the EHD contact under these conditions.

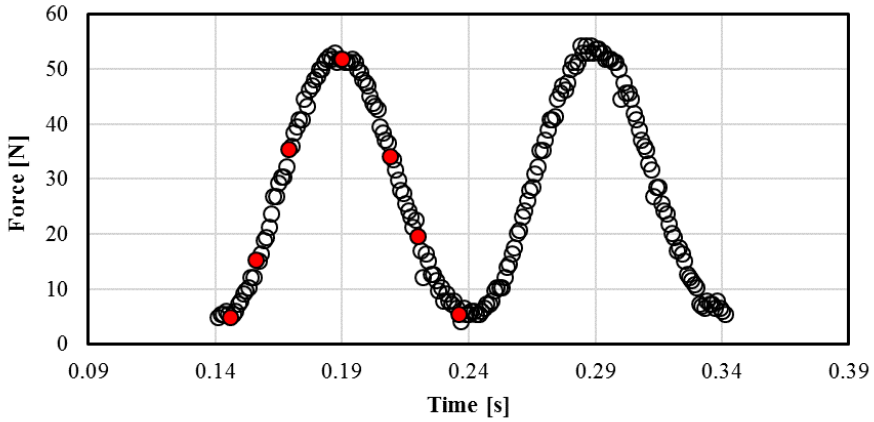

Figure 6.27 (a): Example of load variation, **10 Hz**, SBM Base oil at $40^{\circ}C$ vibration test.

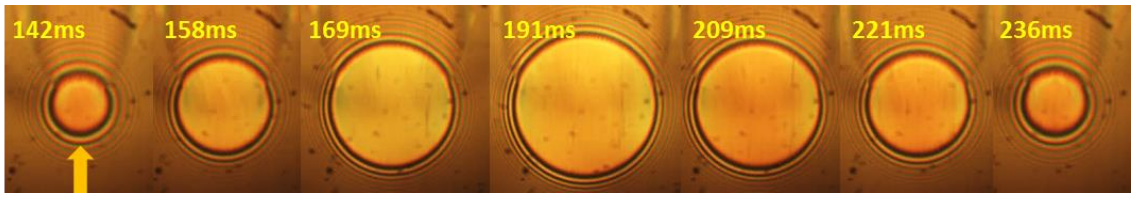

Figure 6.27 (b): Interferograms of SBM Base oil at $40^{\circ}C$, captured at 10 Hz, **0.1 m/s**.

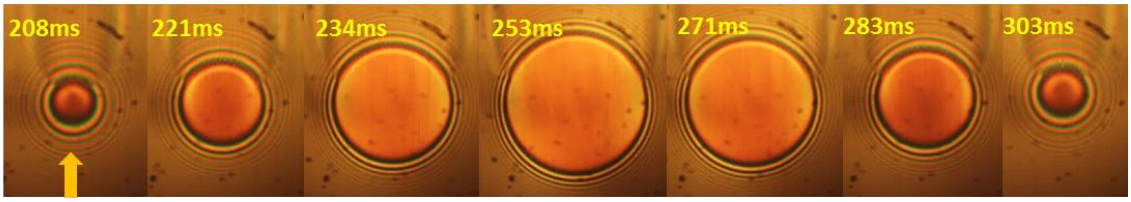

Figure 6.27 (c): Interferograms of SBM Base oil at $40^{\circ}C$, captured at 10 Hz, **0.3 m/s**.

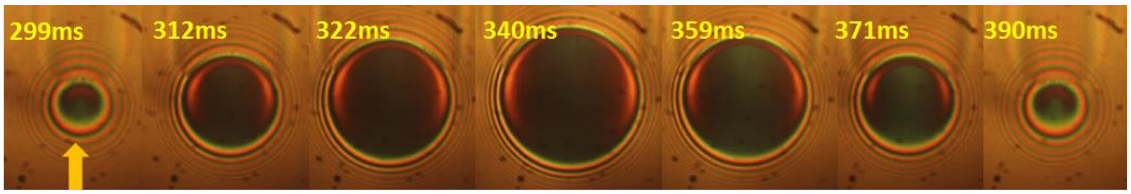

Figure 6.27 (d): Interferograms of SBM Base oil at $40^{\circ}C$, captured at 10 Hz, **0.5 m/s**.

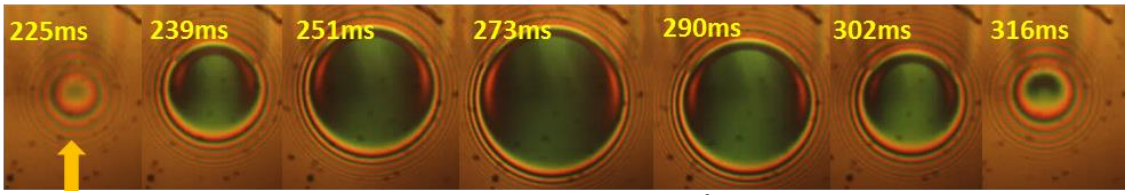

Figure 6.27 (e): Interferograms of SBM Base oil at $40^{\circ}C$, captured at 10 Hz, **0.7 m/s**.

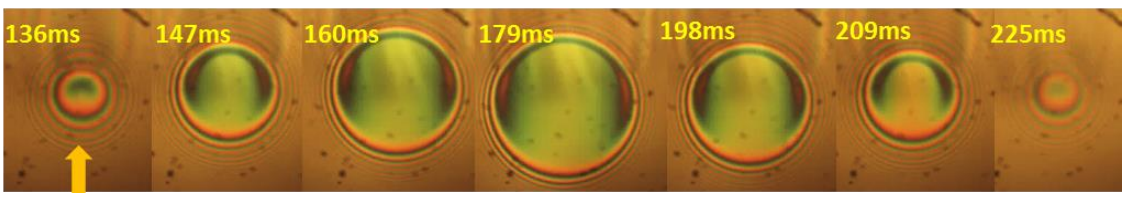

Figure 6.27 (f): Interferograms of SBM Base oil at $40^{\circ}C$, captured at 10 Hz, **0.9 m/s**.

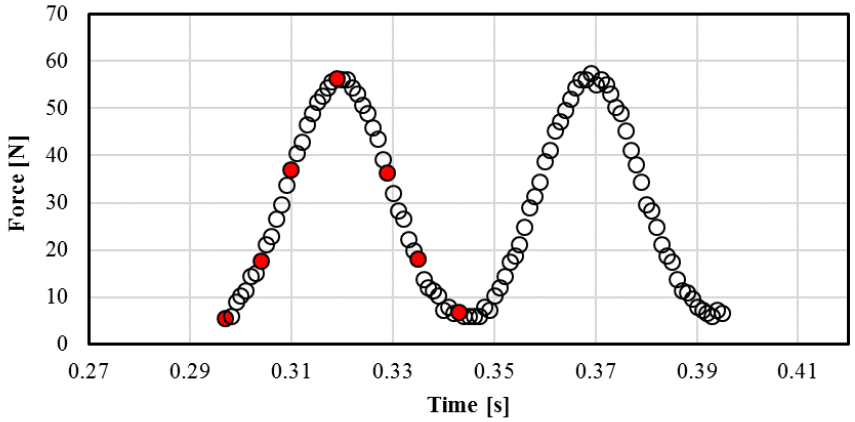

Figure 6.28 (a): Example of load variation, **20 Hz**, SBM Base oil at $40^{\circ}C$ vibration test.

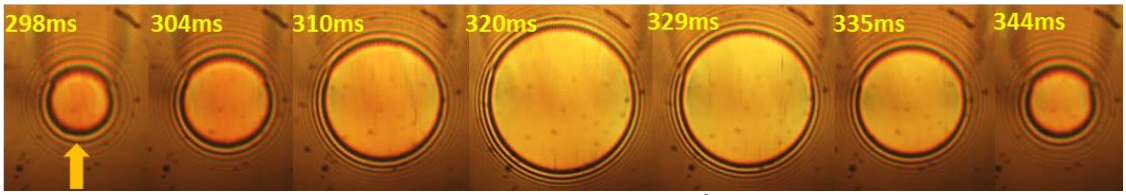

Figure 6.28 (b): Interferograms of SBM Base oil at $40^{\circ}C$, captured at 20 Hz, **0.1 m/s**.

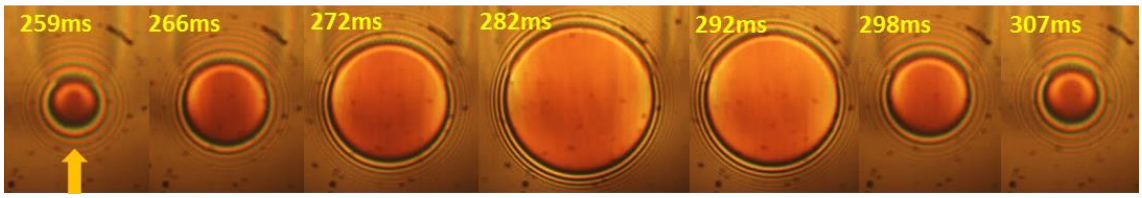

Figure 6.28 (c): Interferograms of SBM Base oil at $40^{\circ}C$, captured at 20 Hz, **0.3 m/s**.

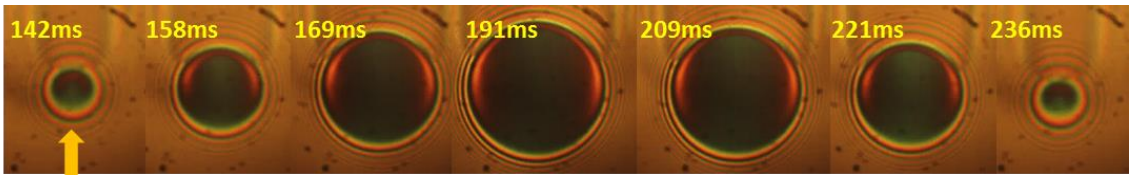

Figure 6.28 (d): Interferograms of SBM Base oil at $40^{\circ}C$, captured at 20 Hz, **0.5 m/s**.

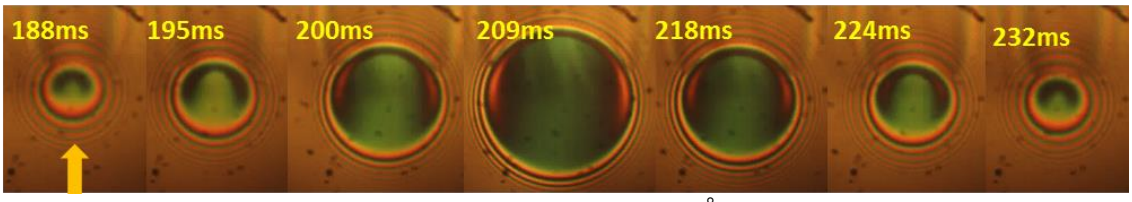

Figure 6.28 (e): Interferograms of SBM Base oil at $40^{\circ}C$, captured at 20 Hz, **0.7 m/s**.

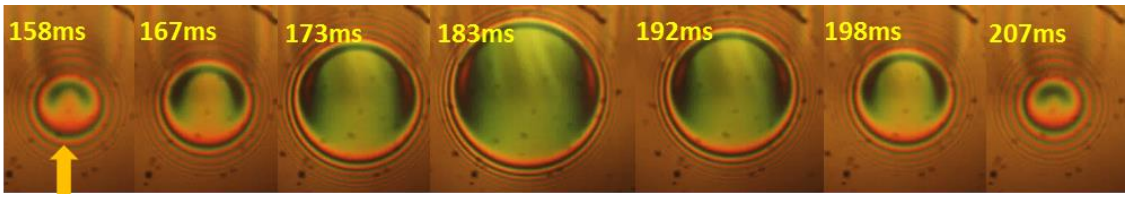

Figure 6.28 (f): Interferograms of SBM Base oil at $40^{\circ}C$, captured at 20 Hz, **0.9 m/s**.

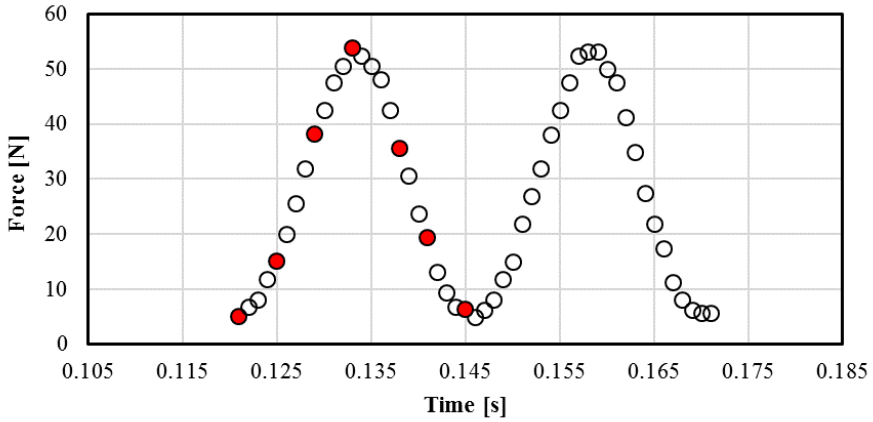

Figure 6.29 (a): Example of load variation, **40 Hz**, SBM Base oil at $40^{\circ}C$ vibration test.

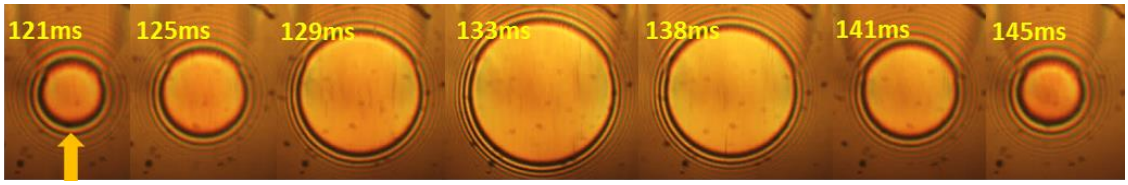

Figure 6.29 (b): Interferograms of SBM Base oil at $40^{\circ}C$, captured at 40 Hz, **0.1 m/s**.

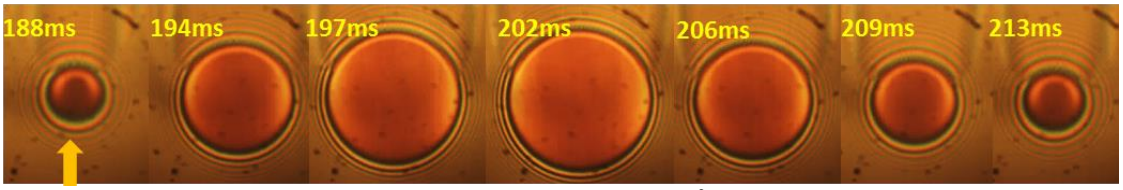

Figure 6.29 (c): Interferograms of SBM Base oil at $40^{\circ}C$, captured at 40 Hz, **0.3 m/s**.

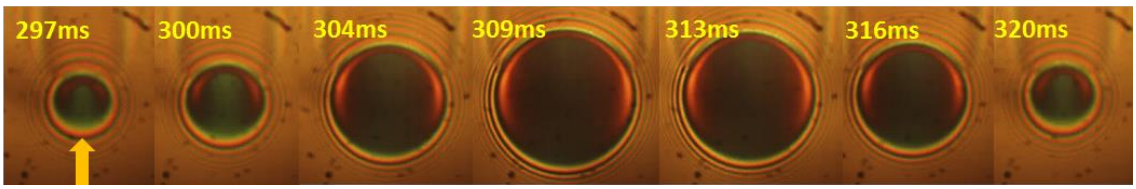

Figure 6.29 (d): Interferograms of SBM Base oil at $40^{\circ}C$, captured at 40 Hz, **0.5 m/s**.

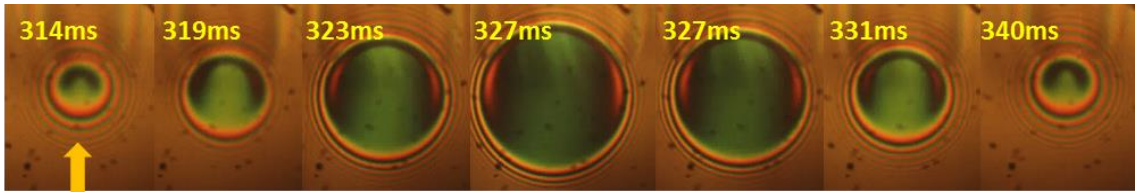

Figure 6.29 (e): Interferograms of SBM Base oil at $40^{\circ}C$, captured at 40 Hz, **0.7 m/s**.

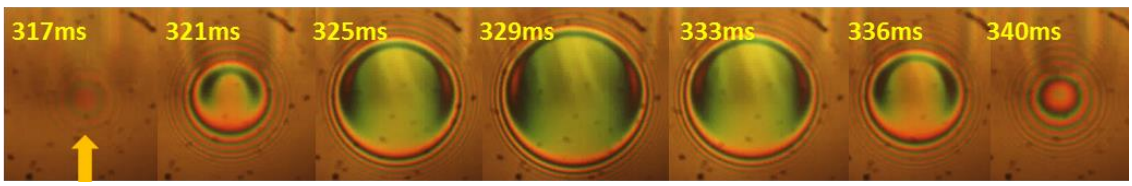

Figure 6.29 (f): Interferograms of SBM Base oil at $40^{\circ}C$, captured at 40 Hz, **0.9 m/s**.

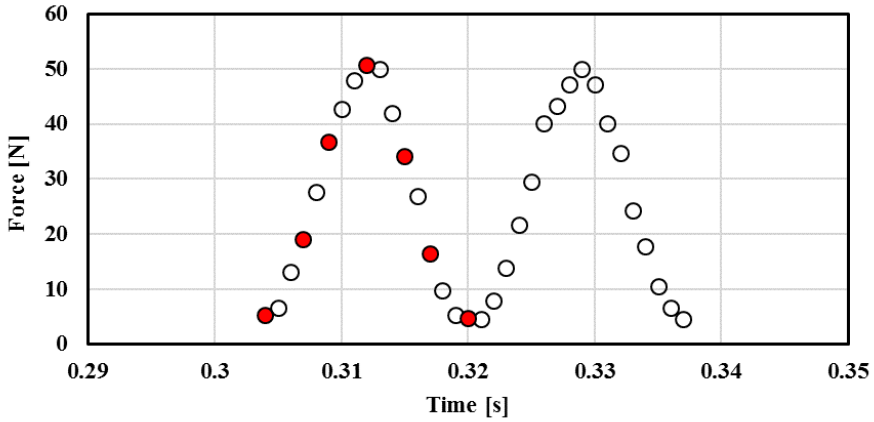

Figure 6.30 (a): Example of load variation, **60 Hz**, SBM Base oil at $40^{\circ}C$ vibration test.

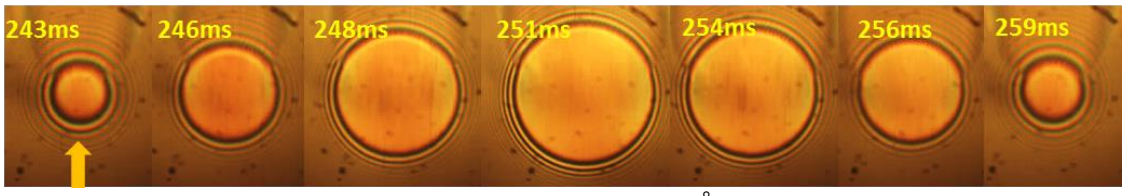

Figure 6.30 (b): Interferograms of SBM Base oil at $40^{\circ}C$, captured at 60 Hz, **0.1 m/s**.

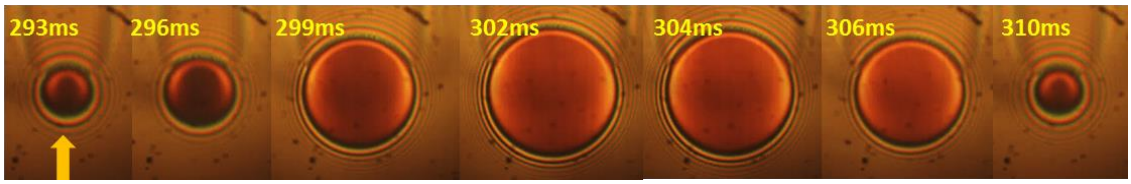

Figure 6.30 (c): Interferograms of SBM Base oil at $40^{\circ}C$, captured at 60 Hz, **0.3 m/s**.

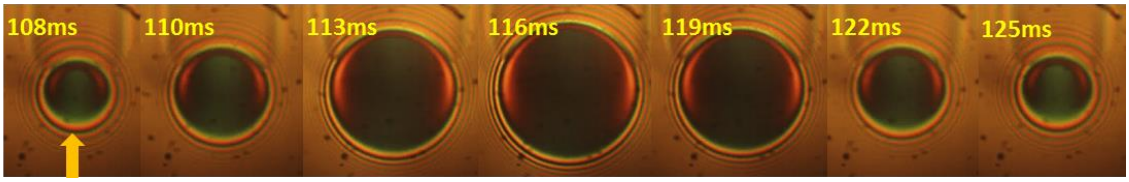

Figure 6.30 (d): Interferograms of SBM Base oil at $40^{\circ}C$, captured at 60 Hz, **0.5 m/s**.

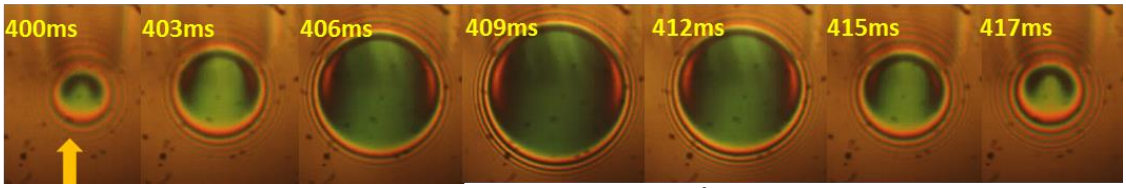

Figure 6.30 (e): Interferograms of SBM Base oil at $40^{\circ}C$, captured at 60 Hz, **0.7 m/s**.

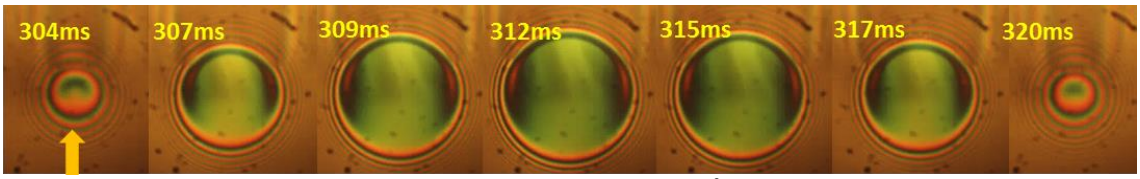

Figure 6.30 (f): Interferograms of SBM Base oil at $40^{\circ}C$, captured at 60 Hz, **0.9 m/s**.

The reasons for choosing SBM base oil are to compare EHD film behaviour under vibration with its corresponding SBM grease EHD film under vibration and to ensure a full lubricant viscosity testing range. Entrainment speed is set up to 0.9 m/s to further study the behaviour of EHD oil film under vibration at even higher entrainment speed. Results presented here will be discussed and compared with grease in the following chapter.

6.1.7 PAO 4 at 40℃

The lest viscous lubricant tested was PAO 4 at a temperature of 40 ± 1℃, with general properties showed in Chapter 4. Tests were carried out at entrainment speed with values between 0.1 m/s and 0.5 m/s. The maximum and minimum applied load were about 1.7 N to 57 N, which led to the corresponding Hertzian pressure variation between 0.22 GPa and around 0.72 GPa.

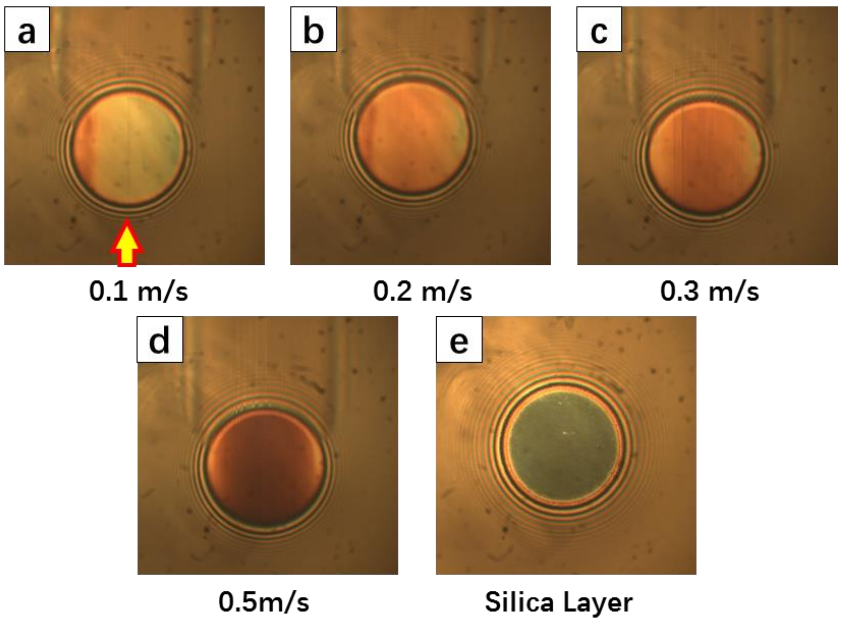

Figure 6.31: Dry static contact image of silica layer (e) and steady state condition of EHD contact lubricated with PAO 4 at different entrainment speeds (a-d), 40℃.

Like for the other lubricants, steady state conditions were evaluated first from images similar to those shown in figures 6.31 (a-d). A constant load of 35 N was applied to the EHD contact in these tests conditions.

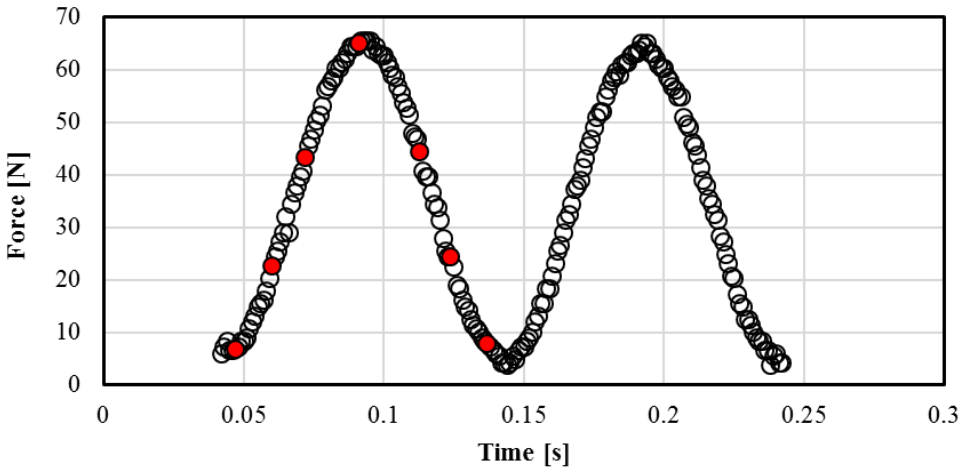

Figure 6.32 (a): Example of load variation, **10 Hz**, PAO 4 at $40^{\circ}C$ vibration test.

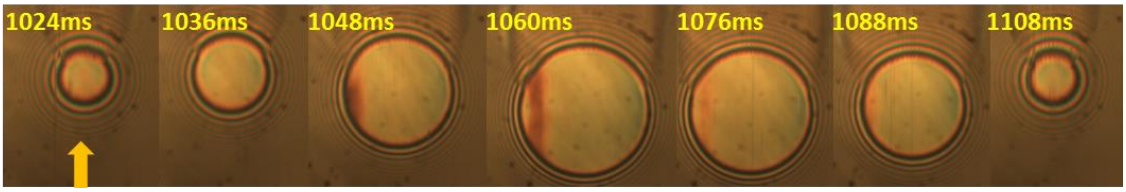

Figure 6.32 (b): Interferograms of the PAO 4 at $40^{\circ}C$, captured at 10 Hz, **0.1 m/s**.

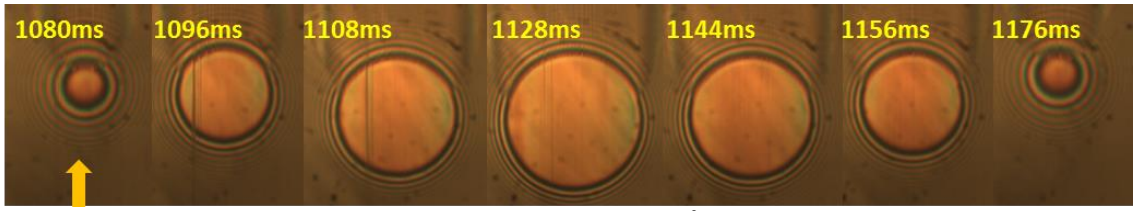

Figure 6.32 (c): Interferograms of the PAO 4 at $40^{\circ}C$, captured at 10 Hz, **0.2 m/s**.

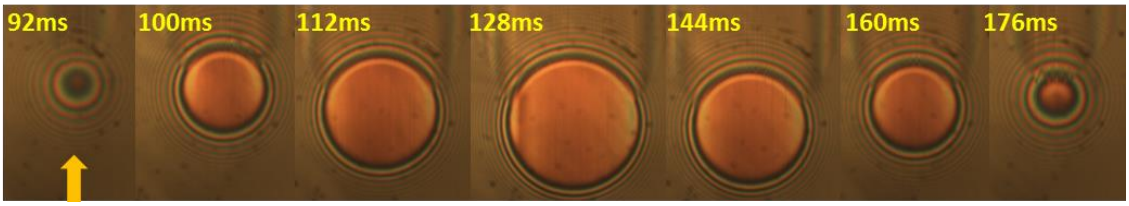

Figure 6.32 (d): Interferograms of the PAO 4 at $40^{\circ}C$, captured at 10 Hz, **0.3 m/s**.

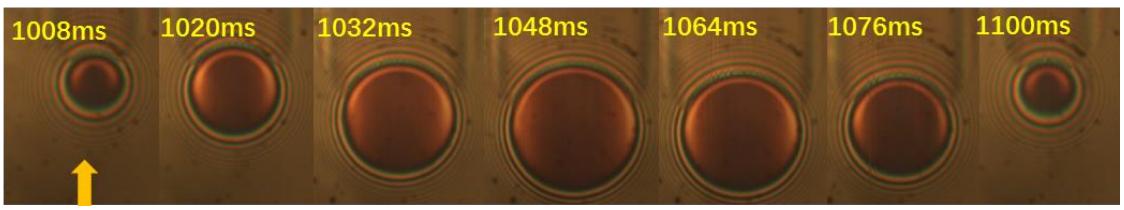

Figure 6.32 (e): Interferograms of the PAO 4 at $40^{\circ}C$, captured at 10 Hz, **0.5 m/s**.

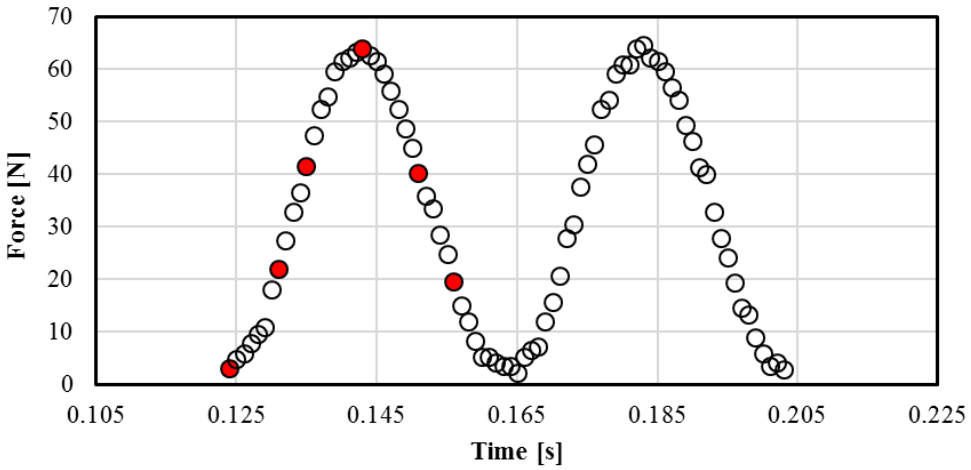

Figure 6.33 (a): Example of load variation, **25 Hz**, PAO 4 at $40^{\circ}C$ vibration test.

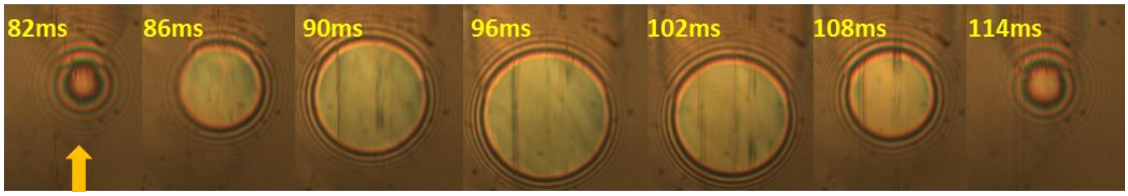

Figure 6.33 (b): Interferograms of the PAO 4 at $40^{\circ}C$, captured at 25 Hz, **0.1 m/s**.

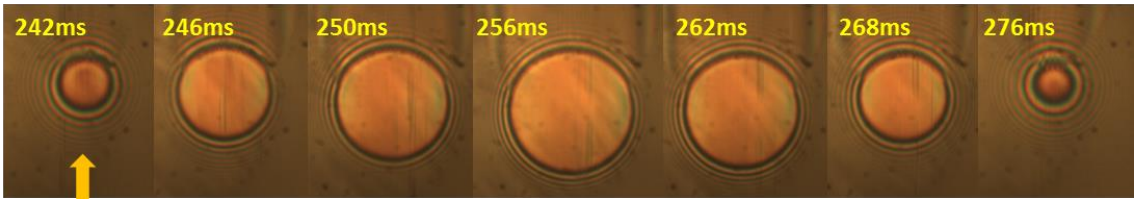

Figure 6.33 (c): Interferograms of the PAO 4 at $40^{\circ}C$, captured at 25 Hz, **0.2 m/s**.

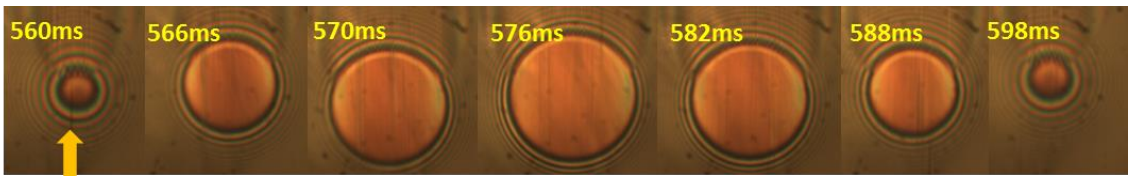

Figure 6.33 (d): Interferograms of the PAO 4 at $40^{\circ}C$, captured at 25 Hz, **0.3 m/s**.

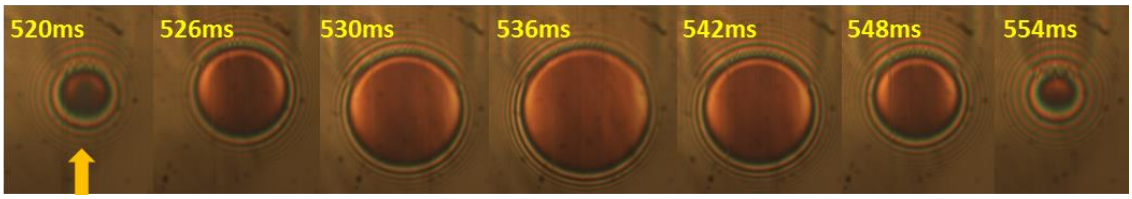

Figure 6.33 (e): Interferograms of the PAO 4 at $40^{\circ}C$, captured at 25 Hz, **0.5 m/s**.

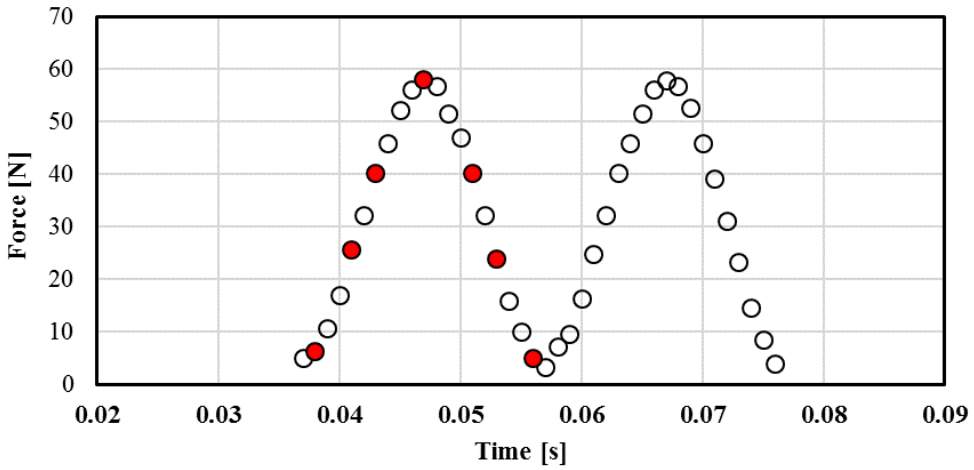

Figure 6.34 (a): Example of load variation, **50 Hz**, PAO 4 at $40^{\circ}C$ vibration test.

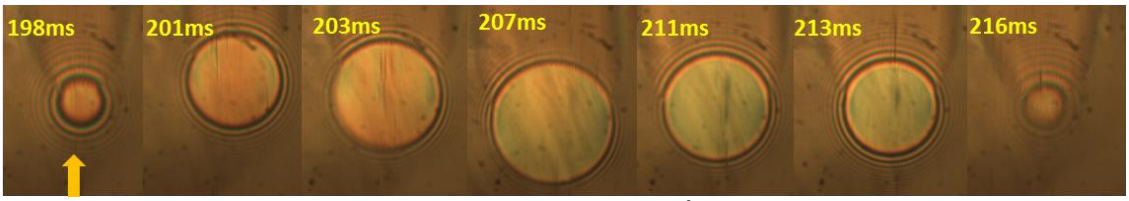

Figure 6.34 (b): Interferograms of the PAO 4 at $40^{\circ}C$, captured at 50 Hz, **0.1 m/s**.

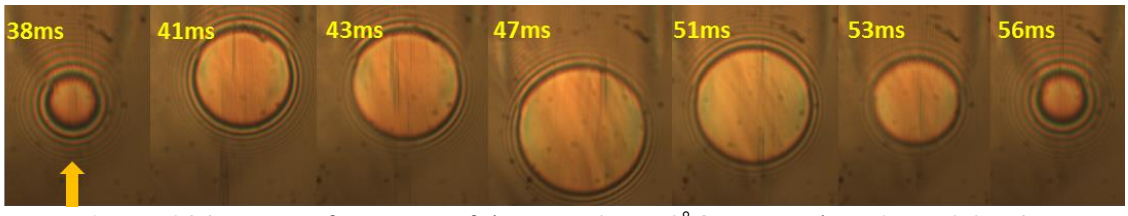

Figure 6.34 (c): Interferograms of the PAO 4 at $40^{\circ}C$, captured at 50 Hz, **0.2 m/s**.

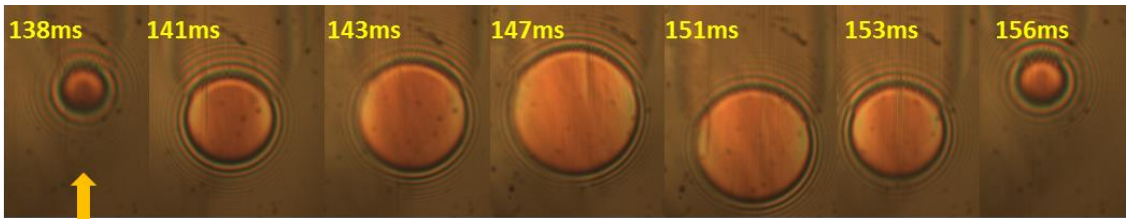

Figure 6.34 (d): Interferograms of the PAO 4 at $40^{\circ}C$, captured at 50 Hz, **0.3 m/s**.

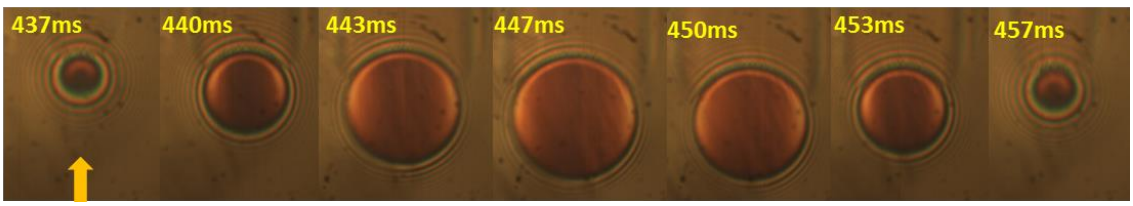

Figure 6.34 (e): Interferograms of the PAO 4 at $40^{\circ}C$, captured at 50 Hz, **0.5 m/s**.

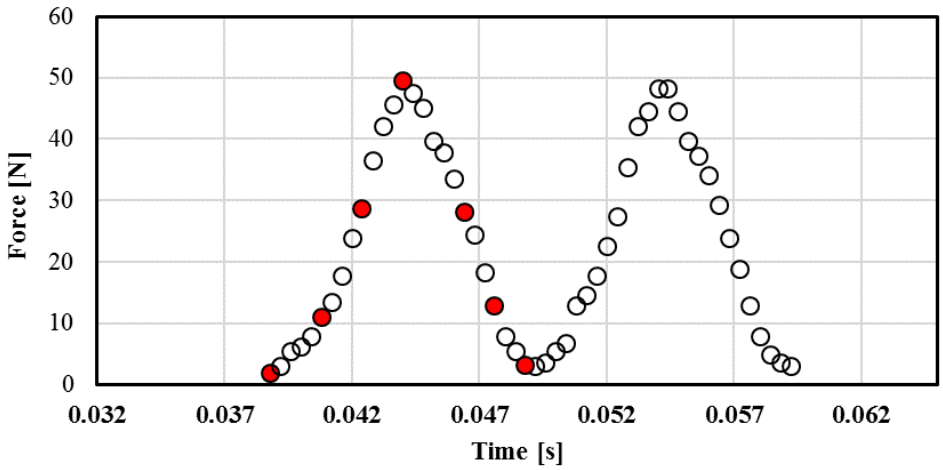

Figure 6.35 (a): Example of load variation, **100 Hz**, PAO 4 at $40^{\circ}C$ vibration test.

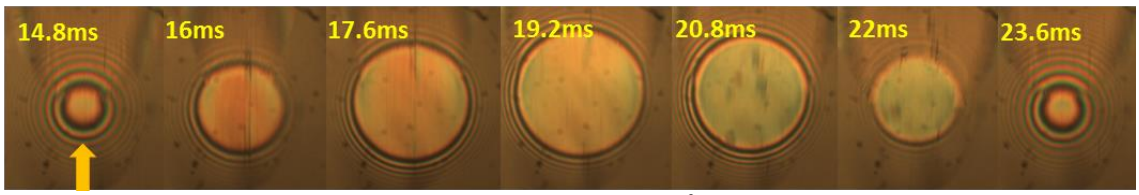

Figure 6.35 (b): Interferograms of the PAO 4 at $40^{\circ}C$, captured at 100 Hz, **0.1 m/s**.

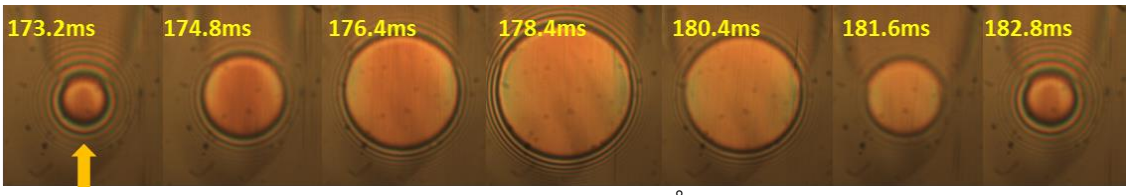

Figure 6.35 (c): Interferograms of the PAO 4 at $40^{\circ}C$, captured at 100 Hz, **0.2 m/s**.

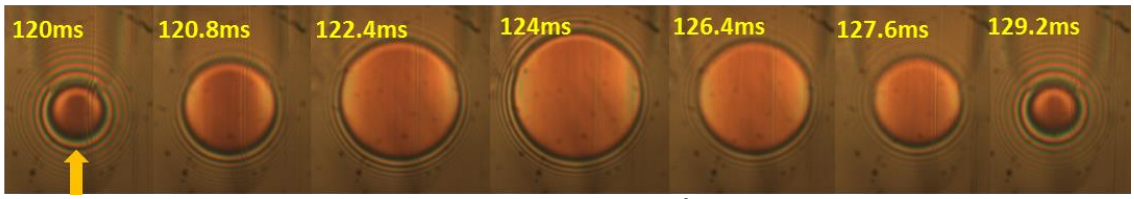

Figure 6.35 (d): Interferograms of the PAO 4 at $40^{\circ}C$, captured at 100 Hz, **0.3 m/s**.

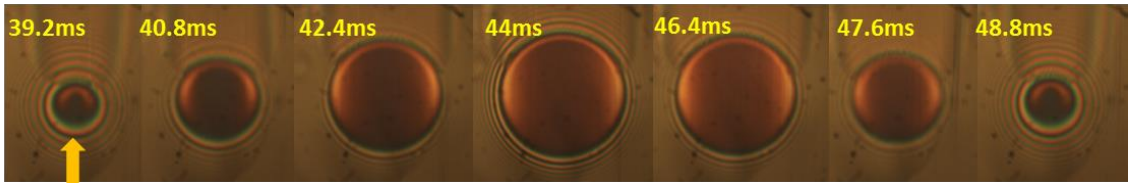

Figure 6.35 (e): Interferograms of the PAO 4 at $40^{\circ}C$, captured at 100 Hz, **0.5 m/s.**

.

6.2 EHD oil films subjected to vibrations of various load amplitude

The experiments presented in this section, were carried out in two types of vibration with different amplitude levels. In the first type of experiments, the EHD contact vibrated under a harmonic force oscillating between nearly zero and a maximum, pre-set level, this may be called pulsating load cycle. In the second type, a constant preload value of 30 N was set to the dynamic shaker to ensure that EHD contact to oscillates at increasing amplitude about the pre-set level, this is called alternating load cycle. The lubricant was PAO 40 with a constant temperature of $40^{\circ}C$. For all the tests in this section, the frequency of oscillation was kept constant at 60 Hz and entrainment speed was also kept constant at 0.1 m/s.

6.2.1 EHD contact under sinusoidal oscillation without preloading (pulsating load **cycle)**

Figures 6.36–6.40 show load variation and typical interferometric images of the EHD contact in pulsating cycles, at various load amplitudes.

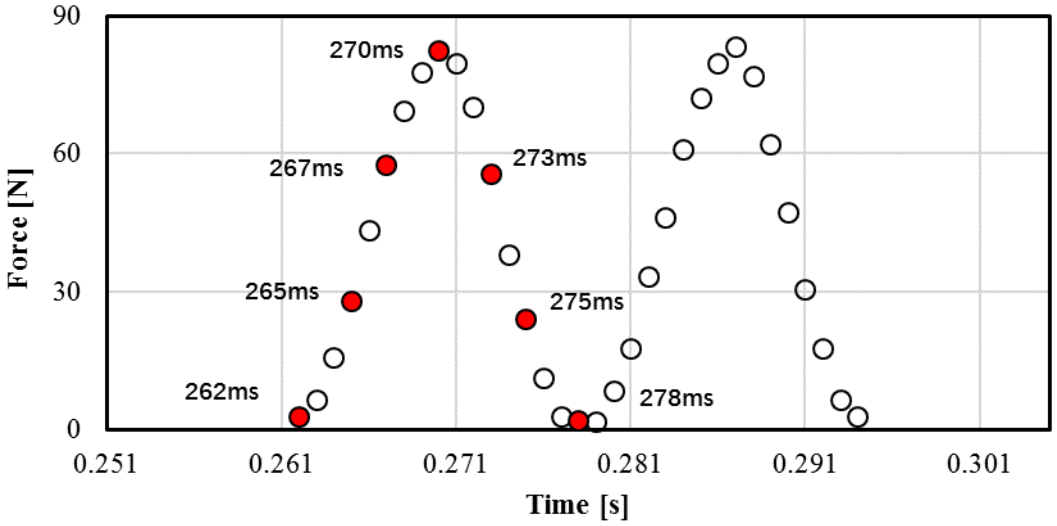

Figure 6.36 (a): Load variation for pulsating cycle **80 N**, 60 Hz, 0.1m/s.

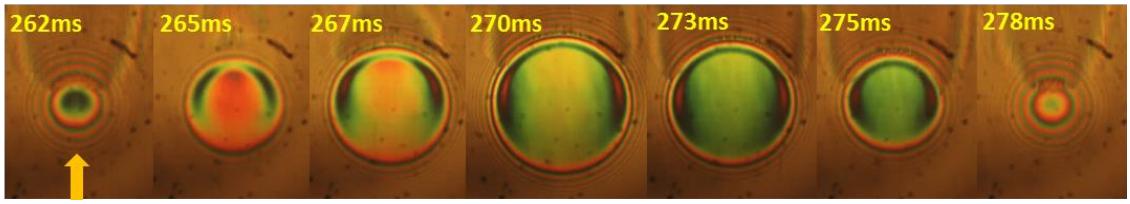

Figure 6.36 (b): Interferograms for pulsating cycle **80N**, 60 Hz, 0.1 m/s.

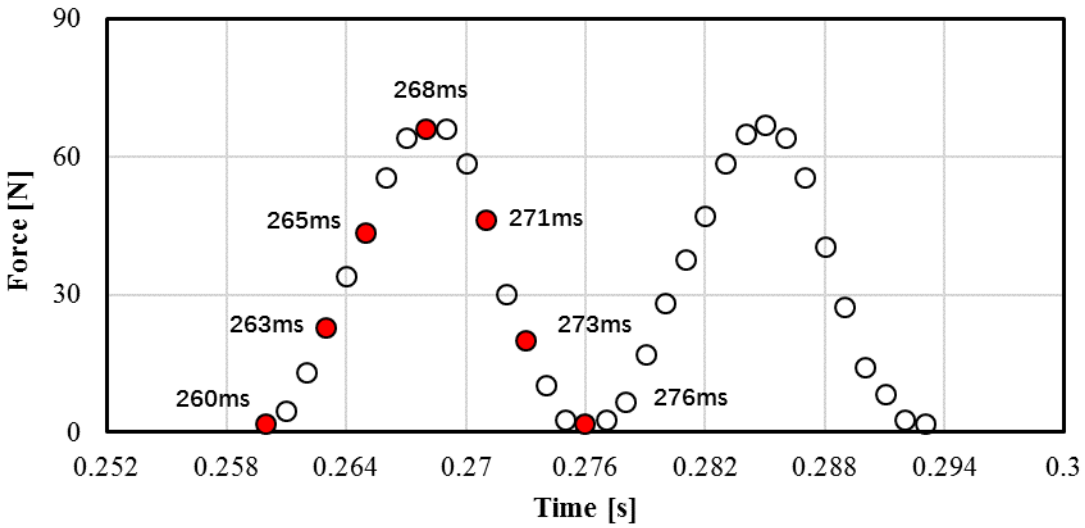

Figure 6.37 (a): Load variation for pulsating cycle **65 N**, 60 Hz, 0.1m/s.

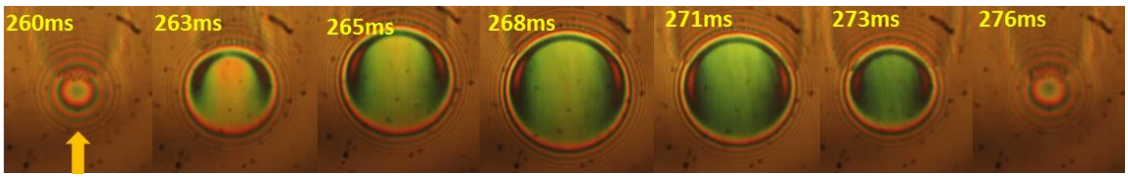

Figure 6.37 (b): Interferograms of EHD contact for pulsating cycle **65 N**, 60 Hz, 0.1 m/s.

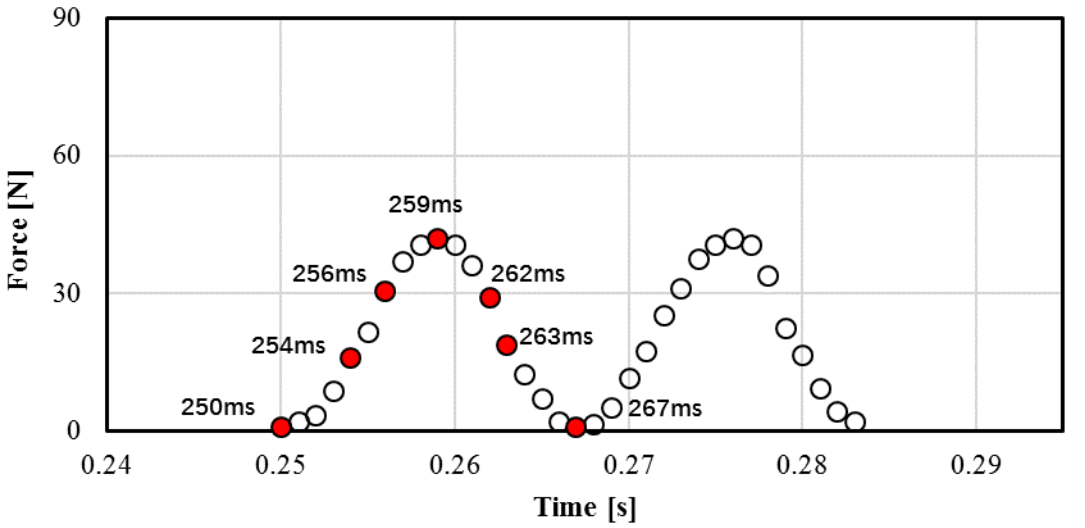

Figure 6.38 (a): Load variation for pulsating cycle **43 N**, 60 Hz, 0.1m/s.

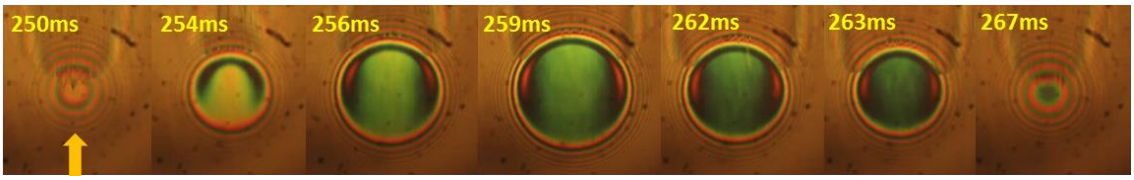

Figure 6.38 (b): Interferograms for pulsating cycle **43 N**, 60 Hz, 0.1 m/s.

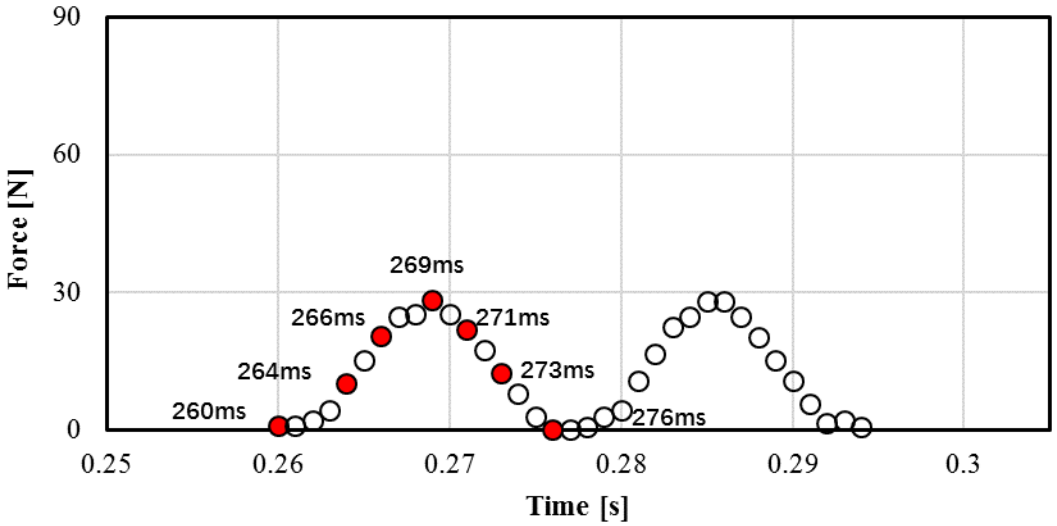

Figure 6.39 (a): Load variation for pulsating cycle **29 N**, 60 Hz, 0.1m/s.

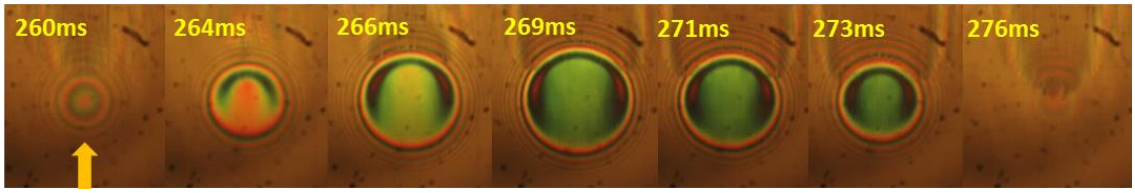

Figure 6.39 (b): Interferograms for pulsating cycle **29 N**, 60 Hz, 0.1 m/s.

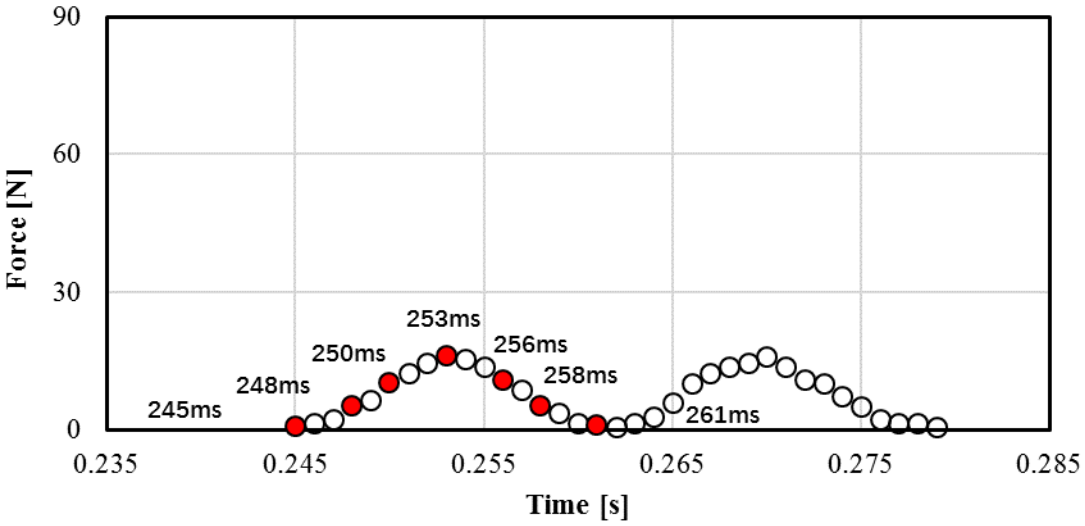

Figure 6.40 (a): Load variation for pulsating cycle **18 N**, 60 Hz, 0.1m/s.

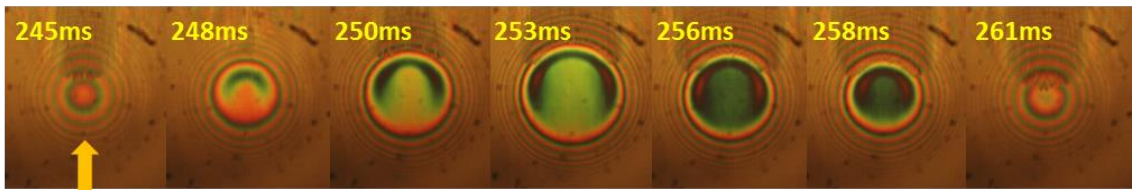

Figure 6.40 (b): Interferograms for pulsating cycle **18 N**, 60 Hz, 0.1 m/s.

6.2.2 EHD contact under sinusoidal oscillation with constant preloading (alternating load cycle)

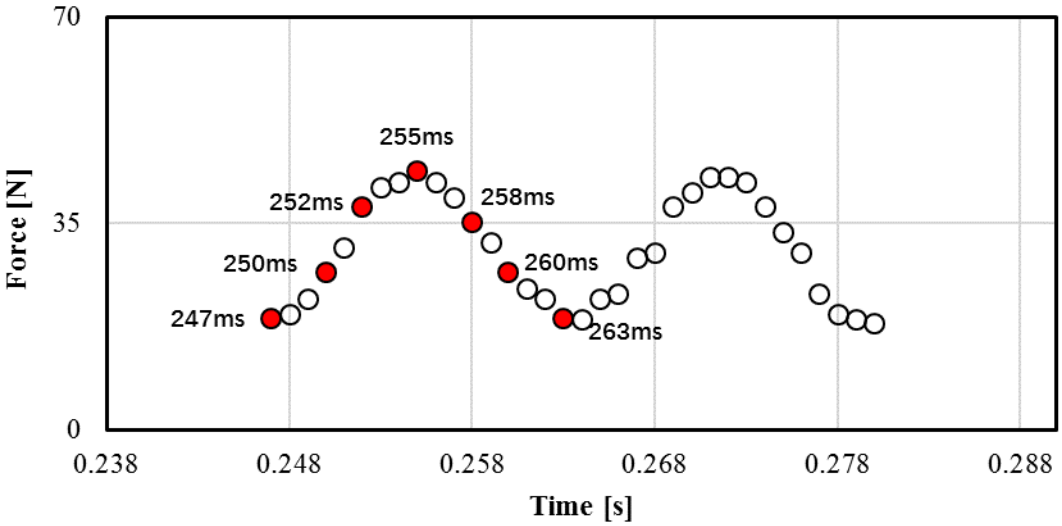

Figure 6.41 (a): Load variation for alternating cycle **13 N** amplitude, 60 Hz, 0.1 m/s.

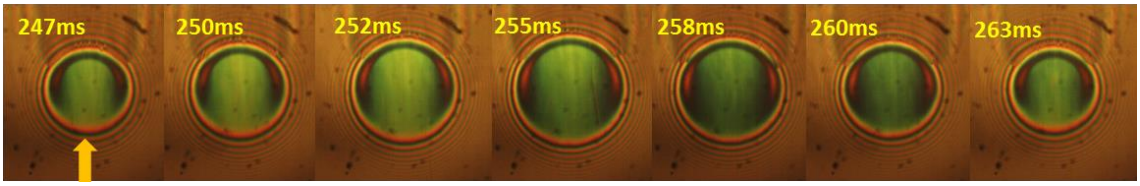

Figure 6.41 (b): Interferograms of contact, alternating cycle **13 N** amplitude, 60 Hz, 0.1 m/s.

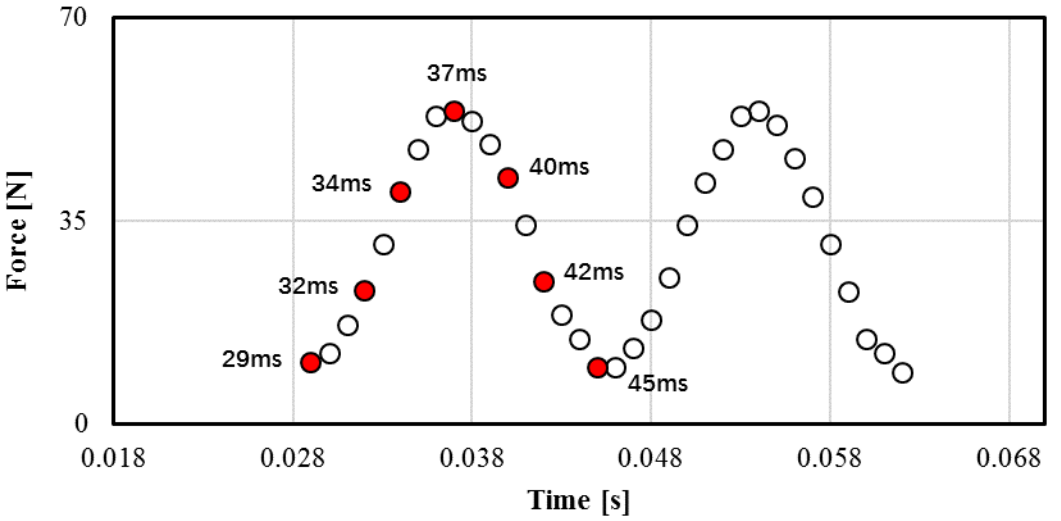

Figure 6.42 (a): Load variation for alternating cycle **20 N** amplitude, 60 Hz, 0.1m/s.

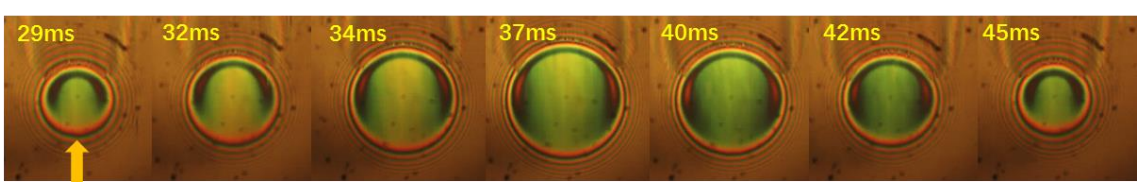

Figure 6.42 (b): Interferograms of contact, alternating cycle **20 N** amplitude 60 Hz, 0.1 m/s.

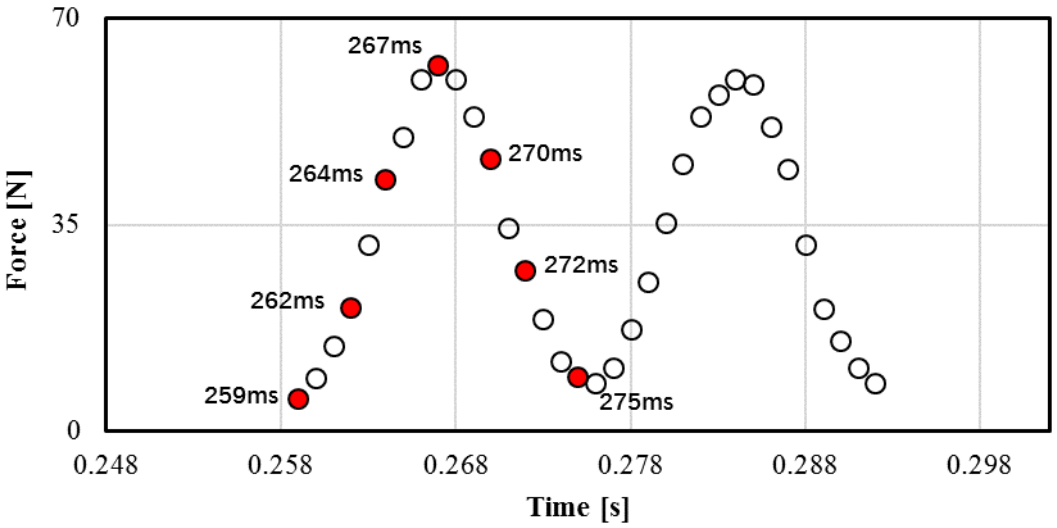

Figure 6.43 (a): Load variation for alternating cycle **29 N** amplitude, 60 Hz, 0.1m/s.

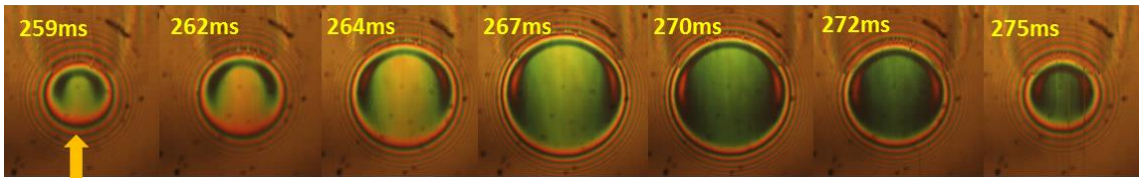

Figure 6.43 (b): Interferograms of contact, alternating cycle **29 N** amplitude, 60 Hz, 0.1 m/s.

Figures 6.41 to 6.43 show the load variation and typical interferograms of the contact subjected to vibrations in alternating cycles with various amplitudes.

6.3 EHD oil film subjected to vibrations with limited lubricant supply

In all the tests shown in previous sections, plenty of lubricant was present in the contact inlet, ensuring that the EHD film was in fully flooded conditions. In practical situations, EHD contacts often forced to work with limited supply of lubricant. Therefore, tests were carried out at frequencies of 10 Hz, 25 Hz and 50 Hz and restricting the amount of lubricant supplied to the contact which are described in the present section. The lubricant used was PAO 40 at a temperature of the tests of 40°C. The ball was about one third immersed into the oil bath and in normal conditions drag the oil into the inlet of the contact ensuring fully flooded conditions. In the present tests, restricted lubricant supply was obtained by placing wipers (customized and manufactured to fit with current lubricant chamber) in front of the ball and disc as seen in figure 6.44. This was not intended as a method to control the exact quantity of lubricant, but just to make sure that there was little lubricant supply in the inlet. The speed for all tests was 0.1 m/s.

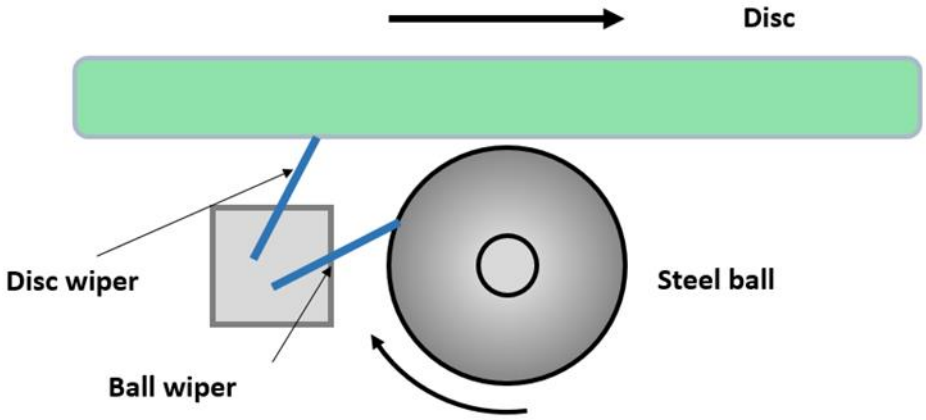

Figure 6.44: Restricted lubricant supply condition setup

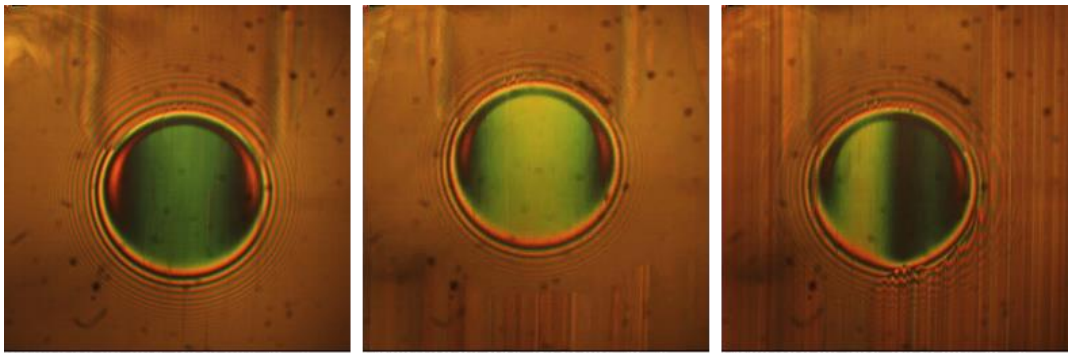

Figure 6.45: Images of the contact showing three different inlet supply conditions under steady state condition

Figure 6.45 shows images of the contact in three different conditions: fully flooded, partially flooded and starved (from left to right). In the image on the left-hand side, the oil fills completely the inlet region which ensures fully flooded conditions. In the middle image, the inlet meniscus boundary can be clearly seen closer to the contact leading edge. This was obtained using only the wiper only on the ball. Finally, the image on the right-hand side shows a contact with even less lubricant supply, obtained by placing the wiper both in front of the ball and the disc. Results published by other researchers (referenced in the discussion chapter) showed that vibrations of very low frequency may help the supply of lubricant mechanism in starved conditions. In order to investigate the effect of vibrations of larger frequencies upon the behaviour of EHD films working in restricted lubricant supply conditions, film thickness measurements for the conditions shown above were conducted with forced harmonic load variation at 10 Hz, 25 Hz and 50 Hz. Interference images of the contact in these conditions are shown in figures 6.46 to 6.48. Analysis of the results is going to be presented in the next chapter.

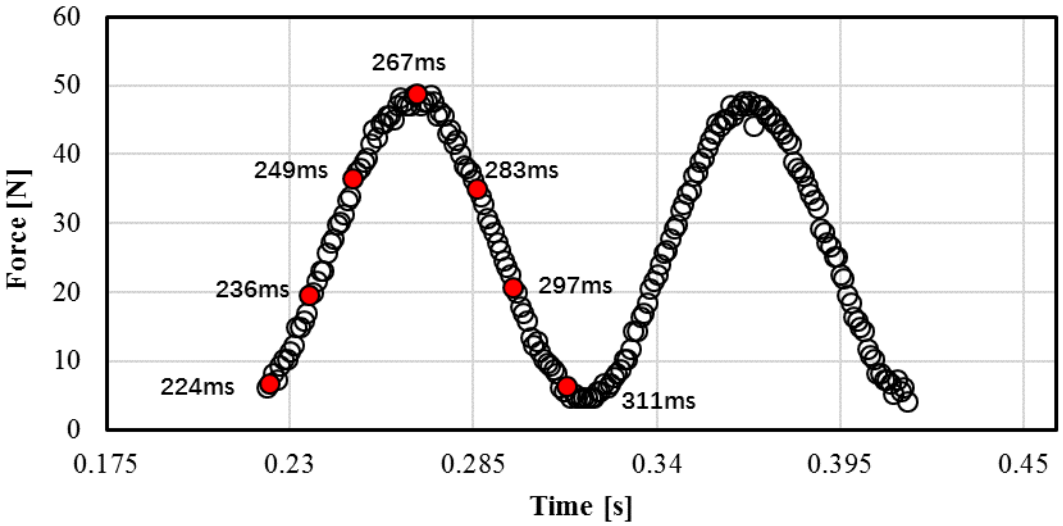

Figure 6.46 (a): Load variation, **10 Hz**, 0.1 m/s, low lubricant supply test.

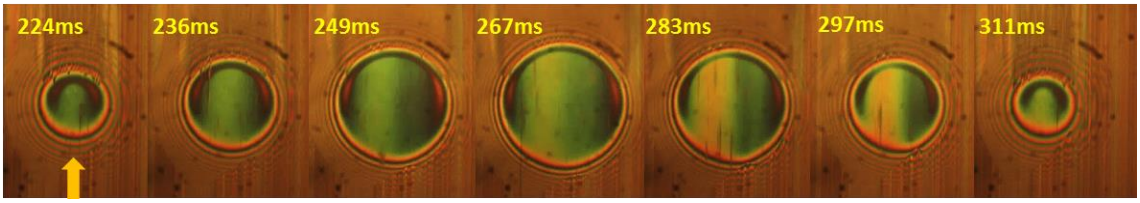

Figure 6.46 (b): Interferograms of PAO 40 at $40^{\circ}C$ for **10 Hz**, 0.1 m/s, captured at low lubricant supply condition.

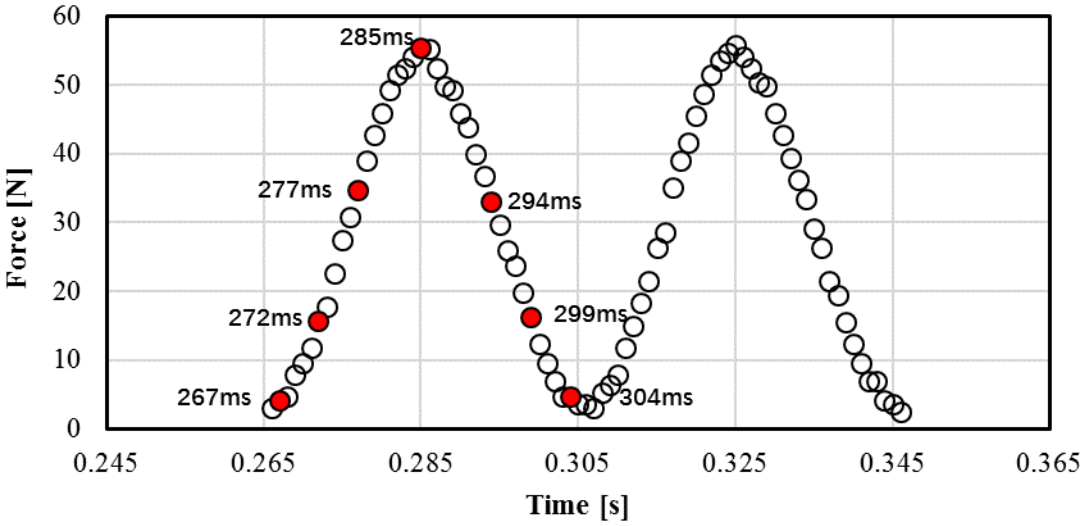

Figure 6.47 (a): Load variation, **25 Hz,** 0.1 m/s, low lubricant supply test.

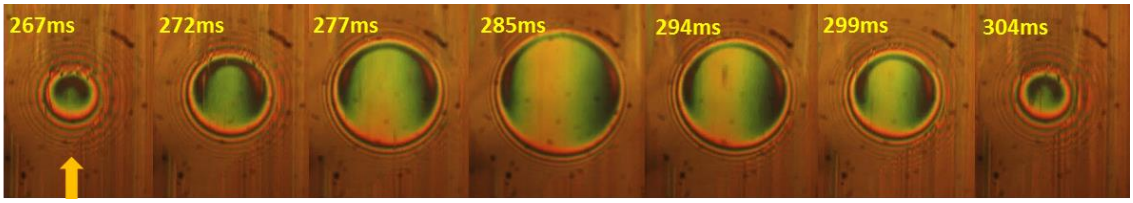

Figure 6.47 (b): Interferograms of PAO 40 at $40^{\circ}C$ for **25 Hz**, 0.1 m/s, captured at low lubricant supply condition.

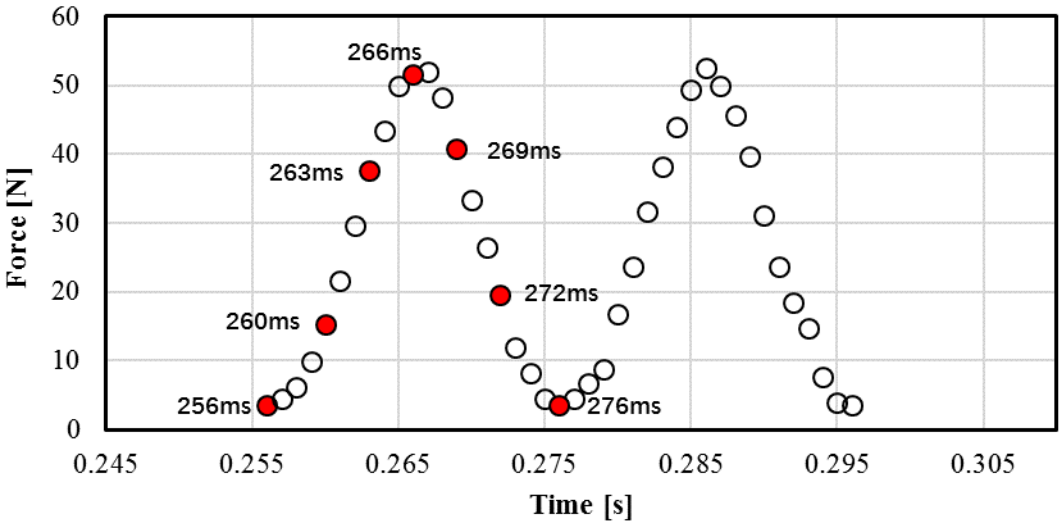

Figure 6.48 (a): Load variation, **50 Hz**, 0.1 m/s, low lubricant supply test.

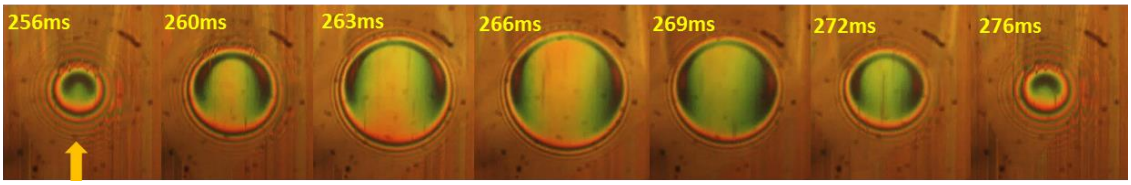

Figure 6.48 (b): Interferograms of PAO 40 at $40^{\circ}C$ for **50 Hz**, 0.1 m/s, captured at low lubricant supply condition.

6.4 Results of grease lubricated EHD films subjected to vibrations.

Greases are lubricants used in many applications and especially in rolling element bearings. As rolling bearings are so often subjected to vibrations, testing of greases behaviour in contacts under oscillatory load conditions, is one of the most important tasks of this research. In this section, the experiments were conducted under frequencies of 10 Hz, 20 Hz, 40 Hz and 60 Hz for three types of greases, SBM, SRL and RL2. The properties of these three greases are found in Chapter 4. The temperature of tested greases was kept at $40^{\circ}C$ during all tests. The pair of materials forming EHD contact was kept as the same. It was documented that the film thickness in grease – lubricated contacts decrease constantly after short period of rolling under steady state condition. This is due to the semi-solid consistency of greases, which results in them being pushed away from the rolling track which in turn restricts the supply of oil to the contact. Thus, film thickness of the base oil and grease were initially measured with the increasing entrainment speed to locate the entrainment velocity at where starvation starts to occur for each grease. The behaviour of grease film thickness decreasing with time was monitored by images taken at one-minute interval until starved EHD contact became fully established. After this, the load was set into oscillatory mode and the film thickness was measured over a period up to 20 minutes.

6.4.1 Results of SBM grease at 40℃

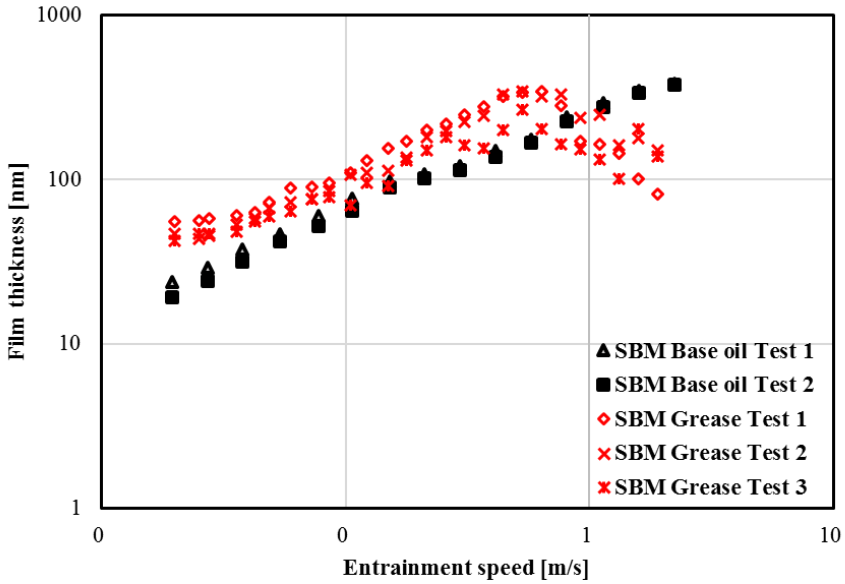

Figure 6.49: Central film thickness of SBM grease and its base oil as a function of rolling speed under steady state conditions, 40℃.

Figure 6.49 presents the relationship between film thickness and entrainment speed of SBM grease and its base oil. Three sets of measurements for the grease and two for the base oil results can be seen above. It is obvious that film thickness of base oil increases with the power of the entrainment speed which shows as a line in a log-log plot. Unlike the results of base oil, the grease lubricated contact starts to become starved at the entrainment speed of about 0.55 m/s and at larger speeds the film thickness decreases continuously with the increasing entrainment speed.

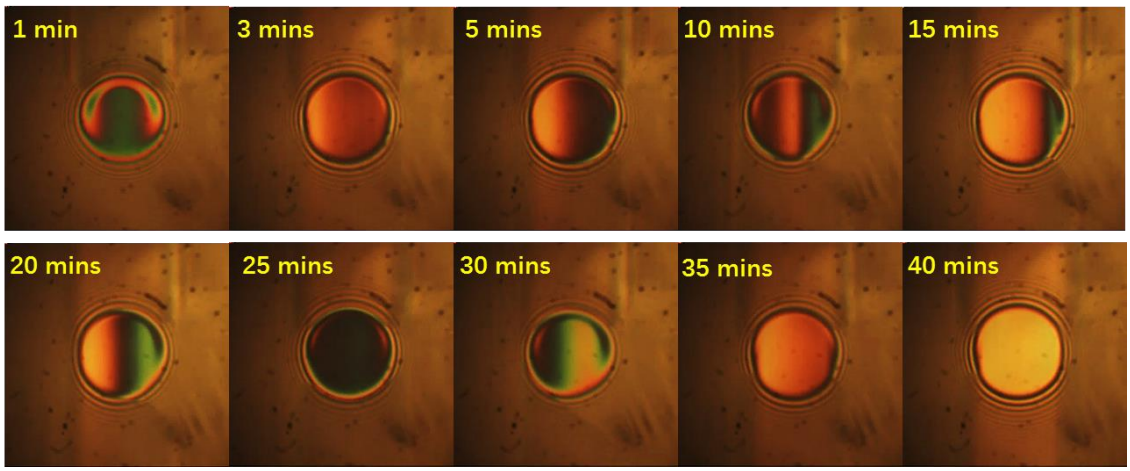

Figure 6.50: SBM grease at constant entrainment speed of 0.55 m/s, 40℃.

To further investigate the conditions of starvation, images of the contact rolling at constant an entrainment speed of 0.55m/s and a constant load of 20 N were recorded at every two minutes interval for the first ten minutes and at every five minutes until the contact is severely starved (seen in figure 6.50). After one minute's rolling, it can be seen the contact remains fully flooded.

Then, starvation becomes more visible until the EHD contact resembling nearly a dry Hertzian contact after about 40 minutes of rolling. Central film thickness of the EHD contact lubricated with SBM grease rolling at constant an entrainment speed of 0.55 m/s and a constant load of 20 N is shown in figure 6.51.

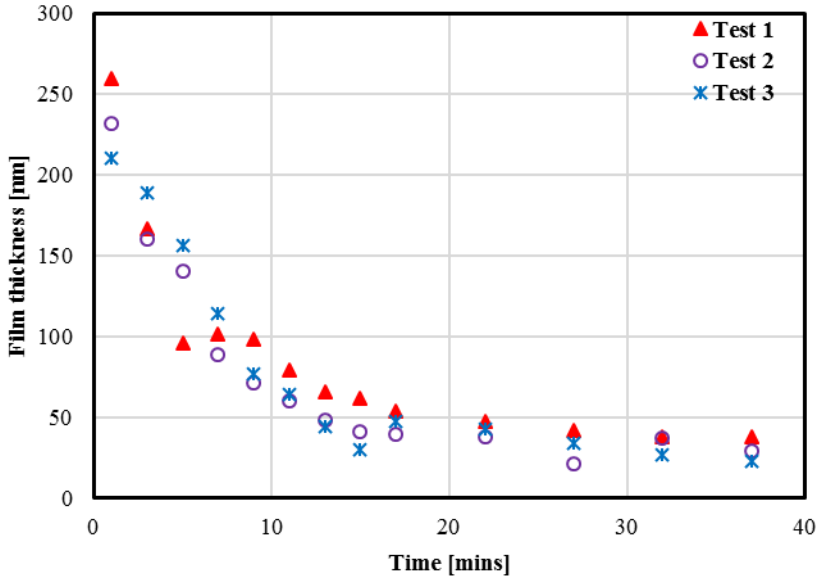

Figure 6.51: Central film thickness of SBM grease decay at constant entrainment speed of 0.55 m/s, 40℃.

The following figures, from 6.52 to 6.55 illustrate the typical behaviour of starved SBM grease lubricated EHD contact under harmonic load oscillation.

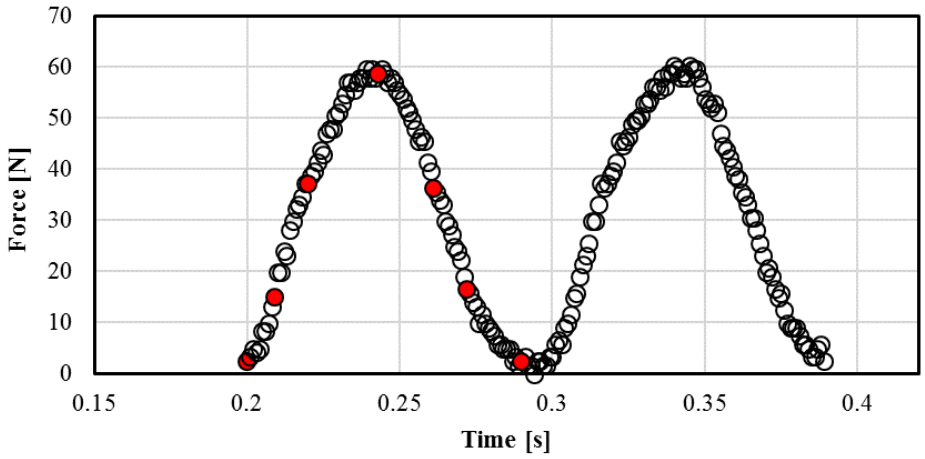

Figure 6.52 (a): Example of load variation, SBM grease at $40^{\circ}C$, 10 Hz, 0.55m/s.

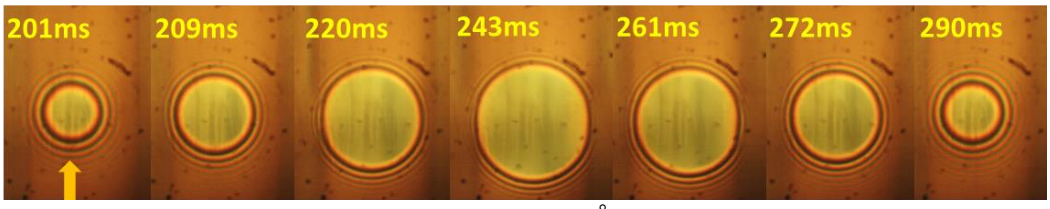

Figure 6.52 (b): Interferograms of SBM grease at $40^{\circ}C$ for 10 Hz, 0.55 m/s, captured after 5 mins' vibration.

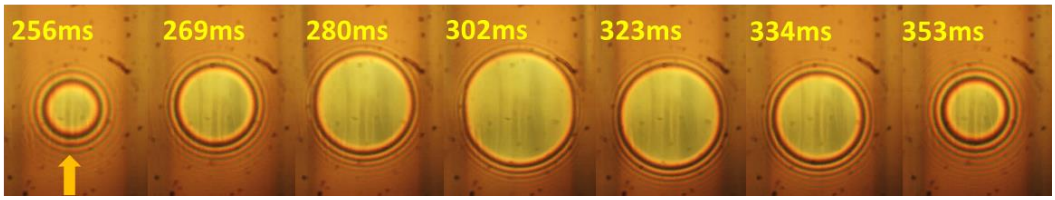

Figure 6.52 (c): Interferograms of SBM grease at $40^{\circ}C$ for 10 Hz, 0.55 m/s, captured after 10 mins' vibration.

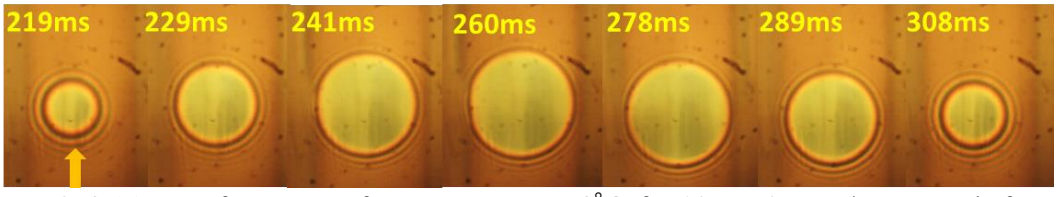

Figure 6.52 (d): Interferograms of SBM grease at $40^{\circ}C$ for 10 Hz, 0.55 m/s, captured after 15 mins' vibration.

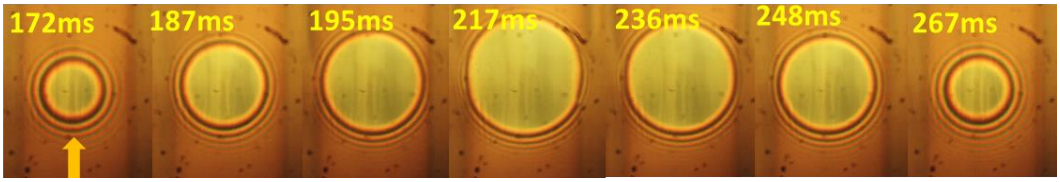

Figure 6.52 (e): Interferograms of SBM grease at $40^{\circ}C$ for 10 Hz, 0.55 m/s, captured after 20 mins' vibration.

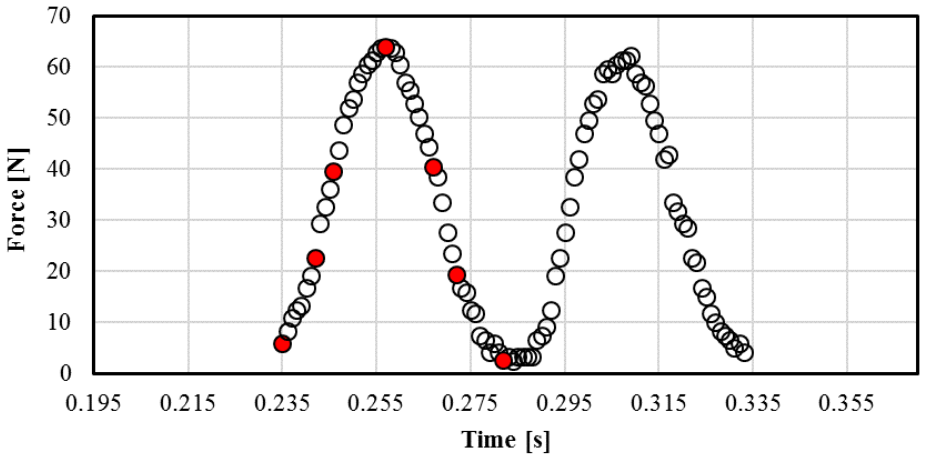

Figure 6.53 (a): Example of load variation, SBM grease at $40^{\circ}C$, 20 Hz, 0.55m/s.

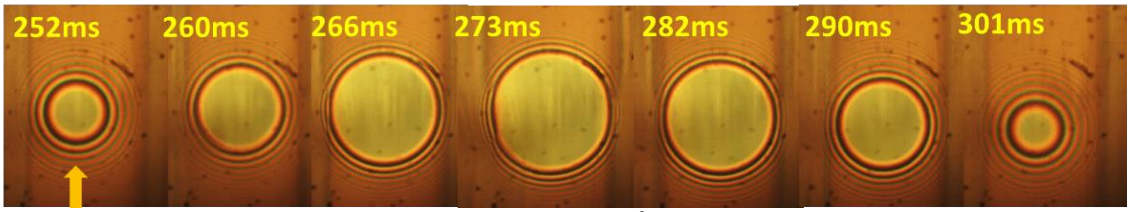

Figure 6.53 (b): Interferograms of SBM grease at $40^{\circ}C$ for 20 Hz, 0.55 m/s., captured after 5 mins' vibration.

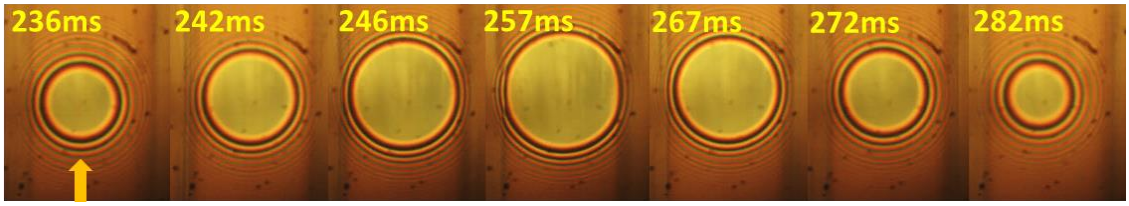

Figure 6.53 (c): Interferograms of SBM grease at $40^{\circ}C$ for 20 Hz, 0.55 m/s., captured after 10 mins' vibration.

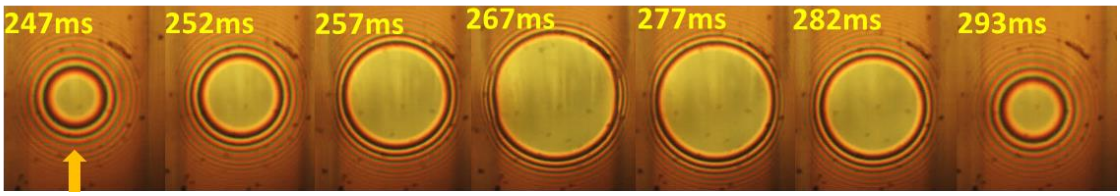

Figure 6.53 (d): Interferograms of SBM grease at $40^{\circ}C$ for 20 Hz, 0.55 m/s., captured after 15 mins' vibration.

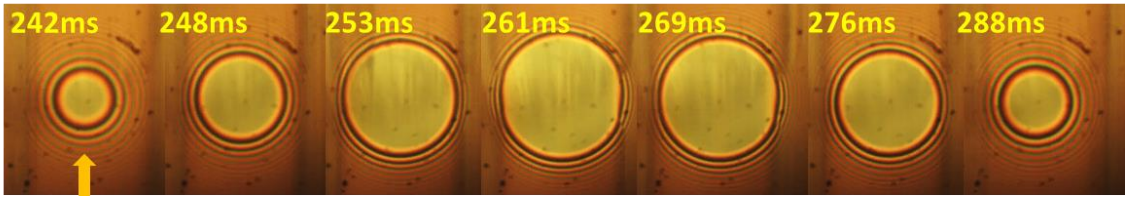

Figure 6.53 (e): Interferograms of SBM grease at $40^{\circ}C$ for 20 Hz, 0.55 m/s., captured after 20 mins' vibration.

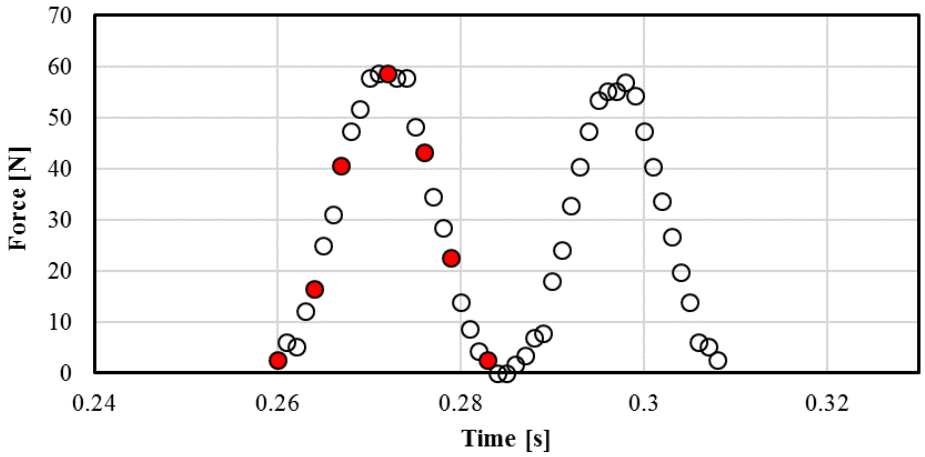

Figure 6.54 (a): Example of load variation, SBM grease at $40^{\circ}C$,40 Hz, 0.55m/s.

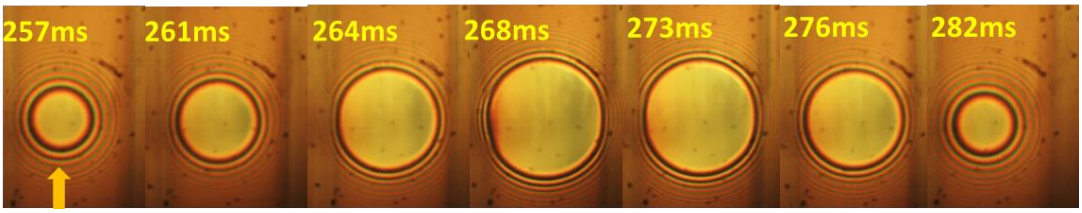

Figure 6.54 (b): Interferograms of SBM grease at $40^{\circ}C$ for 40 Hz, 0.55 m/s., captured after 5 mins' vibration.

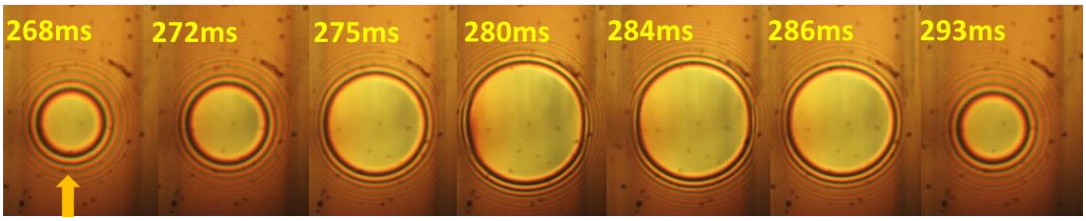

Figure 6.54 (c): Interferograms of SBM grease at $40^{\circ}C$ for 40 Hz, 0.55 m/s, captured after 10 mins' vibration.

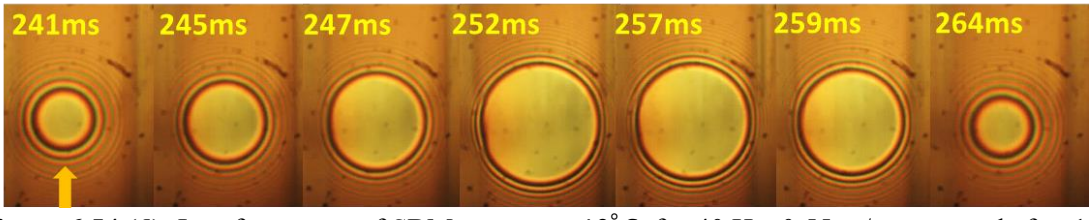

Figure 6.54 (d): Interferograms of SBM grease at $40^{\circ}C$ for 40 Hz, 0.55 m/s., captured after 15 mins' vibration.

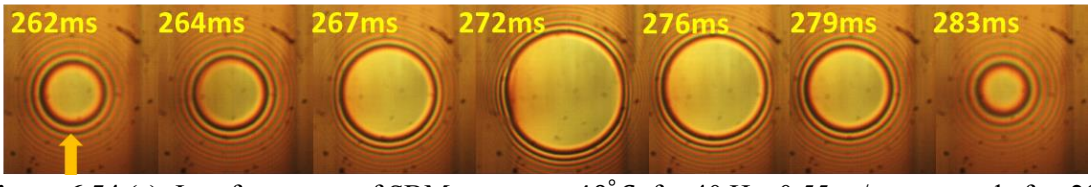

Figure 6.54 (e): Interferograms of SBM grease at $40^{\circ}C$ for 40 Hz, 0.55 m/s., captured after 20 mins' vibration.

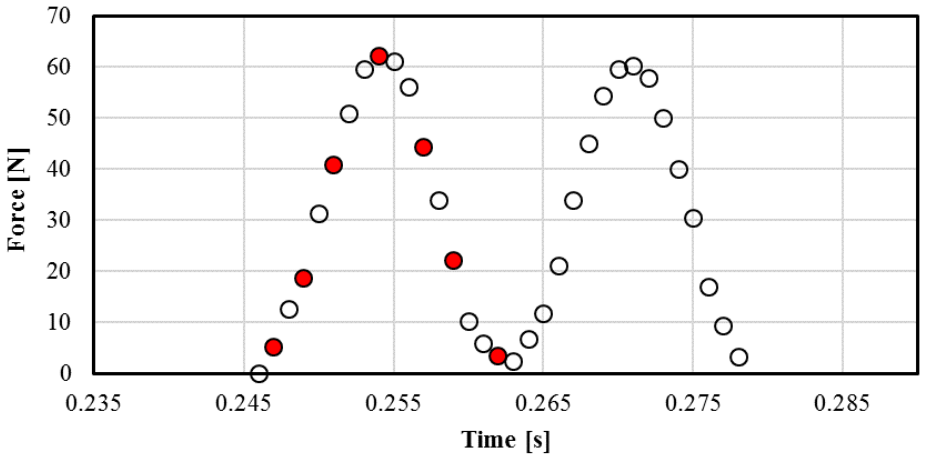

Figure 6.55 (a): Example of load variation, SBM grease at $40^{\circ}C$, 60 Hz, 0.55m/s.

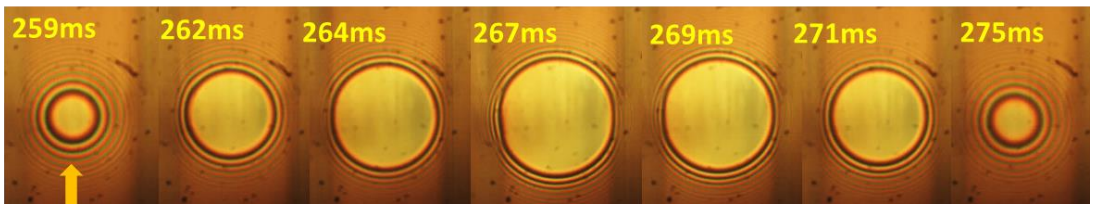

Figure 6.55 (b): Interferograms of SBM grease at $40^{\circ}C$ for 60 Hz, 0.55 m/s, captured after 5 mins' vibration.

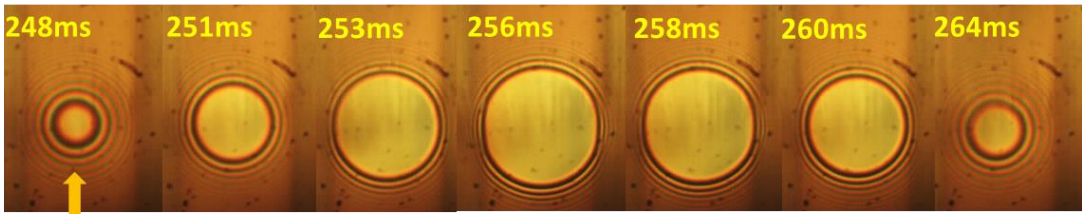

Figure 6.55 (c): Interferograms of SBM grease at $40^{\circ}C$ for 60 Hz, 0.55 m/s, captured after 10 mins' vibration.

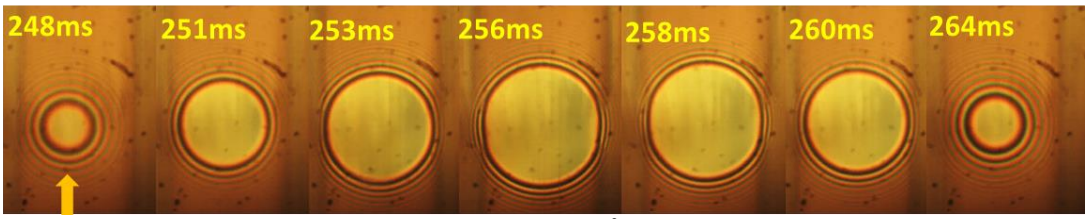

Figure 6.55 (d): Interferograms of SBM grease at $40^{\circ}C$ for 60 Hz, 0.55 m/s, captured after 15 mins' vibration.

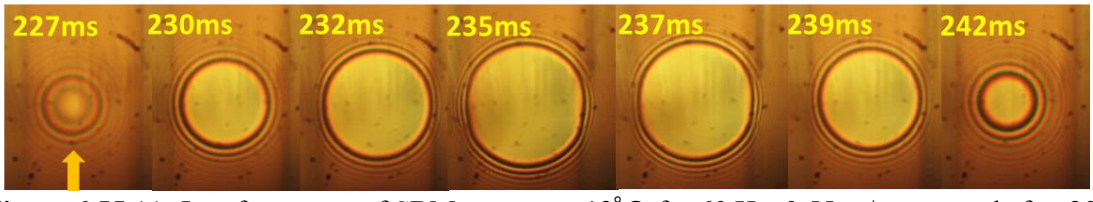

Figure 6.55 (e): Interferograms of SBM grease at $40^{\circ}C$ for 60 Hz, 0.55 m/s, captured after 20 mins' vibration.

6.4.2 Results of SRL grease at 40℃

In figure 6.56 variation of central film thickness with entrainment speed for the SRL grease and its base oil are shown. Again, three sets of measurements were taken for the grease and two for the base oil. As seen the results are reasonably repeatable. The SRL grease lubricated contact starts to become starved at the entrainment speed of around 0.38 m/s.

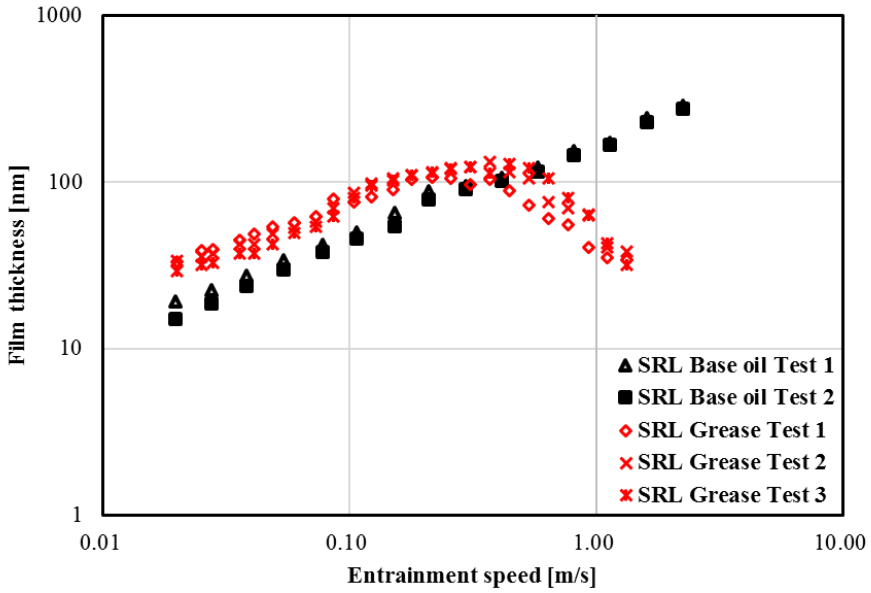

Figure 6.56: Central film thickness of SRL grease and its base oil as a function of rolling speed under steady state conditions, 40℃.

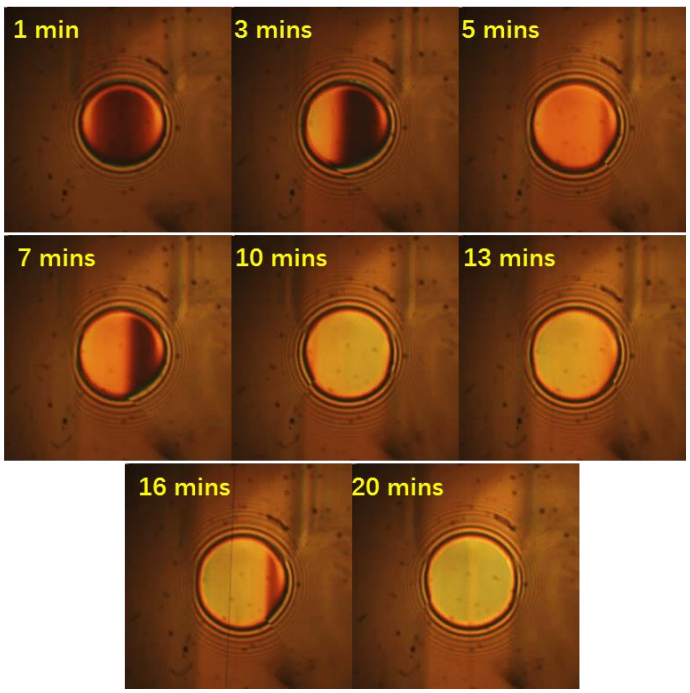

Figure 6.57: Film behaviour of SRL grease at constant entrainment speed of 0.38 m/s in 20 minutes' rolling period, 40℃.

Figures 6.57 shows the evolution of the EHD film lubricated with SRL grease, from fully flooded to severely starved. In figure 6.58 the change of the central film thickness with time is plotted. At a rolling speed of 0.38 m/s starvation settles in after ten minutes of running.

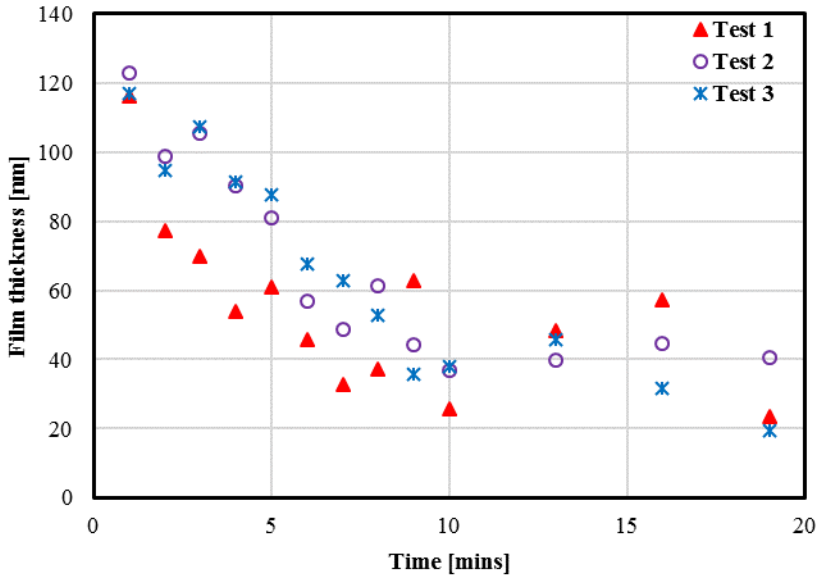

Figure 6.58: Central film thickness of SRL grease decrease at constant entrainment speed of 0.38 m/s, 40℃.

The following figures from 6.59 to 6.62 illustrate the typical behaviour of starved SRL grease lubricated EHD contact under sinusoidal load oscillation, at a range of frequencies and entrainment speeds.

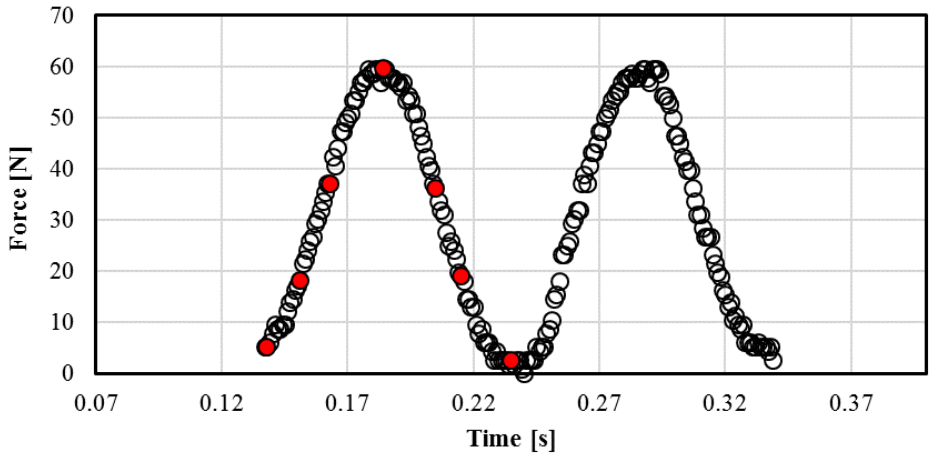

Figure 6.59 (a): Example of load variation, SRL grease at $40^{\circ}C$, 10 Hz, 0.38m/s.

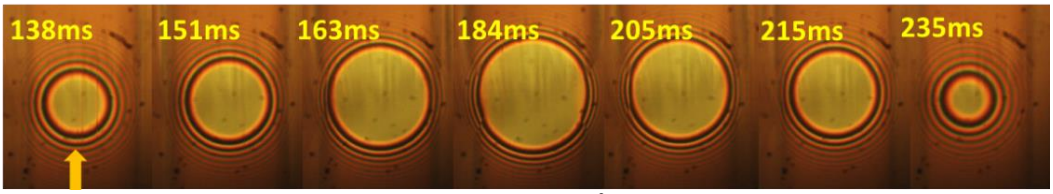

Figure 6.59 (b): Interferograms of SRL grease at $40^{\circ}C$ for 10 Hz, 0.38 m/s, captured after 5 mins' vibration.

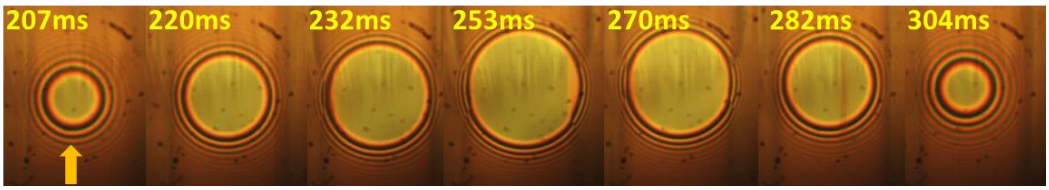

Figure 6.59 (c): Interferograms of SRL grease at $40^{\circ}C$ for 10 Hz, 0.38 m/s, captured after 10 mins' vibration.

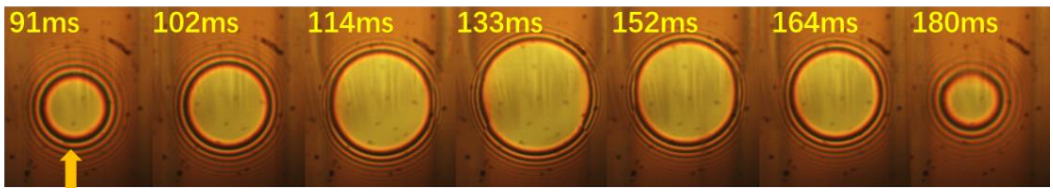

Figure 6.59 (d): Interferograms of SRL grease at $40^{\circ}C$ for 10 Hz, 0.38 m/s, captured after 15 mins' vibration.

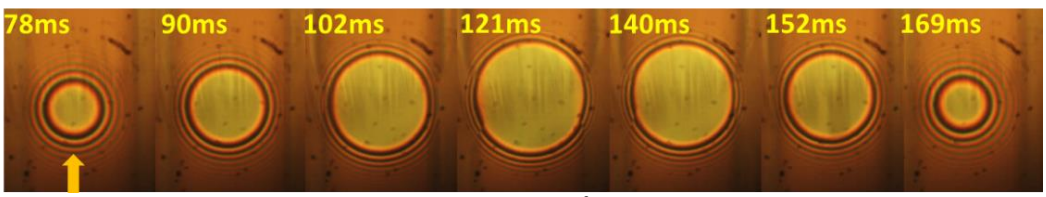

Figure 6.59 (e): Interferograms of SRL grease at $40^{\circ}C$ for 10 Hz, 0.38 m/s, captured after 20 mins' vibration

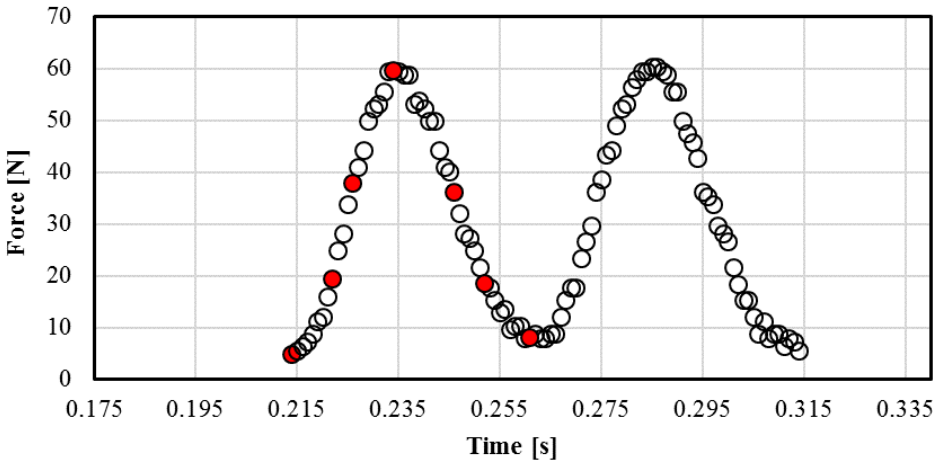

Figure 6.60 (a): Example of load variation, SRL grease at $40^{\circ}C$, 20 Hz, 0.38m/s.

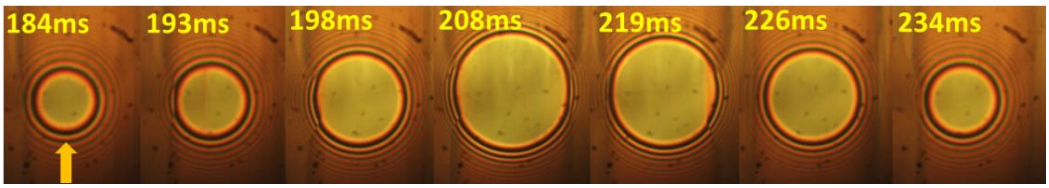

Figure 6.60 (b): Interferograms of SRL grease at $40^{\circ}C$ for 20 Hz, 0.38 m/s, captured after 5 mins' vibration.

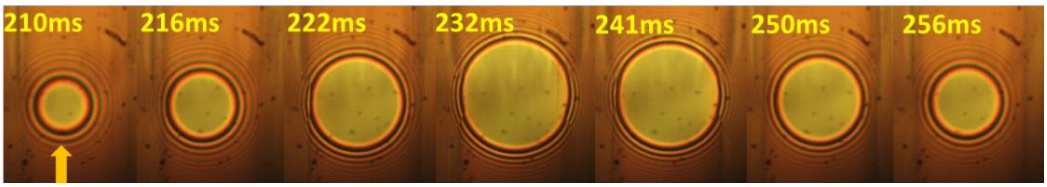

Figure 6.60 (c): Interferograms of SRL grease at $40^{\circ}C$ for 20 Hz, 0.38 m/s, captured after 10 mins' vibration

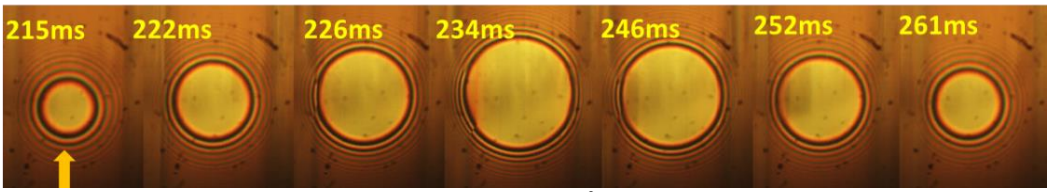

Figure 6.60 (d): Interferograms of SRL grease at $40^{\circ}C$ for 20 Hz, 0.38 m/s, captured after 15 mins' vibration

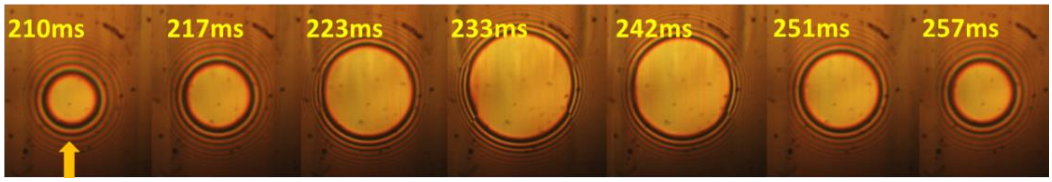

Figure 6.60 (e): Interferograms of SRL grease at $40^{\circ}C$ for 20 Hz, 0.38 m/s, captured after 20 mins' vibration

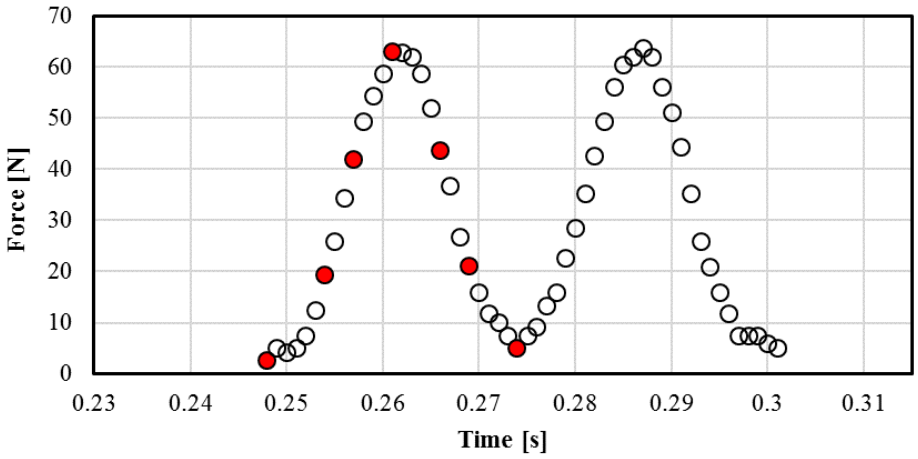

Figure 6.61 (a): Example of load variation, SRL grease at $40^{\circ}C$, 40 Hz, 0.38m/s.

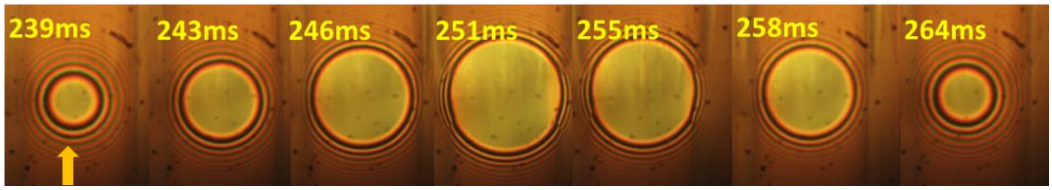

Figure 6.61 (b): Interferograms of SRL grease at $40^{\circ}C$ for 40 Hz, 0.38 m/s, captured after 5 mins' vibration.

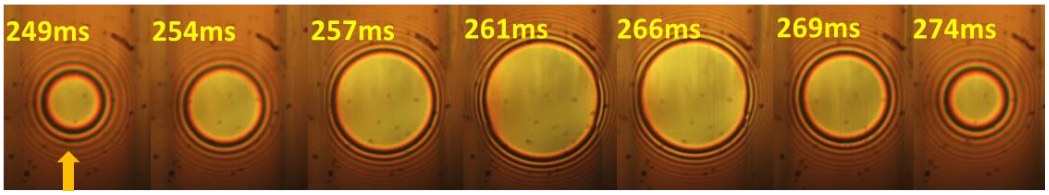

Figure 6.61 (c): Interferograms of SRL grease at $40^{\circ}C$ for 40 Hz, 0.38 m/s, captured after 10 mins' vibration.

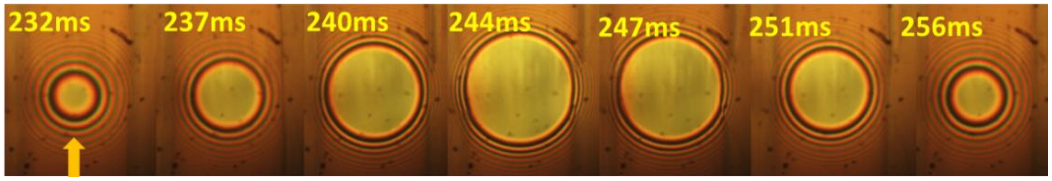

Figure 6.61 (d): Interferograms of SRL grease at $40^{\circ}C$ for 40 Hz, 0.38 m/s, captured after 15 mins' vibration.

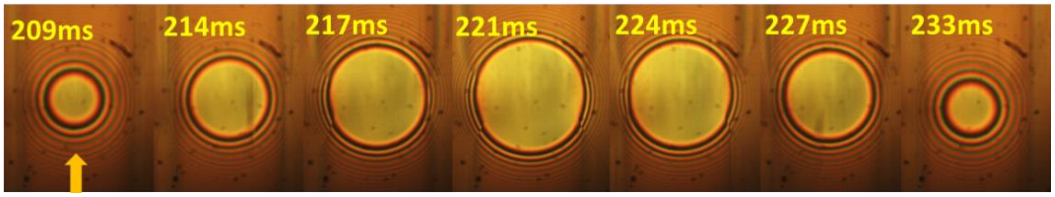

Figure 6.61 (e): Interferograms of SRL grease at $40^{\circ}C$ for 40 Hz, 0.38 m/s, captured after 20 mins' vibration.

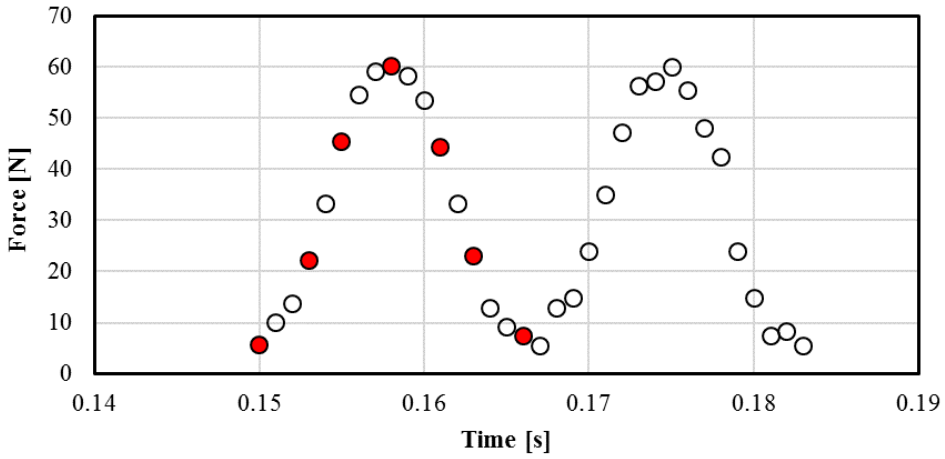

Figure 6.62 (a): Example of load variation, SRL grease at $40^{\circ}C$, 60 Hz, 0.38m/s.

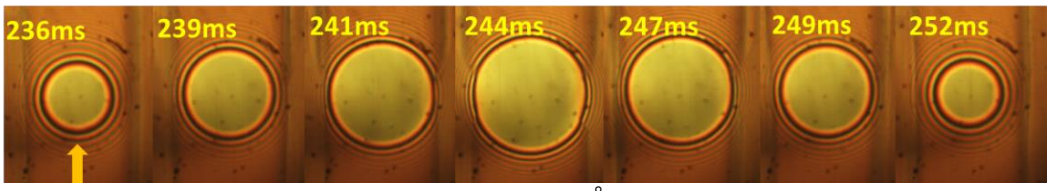

Figure 6.62 (b): Interferograms of SRL grease at $40^{\circ}C$ for 60 Hz, 0.38 m/s, captured after 5 mins' vibration.

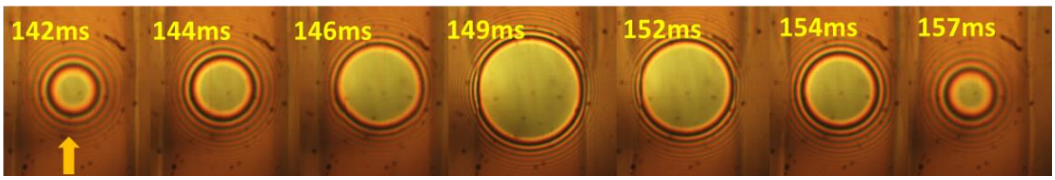

Figure 6.62 (c): Interferograms of SRL grease at $40^{\circ}C$ for 60 Hz, 0.38 m/s, captured after 10 mins' vibration.

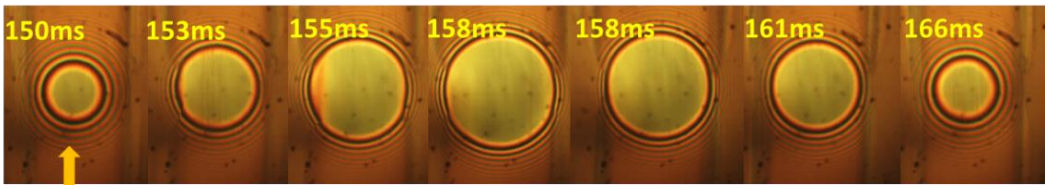

Figure 6.62 (b): Interferograms of SRL grease at $40^{\circ}C$ for 60 Hz, 0.38 m/s, captured after 15 mins' vibration.

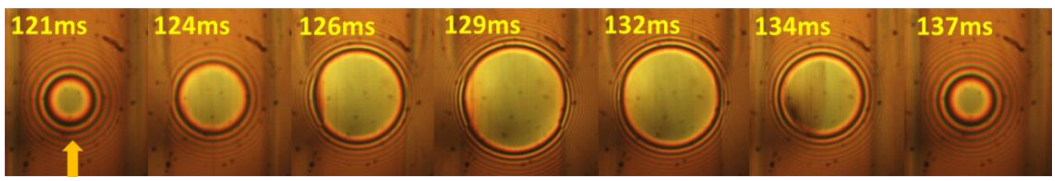

Figure 6.62 (e): Interferograms of SRL grease at $40^{\circ}C$ for 60 Hz, 0.38 m/s, captured after 20 mins' vibration.

6.4.3 Results of RL2 grease at 40℃

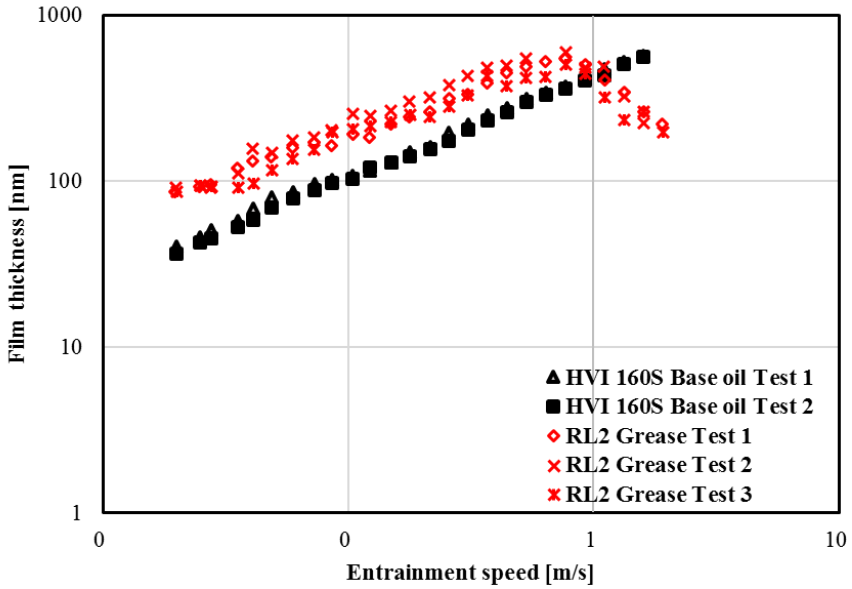

Figure 6.63: Central film thickness of RL2 grease and its base oil as a function of rolling speed under steady state conditions, 40℃.

The dependence of the central film thickness of RL2 grease and its base oil on the entrainment speed is shown in figure 6.63. RL2 grease lubricated contact start to become starved at an entrainment speed of 0.769 m/s.

The transition time from fully flooded to starved condition takes longer than that for the other two greases as shown in figure 6.64. With the contact running at 0.769 m/s the film becomes relatively thinner after only one minute of rolling, however it takes as long as between sixty to eighty minutes for it to become severely starved.

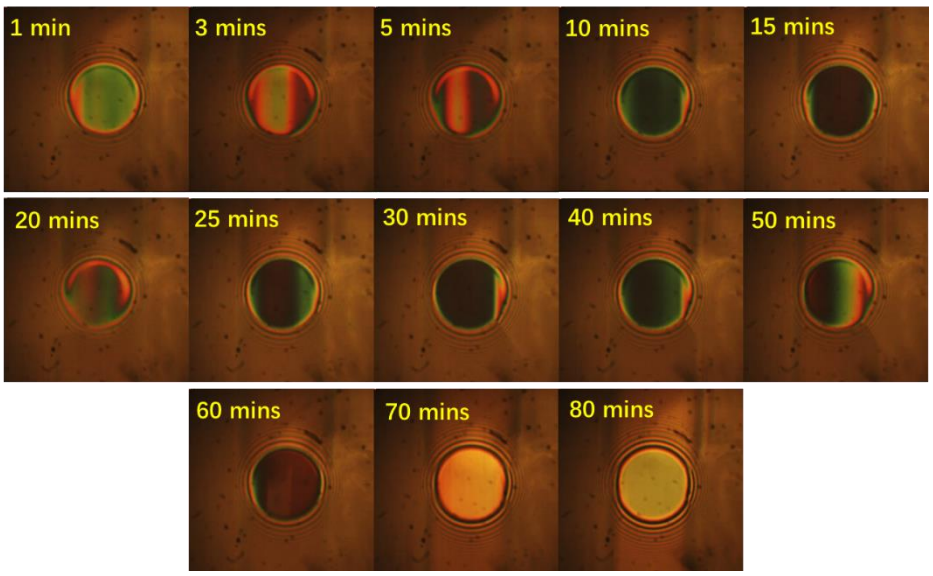

Figure 6.64: Film behaviour of RL2 grease at constant entrainment speed of 0.769 m/s in 80 minutes' rolling period, 40℃.

To further investigate the central film thickness of grease lubricated contact decreasing at the entrainment speed when starvation happens, central film thickness of the EHD contact lubricated with SRL grease rolling at constant an entrainment speed of 0.769 m/s and a constant load of 20 N were measured during minutes' intervals (see figure 6.65).

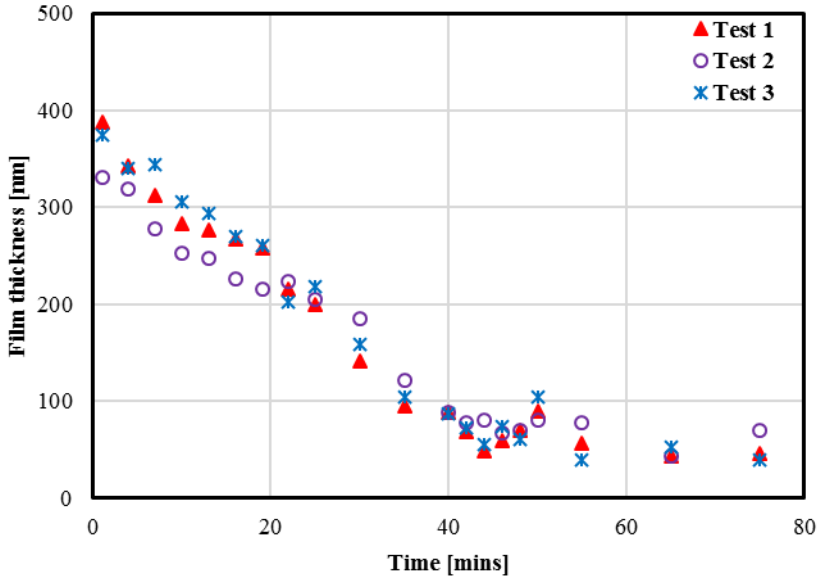

Figure 6.65: Central film thickness of RL2 grease decrease at constant entrainment speed of 0.77 m/s, 40°C.

The following figures from 6.66 to 6.69 illustrate the typical behaviour of starved RL2 grease lubricated EHD contact under sinusoidal load oscillations.

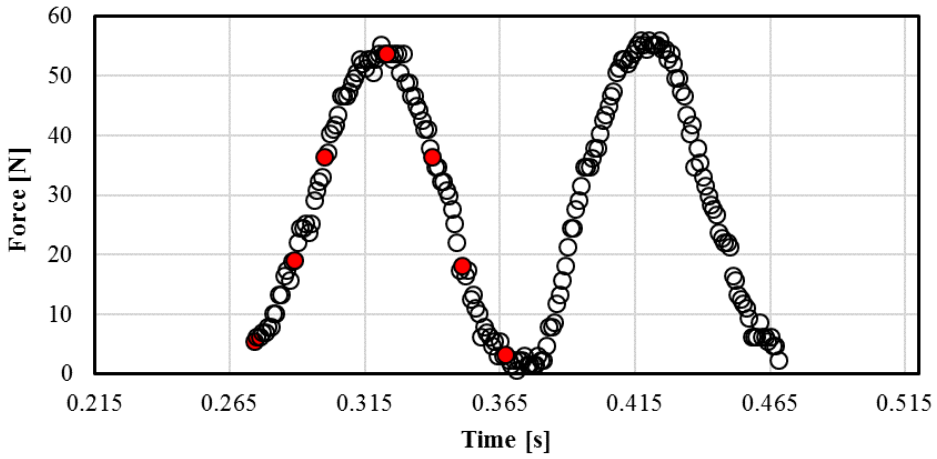

Figure 6.66 (a): Example of load variation, RL2 grease at $40^{\circ}C$, 10 Hz, 0.77m/s.

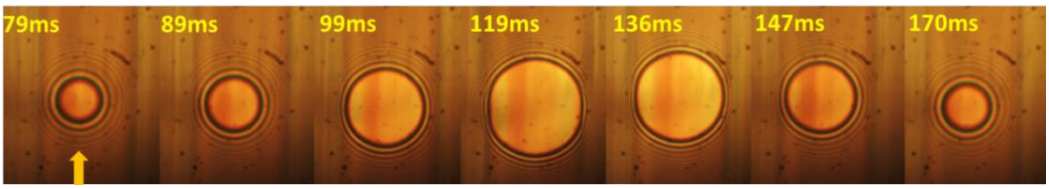

Figure 6.66 (b): Interferograms of RL2 grease at $40^{\circ}C$ for 10 Hz, 0.75 m/s, captured after 5 mins' vibration.

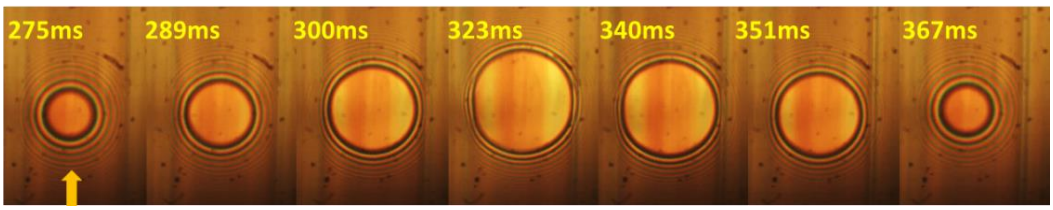

Figure 6.66 (c): Interferograms of RL2 grease at $40^{\circ}C$ for 10 Hz, 0.75 m/s, captured after 10 mins' vibration.

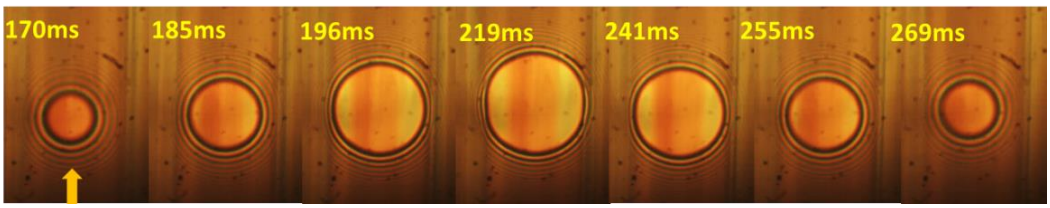

Figure 6.66 (d): Interferograms of RL2 grease at $40^{\circ}C$ for 10 Hz, 0.75 m/s, captured after 15 mins' vibration.

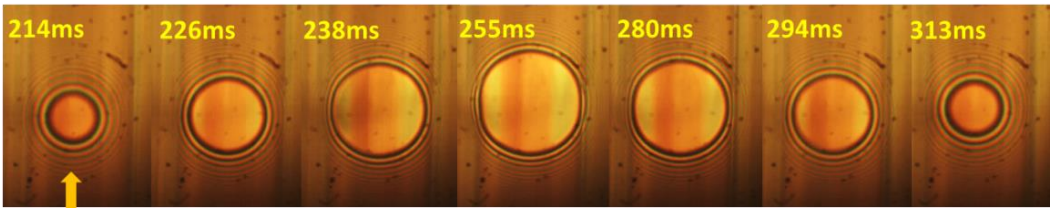

Figure 6.66 (e): Interferograms of RL2 grease at $40^{\circ}C$ for 10 Hz, 0.75 m/s, captured after 20 mins' vibration.

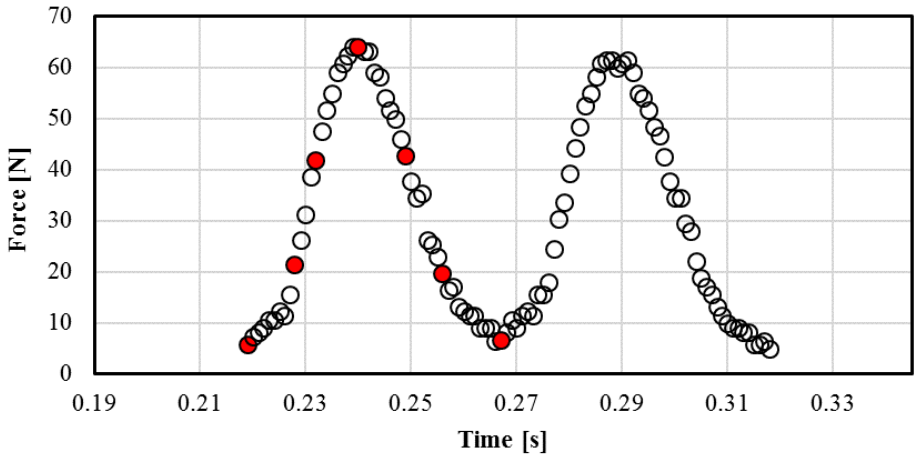

Figure 6.67 (a): Example of load variation, RL2 grease at $40^{\circ}C$, 20 Hz, 0.77m/s.

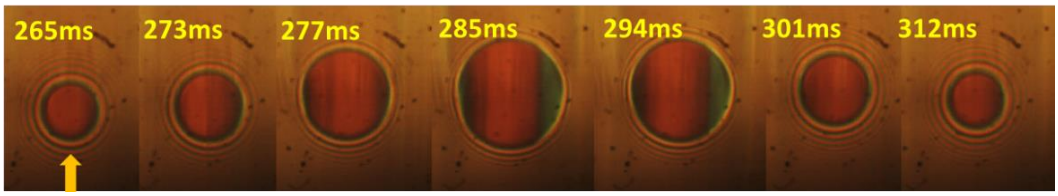

Figure 6.67 (b): Interferograms of RL2 grease at $40^{\circ}C$ for 20 Hz, 0.77 m/s, captured after 5 mins' vibration.

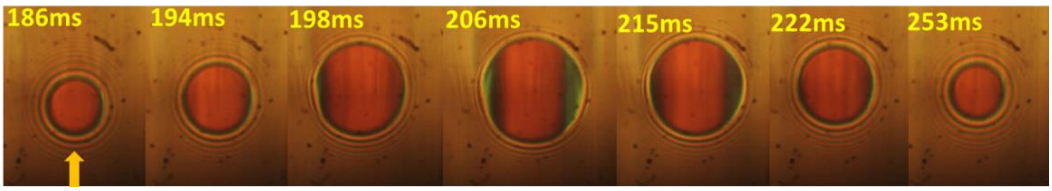

Figure 6.67 (c): Interferograms of RL2 grease at $40^{\circ}C$ for 20 Hz, 0.77 m/s, captured after 10 mins' vibration.

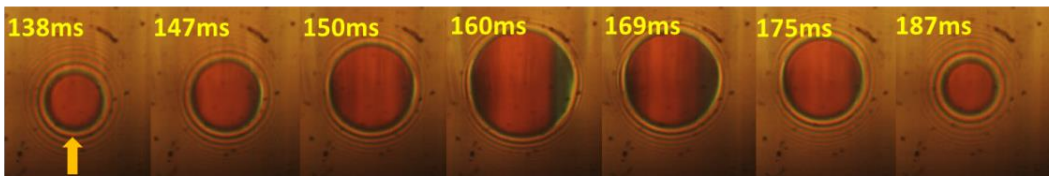

Figure 6.67 (d): Interferograms of RL2 grease at $40^{\circ}C$ for 20 Hz, 0.77 m/s, captured after 15 mins' vibration.

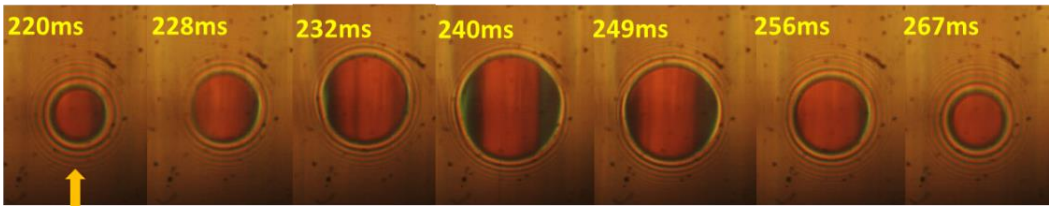

Figure 6.67 (e): Interferograms of RL2 grease at $40^{\circ}C$ for 20 Hz, 0.77 m/s, captured after 20 mins' vibration.

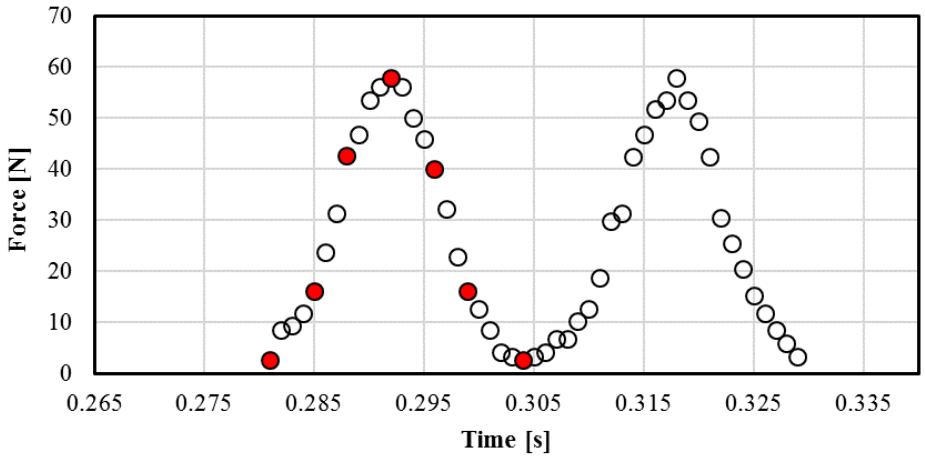

Figure 6.68 (a): Example of load variation, RL2 grease at $40^{\circ}C$, 40 Hz, 0.77 m/s

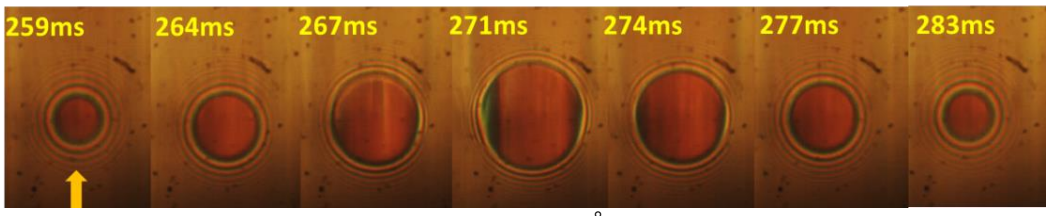

Figure 6.68 (b): Interferograms of RL2 grease at $40^{\circ}C$ for 40 Hz, 0.77 m/s, captured after 5 mins' vibration.

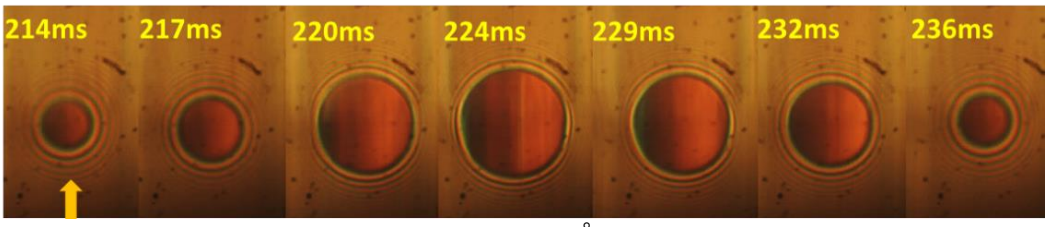

Figure 6.68 (c): Interferograms of RL2 grease at $40^{\circ}C$ for 40 Hz, 0.77 m/s, captured after 10 mins' vibration.

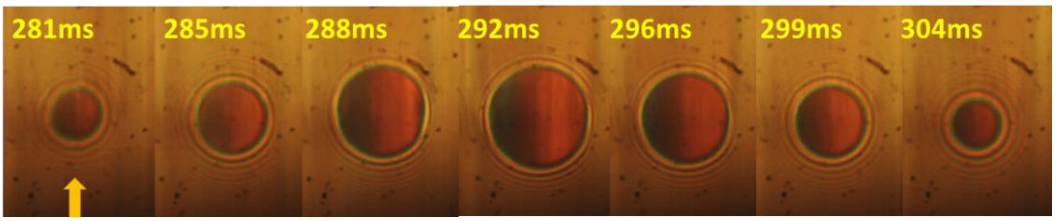

Figure 6.68 (d): Interferograms of RL2 grease at $40^{\circ}C$ for 40 Hz, 0.77 m/s, captured after 15 mins' vibration.

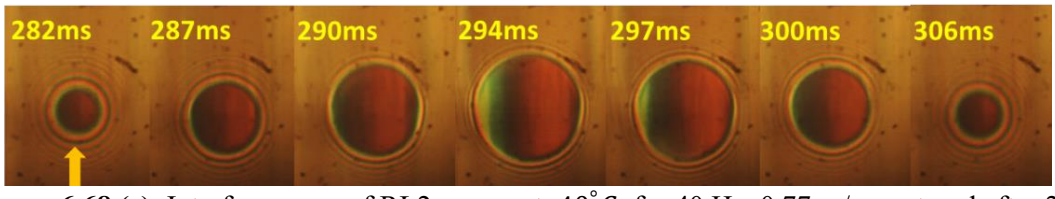

Figure 6.68 (e): Interferograms of RL2 grease at $40^{\circ}C$ for 40 Hz, 0.77 m/s, captured after 20 mins' vibration.

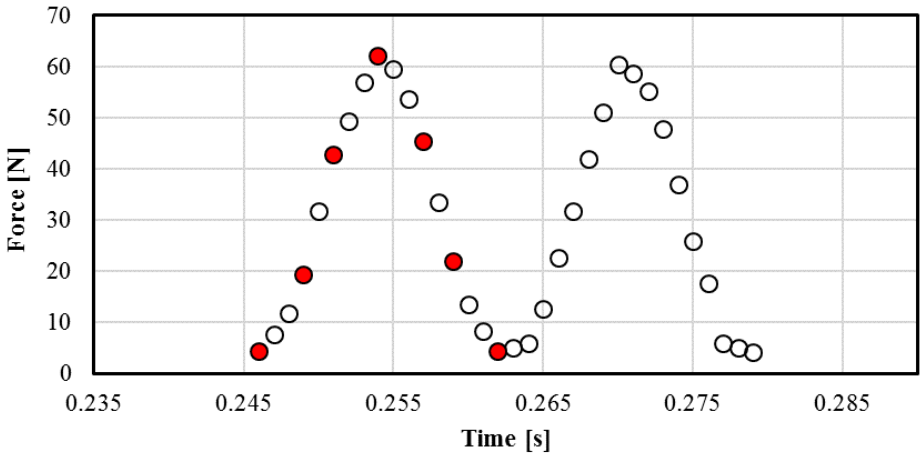

Figure 6.69 (a): Example of load variation, RL2 grease at $40^{\circ}C$, 60 Hz, 0.77 m/s.

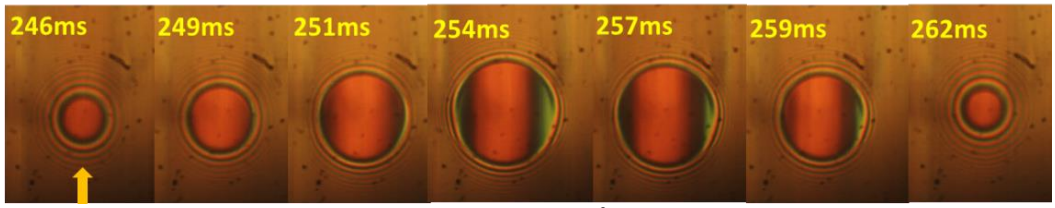

Figure 6.69 (b): Interferograms of RL2 grease at $40^{\circ}C$ for 60 Hz, 0.77 m/s, captured after 5 mins' vibration.

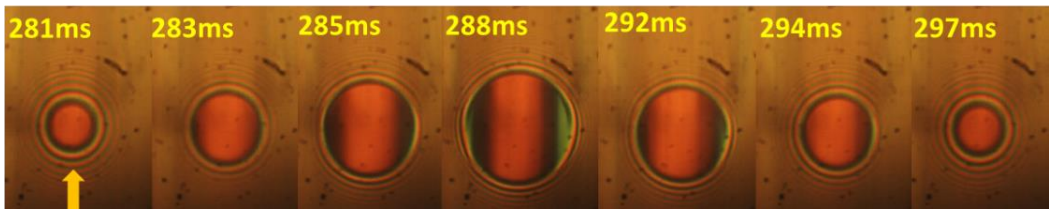

Figure 6.69 (c): Interferograms of RL2 grease at $40^{\circ}C$ for 60 Hz, 0.77 m/s, captured after 10 mins' vibration.

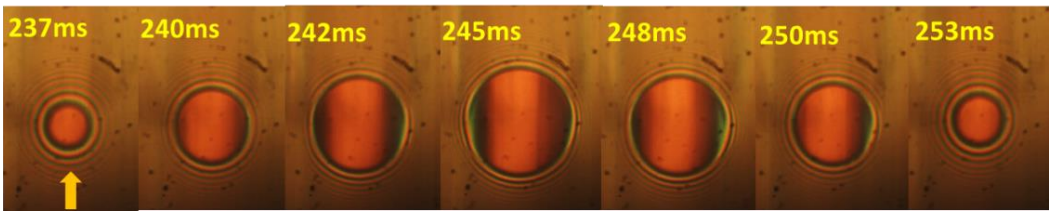

Figure 6.69 (d): Interferograms of RL2 grease at $40^{\circ}C$ for 60 Hz, 0.77 m/s, captured after 15 mins' vibration

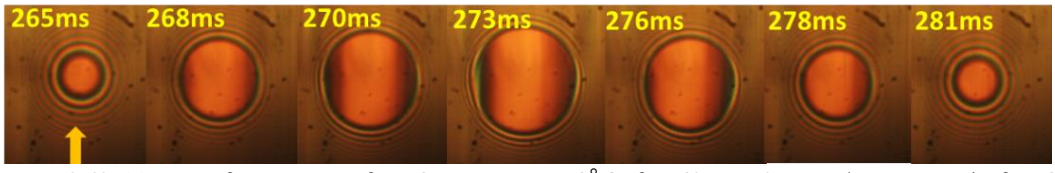

Figure 6.69 (e): Interferograms of RL2 grease at $40^{\circ}C$ for 60 Hz, 0.77 m/s, captured after 20 mins' vibration.

6.5 Conclusions

A detailed experimental work was designed and carried out in order to evaluate the behaviour of EHD contacts subjected to harmonic vibrations. The focus was on the effect of various working parameters such as frequency, load amplitude, entrainment speed, as well as on the properties of the lubricant.

It was found that in fully flooded, oil lubricated contacts, film thickness perturbations are formed in the inlet of the contact, during load increasing phase. These perturbations then travel through the contact at a speed which is not constant across the diameter of the contact. When the amplitude of the load is larger than the mean value of the cycle, film thickness perturbations are not frequency dependent, however in the reverse situation film perturbation occurs only at the largest two frequencies employed, that is 50 Hz and 100 Hz.

The entrainment speed plays also a role in the behaviour of the film, as it was noticed that perturbations of the film did not occur at large speeds. The viscosity of the lubricant has a similar effect with the film perturbation about 4.5 times the steady state film thickness, at low viscosity lubricants, and about 75 percent larger at high viscosity lubricants.

In case of contacts working in limited supply of lubricant in the inlet, it was observed that harmonic variation of load, normal to the surface of the contact helps replenish the inlet and recovery of the film thickness. The recovery was found to be proportional to the frequency of the load variation. For severely starved contacts, lubricated by grease, film recovery was observed, but this phenomenon was less pronounced. An analysis of these results including a theoretical modelling is included in the following chapter.

Chapter 7: Discussion

The behaviour of EHD films subjected to vibrations normal to the plane of the contact is influenced by two mechanisms: fluid entrainment and film squeeze. These mechanisms shape two phenomena which determine the lubricant film thickness:

- film's dynamic response,
- film's deviation from the normal EHD – film shape.

The first of these phenomena is dominated by the lubricant state and flow in the inlet of the contact, while the second is dominated by the flow of the fluid over the whole contact area and in the immediate vicinity of it. In the next subchapter, a simplified analysis of the dynamic response of the system was carried out to evaluate the behaviour of the EHD film.

7.1 Analysis of dynamic response of the EHD film

Quantitative evaluation of the damping of EHD contacts was not one of the initial objectives of this research, but the results obtained showed the opportunity to try a rather qualitative analysis. Figure 7.1 (a) shows a schematic of the contact and the vibrating masses.

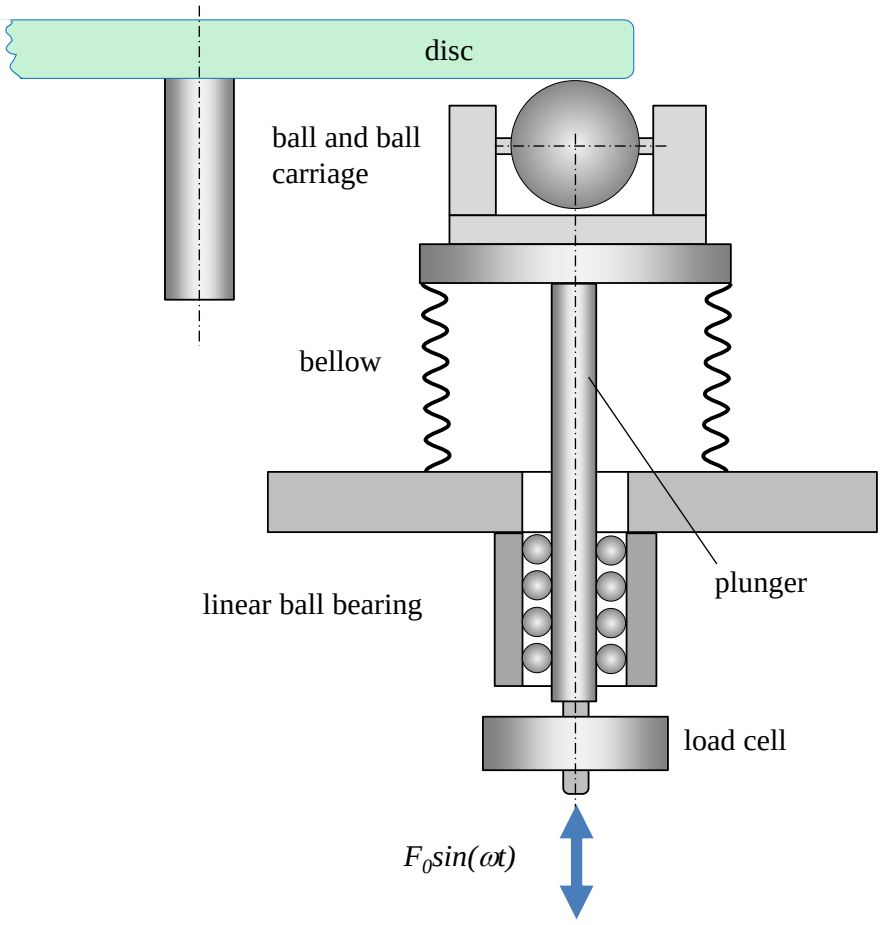

Figure 7.1 (a): Schematic of contact vibration system

The load cell records the variable force applied to the plunger and thus to the ball and the EHD contact. The stainless-steel bellow is intended to avoid any leakage of lubricant form the working chamber, but its construction makes it practically a linear spring. In figure 7.1 (b), the model of the vibrating system is shown.

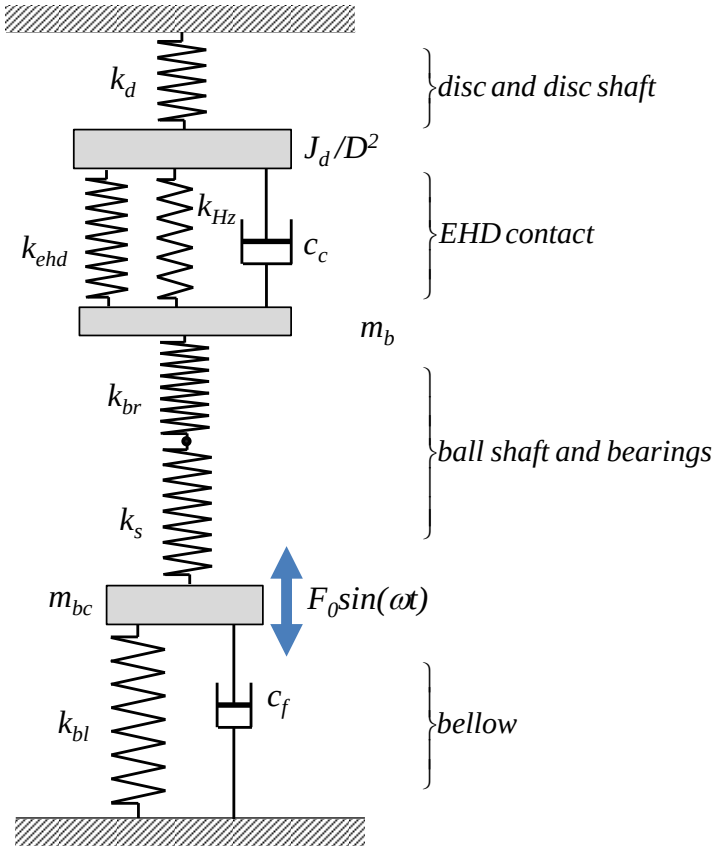

Figure 7.1 (b): Model of the vibrating system

The EHD contact acts as a spring and damper; its stiffness and damping coefficient are denoted with k_c and c_c respectively. The contact (as an elastic element) is connected to the oscillating mass of the ball via the shaft supporting the ball and the bearings supporting the ball shaft. The stiffness of these elements is denoted by k_s for the shaft and k_{br} for the bearings. The contact is connected to the fixed support through the disc which is considered a spring of constant k_d. The second mass of this system is that of the ball carriage and plunger denoted by m_{bc}. These in their turn are connected to the rigid support through the bellow seen as a spring of stiffness k_{bl}. There is also friction in the linear bearing supporting the plunger, represented here by the damper c_f. The model of the vibrating system shown in figure 7.1 (b) reveals that the contact belongs to a multi-degree of freedom, discrete system. This is a three-degree of freedom, forced vibration system with damping, which can be solved for the motion of the mass of the ball and disc, which are of interest. The stiffness of the dry Hertzian contact can be found from the relationship between the displacement of two distant points and the load [2]:

$$\delta = \left(\frac{9P^2}{16E^{*2}R} \right)^{1/3} \tag{7.1}$$

Obviously the EHD contact is a non-linear spring with the stiffness depending on the load. In order to find the stiffness, the displacement δ is differentiated with respect to the load P.

$$\frac{d\delta}{dP} = \left(\frac{9}{16E^{*2}R} \right)^{1/3} \frac{2P^{-1/3}}{3} \tag{7.2}$$

The inverse of this ratio is the stiffness of the dry Hertzian contact, that is:

$$k_{Hz} = \frac{dP}{d\delta} = \left(6E^{*2}RP\right)^{1/3} \tag{7.3}$$

This stiffness varies with load as seen in figure 7.2. After a sharp rise at lower loads, the gradient of the curve becomes smaller and the curve would eventually flatten out at much higher loads.

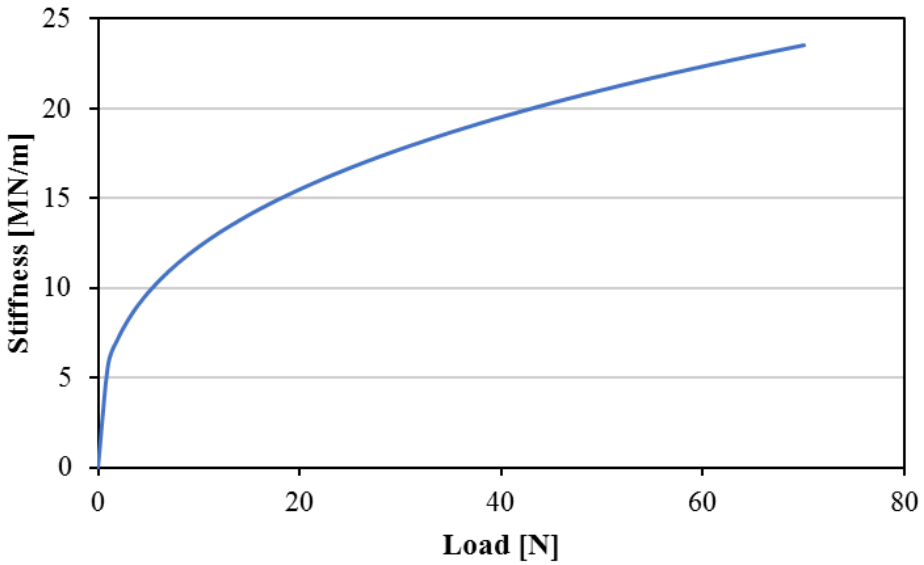

Figure 7.2: Stiffness of contact variation with load

This small change of the stiffness with load, at loads higher than about 4 N, prompts another assumption: the dry Hertzian contact can be considered as a linear spring, over the most part of the loading cycle. As seen in figure 7.3, the graph of the load versus displacement strengthens this assumption as it is obvious that the load variation is almost linear for most part of the curve.

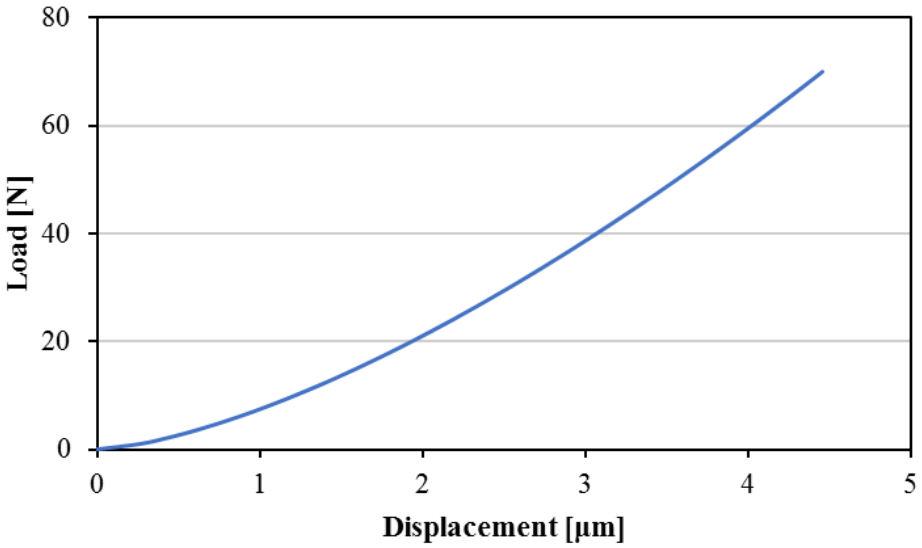

Figure 7.3: Load versus displacement curve

The EHD film also depends on the load so it too can be considered as a non – linear spring. In order to find the stiffness of this spring, the same method is applied. The central film thickness for a circular contact is given by the relationship:

$$\frac{h_c}{R_x}=2.69\overline{U}^{0.67}\overline{G}^{0.53}\overline{P}^{-0.067} \tag{7.4}$$

The factors in this relationship are those defined in Chapter 2, where $\overline{P}$ is the load factor in this case. Grouping all factors that do not depend of the load in one constant A, the film thickness becomes:

$$h=A\cdot P^{-2/30} \tag{7.5}$$

The derivative of film thickness with respect to load is:

$$\frac{\partial h}{\partial P}=-\frac{2}{30}A\cdot P^{-32/30} \tag{7.6}$$

The inverse of this ratio is the stiffness of the EHD film.

$$k_{EHD}=\frac{\partial P}{\partial h}=-\frac{15}{A}\cdot P^{32/30} \tag{7.7}$$

The variation of this stiffness with load is depicted in figure 7.4.

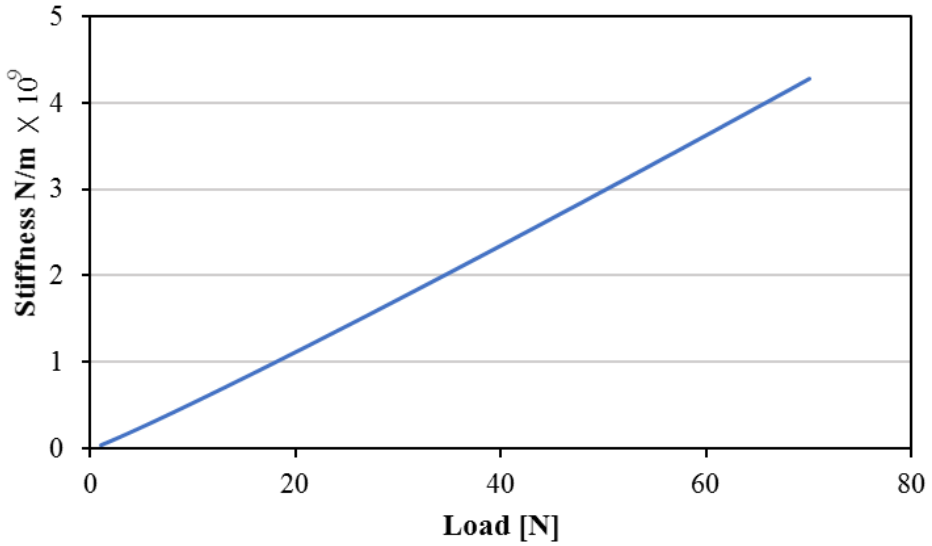

Figure 7.4: Stiffness of the EHD film

The stiffness of the dry contact and that of the EHD film are connected in series thus the combined stiffness is given by:

$$\frac{1}{k_c} = \frac{1}{k_{Hz}} + \frac{1}{k_{EHD}} \tag{7.8}$$

Comparing the values of stiffness in figures 7.2 and 7.4, it is seen that the stiffness of the film (k_{EHD}) is three orders of magnitude larger than that of the dry Hertzian contact (k_{Hz}), thus from equation (7.8) it is clear that the later dominates the stiffness of the whole EHD contact. It thus appears that the stiffness of the EHD contact (k_c) is equal to that of the Hertzian dry contact (k_{Hz}) and it can be assumed as a linear spring, which simplifies considerably the modelling of the system.

On the other hand, the damping constant of the EHD film (c_c) can also be assumed as non – linear and it is unknown at this stage. For the sake of simplicity of this analysis, it is further assumed that the damping is of viscous type, thus the motion – resisting force is proportional to the speed.

Denoting the diameter of the ball shaft by d_s, its cross-sectional moment of inertia by I and its length between supports by l, the shaft supporting the ball has a stiffness given by:

$$k_s = \frac{48EI}{l^3} = \frac{2.35619Ed_s^{\,4}}{l^3} = 2.676\times10^6\ N/m \tag{7.9}$$

There are three bearings supporting the ball shaft: one needle bearing on one side and two angular contact bearings on the other side, which means that the load on these bearings is half the contact load on each side. The stiffness of bearings depends of their dimensions, geometry and load. The needle bearing is much stiffer than the ball bearings because it has linear contacts with the ball shaft. On the other hand, load on each angular contact bearing is half the load acting on the needle bearing. Moreover, the angular contact bearings are fitted with preloading which increases their stiffness. A thorough calculation of the stiffness for these bearings is not needed, so it is considered that the combined stiffness of these bearings is 100×10^6 N/m [121-123], which is a reasonable assumption given values found in various sources. These bearings are springs connected in parallel thus their combined stiffness is the sum of each individual stiffness. Further on the bearings are connected in series with the shaft thus their combined stiffness is:

$$k_b = \left(\frac{1}{k_{br}} + \frac{1}{k_s} \right)^{-1} = 2.64\times10^6 \; N/m \tag{7.10}$$

The construction of the bellow makes it practically a linear spring with a stiffness (k_{bl}) of 8170 N/m according to the manufacturer.

On the other hand, the friction force acting in the linear bearing is equal to the friction force in the EHD contact times the friction coefficient in the linear bearing. The friction force in the EHD contact can be calculated as the normal load times the traction coefficient of the lubricant film. The later can be taken as the value at the limit of the linear part of the traction curve, that is about 0.06 for the lubricants used in these experiments. The friction coefficient in the linear ball bearing is about 0.001 – 0.0015. It follows that the maximum friction force in the linear bearing is:

$$F_f = F_0 \mu_{EHD} \mu_{bearing} = 0.00009 \, F_0 \tag{7.11}$$

Where F_0 is the amplitude of the variable load. Clearly this friction force, and together with the damping generated by it, can be neglected in comparison to the harmonic load applied to the contact.

Finally, the stiffness of the disc (k_d) is evaluated from the elastic deflection at the point of contact with the ball. Support arrangement of the disc is considered, as the schematic illustrated in figure 7.5.

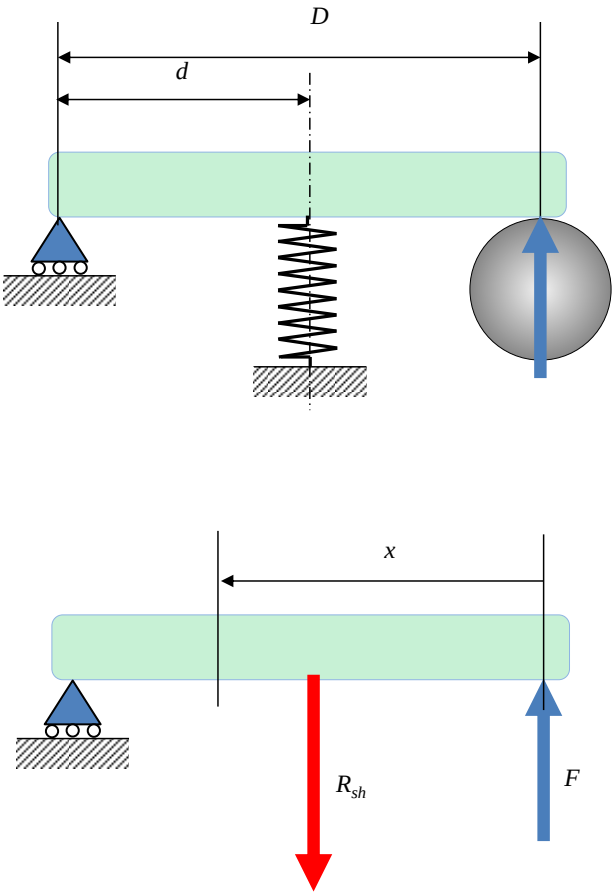

Figure 7.5: Statics of disc-shaft system

The shaft supporting the disc is basically subjected to tension deflecting under loading thus it can be treated as a linear spring with the stiffness given by EA/L, where E is the elastic modulus of the material of the shaft (steel), A is the cross-section area and L is the length.

The force generated in the shaft is determined straight forward from the static equilibrium equation of the disc, which gives $R_{sh} = FD/d$. The deflection, at the point of contact between disc and ball is derived using Castigliano's theorem.

$$v_d = \frac{1}{EI}\int M(x)\frac{\partial M}{\partial F}dx$$

The bending moment has to be evaluated in two sections;

for $x = 0$ to $(D\text{-}d)$ $\quad M(x) = Fx \quad\quad \frac{\partial M(x)}{\partial F} = x$

for $x = (D\text{-}d)$ to D $\quad M(x) = Fx - F\frac{D}{d}\left[x-(D-d)\right] \quad\quad \frac{\partial M(x)}{\partial F} = x - \frac{D}{d}\left[x-(D-d)\right]$

Performing the integration, the stiffness of the disc becomes:

$$k_d = \frac{F}{v_d} = EI\left\{\frac{D^3}{3} - \frac{2}{3}\frac{D^4}{d} + \frac{1}{3}\frac{D^5}{d^2} + D(D-d)\left[-\frac{D-d}{d} + \frac{2}{3}\frac{(D-d)}{d} + \right.\right.$$
$$\left.\left. + \frac{2D}{d} - 1 + \frac{D(D-d)}{3d^2} - \frac{D^2}{d^2} + \frac{D^3}{d^2(D-d)} - \frac{2D^2}{d(D-d)} + \frac{D}{D-d}\right]\right\}^{-1} \quad (7.12)$$

Introducing all numerical values, the stiffness of the disc (k_d) becomes 1.03×10^6 N/m

With the mechanical characteristics of the systems known, the equations of motion can be written in matrix form [124] as:

$$\begin{bmatrix} 1 & 0 & 0 & 0 & 0 & 0 \\ 0 & 1 & 0 & 0 & 0 & 0 \\ 0 & 0 & 1 & 0 & 0 & 0 \\ 0 & 0 & 0 & m_{bc} & 0 & 0 \\ 0 & 0 & 0 & 0 & m_b & 0 \\ 0 & 0 & 0 & 0 & 0 & J/D^2 \end{bmatrix} \frac{d}{dt} \begin{bmatrix} x_{bc} \\ x_b \\ x_d \\ \dot{x}_{bc} \\ \dot{x}_b \\ \dot{x}_d \end{bmatrix} + \begin{bmatrix} 0 & 0 & 0 & -1 & 0 & 0 \\ 0 & 0 & 0 & 0 & -1 & 0 \\ 0 & 0 & 0 & 0 & 0 & -1 \\ (k_{bl}+k_b) & -k_b & 0 & 0 & 0 & 0 \\ -k_b & (k_b+k_c) & -k_c & 0 & c_c & -c_c \\ 0 & -k_c & (k_c+k_d) & 0 & -c_c & c_c \end{bmatrix} \begin{bmatrix} x_{bc} \\ x_b \\ x_d \\ \dot{x}_{bc} \\ \dot{x}_b \\ \dot{x}_d \end{bmatrix} = \begin{bmatrix} 0 \\ 0 \\ 0 \\ 0 \\ F_0 \\ 0 \end{bmatrix} \cos\omega t \quad (7.13)$$

In this equation $\dot{x}_b$, $\dot{x}_{bc}$ and $\dot{x}_d$ are the velocities of the ball, ball carriage and disc respectively, while J is the moment of inertia of the disc about the fixed support shown in figure 7.1. This equation can be put in the following form:

$$\mathbf{M}\frac{d\mathbf{y}}{dt} + \mathbf{D}\mathbf{y} = \mathbf{f}\cos\omega t \quad (7.14)$$

where **M** is the mass matrix, **D** is the stiffness/damping matrix while **y** and **f** are the generalised displacement and force vectors. By using Euler's formula $\cos x = \left(e^{ix} + e^{-ix}\right)/2$ this can be further transformed into:

$$\mathbf{M}\frac{d\mathbf{y}}{dt} + \mathbf{D}\mathbf{y} = \mathbf{f}\left\{e^{i\omega t} + e^{-i\omega t}\right\}/2 \quad (7.15)$$

A solution of this equation of the form shown in equation 7.16 is tried.

$$\mathbf{y} = \left\{\mathbf{Y}e^{i\omega t} + \overline{\mathbf{Y}}e^{-i\omega t}\right\}/2 \quad (7.16)$$

$\mathbf{Y}$ and $\overline{\mathbf{Y}}$ are found by solving the equations:

$$[i\omega\mathbf{M}+\mathbf{D}]\mathbf{Y}=\mathbf{f} \qquad \text{and} \qquad [-i\omega\mathbf{M}+\mathbf{D}]\overline{\mathbf{Y}}=\mathbf{f}$$

These equations are easily solved using a simple MATLAB routine. Finally, the displacement of the ball and the disc are given by:

$$x_b=\sqrt{Y_b\overline{Y}_b} \tag{7.17}$$

$$x_d=\sqrt{Y_d\overline{Y}_d} \tag{7.18}$$

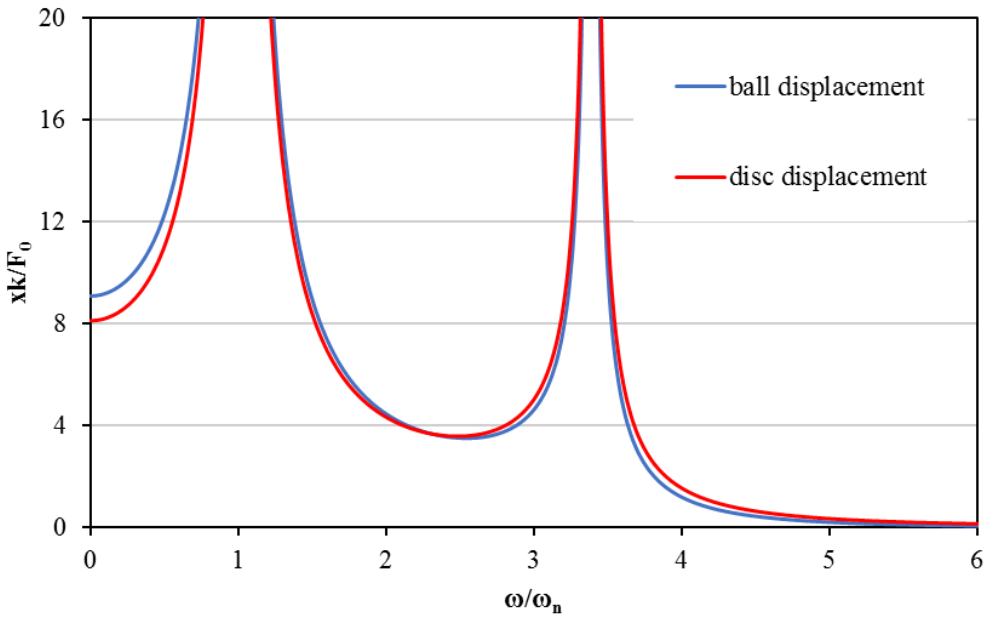

Figure 7.6 (a): Displacement of ball and disc as a function of frequency

The normalised displacements of the ball and the disc which are of interest here are shown in figure 7.6 (a). The first mode for the oscillations of the ball and disc is at 2140 Hz and the second is at 7270 Hz. Obviously, these are much larger than the frequency of variation of the force employed in these tests. The absolute values of the displacement of the ball and disc are of no real practical interest, but the difference between them it is. The variation of this difference is shown in figure 7.6 (b), for frequencies around the first mode, which are more relevant in any applications.

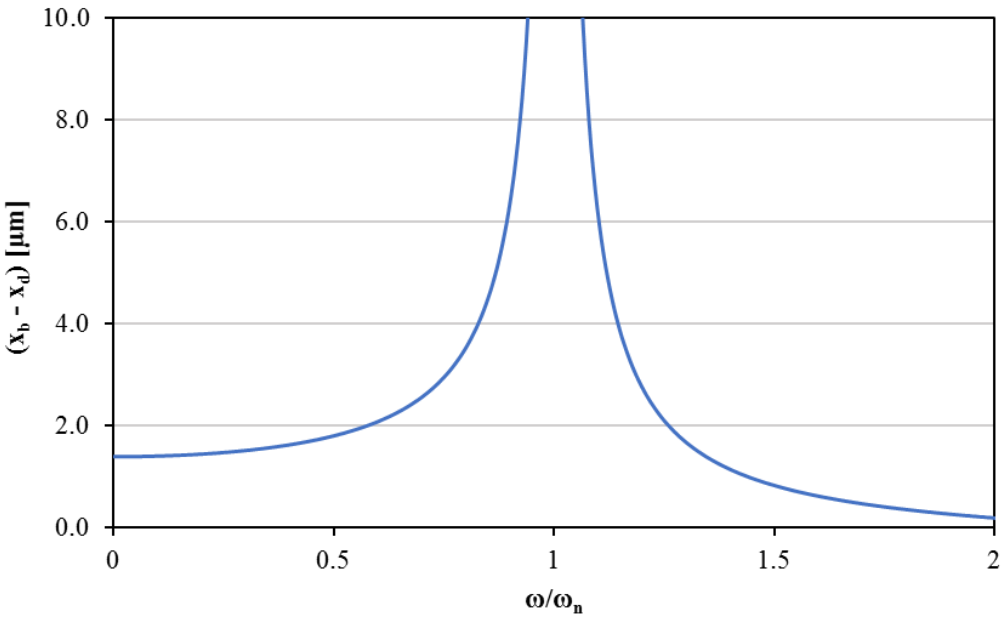

Figure 7.6 (b): Displacement of ball relative to disc

The displacement of the ball relative to the disc is shown in real values instead of normalised ones. This gives a better idea of how realistic this simulation is. The relative displacement is in fact the absolute approach of ball and disc, that is the maximum, cumulative deflection of both surfaces, given by Hertz's theory. It can be seen that the value, 1.39 µm, at the largest frequency of the test that is 100 Hz, is remarkably close to the amplitude resulted from Hertz's theory, which is 1.67 µm.

The damping constant used in the above calculations varied between 0.01 Ns/m and 314 Ns/m, but the results show that at least at lower frequencies the displacement of the masses is insensitive to this parameter.

There are other observations which can be extracted from this analysis. If the disc is made rigid, then the natural frequencies of the system shift toward larger values. For example, the first mode changes from 2140 Hz to 3600 Hz. The degree of freedom of the system reduces by one in this case. For a two – degree of freedom the system's response changes with the damping constant, but only at larger frequencies. This is shown in figure 7.7, where the response of a two – degree of freedom is shown. As seen, the values of the damping constant change the response at frequencies around the second mode. This dynamic analysis can be used to evaluate the damping constant of the EHD films. By attaching a large mass to the ball carriage, the natural frequency of the system can be lowered to values around 70 Hz - 80 Hz, which is within the range conveniently covered by the current optical system. Subsequently measuring the lubricant film thickness over a sweep of frequencies, encompassing the natural system, the damping characteristics of the EHD film can be evaluated by fitting the model to the experimental values.

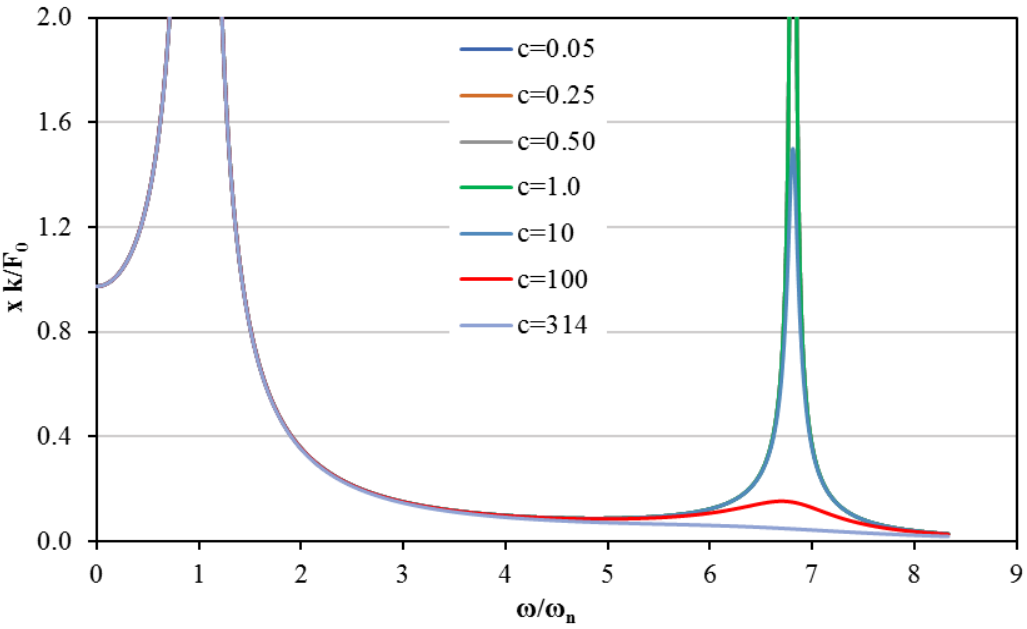

Figure 7.7: Response of the system as a function to frequency

7.2 EHD films under cyclic load variation; experimental observations

In the previous chapter, many graphs of the load variation cycle were shown. Before an analysis of the effect of various parameters upon the behaviour of EHD films subjected to vibrations take place, a distinction should be made between two sets of results. In some tests, the displacement amplitude of the vibration of the ball did not result into a complete separation of the ball and disc surfaces. In this case the load variation form was a sinusoid. In others the amplitude was large enough to completely separate the contact.

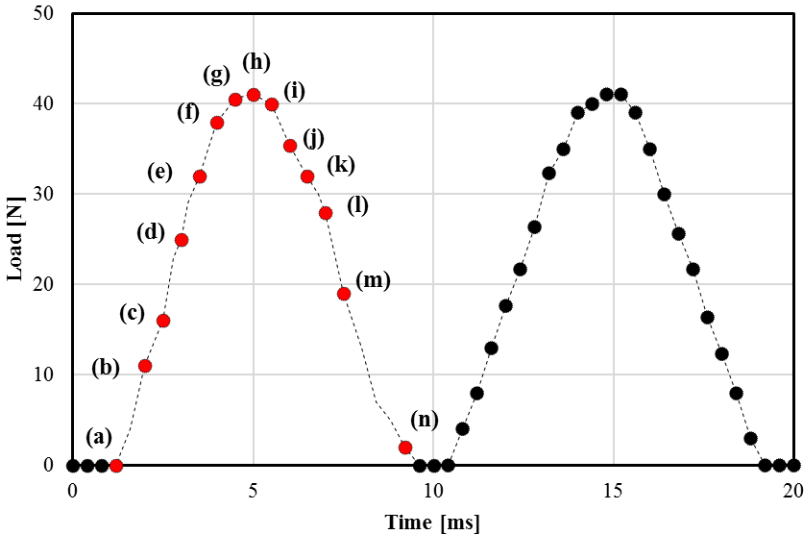

Figure 7.8: Forced vibration load curve, 100 Hz, 0.05 m/s, PAO 40, ambient temperature.

In this case, the load applied to the contact was not a full sinusoid but a truncated one, as seen in figure 7.8, which shows a forced sinusoidal vertical vibration load curve of two vibration cycles at a frequency of 100 Hz. The initial load applied to the contact is 0 N and the maximum applied load is 41N ($p_0 = 0.65\ GPa$). As seen for about three milliseconds, at the bottom of the load variation curve, the load stays at zero value. This implies that in those tests the load was applied with impact and the effect of parameters such as frequency or load amplitude was less important; this is because it was documented before that impact loading even on a static, lubricated contact generates a fluid entrapment due to the squeeze effect. Impact loading was not sought in these experiments, but it happened at the largest frequency and it was very difficult to control. The way it was dealt with was by gradually applying a constant load (also called preloading in this thesis) such that the minimum load is as close as possible to zero. As this load adjustment was done while the load oscillated at large frequency, it was difficult to guarantee a perfect sinusoidal pulsating cycle. For this reason, some of the load variation curves show a flat region at zero load.

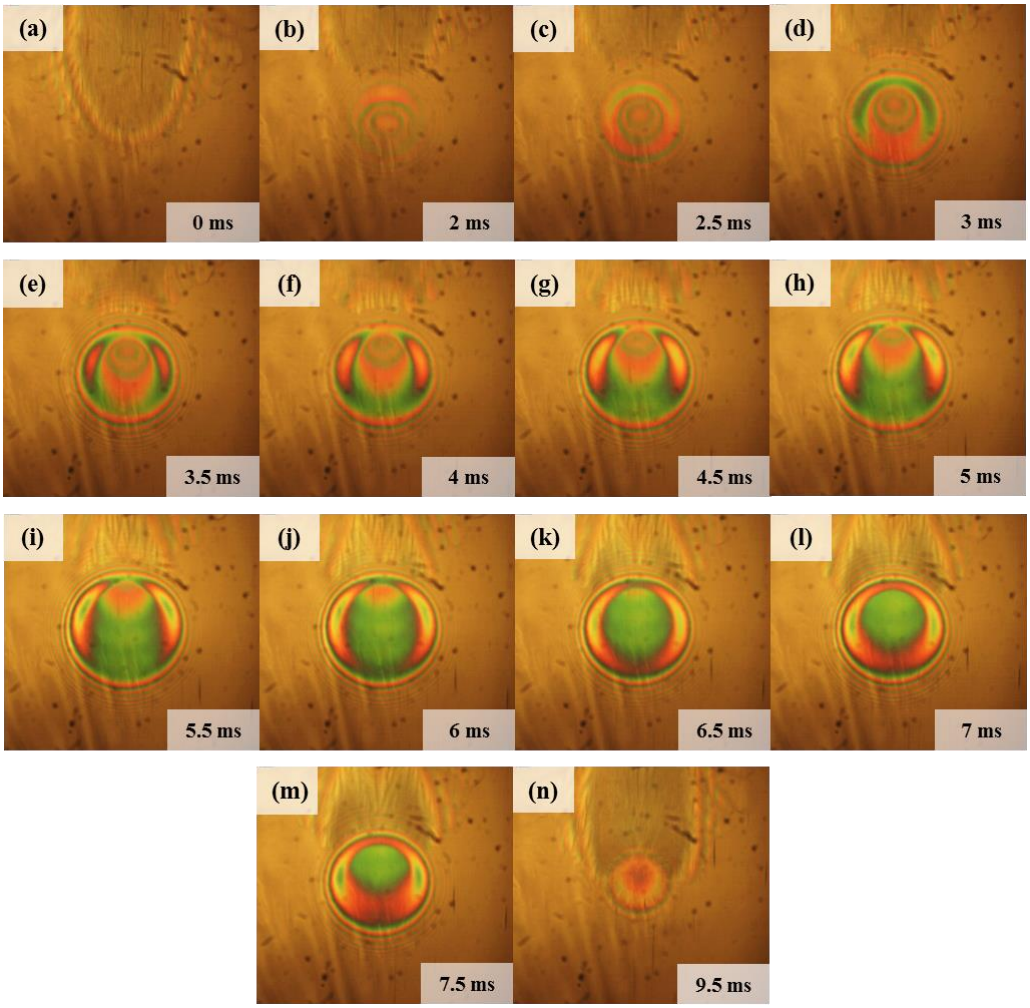

Figure 7.9: EHD contact in sinusoidal load cycle, 100 Hz, 0.05 m/s, PAO 40, ambient temperature.

The coloured interferograms shown in figure 7.9 are corresponding to the red dots (a) – (n) in the loading cycle from figure 7.8. The entrainment speed in these tests is 0.05 m/s and the direction of entraining motion is from the bottom to the top. The sudden increase of the load in the loading phase of the vibration cycle makes the contact size increase nearly four times over the first two millisecond interval and produce a significant perturbation in the film thickness. This film perturbation appears as a dimple as observed in figures 7.9(b, c). This phenomenon is similar to that found in [114] under static loading condition. Due to the continuity of flow and the fact that the lubricant flow is predominately Couette, after formation, it is expected that the film perturbation travels through the EHD contact at the rolling speed of the surfaces as reported in [115].

These images were converted into film thickness at various points over the contact area. In figures 7.10(b to n) film thickness profiles along the rolling direction are shown together with the corresponding images. The boundaries of the contact are also shown with broken lines. Yellow arrow with broken line is indicating both the direction of the entraining motion and the direction of film thickness profile taken from. At the beginning of the load increasing phase of the vibration cycle, the perturbed film stays in the centre of the contact region for a short period of about 0.5 ms. This is because the contact size increasing rate at 100 Hz is larger than the lubricant entraining speed at 0.05 m/s, thus the contact expands at a speed larger than the perturbation travelling speed.

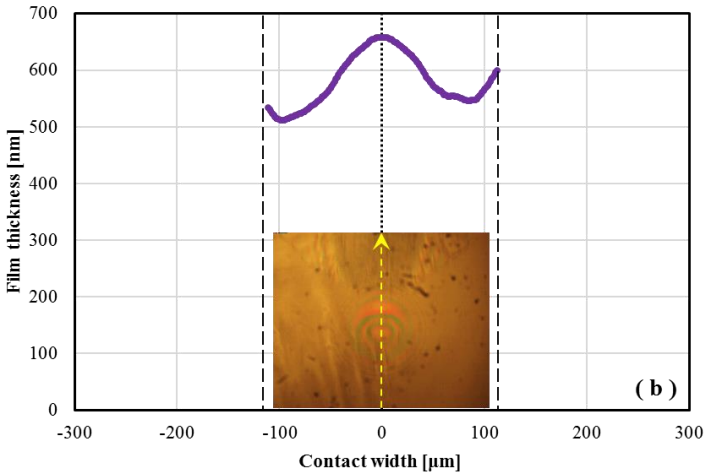

Figure 7.10(b): Film thickness profile along the entraining direction at 100 Hz, 0.05 m/s, 2 ms within vibration cycle.

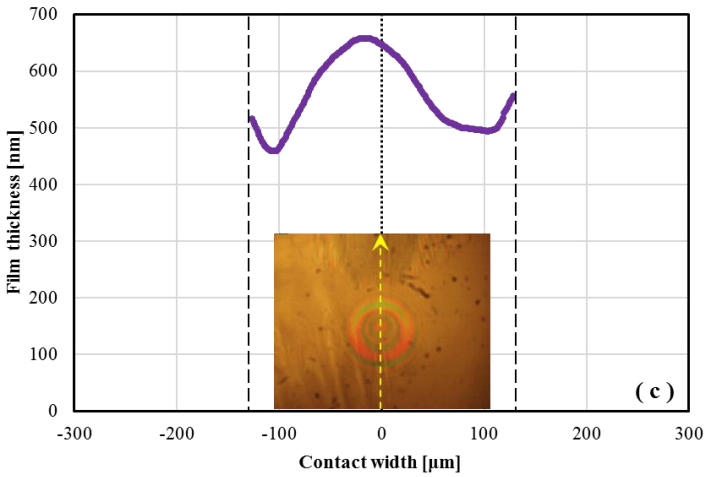

Figure 7.10(c): Film thickness profile along the entraining direction at 100 Hz, 0.05 m/s, 2.5 ms within vibration cycle.

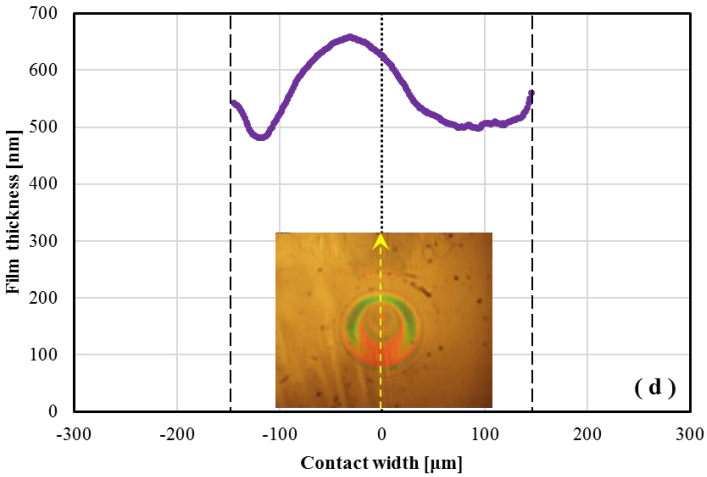

Figure 7.10(d): Film thickness profile along the entraining direction at 100 Hz, 0.05 m/s, 3 ms within vibration cycle.

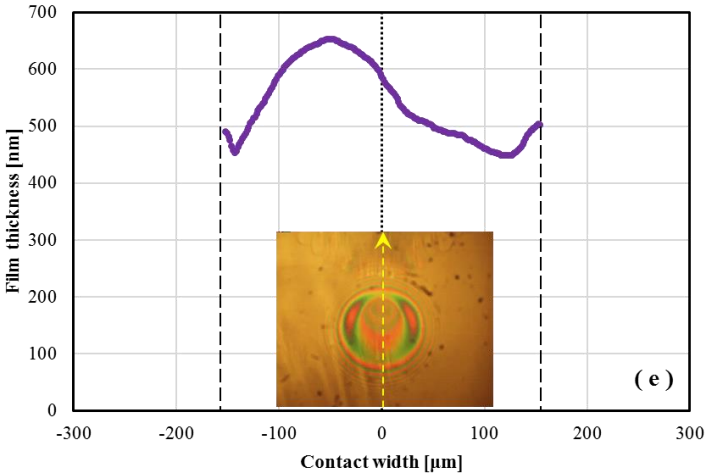

Figure 7.10(e): Film thickness profile along the entraining direction at 100 Hz, 0.05 m/s, 3.5 ms within vibration cycle.

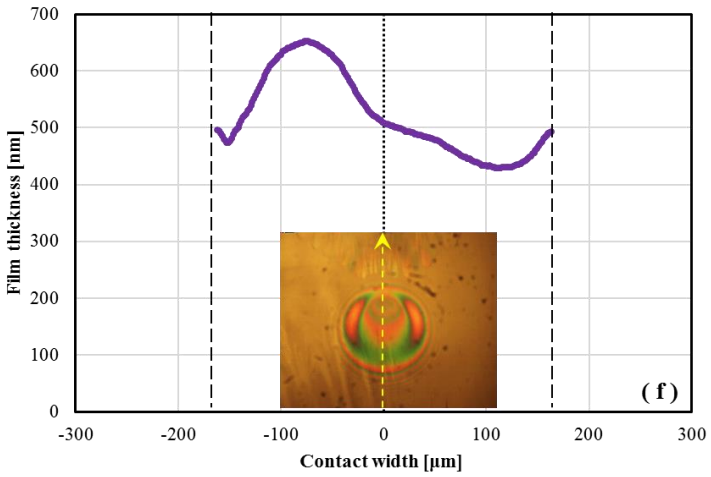

Figure 7.10(f): Film thickness profile along the entraining direction at 100 Hz, 0.05 m/s, 4 ms within vibration cycle.

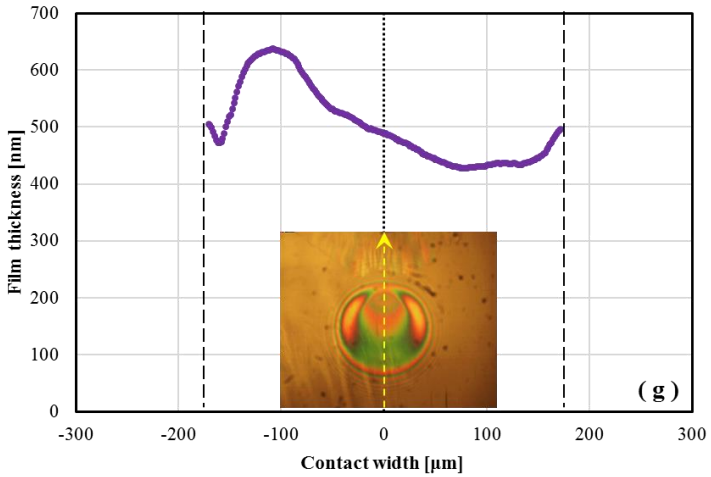

Figure 7.10(g): Film thickness profile along the entraining direction at 100 Hz, 0.05 m/s, 4.5 ms within vibration cycle.

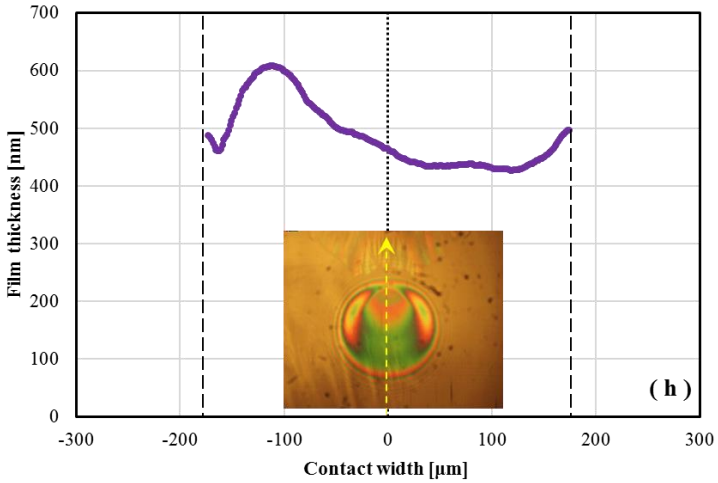

Figure 7.10(h): Film thickness profile along the entraining direction at 100 Hz, 0.05 m/s, 5 ms within vibration cycle.

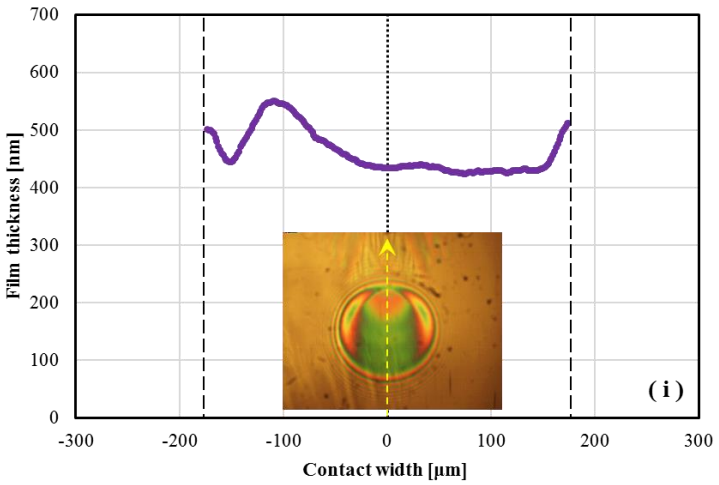

Figure 7.10(i): Film thickness profile along the entraining direction at 100 Hz, 0.05 m/s, 5.5 ms within vibration cycle.

In figure 7.10 (i), the central part of the perturbation has already left the contact, however the continuously increasing of the load further expands of the contact area and it creates new perturbations in the inlet which propagate through the contact. They appear as waviness in the film thickness profile.

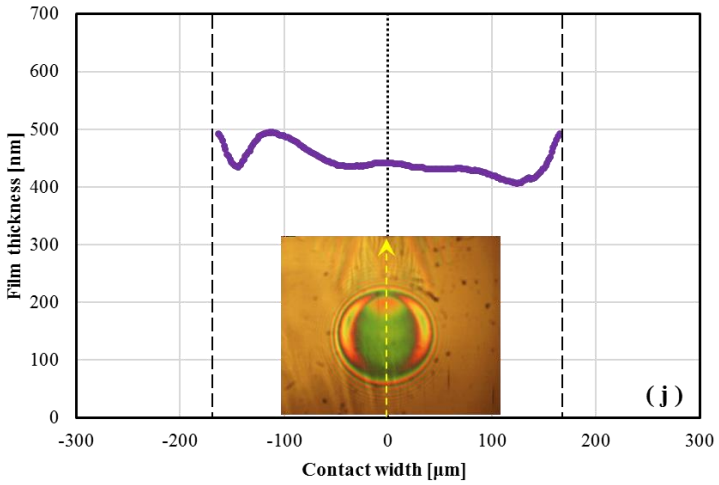

Figure 7.10(j): Film thickness profile along the entraining direction at 100 Hz, 0.05 m/s, 6 ms within vibration cycle.

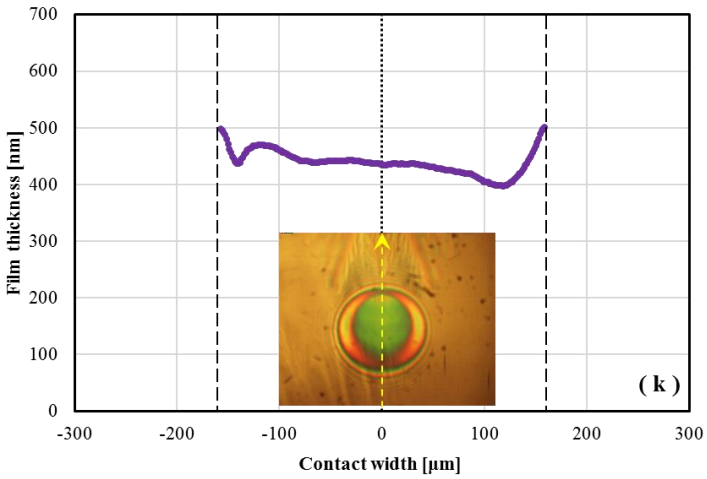

Figure 7.10(k): Film thickness profile along the entraining direction at 100 Hz, 0.05 m/s, 6.5 ms within vibration cycle.

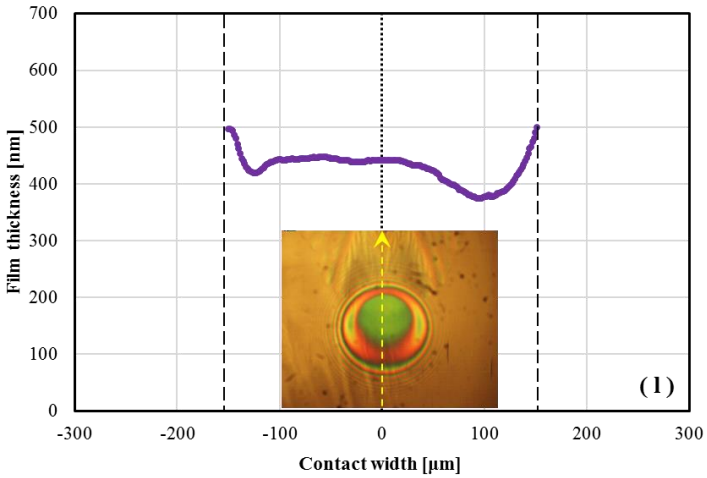

Figure 7.10(l): Film thickness profile along the entraining direction at 100 Hz, 0.05 m/s, 7 ms within vibration cycle.

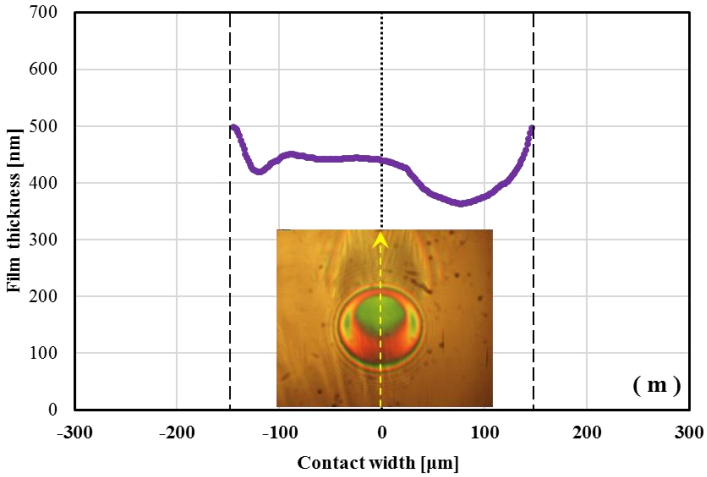

Figure 7.10(m): Film thickness profile along the entraining direction at 100 Hz, 0.05 m/s, 7.5ms within vibration cycle.

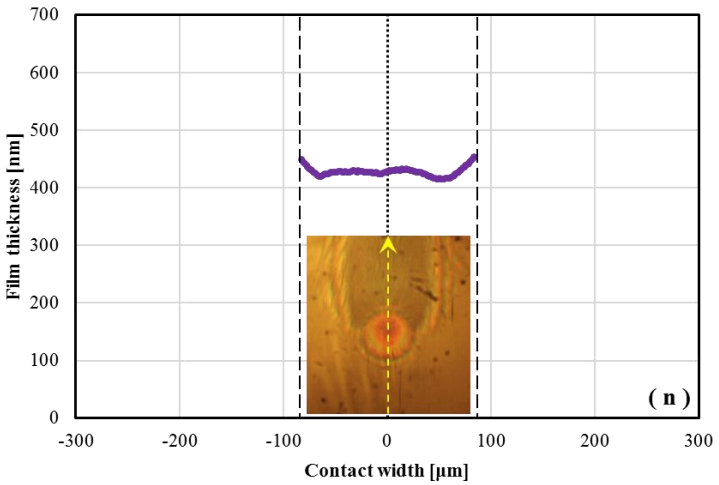

Figure 7.10(n): Film thickness profile along the entraining direction at 100 Hz, 0.05 m/s, 9.5 ms within vibration cycle.

The magnitude of maximum perturbed film thickness in the loading phase of vibration cycle is 658 nm, as shown in figure 7.10(b), which is about 71 percent greater than the film thickness under steady state condition. This value of the film thickness is maintained until 4.5 ms within the vibration cycle as showed in figure 7.10(g). It starts to decrease to 608 nm when perturbed film entering the region near the exit constriction of the contact, as shown in figure 7.10(h). The local film thickness perturbation observed in figure 7.10(i) is found to be about 12 nm. As the load continues to decrease, which leads further decreasing the size of contact region. As a result, film thickness at the contact inlet periphery is reduced, although part of the perturbed film thickness is kept inside the contact, seen in figure 7.10(j) to (m). Finally, the film thickness drops back to 424 nm at the end of this vibration cycle, which is nearly the steady state film thickness under the corresponding load.

Analysing the film profiles between 2 ms and 5 ms (figures 7.10(b) to 7.10(h)), it is seen that the perturbation initially forms in the centre of the contact and it reaches the exit constriction in about 3 milliseconds. In this time interval, the perturbation travels over a distance of about 100 micrometres. This means that the speed at which the perturbation travels is around 33.3 mm/s which evidently is smaller than the entrainment speed of 50 mm/s. As 33.3 mm/s is the absolute velocity (v_a, the one measured) and 50 mm/s is the transport velocity (v_{tr}, entrainment velocity of contact) it follows that the velocity of the perturbation relative to the contact is:

$$v_r = v_a - v_{tr} = 33.3 - 50 = -16.6 \ mm/s \qquad (7.19)$$

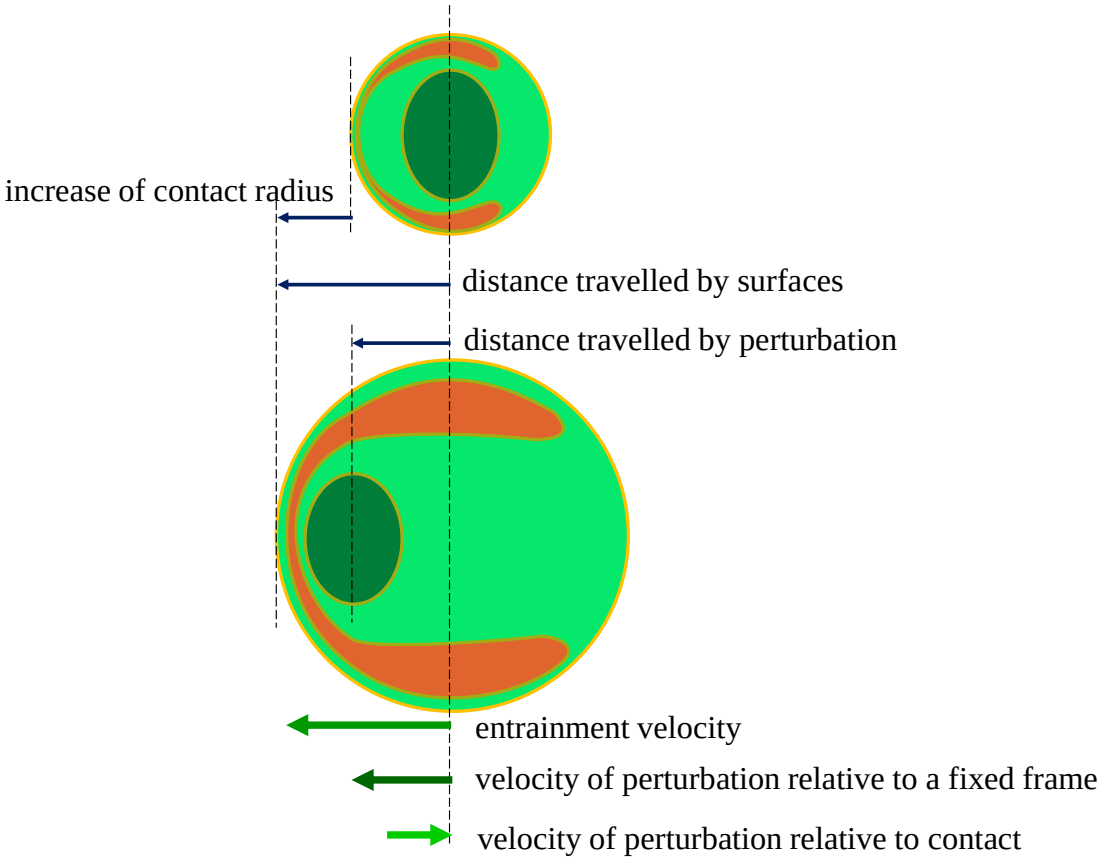

Figure 7.11: Schematic of displacement of film perturbation

The minus sign in Eq. 7.19 means that the perturbation moves relative to the contact in the direction opposite to the entrainment speed. Indeed, the exist of the contact moves away from the perturbation as the contact expands quickly. Multiplying the relative velocity by the time considered gives the increase of the radius of the contact that is 50 micrometres. From figure 7.10 (h), it can be seen that indeed, this is the increase of the radius of the contact between 2 milliseconds and 5 milliseconds within the cycle.

7.3 EHD films under cyclic load variation; theoretical modeling

The formation of the EHD film is a complex phenomenon. Combining entrainment with squeeze makes it even more complex and a quantitative analytical solution is not possible. Numerical solutions exist, but they are out of the scope of this thesis. It is possible, though to make a qualitative evaluation of the effect of the load variation by observing that the contact dimension increases, during load increasing phase is somehow equivalent in the inlet, with an increase of the entrainment velocity.

The central film thickness in a circular contact like the one studied here can be predicted by the well – known Hamrock & Dowson equation 2.53 and equation 2.54, given in Chapter 2. Written in terms of the load, the central film thickness becomes:

$$h_c = A \cdot u^{0.67} P^{-0.067} \tag{7.20}$$

where u is the entrainment speed, P is the load and A is a factor which does not depend of the speed or load. This can be further written as:

$$h_c = A \cdot u^{2/3} P^{-2/30} \tag{7.21}$$

The load varies according to a sine law as:

$$P(t) = P_0(1 + \sin \omega t) \tag{7.22}$$

With P_0 the amplitude and ω the circular frequency of the load cycle. As the load increases, the contact radius also increases, which is equivalent with an increase of the entrainment speed as the contact edge moves in opposite direction to the entrainment. This implies that the entrainment speed becomes:

$$u = u_0 + \frac{da}{dt} \tag{7.23}$$

where u_0 is the absolute velocity of the surfaces of the ball and disc and da/dt is the relative velocity that is speed of the change of the contact radius. Introducing (7.23) into (7.21), the transient film thickness becomes:

$$h(t) = A \cdot \left(u_0 + \frac{da}{dt}\right)^{2/3} P^{-2/30} \tag{7.24}$$

By extracting u_0 as a common factor this relationship yields:

$$h(t) = A \cdot u_0^{2/3} \left(1 + \frac{1}{u_0}\frac{da}{dt}\right)^{2/3} P^{-2/30} \tag{7.25}$$

At the same time the radius of the Hertzian, circular contact, which can be assumed equal to the EHD contact radius, is given by [2]:

$$a = \left(\frac{3R}{4E^*}\right)^{1/3} P^{1/3} \tag{7.26}$$

The variation of the radius with respect to time can be derived after introducing equation 7.22 into 7.26, given the fact that the load is the only parameter which varies with time:

$$\frac{da}{dt}=\frac{da}{dP}\frac{dP}{dt}=\frac{1}{3}\left(\frac{3R}{4E^*}\right)^{1/3}P^{-2/3}P_0\omega\cos\omega t=\left(\frac{RP_0}{36E^*}\right)^{1/3}\frac{\omega\cos\omega t}{(1+\sin\omega t)^{2/3}} \qquad (7.27)$$

Introducing (7.27) into equation (7.25) yields:

$$h(t)=A\cdot u_0^{2/3}\left(1+\frac{1}{u_0}\left(\frac{RP_0}{36E^*}\right)^{1/3}\frac{\omega\cos\omega t}{(1+\sin\omega t)^{2/3}}\right)^{2/3}P^{-2/30} \qquad (7.28)$$

According to (7.21) the term $Au_0^{2/3}P^{-2/30}$ is the steady state film thickness corresponding to the static application of the load and is denoted by h_{st}. With this notation, the ratio of the transient film thickness to the steady state film thicknesses becomes:

$$\frac{h(t)}{h_{st}}=\left[1+\frac{1}{u_0}\left(\frac{RP_0}{36E^*}\right)^{1/3}\frac{\omega\cos\omega t}{(1+\sin\omega t)^{2/3}}\right]^{2/3} \qquad (7.29)$$

The variation of this ratio, together with the normalized load (current load/ maximum load) as a function of non – dimensional time (time/period of load cycle) is shown in figure 7.12. The parameters of this simulation are: frequency 100 Hz, load variation amplitude 20.5 N, entrainment speed 0.05 m/s. This graph shows that at the beginning of the load – increasing phase the transient film thickness is more than two times larger than the theoretical film thickness. As the load increases towards its maximum value, the transient film thickness tends towards the steady state value.

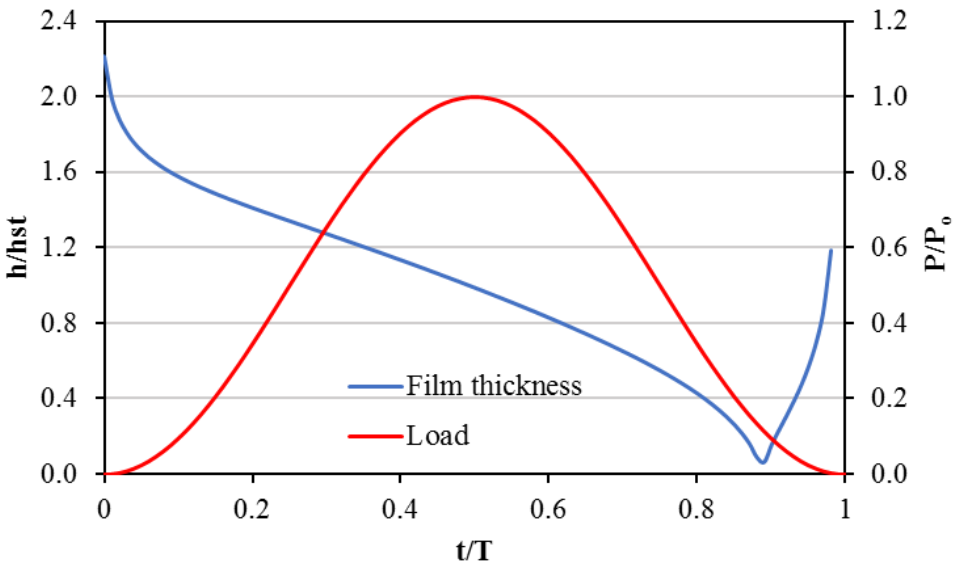

Figure 7.12: Ratio of transient film thickness and steady state film thickness at 100 Hz

During the load decreasing phase, the speed of contact size change becomes negative and continues to increase until equals, in magnitude, the entrainment speed. At this point, theoretically there is not entrainment mechanism and the film thickness is zero, which for the data simulated here it happens at about ninety percent of the period, as seen in the diagram. After this point, the speed of change of contact radius becomes increasingly greater than the entrainment speed thus theoretically the film thickness starts to increase again, but with the entrainment in opposite direction. The squeeze of the lubricant film prevents the film thickness to vanish so in experiments the film thickness does not become zero, however it is believed that the waves in the film thickness observed in figure 7.11(i) are due to this phenomenon.

An obvious question can be asked for the variation of the film thickness over the whole cycle: why are the values of the film thickness at the beginning and the end of the cycle not equal? The answer is that they are, but because they are infinite so that they cannot be shown in the graph. At the beginning of the cycle, the load is zero and obviously in this case Dowson and Hamrock equation predicts infinite film, or rather no film. The case when the minimum load in vibration cycle is not zero will be treated in a later subchapter.

This analysis is evidently simplified and does not take into account the squeeze effect and the time of passage of the lubricant through the contact, however it is able to explain, at least partially the behaviour of the film under cyclically variable loading.

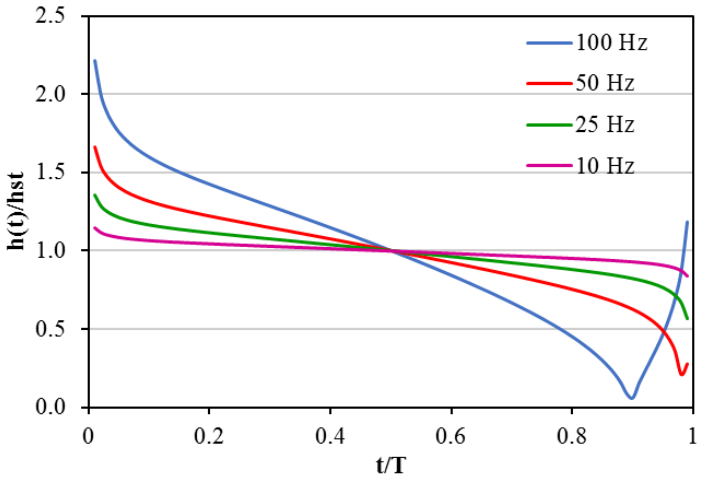

Figure 7.13: The effect of frequency upon transient film thickness

The effect of some working parameters can be evaluated from relationship (7.29). The frequency increases the transient effect as shown in figure 7.13, where four frequencies used in these experiments are compared. It is obvious that at lower frequencies the film thickness is almost equal to the steady state value over the whole vibration cycle, while at the largest frequency employed in these tests, 100 Hz, the transient formula predicts a film thickness 2.3 times larger than steady state at the beginning of the vibration cycle.

Another parameter which strongly influences the transient behaviour of EHD films is the entrainment speed of the contact. This effect is shown in figure 7.14 where the frequency was kept constant at 100 Hz and the entrainment speed changes as seen. Is it obvious that an increase of entrainment speed is equivalent to a decrease of frequency in the same proportion.

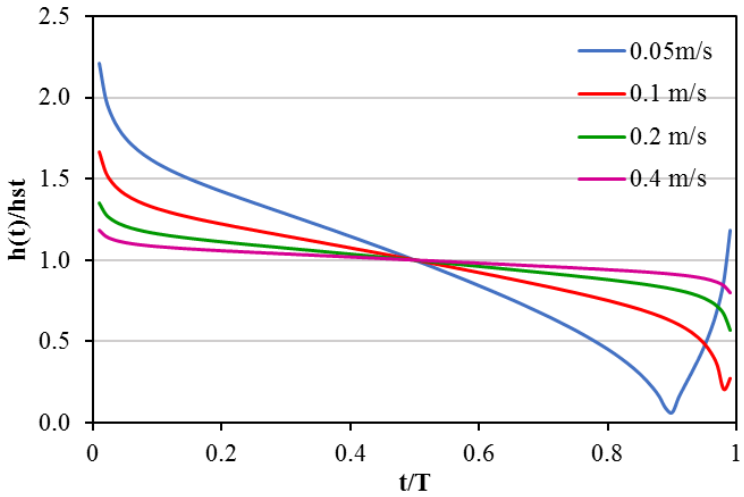

Figure 7.14: The effect of entrainment speed upon transient film thickness

Finally, the other parameter which influences the film thickness is the load. Figure 7.15 shows this effect for a contact running at the same frequency and speed. It is known that the effect of the load upon the steady state film thickness is almost negligible, in comparison to the effect of speed for example, however as seen in figure 7.15 in case of transient films this parameter influences the film thickness as strongly as the entrainment speed. This is because by keeping the frequency constant, the change of the amplitude of the load is equivalent to a more rapid variation of contact dimensions, thus the entrainment speed increases, according to equation (7.27).

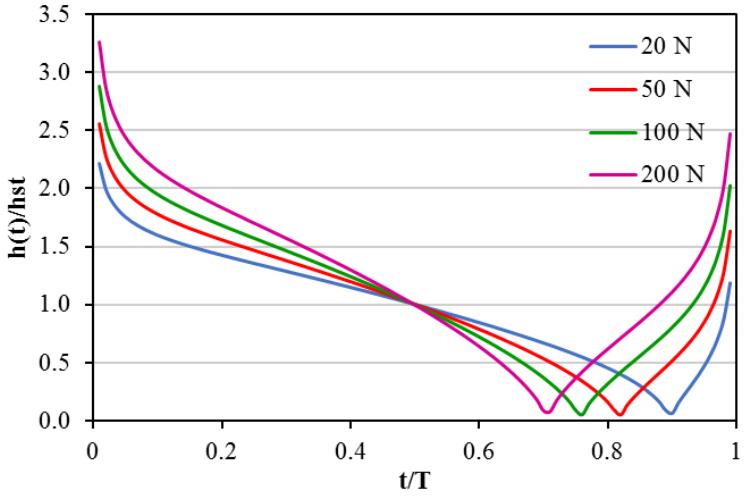

Figure 7.15: Effect of load amplitude upon transient film thickness

This theoretical analysis was intended to give a qualitative and not quantitative insight to the behaviour of film thickness under cyclically load variation, however it is interesting to make a direct comparison to experimental values of the film thickness. Figure 7.16 shows such comparison.

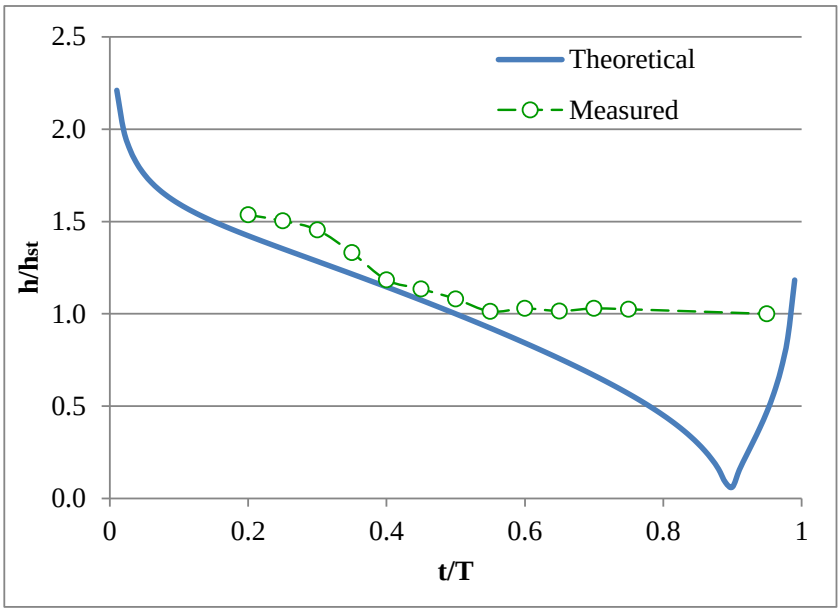

Figure 7.16: Comparison between theoretical and experimental central film thickness (50 Hz, 20.5 N, 0.05 m/s)

Obviously, the experimental values show a descending trend, like the theoretical curve, but the values are sensibly larger for the measured values. For the first half of the load variation cycle, the values do not differ too much, however the measured values are much larger than theoretical values in the second half. As mentioned previously, squeeze and the time taken for the lubricant to travel across the contact are phenomena not taken into account in the theoretical analysis. The squeeze effect during the rapid decrease of the velocity (and the film thickness with it) results into a film larger than the steady state predictions, as proved experimentally [33, 34] and theoretically [35, 38]. The EHD film thickness is established in the inlet of the contact, thus any change of the conditions in the inlet are translated into a change of film thickness at the centre of the contact later, as the new film takes some time to travel from the inlet to the centre of contact.

7.4 EHD films under cyclic load variation; experimental observation of the effect of frequency

In this subchapter, the experimental results are analysed from the point of view of the influence of the frequency. As shown in the theoretical analysis, the smaller frequency diminishes the transient effects on the film thickness. The results for 100 Hz were shown in the previous subchapter; in this section the results for 50 Hz, 25 Hz and 10 Hz will be comparatively analysed.

Load variation over one cycle, representative images of the contact and film thickness profiles will be shown.

Keeping entrainment speed at 0.05m/s, the typical load curve for the case of 50 Hz can be seen in figure 7.17. The initial load applied to the contact is 0 N ($p_0 = 0\ GPa$) and the maximum applied load is 54 N ($p_0 \approx 0.71\ GPa$). Typical images of the EHD contact in the 50 Hz vibration cycle can be found in figures 7.18, and film thickness profiles longitudinal to the direction of rolling, corresponding to those images are presented in and figures 7.19(b)–(h).

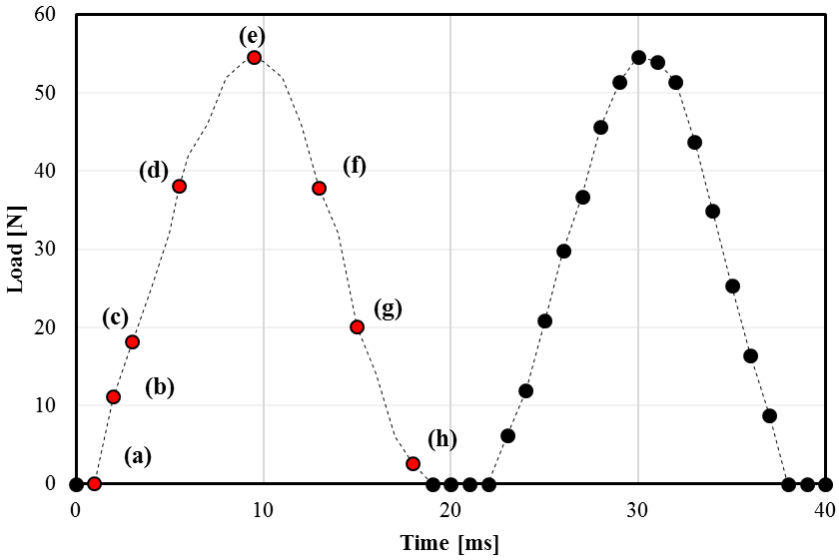

Figure 7.17: Forced sinusoidal vibration load curve, 50 Hz, 0.05 m/s, PAO 40, ambient temperature.

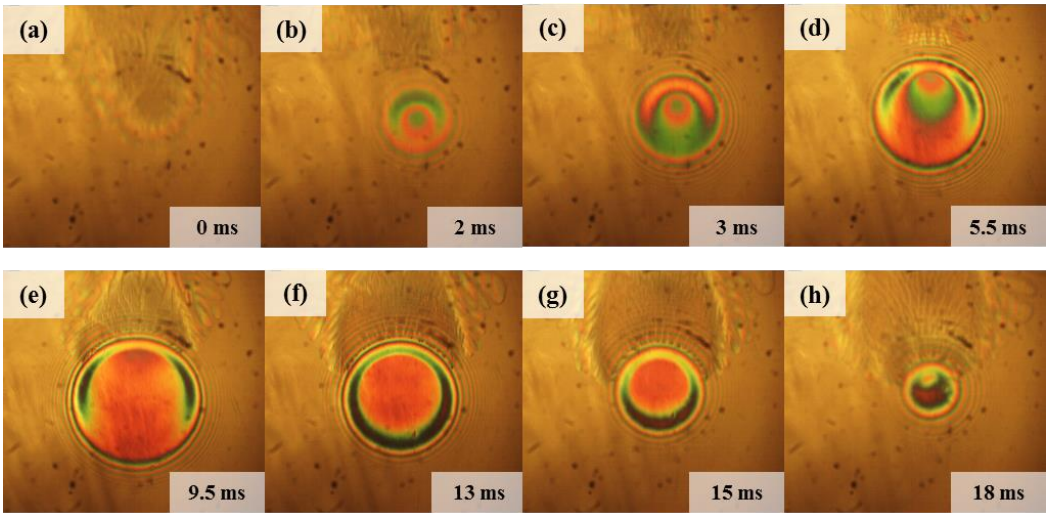

Figure 7.18: Selected typical images of EHD contact, 50 Hz, 0.05 m/s, PAO 40, ambient temperature.

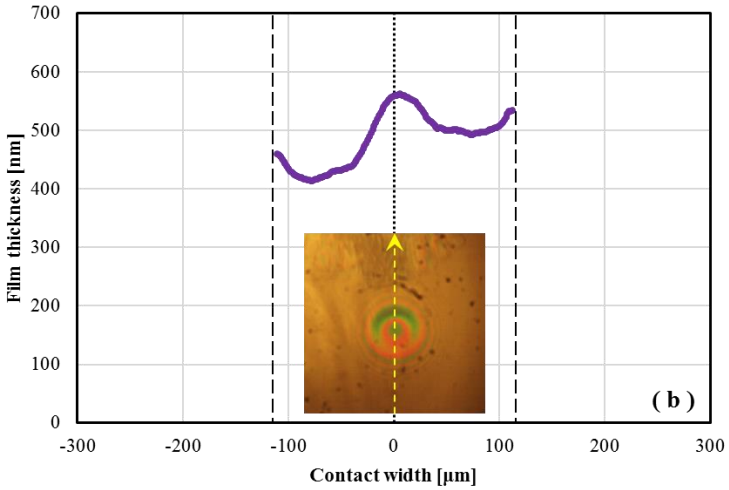

Figure 7.19(b): Film thickness profile along entraining direction, 50 Hz, 0.05 m/s, 2ms within vibration cycle.

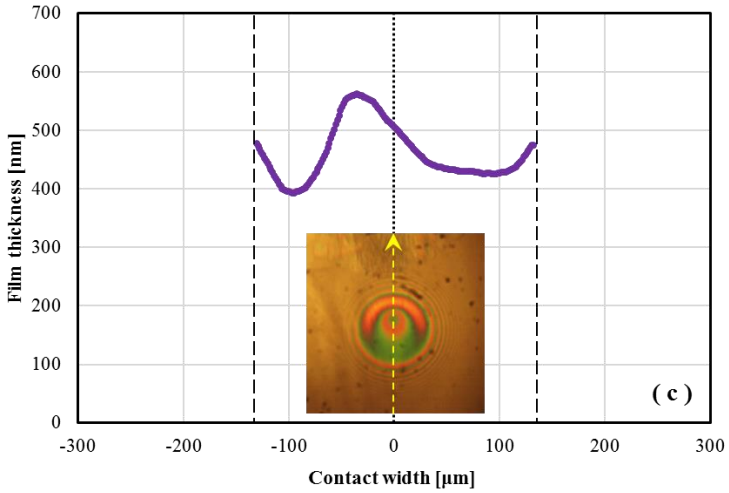

Figure 7.19(c): Film thickness profile along entraining direction, 50 Hz, 0.05 m/s, 3ms within vibration cycle.

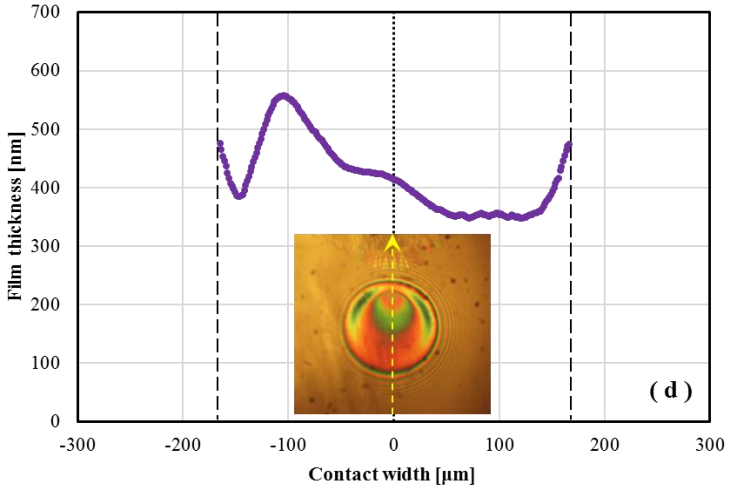

Figure 7.19(d): Film thickness profile along entraining direction, 50 Hz, 0.05 m/s, 5.5ms within vibration cycle.

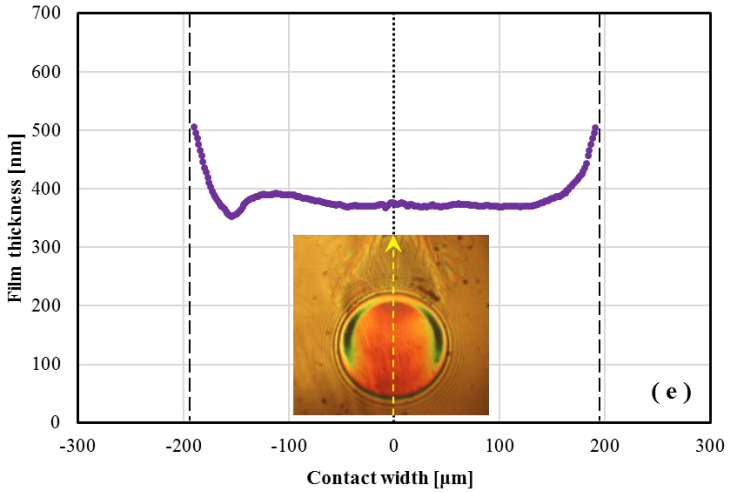

Figure 7.19(e): Film thickness profile along entraining direction, 50 Hz, 0.05 m/s, 9.5ms within vibration cycle.

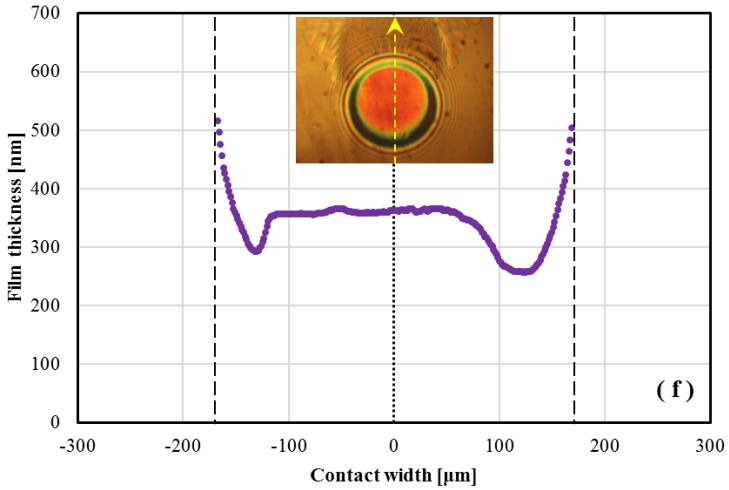

Figure 7.19(f): Film thickness profile along entraining direction, 50 Hz, 0.05 m/s, 13ms within cycle

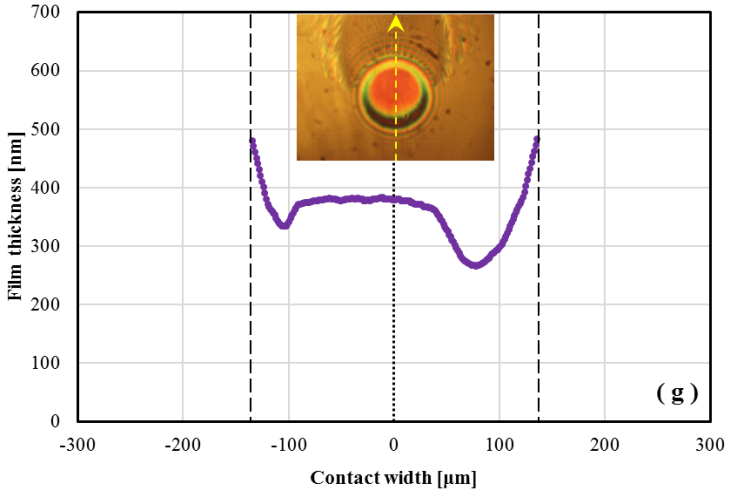

Figure 7.19(g): Film thickness profile along entraining direction, 50 Hz, 0.05 m/s, 15ms within vibration cycle.

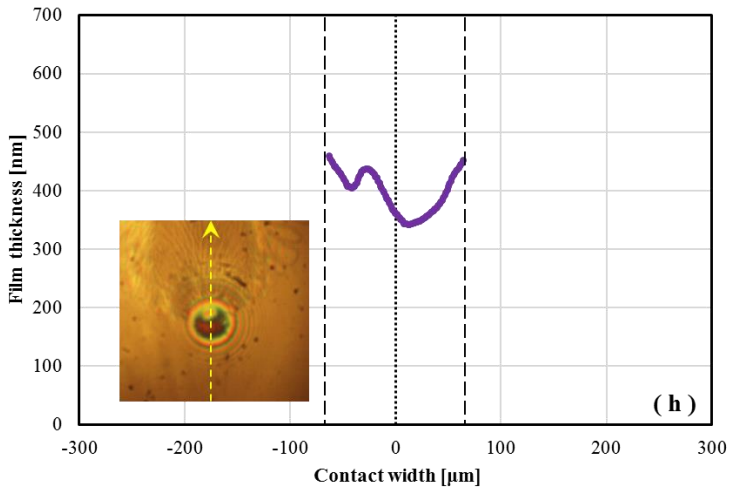

Figure 7.19(h): Film thickness profile along entraining direction, 50 Hz, 0.05 m/s, 18ms within vibration cycle.

As it was the case like the 100 Hz tests, a clearly visible film perturbation (dimple) can be seen again at 2 ms in the loading phase of this vibration cycle, as observed in figure 7.19(b). It generates a maximum perturbed film thickness of 562 nm, which is about 46 percent greater than the steady state film thickness corresponding to the largest load. Obviously, the maximum perturbed film thickness in 50 Hz vibration cycle is smaller than that of the case in 100 Hz because of the lower contact size changing rate. The perturbed film flows towards the exit of the contact and completely leaves the contact at 9.5 ms (see figure 7.19(e)) when the load reaches peak value in the vibration cycle. As the load starts decreasing, the film thickness at inlet periphery of the contact starts to decrease to balance the load over the whole contact area.

The load variation for the 25 Hz tests is seen in figure 7.20. The load applied to the contact varies between 0 N ($p_0 = 0\ GPa$) and a maximum applied load of 56 N ($p_0 \approx 0.72\ GPa$). Figures 7.21 and figures 7.22 show typical images of the EHD contact in a 25 Hz vibration cycle and the analysed film thickness profiles longitudinal to the direction of entraining motion respectively. Although the disc and ball surfaces are separated at the beginning of the cycle, the film experiences very little film perturbation, unlike the previous cases, as seen in figure 7.18. This is because the loading velocity and contact size changing rate are much lower at this lower frequency. Obviously, the entrainment effect dominates the effect of radius change, thus only at about 23 ms (see figure 7.21(g)) within the loading cycle a rather modest film perturbation of 20 nm is observed. During the load decreasing phase, the film thickness in the inlet of the contact does not change due to the balance between load and pressure is maintained at this contact size changing rate.

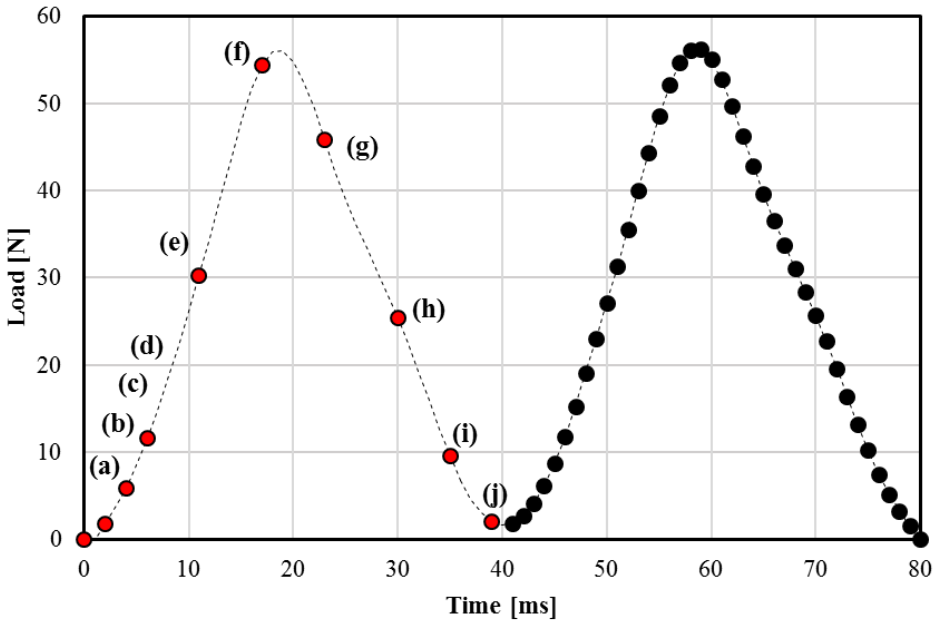

Figure 7.20: Forced sinusoidal vibration load curve, 25 Hz, 0.05 m/s, PAO 40, ambient temperature.

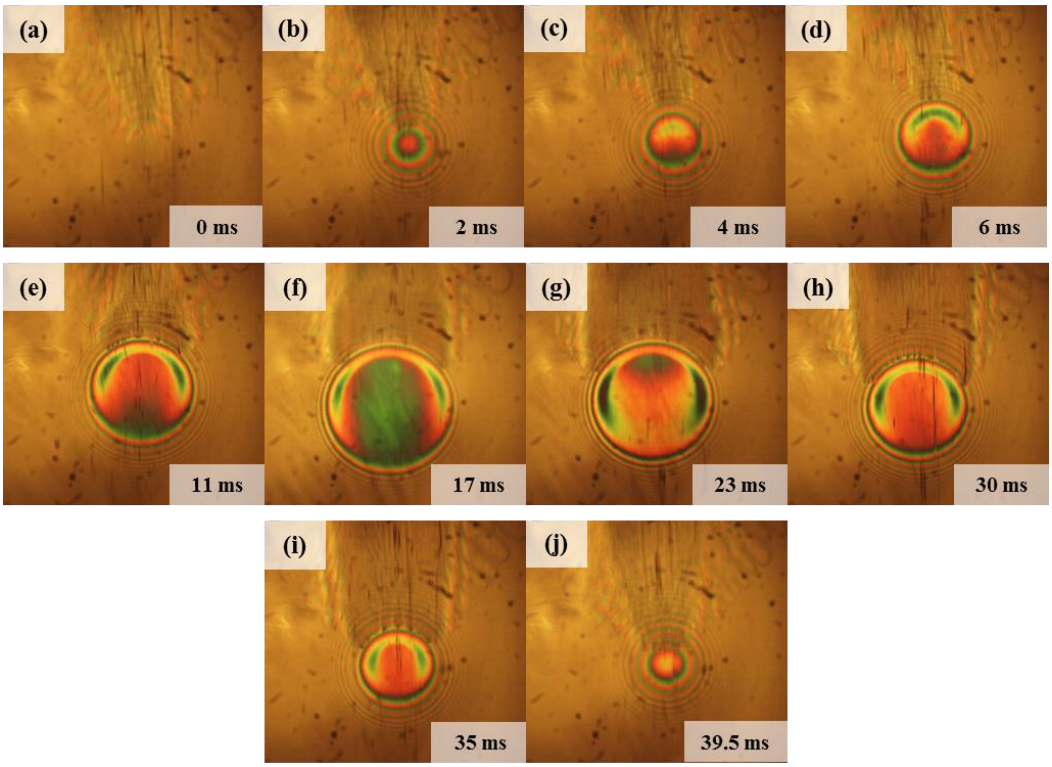

Figure 7.21: Selected images of the EHD contact, 25 Hz, 0.05 m/s, PAO 40, ambient temperature.

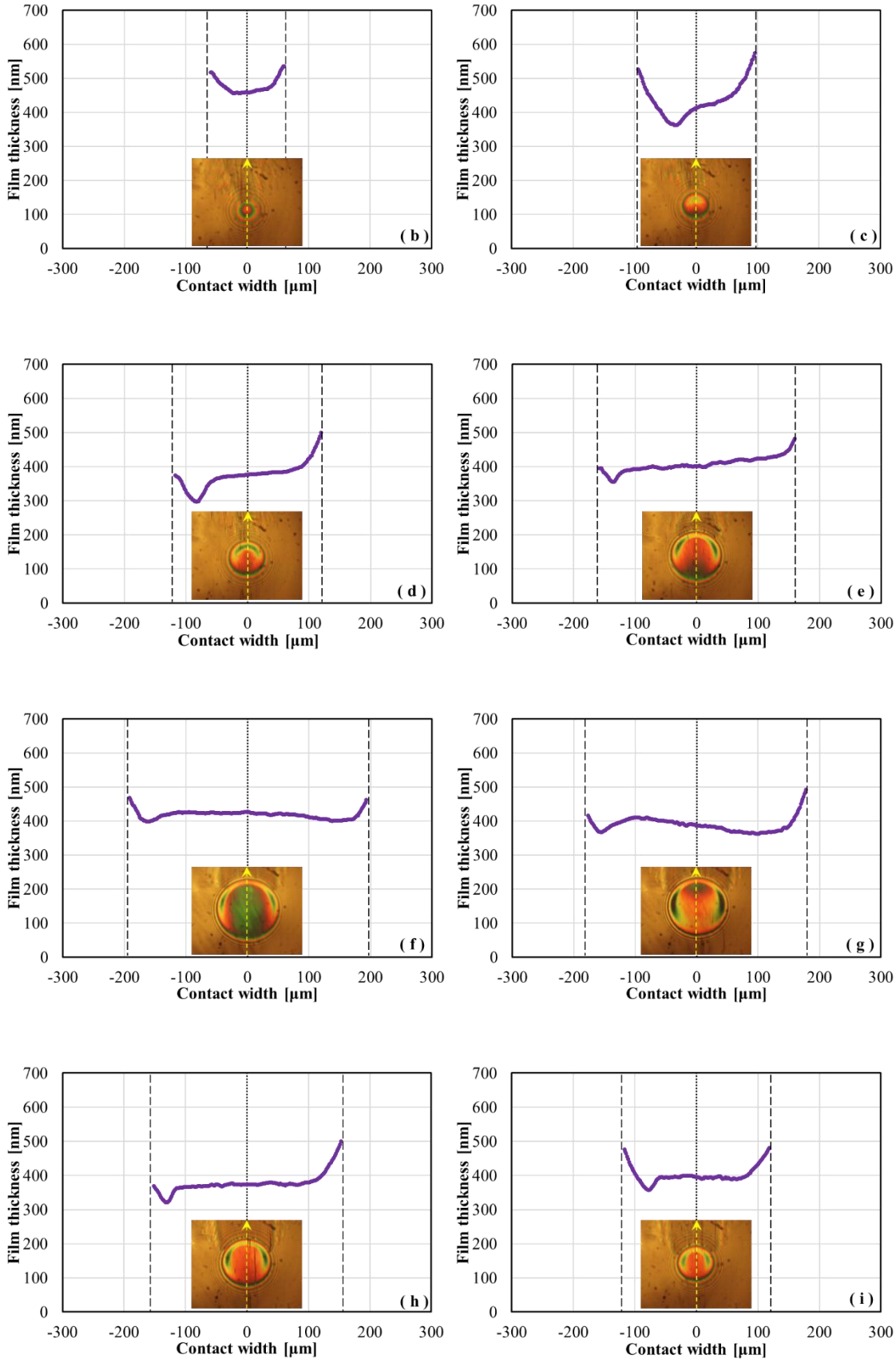
Film thickness [nm]
Contact width [μm]
(b)
(c)
(d)
(e)
(f)
(g)
(h)
(i)

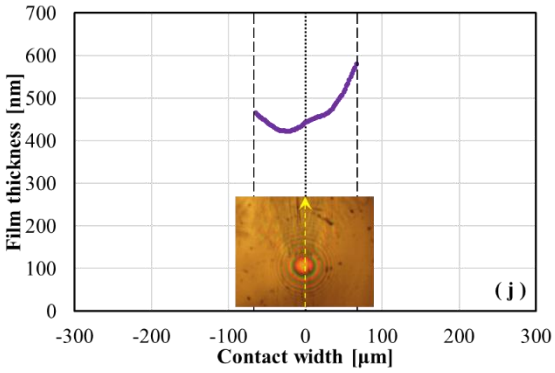

Figure 7.22 (b)-(j): Film thickness profiles along the entraining direction at 25 Hz, 0.05 m/s.

The load variation in the 10 Hz vibration cycle is shown in figure 7.23. The initial load applied to the contact is 0 N ($p_0 = 0\ GPa$) and the maximum applied load is 54 N ($p_0 = 0.71\ GPa$). Interferometric images of the contact, at different times marked by the red dots in the load curve are shown in figure 7.24. It is obvious from these images that film thickness perturbation does not occur. All analysed film thickness profiles shown in figures 7.25 exhibit the classic flat central film region, which characterises the steady state film behaviour. In these tests, the speed of change of contact radius is too small to influence significantly the film thickness. Squeeze effect is also not evident, so no film perturbation phenomenon can be seen in these tests.

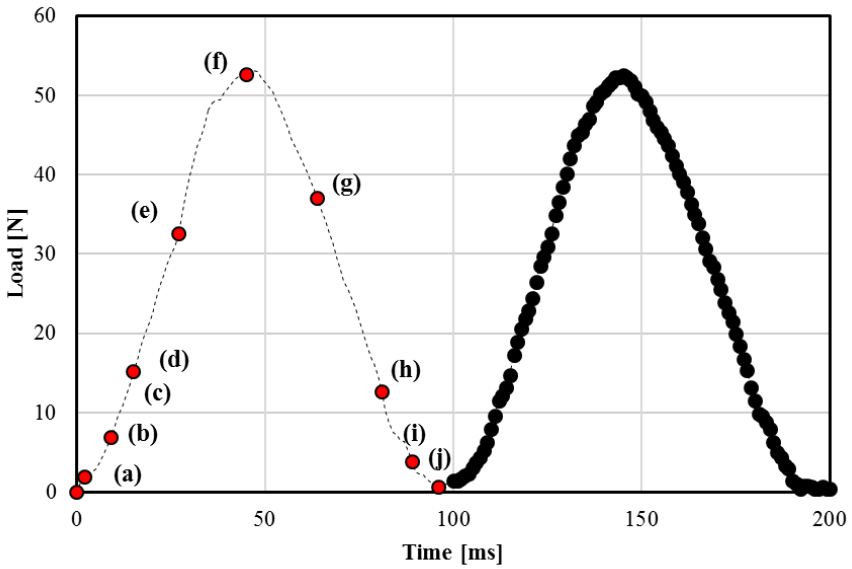

Figure 7.23: Forced sinusoidal vibration load curve, 10 Hz, 0.05 m/s, PAO 40, ambient temperature.

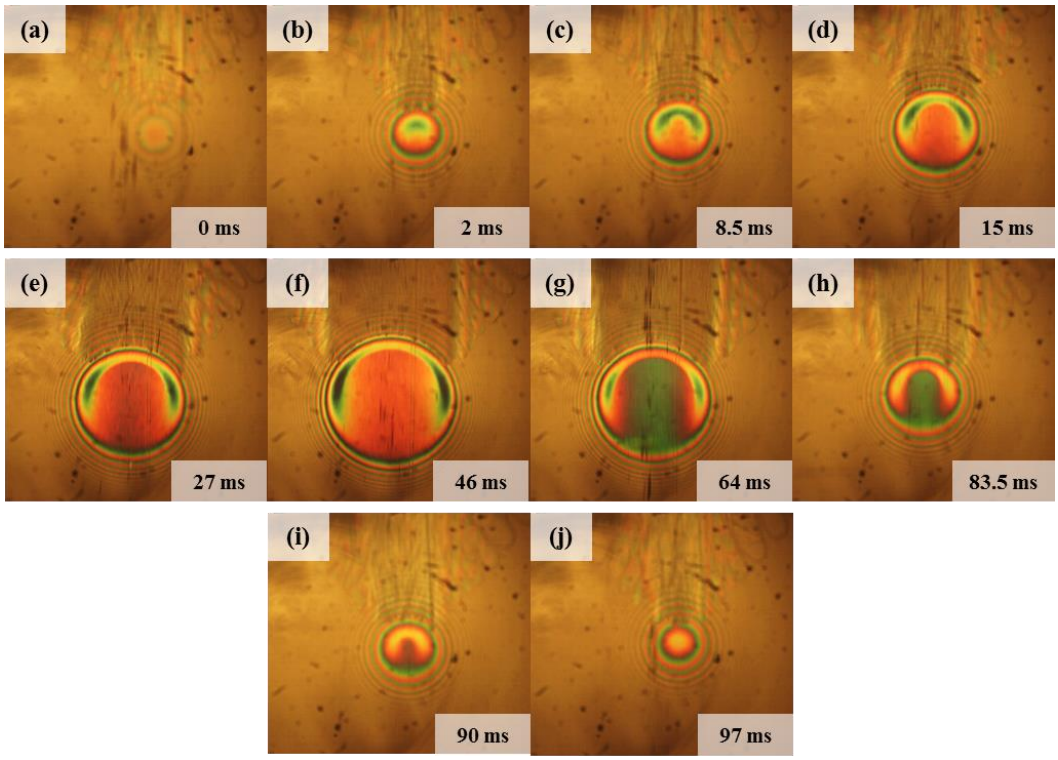

Figure 7.24: Selected images of the EHD contact, 10 Hz, 0.05 m/s, PAO 40, ambient temperature.

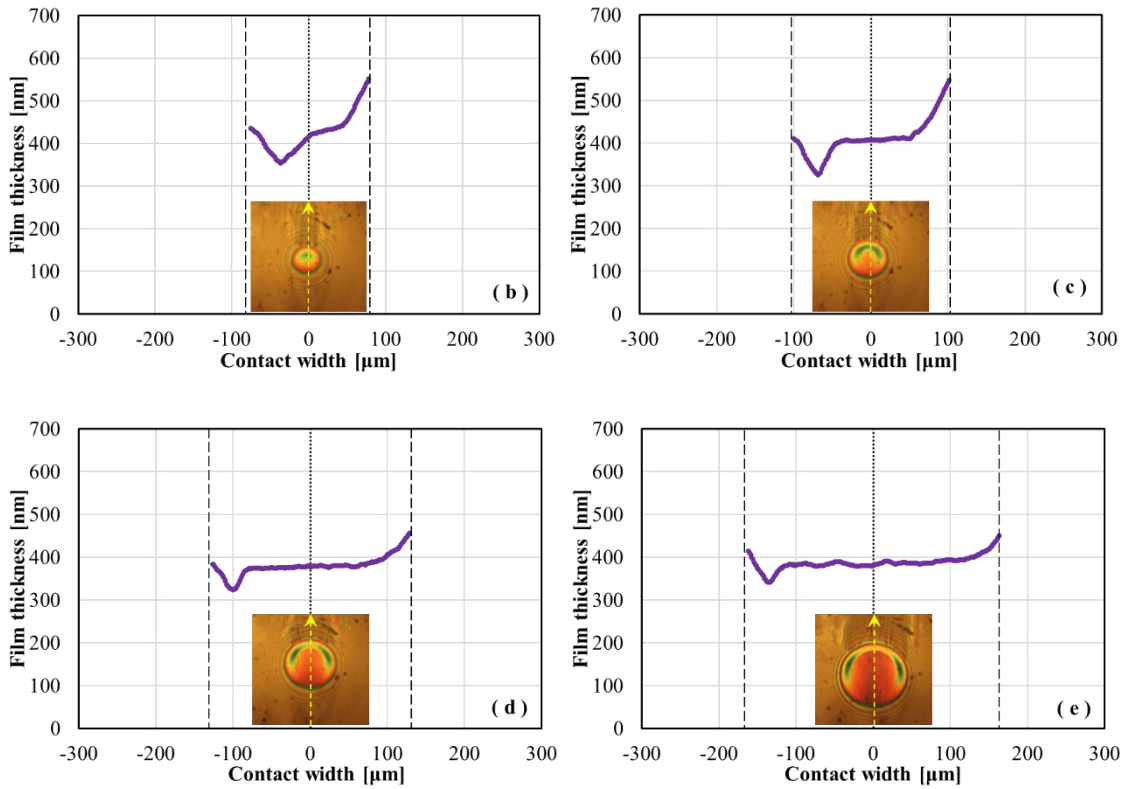

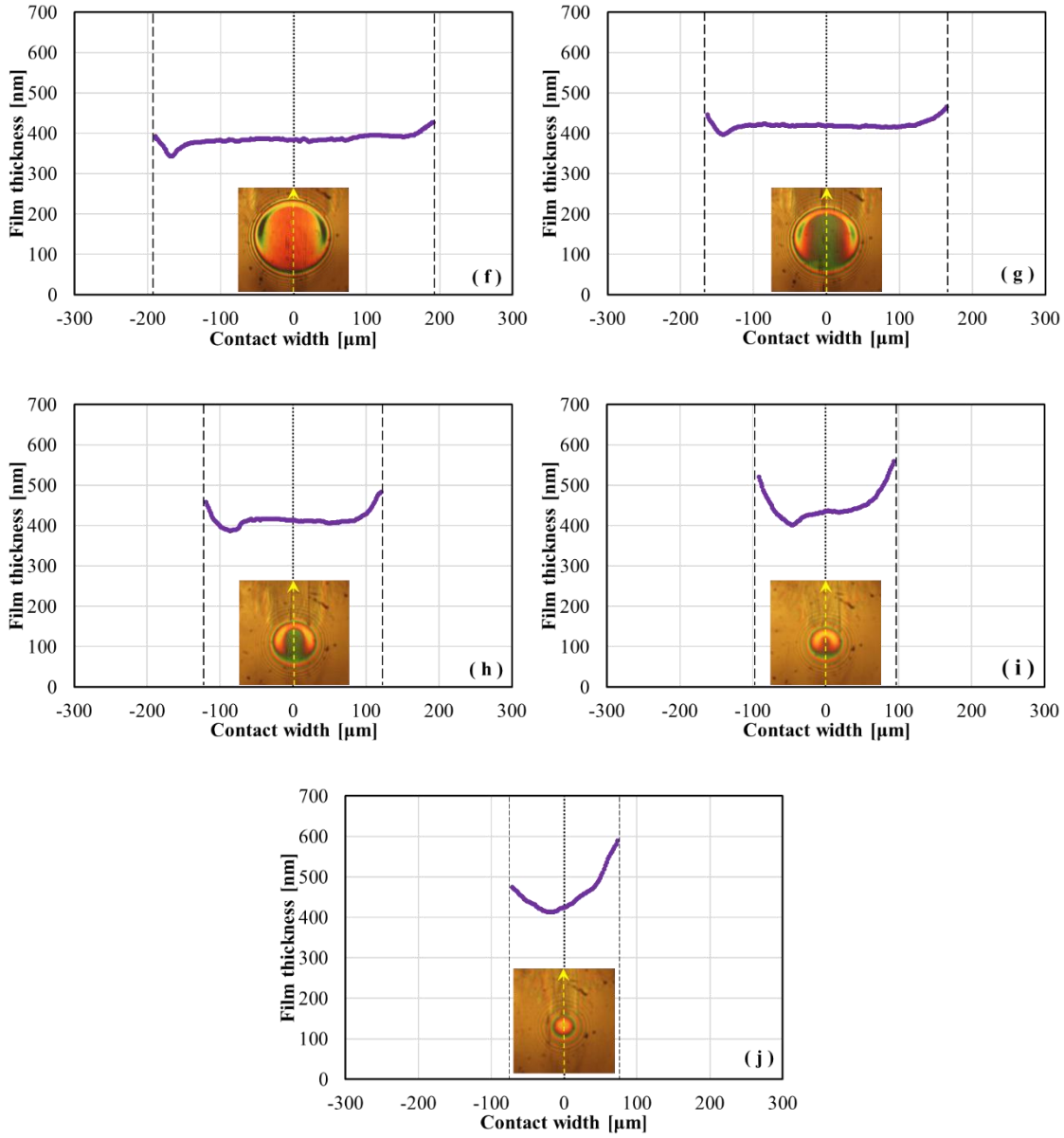

Figure 7.25 (b)-(j): Film thickness profiles along the entraining direction at 10 Hz, 0.05 m/s.

A comparison between experimental, film thickness in cycles at frequencies of 10 Hz, 25 Hz, 50 Hz and 100 Hz is shown in figure 7.26 (a). The values of the film thickness were measured at the centre of the contact. The load variation over one cycle is also shown.

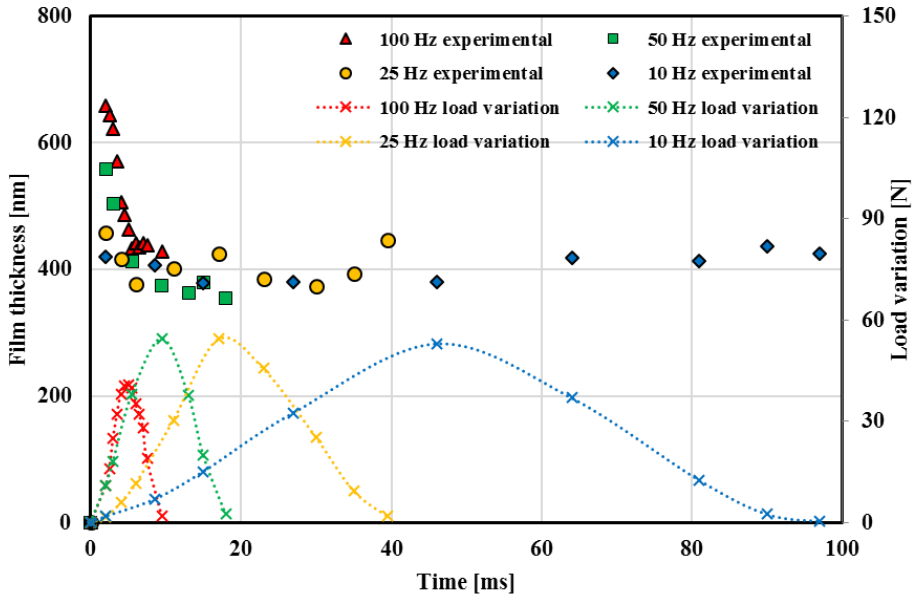

Figure 7.26 (a): Comparison of experimental film thickness, PAO 40, ambient temperature, 0.05 m/s, 10 Hz, 25 Hz, 50 Hz and 100 Hz.

As mentioned previously the effect of frequency is clearly seen. At lower frequency, 10 Hz and 25 Hz, the film thickness variation over one cycle is symmetrical, however at larger frequencies it is strongly skewed towards the load increasing phase. This effect is even better emphasised in figure 7.26 (b), which shows comparatively the experimental with theoretical, steady state film thickness, over one cycle of load variation. The steady state values were calculated with Hamrock-Dowson relationship, using the measured load at various points within the cycle.

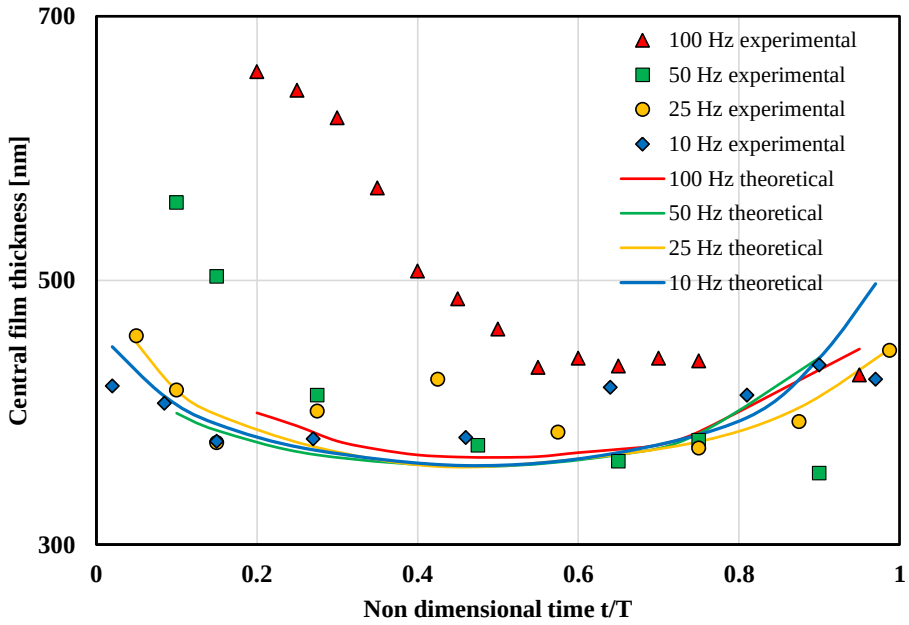

Figure 7.26 (b): Comparison of experimental and theoretical steady state film thickness, PAO 40, ambient temperature, 0.05 m/s, 10 Hz, 25 Hz, 50 Hz and 100 Hz.

The transient film thickness follows closely, within the error of the method, the steady state values at the lowest two frequencies employed, however the departure from steady state behaviour is remarkably strong at 50 Hz and 100 Hz. During the load increasing phase the film thickness increases due to the increased of the entrainment speed caused by the increase of contact dimensions with the load. This makes the film thickness during the first half of the cycle, for 100 Hz and 50 Hz noticeably larger than the theoretical, steady state values.

Figure 7.27 illustrates how the effective entrainment speed increases over the steady state value, during the load increasing phase. As it can be seen at the beginning of the cycle the effective entrainment speed is more than three times larger than the steady state value.

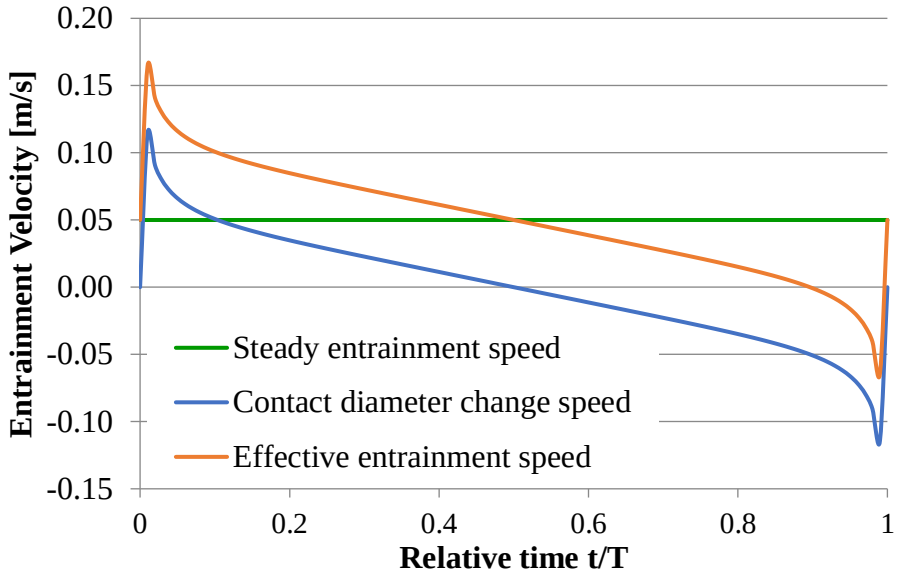

Figure 7.27: Steady state and effective entrainment speed

During the load decreasing phase, the entrainment speed decreases which normally is accompanied by a decrease of the film thickness, however, the rapid film collapse promotes the squeeze effect which delays the drop of the film thickness (the lubricant is squeezed out of the contact but it cannot flow quickly enough due to large pressure inside and just around contact). As the entrainment speed continues to decrease the film thickness in the inlet decreases too as seen in figures 7.10 and 7.19, however, due to the time needed for the lubricant to travel through the contact, this diminished film is only found in the centre of the contact with a time lag.

7.5 The effect of overall film thickness

Several experiments were carried out in this research as shown in the previous chapter. Not all those results are discussed, but only those which gave an insight upon the effect of various parameters upon EHD film behaviour. At this point, it is worth mentioning that tests performed

with lubricants of lower viscosity (higher temperature or simply different lubricants) have shown that deviations form steady state film thickness become less and less pronounced as the viscosity of the lubricant decreases. This is illustrated by the images and film thickness profiles shown in figures 7.28 and 7.29. The images shown in figure 7.28 were recorded at 100 Hz, 0.05 m/s, for PAO 40 at a temperature of 40°C while those from figure 7.29 are for the same lubricant but at 60°C.

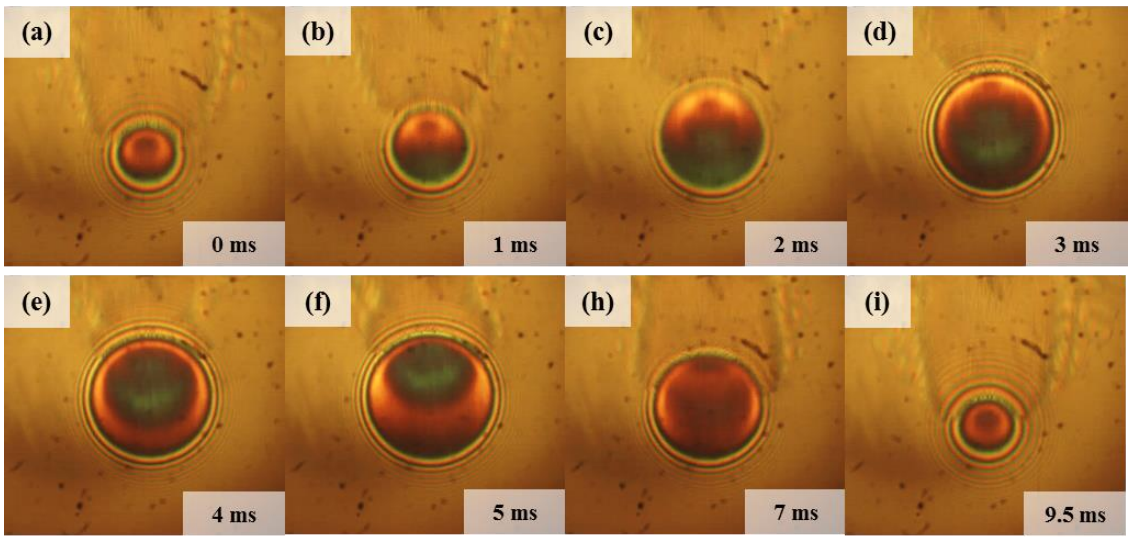

Figure 7.28: Selected images of the EHD contact for 100 Hz, 0.05 m/s, PAO 40 at **40**°C.

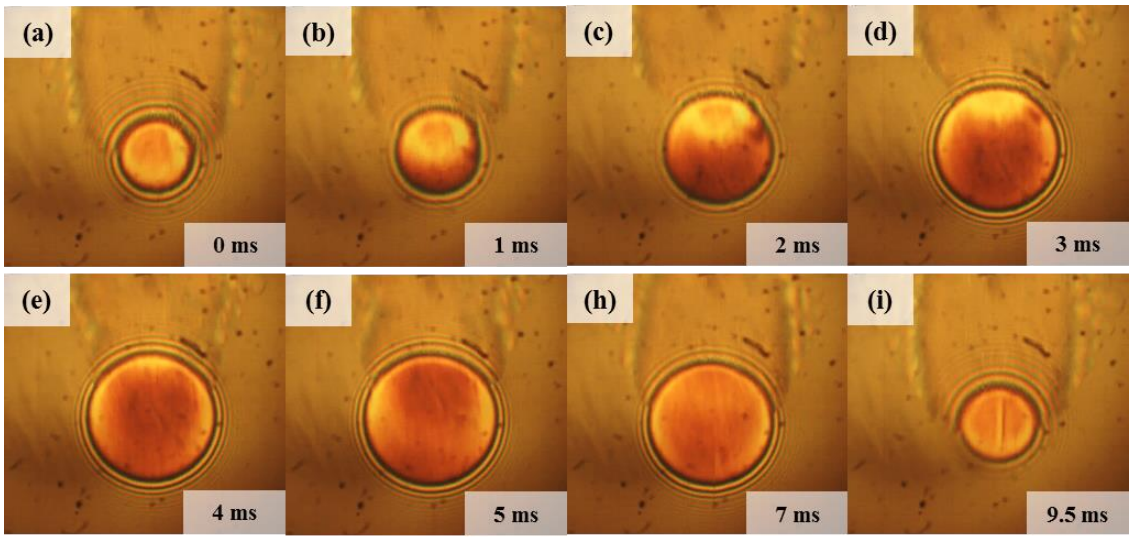

Figure 7.29: Selected images of the EHD contact for 100 Hz, 0.05 m/s, PAO 40 at **60**°C.

In terms of the actual values of film perturbation, the difference is clear in figure 7.30, which captures the film thickness profiles at the same time during the loading cycle, for 40°C and 60°C.

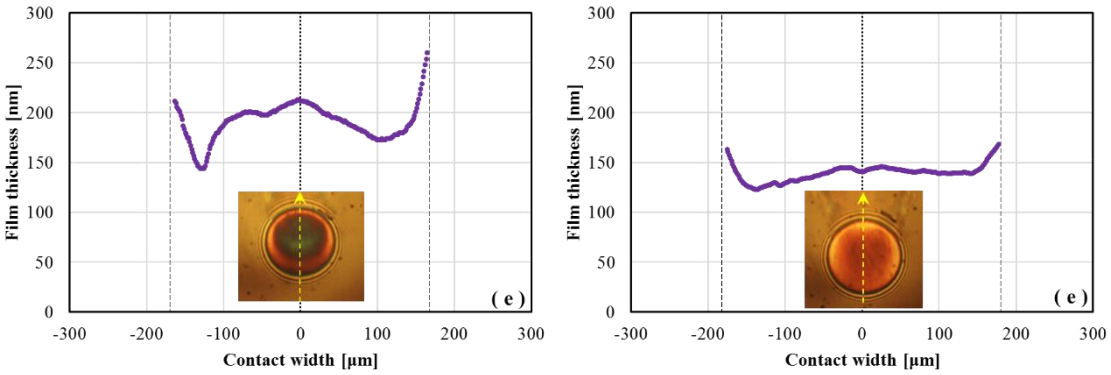

Figure 7.30: Film thickness profiles at different viscosities, 40°C (left) and 60°C (right).

Comparing this plot with the images shown in figure 7.30 the trend is clear; significantly lower film perturbations are generated at lower overall film thickness. The film perturbation decreases from about 234 nm at ambient temperature, to about 62 nm at 40°C and to around 22 nm at 60°C, while the viscosity decreases from 922.5 mm^2s^{-1} to 135.8 mm^2s^{-1}.

There is though, a case in which large film perturbations are formed even at low overall film thickness. This is when the amplitude of the oscillatory motion is significantly larger than the deformations of the surfaces under loading. In this case the rebounding of the surfaces is large which in turn generate large impact forces. The fluid entrainment is less important in this situation and film squeeze plays the dominant role in the film behaviour. In a way, this is similar to pure squeeze or sudden halting of motion, where larger dimples are formed and trapped inside the contact as reported for example in [67, 116]. In the context of this research, this observation is proved by the experiments carried out with PAO 4, a lubricant with viscosity significantly lower than PAO 40. The load variation during 100 Hz cycle shows a relatively longer period of zero load, as seen in figure 7.31. The initial load applied to the contact is 0 N and the maximum applied load is 39N ($P_0 = 0.64\ GPa$).

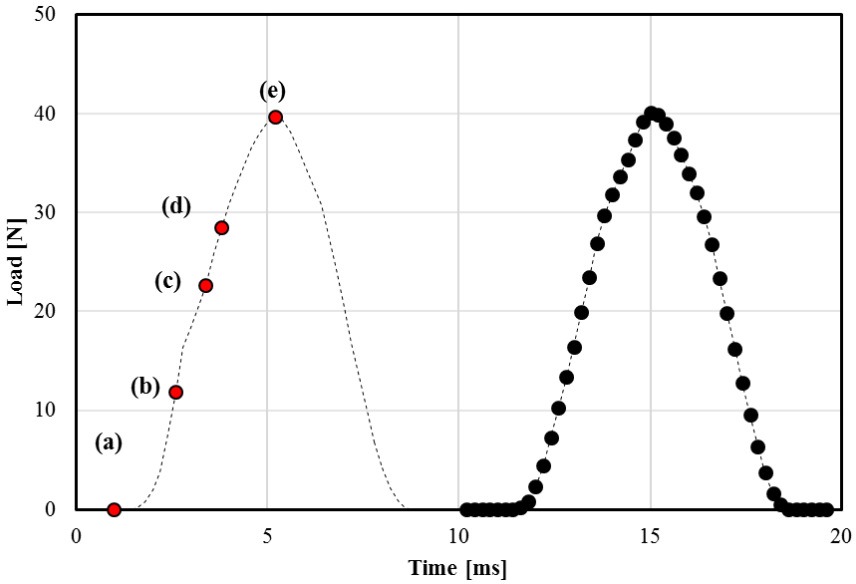

Figure 7.31: Load variation curve, 100Hz, 0.05 m/s, PAO 4 at 40°C.

Interferometric images of the contact at various points within the load increasing phase are seen in figure 7.32. Large fluid entrapment is formed even at an entrainment speed of 0.1 m/s.

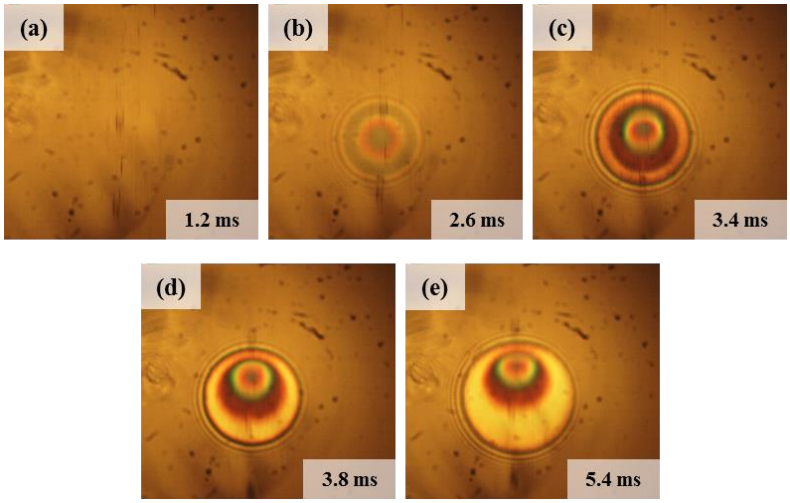

Figure 7.32: Selected images of the EHD contact at 100 Hz, 0.1 m/s, PAO 4 at 40°C.

Analysis of these images in order to extract film thickness profiles yields the results shown in figures 7.33.

As seen from the film thickness profile illustrated in these figures, the maximum perturbed film thickness is 224 nm, which is nearly 4.5 times greater than the value under steady state condition.

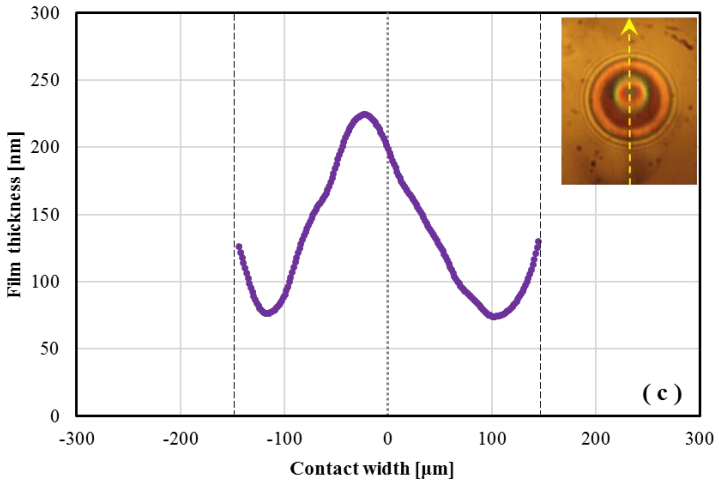

Figure 7.33(c): Film thickness profile along the entraining direction at 3.4 ms within the vibration cycle, 100 Hz, 0.1 m/s, PAO 4 at 40°C.

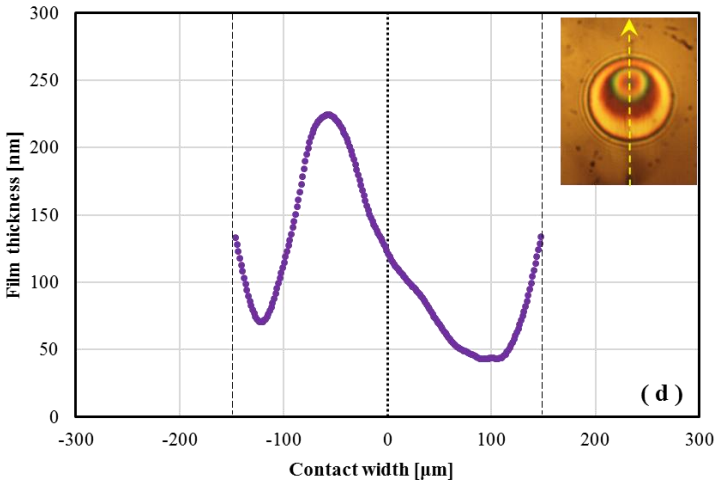

Figure 7.33(d): Film thickness profile along the entraining direction at 3.8 ms within the vibration cycle, 100 Hz, 0.1 m/s, PAO 4 at 40°C.

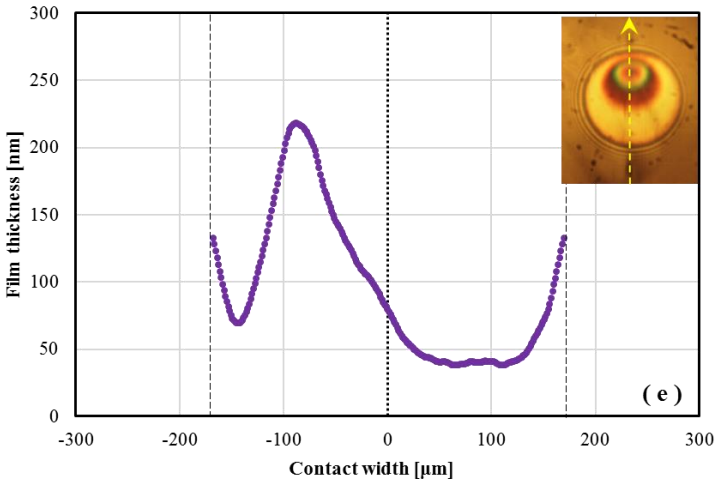

Figure 7.33(e): Film thickness profile along the entraining direction at 5.4 ms within the vibration cycle, 100 Hz, 0.1 m/s, PAO 4 at 40°C.

7.6 The effect of entrainment speed

The effect of the entrainment speed upon film behaviour is studied based on the results of the tests carried out with PAO 40 at ambient temperature as well as tests with lubricant HVI 650 at 40℃. The largest frequency of 100 Hz is used and the entrainment speed varied between 0.05 m/s and 0.5m/s. Typical behaviour of EHD contact at peak load in the 100 Hz vibration cycles for these two lubricants were selected and presented in figures 7.34 and figures 7.35 respectively.

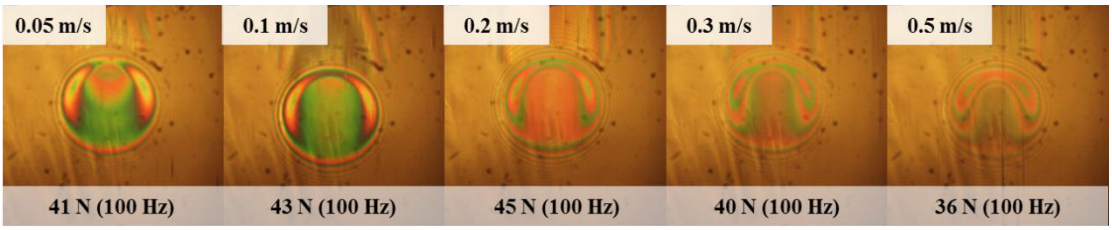

Figure 7.34: EHD contact at peak load, 100 Hz for PAO 40, ambient temperature.

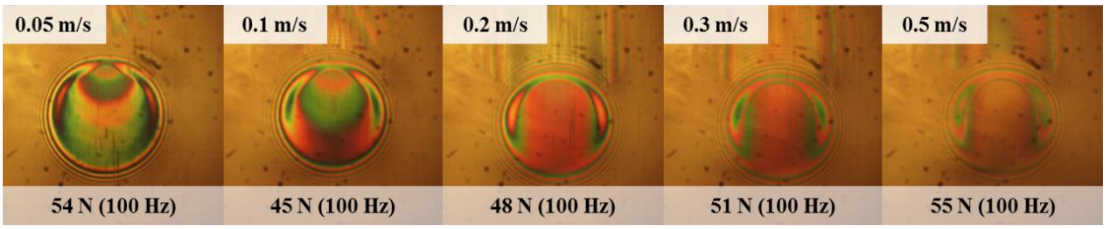

Figure 7.35: EHD contact at peak load, 100 Hz for HVI 650, 40℃.

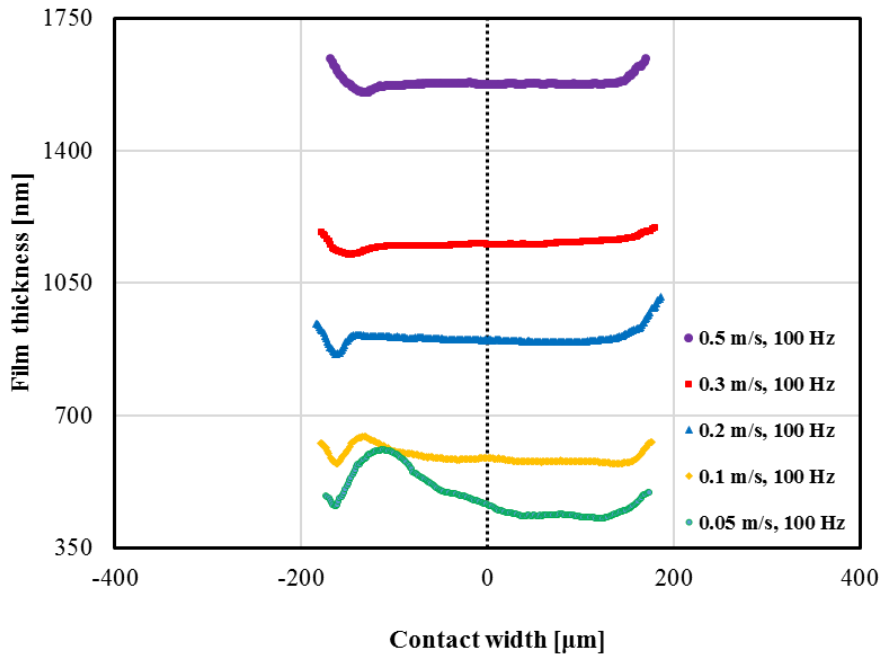

Figure 7.36: Film thickness profiles along the entraining direction at various entrainment speeds, PAO 40 ambient temperature.

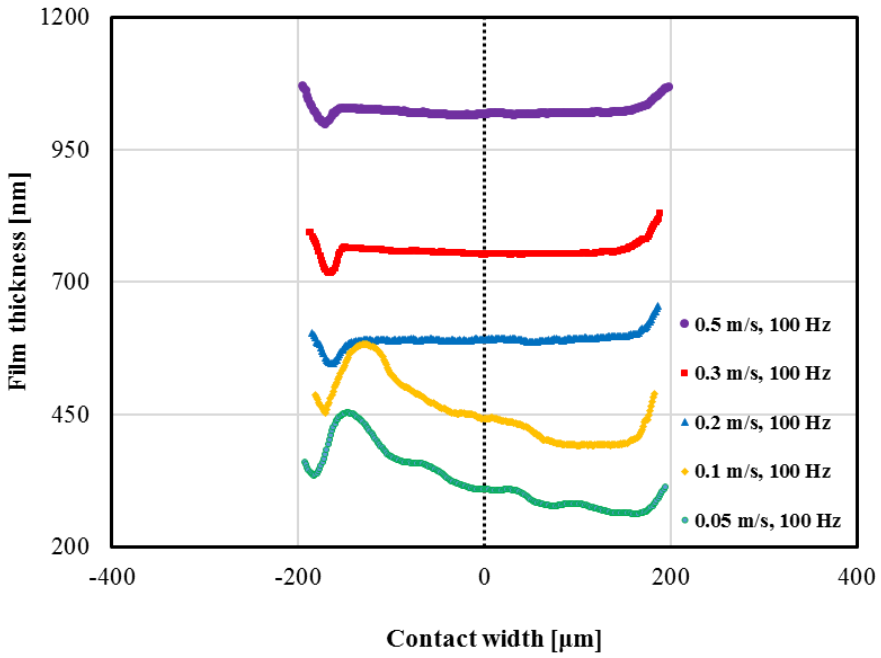

Figure 7.37: Film thickness profiles along the entraining direction at various entrainment speeds, HVI 650, 40°C.

These images were used to extract film thickness maps over the contact area. From these, film thickness profiles along the direction of the entraining motion were taken and are compared in figure 7.36 and figure 7.37. It can be seen that thickness perturbation happens only at lower entrainment speeds tested, that is 0.05 m/s and 0.1 m/s. At the speeds, higher than 0.2 m/s, the film perturbation does not appear within the vibration cycle and film thickness profiles show the classic, flat central film feature. At the beginning of the load increasing phase, the contact diameter is still small and it is thought that at these large entrainment speeds any dimples formed are transported away within the exposure time of the camera.

7.7 The effect of load amplitude

It is well known that the formation of the EHD films is determined by the mechanisms which take place in the inlet region and the film thickness almost insensitive to load variation according to the classical lubrication theory. In the present experiments however, the film thickness is dominated by a combination of entrainment, squeeze and according to the theoretical analysis shown before by the speed of change of contact dimensions. Thus, it is legitimate to attempt to explore the effect of load amplitude upon the behaviour of the film and the film thickness. This was done in two types of experiments: pulsating cycle (load varying between zero and a maximum, pre – set value) and alternating cycle (load varying about a fixed, pre – set value). In all tests PAO 40, at 40°C was used, while the entrainment speed was fixed at 0.1 m/s and the frequency was kept at 60 Hz.

The compared load variation at five different amplitude levels (1, 2, 3, 4 and 5), in the pulsating load cycles, is shown in figure 7.38.

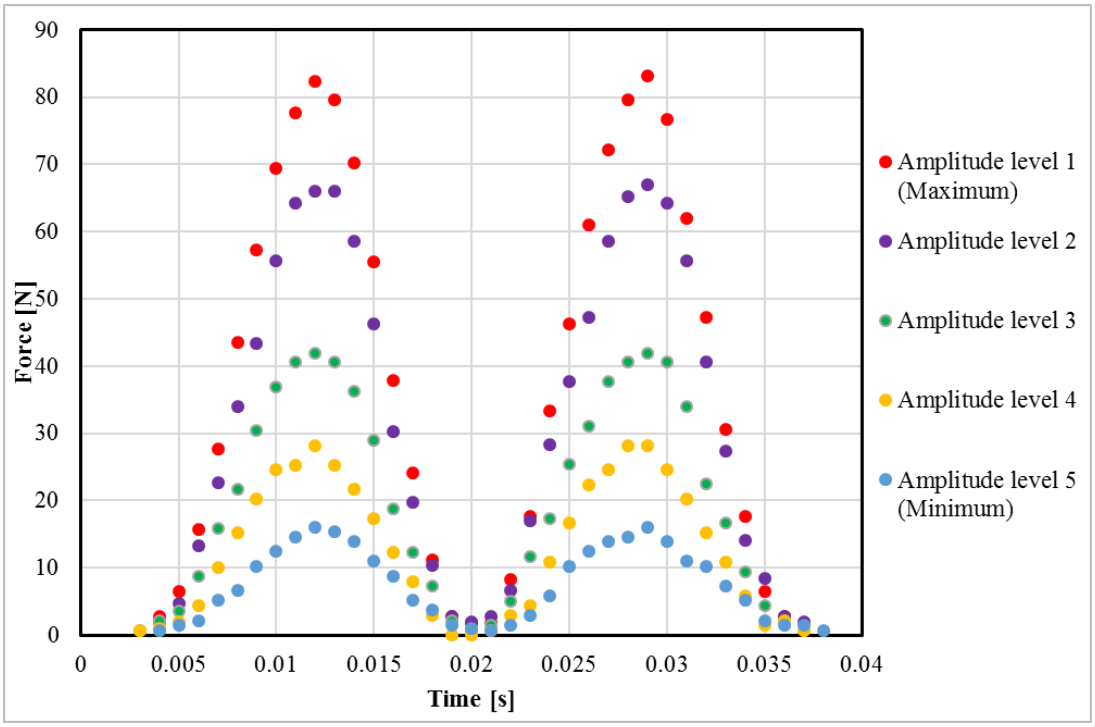

Figure 7.38: Load variation at five levels of amplitude, PAO 40 40°C, 60 Hz, 0.1 m/s.

According to the procedure common in all experiments carried out in this research, interferometry images of the contact were selected at various points within the loading cycle and film thickness values were extracted.

A comparison between experimental film thickness during the vibration cycle and theoretical calculation according to Hamrock-Dowson equation [13] is showed in figure 7.39. The theoretical film thickness under steady state condition was calculated using the measured values of the load at each time instant, so it obviously decreases and then increases as the load increases and decreases during the cycle. For the largest load variation cycle, the central film thickness theoretically decreases about 25 percent from the minimum to maximum load. The measured film thickness also decreases with increasing the load, but at a faster rate, because the film thickness at the beginning of the cycle is much larger than the theoretical one.

When the load decreases, the measured central film thickness is smaller than the theoretical values. This is in accord with the predictions made in subchapter 7.3, on the basis of the variation of the entrainment speed due to the change of contact size.

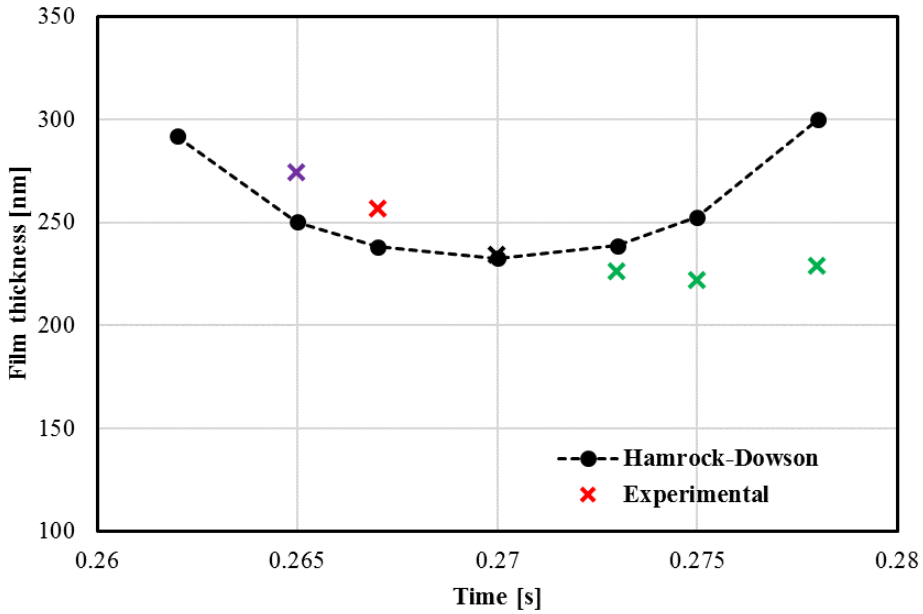

Figure 7.39: Experimental and theoretical central film thickness during load cycle, amplitude level one.

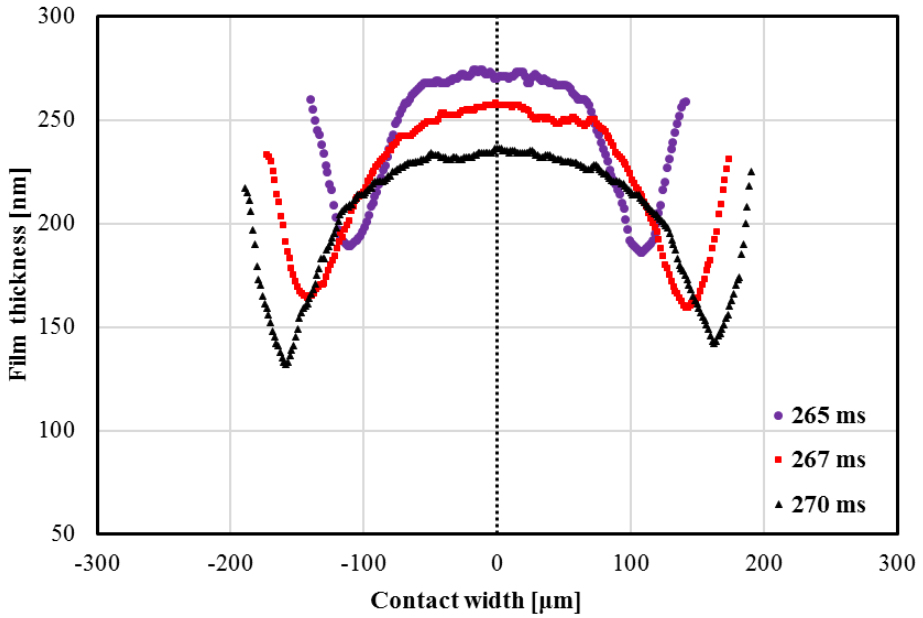

Figure 7.40: Film thickness profile transversal to the entraining direction, amplitude level one.

Figure 7.40 shows film thickness profiles in direction perpendicular to entrainment direction, at three instants of time within the load increasing phase. These correspond to the three marked points, during the load increasing phase, shown with similar colours in figure 7.39. It is seen that the relatively large film perturbation makes the film thickness at the side lobes smaller than would be expected in steady state conditions. In later conditions, the minimum film thickness is about 80 percent of the central film thickness, however in the graph shown this proportion is 68 percent at lower load and decreases to about 59 percent at the larger load. The variation of the perturbation

(dimple) height and the ratio between minimum and central film thickness at the times corresponding to the profiles shown in figure 7.40, can be seen in figure 7.41. This phenomenon can be found at all amplitude level tested.

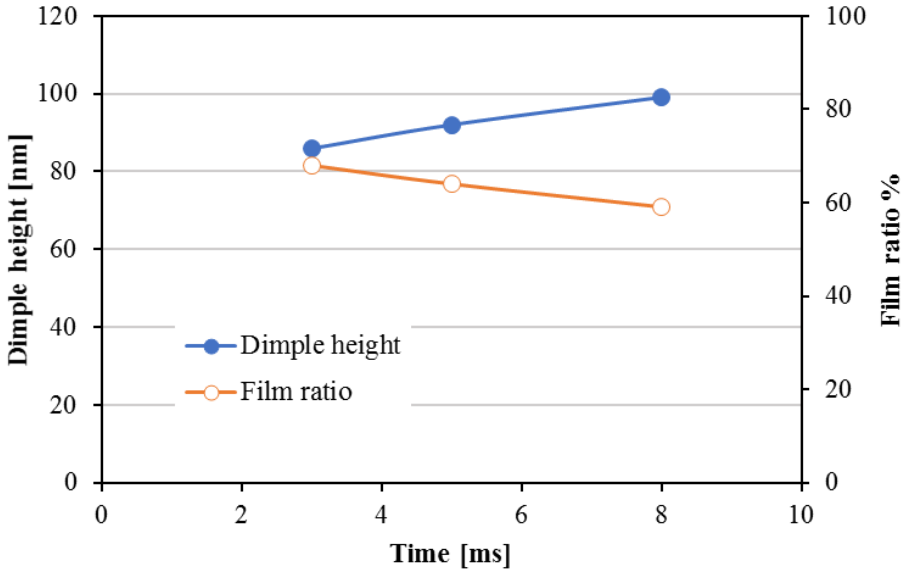

Figure 7.41: Film perturbation during the load – increasing phase

In figure 7.42, the values of the central film thickness at three moments within each vibration cycle at five different amplitude levels are compared. It can be seen higher amplitude level can entrap more lubricant which increases central film thickness due to its faster load changing rate in the loading phase of the vibration cycle.

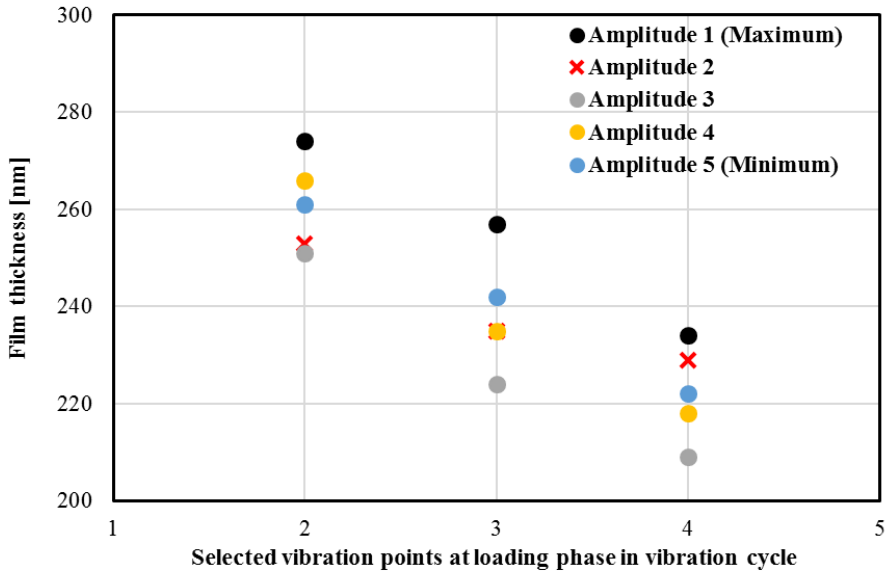

Figure 7.42: Plot of central film thickness at different levels of amplitude, pulsating load cycles.

Tests were also carried out with variable amplitude but fixed mean load at 30 N, the load

variation during 60 Hz cycles are compared in figure 7.43.

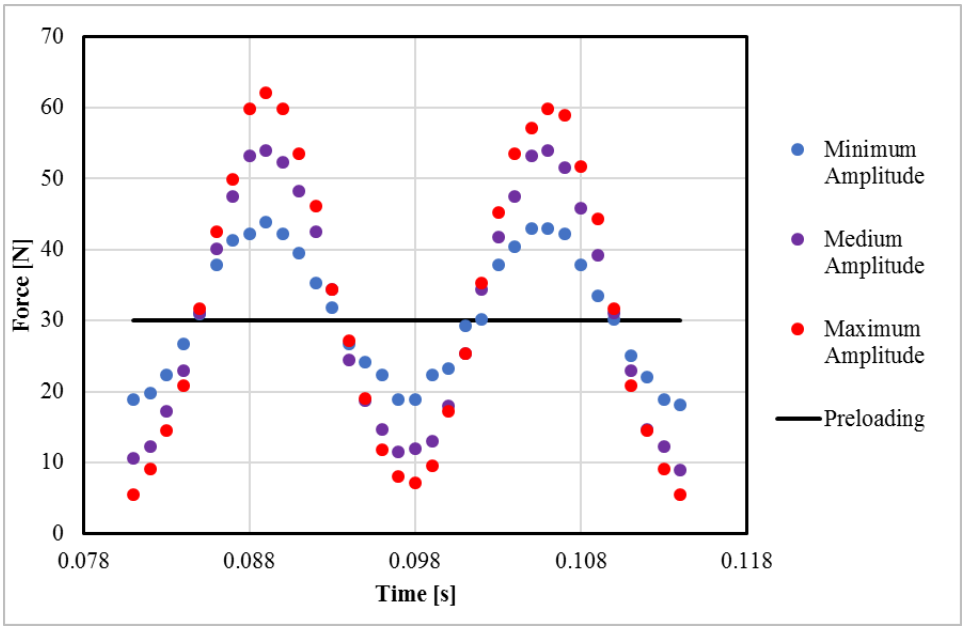

Figure 7.43: Load variation with constant mean load of 30 N, at three levels of amplitude, PAO40 40°C, 60 Hz, 0.1 m/s.

Central film thickness measured during these cycles, together with the theoretical film thickness calculated for the same time instants using the measured values of the load are seen in figures 7.44 to 7.46. To note that the images of the contact at the beginning of the cycle are very small and it was not possible to extract meaningful film thickness values. For this reason, the first theoretical film thickness sometimes does not have a corresponding measured value.

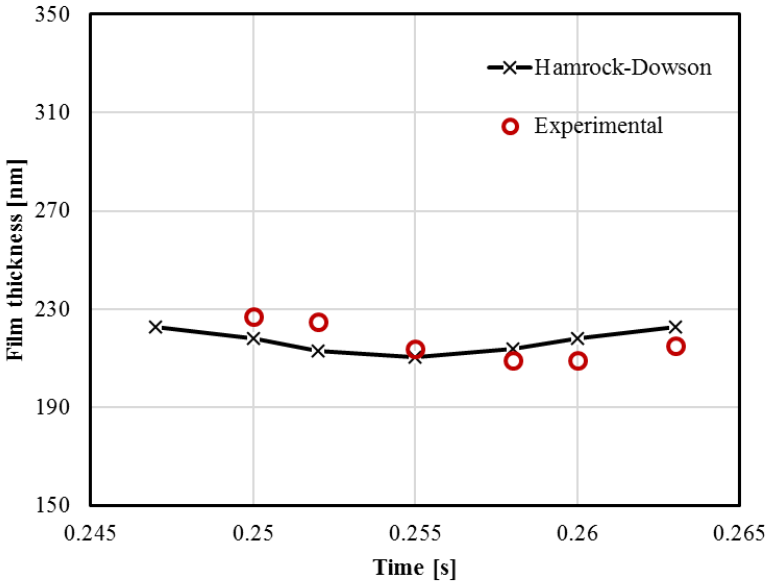

Figure 7.44: Experimental and theoretical central film thickness at ***minimum*** amplitude cycle.

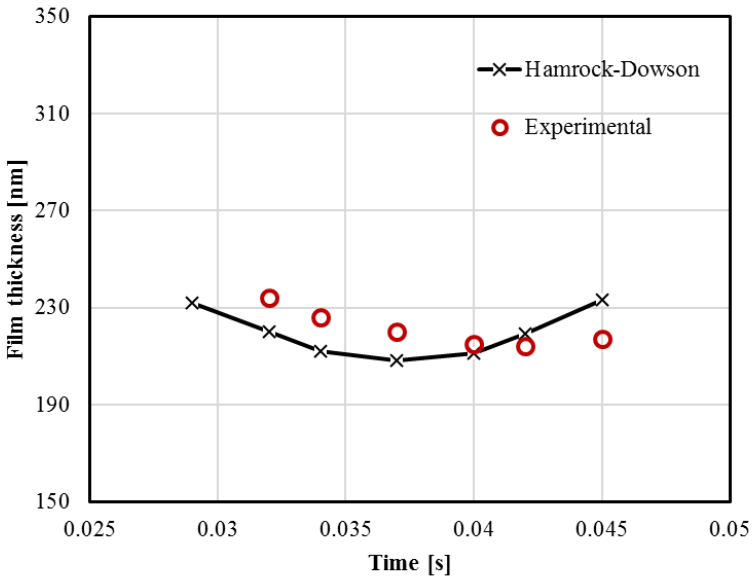

Figure 7.45: Experimental and theoretical central film thickness at ***medium*** amplitude cycle.

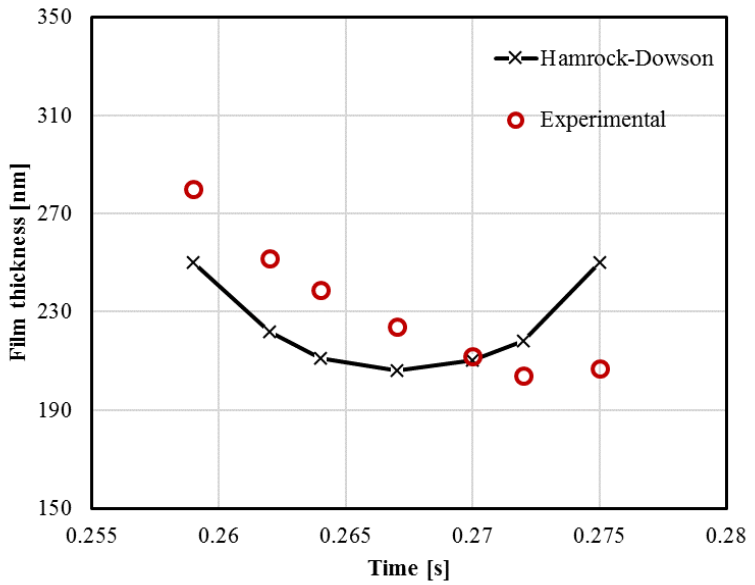

Figure 7.46: Experimental and theoretical central film thickness at ***maximum*** amplitude cycle.

It can be seen that the measured film thickness is larger than the theoretical, steady state value for the load increasing phase and smaller in the load decreasing phase. This is now expected, from the results shown in the pulsating load cycles. It would also be expected that the larger the amplitude of the load variation, the larger the deviation from the steady state condition. During the load increasing phase, central film thickness at three instants of time is shown in figure 7.47. At all amplitudes, the trend of decreasing of the film thickness with increasing the load is obvious. It is also seen that the gradient of the film thickness variation decreases with the decreasing amplitude of load variation, and the gradient is almost in a linear fashion.

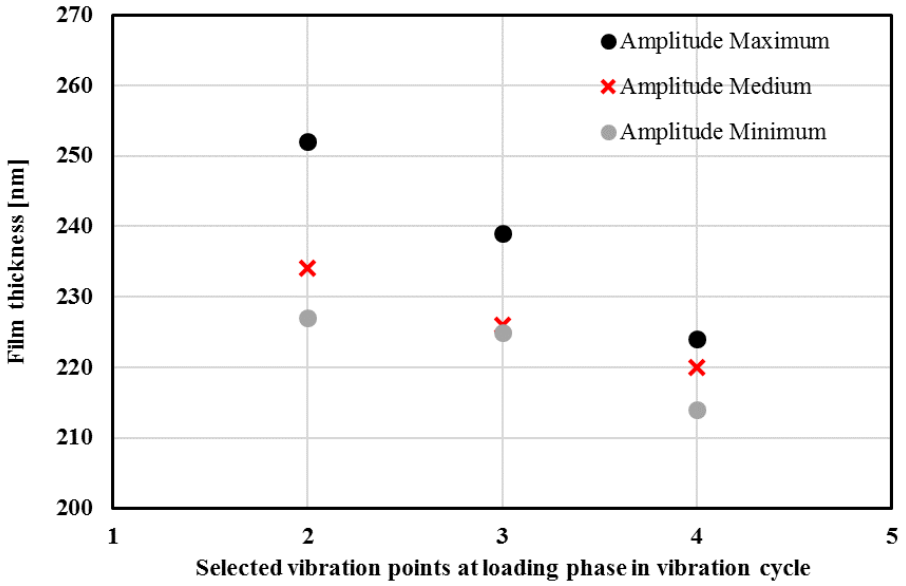

Figure 7.47: Central film thickness at different amplitudes, mean load of 30 N, alternating load cycles.

It is interesting to employ the theoretical formula developed in subchapter 7.3 to see how it predicts the film thickness in case of a load cycle with non – zero minimum load. By denoting the mean load by P_m and keeping P_0 as the amplitude, equation (7.29) can be transformed as follows:

$$\frac{h(t)}{Au_0^{2/3}P_0^{-2/30}} = \left(\frac{P_m}{P_0} + \sin\omega t\right)^{-2/30}\left[1 + \frac{1}{u_0}\left(\frac{RP_0}{36E^*}\right)^{1/3}\frac{\omega\cos\omega t}{(P_m/P_0 + \sin\omega t)^{2/3}}\right]^{2/3} \qquad (7.30)$$

In this equation, the term $Au_0^{2/3}P_0^{-2/30}$ is the constant film thickness corresponding to a load equal to the amplitude of the cycle. In this case, it was preferred to normalise the transient film thickness in this way because it is easier to compare to the experimental values. Figure 7.48 shows the ratio of the theoretical transient and steady state film thickness for a frequency of 60 Hz, 0.1 m/s, for load variation similar to that shown in figure 7.43, that is mean load of 30 N and amplitudes of 29 N, 20 N, and 13 N.

As it can be seen in this figure, the larger the load amplitude, the larger the departure of the film thickness from the steady state value. This is similar to the behaviour shown in figure 7.47. It is also obvious that the three curves meet at a time after the middle of the cycle. For the parameters chosen this time lag is ten milliseconds. This is also in accordance with the experimental results seen above.

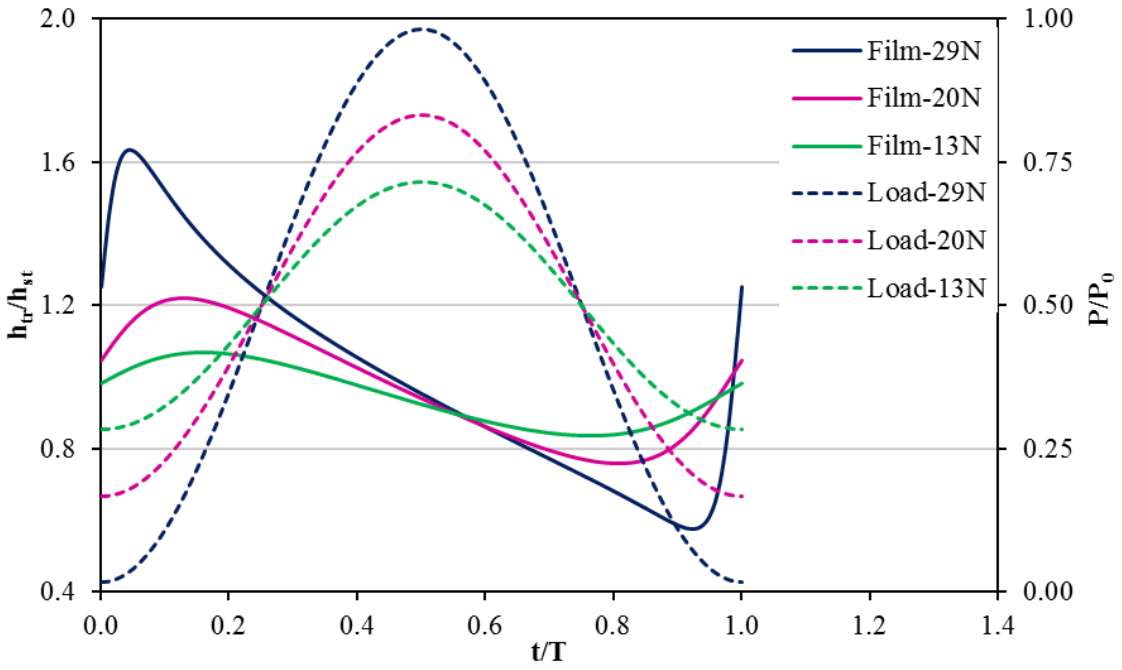

Figure 7.48: Ratio of theoretical transient film thickness and steady state film thickness at various load amplitudes

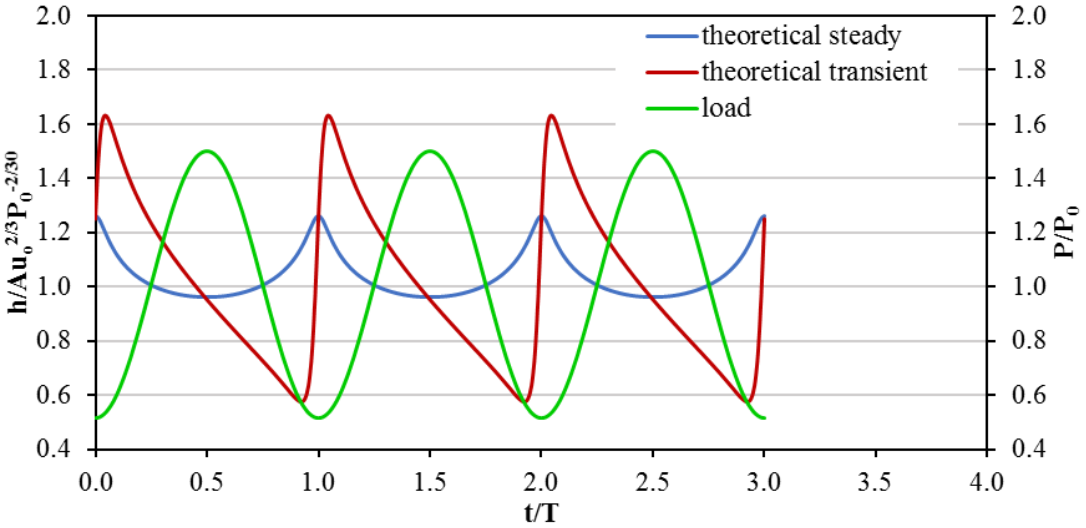

Figure 7.49: Comparison of steady state and transient film thickness

A direct comparison between theoretical steady state (eq. 2.53) with variable load) and transient film thickness is illustrated in figure 7.49, for three cycles of variation of load. The frequency was 60 Hz, the load amplitude 29 N and the mean load 30 N, while the entrainment speed was 0.1 m/s in these simulations. The load is normalised by the amplitude. A comparison between theoretically predicted and measured film thickness, over one cycle is shown in figure 7.50. The blue circles represent the film thickness calculated with Hamrock–Dowson formula (eq. 2.53), using the measured load at different instants of time during the cycle.

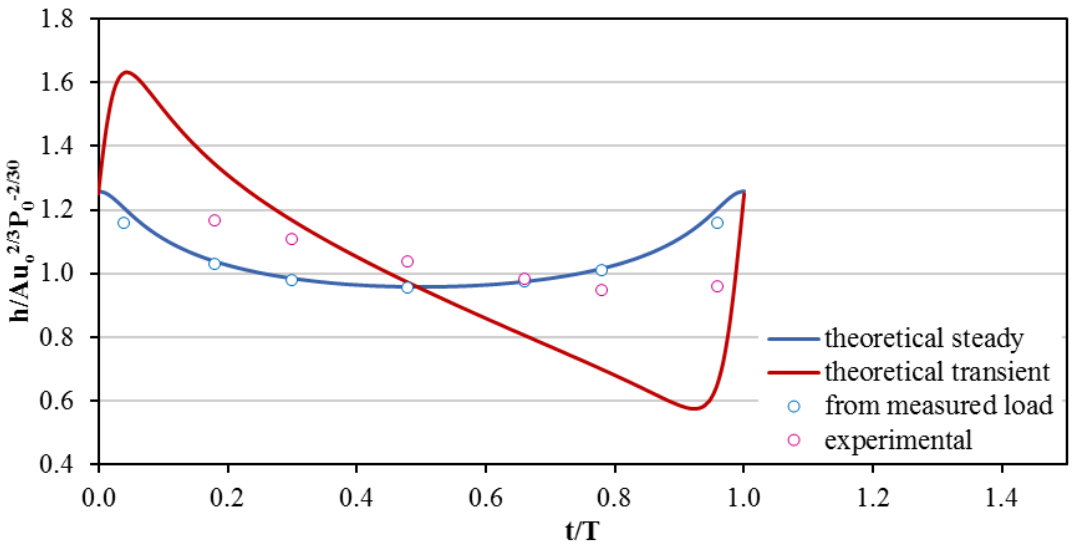

Figure 7.50: Comparison of theoretical and measured film thickness

As seen both the theoretical transient and measured film thicknesses deviate from the steady state values, but the squeeze film effect makes the real film thickness vary less than the theoretically predicted by the transient analysis.

7.8 Summary of occurrence of film thickness perturbation

It is well known that the load changes have small influence on steady state EHD film thickness. Probably, this is why the number of experimental studies carried out on the aspect of vibrating EHD films is much less than the other aspects of transient effects on EHD film, i.e., speed or micro-geometry. Nevertheless, load variation due to vibrations of EHD contacts may be more relevant to practical applications. Previous studies showed that the squeeze effect will generate film perturbations due to a sudden increase of load. This phenomenon becomes significant when both entrainment and squeeze are presented. In practical applications, this type of film perturbation will generate pressure fluctuations, which in turn influences strongly the fatigue life of the contact.

In this research field of lubrication, experimental studies carried out on the effect of dynamic variation of load on the behaviour of EHD point contact are mainly focusing on following directions:

- Pure squeeze [53, 114, 115, 117]
- Pure squeeze combined with sliding motion [118,119]
- Free vibration with pure rolling motion [61, 66, 67, 116, 117]
- Forced sinusoidal vibration [71]

The work described in [71] was the only experimental one so far regarding the effect of sinusoidal variable loading on EHD film, however, the experimental work described was rather limited.

Morales and co – workers [69, 120] recently proposed a simplified, semi-analytical solution to the film thickness fluctuations generated by sinusoidal normal load of EHD film. Their results indicated that film thickness perturbations were introduced by squeeze effect and the change in effective entrainment velocity due to fluctuations of the contact width.

According to the results in the current research, the film thickness will respond differently to variation of load depending whether the two solid surfaces separate completely or not during the cycle. From the point of view of the experimental conditions presented in this thesis, this can be classified as: mean value of variation cycle larger or equal than load amplitude and mean value is smaller than load amplitude. In the first case, the amplitude of the displacement of the vibrating element is smaller than or equal to the cumulative approach of the solids, while in the second is larger. Evidently the second case also corresponds to impact loading of the contact. The systematic research carried out in this thesis fills the gap in the current field and provides a guideline to predicting the occurrence of film thickness perturbation phenomenon.

Mean load larger than amplitude

A graphical summary of film perturbation phenomenon based on the results showed previously is seen in figure 7.51.

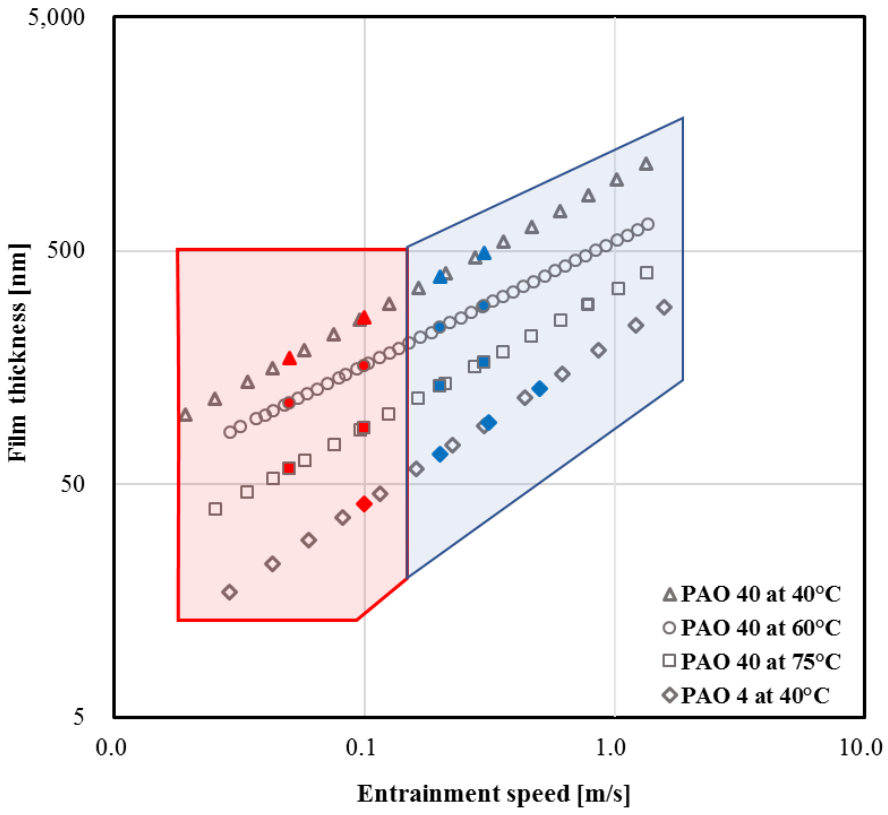

Figure 7.51: Film thickness perturbation map for mean larger than amplitude cycle

Steady state film thickness is shown for four different lubricant viscosities, which appear as straight lines in the logarithmic graph. The grey markers indicate steady state values. Coloured symbols marked within the steady state values, indicating the conditions where vibration tests were performed at any of the working frequencies 10, 25, 50 or 100 Hz. The red markers show the tests when film perturbations occurred, while for the conditions corresponding to the blue markers no significant perturbations occurred. Based on previously discussed results, film thickness perturbation phenomenon is most significant at maximum frequency studied (100 Hz) in the red region, and it is less pronounced at lower test frequencies of 10 Hz and 25 Hz. In the blue region, film thickness perturbation was not observed even at the largest frequency employed in these tests. As a note, this is not a guaranty that film perturbations may not occur at frequencies larger than 100 Hz. Anyway, as seen in these experiments film thickness perturbations do not extend to entrainment speeds higher than approximately 0.1 m/s. This is marked by the blue region in the graph. It thus seems that film perturbation depends on the ratio between the average transient time of the lubricant through the contact and the period of the oscillatory cycle.

Parameter τ, defined as the ratio between the half period of oscillation *T/2* and the average lubricant transit time t_{av} in the loading phase of vibration cycle is used to provide a guideline for the occurrence of film thickness perturbation.

$$\tau = \frac{T}{2t_{av}} \tag{7.31}$$

Analysis of the results shown in previous sections indicates that if τ is greater than 2 no film perturbation occurs, while for smaller values it does. For instance, in the 100 Hz cycle test, the load applied to the EHD contact varied from 1 N to 55 N and the entrainment speed was 0.1 m/s. The diameter of Hertzian contact, in this case, varied between 100 μm and 392 μm and the average lubricant transit time is 2.46 milliseconds. Parameter τ for this case becomes 2.03 which can be taken as 2. For the entrainment speed of 0.2 m/s, τ is obviously double to 4.06 thus results show no film thickness perturbation. Obviously, the value of 2 for parameter τ is only approximate as no tests were carried out at every possible speed in the interval between 0.1 m/s and 0.2 m/s.

More vibration tests are required to be carried out for shaping the more accurate boundary location of the red/blue regions in figure 7.51.

Mean load smaller than amplitude (impact loading)

Figure 7.52 shows film thickness versus entrainment speed in steady state and transient experiments. The transient tests were performed at speeds marked by coloured symbols at 10 Hz, 25 Hz, 50 Hz and 100 Hz. As seen there are no blue symbols, which means that film thickness

perturbations occurred in every single test, no matter the speed, frequency (except the lowest) or lubricant viscosity (overall film thickness).

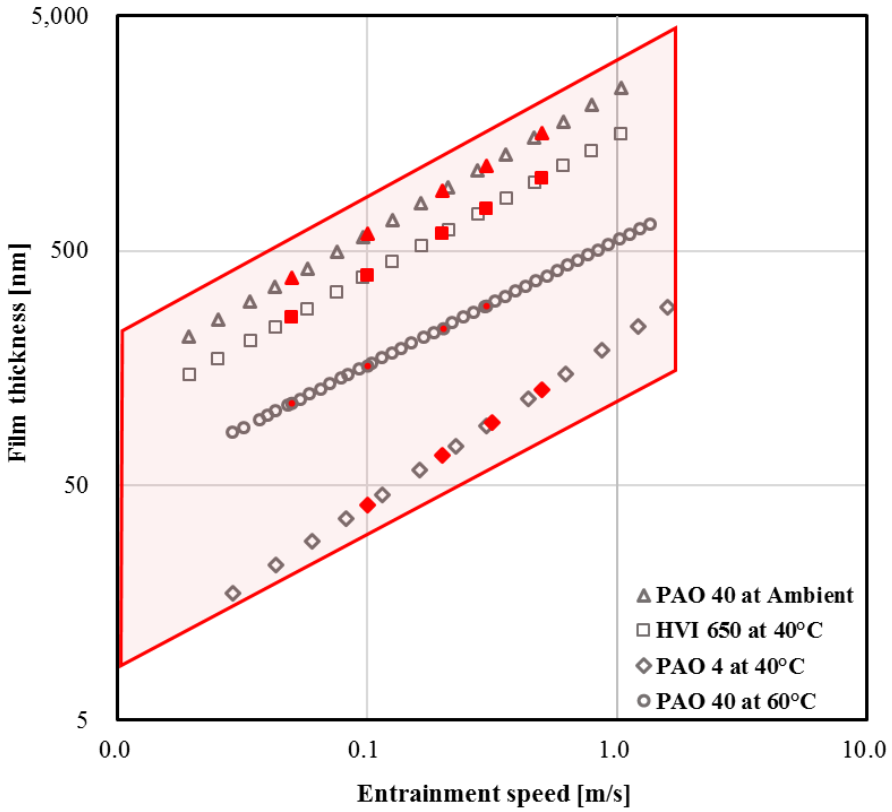

Figure 7.52: Film thickness perturbation map of contact with impact loading

The red region can now be shaped as shown in figure 7.52. Only film thickness values at the maximum load in the cycle is shown in these graphs. It should be speculated that in case of cyclic application of load with impact, film thickness perturbation is generated in any condition of speed that is larger than the speeds employed in these tests, however it may exit the contact before the load has reached the peak value in the vibration cycle.

7.9 The effect of lubricant supply upon lubricant film thickness

One of the objectives of this research is to investigate the behaviour of grease – lubricated EHD films under vibration. The analysis of these results will be presented later in the chapter. In this section, the effect of lubricant supply will be discussed, given the fact that grease lubricated contacts normally suffer from restricted amount of oil in the inlet zone.

In the figure below, three different lubricant supply conditions of the EHD contact are shown, fully flooded (left), partially flooded (middle) and low lubricant supply (right). The inlet meniscus boundary is marked by a yellow line for better visibility for different inlet conditions. There is no inlet meniscus shown in the fully flooded image simply because it is located further away in front of the contact.

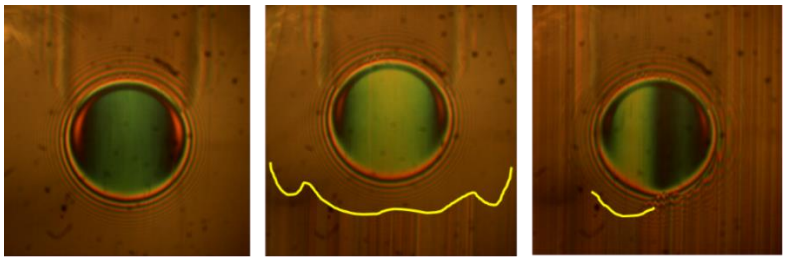

Figure 7.53: Inlet meniscus for different inlet conditions

The lubricant tested is PAO 40 at a temperature of 40°C, and entrainment speed of 0.1 m/s which gives a central film thickness of 214 nm for the fully flooded case. On the other hand, a continuous inlet meniscus can be observed for the partially flooded case, which ensures a uniform film thickness but lower than that of fully flooded condition throughout the contact area. The distance from this boundary to the contact edge is about 59 percent of the contact radius at 109 micrometres. Wedeven et al. [18] carried out a systematic analysis of the EHD films working in starved conditions and concluded that the film thickness depends of the distance where the inlet meniscus is located. The central film thickness is then given by the relationship:

$$\frac{h_0}{(h_0)_f} = \left[\frac{S}{S_f}\left(2 - \frac{S}{S_f}\right)\right]^{1/2} \tag{7.32}$$

In this relationship h_{of} and S_f are the central film thickness under fully flooded condition and inlet distance to achieve a flooded condition, and h_o and S are the same parameters in certain condition of lubricant supply. According to this equation, the film thickness in partially flooded case should be approximately 94 percent of the fully flooded case.

For the low lubricant supply case, the inlet meniscus only covers a small fraction of the contact diameter and it is closer to the inlet edge of the contact. As it can be seen on the left-hand side of low lubricant supply image, the inlet meniscus is located at about 61 micrometres in front of the contact edge. Using Wedeven's equation again, the resulted film thickness is 78 percent of the fully flooded case. On the right-hand side of the low lubricant supply image, the inlet meniscus disappears almost completely. From the ripples in the Newton's rings, the inlet distance can be approximated at less than 25 micrometres. Even for such short inlet meniscus distance, the predicted film thickness calculated in this case is about 50 percent of the fully flooded film thickness. The film thickness profile transversal to the rolling direction, extracted from the low lubricant supply image is shown in figure 7.54. As seen the film thickness in the central region of the contact varies between about 100 nm and 128 nm, which matches well with that predicted by Wedeven's equation.

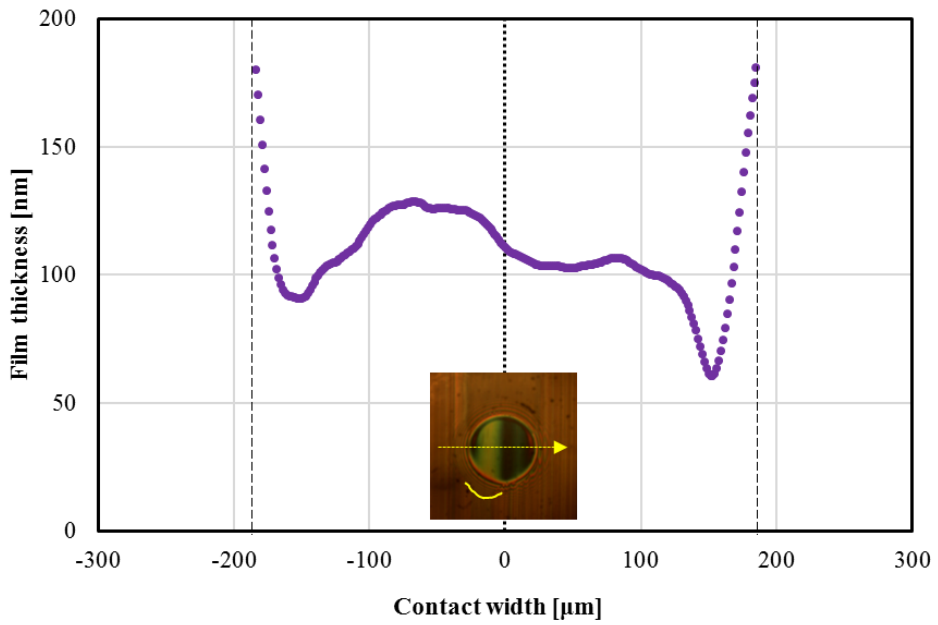

Figure 7.54: Film thickness profile transversal to entraining direction for low lubricant supply steady state condition

It was shown previously in [64] that loading – unloading cycles on grease lubricated, starved contacts help the film recover completely to its fully flooded values. In order to evaluate if this is the case in the present experiments, tests were carried out on which limited supply contacts were subjected to vibrations at various frequencies. Figures 7.55 shows a comparison of typical film behaviour with low lubricant supply under different frequencies of load oscillation.

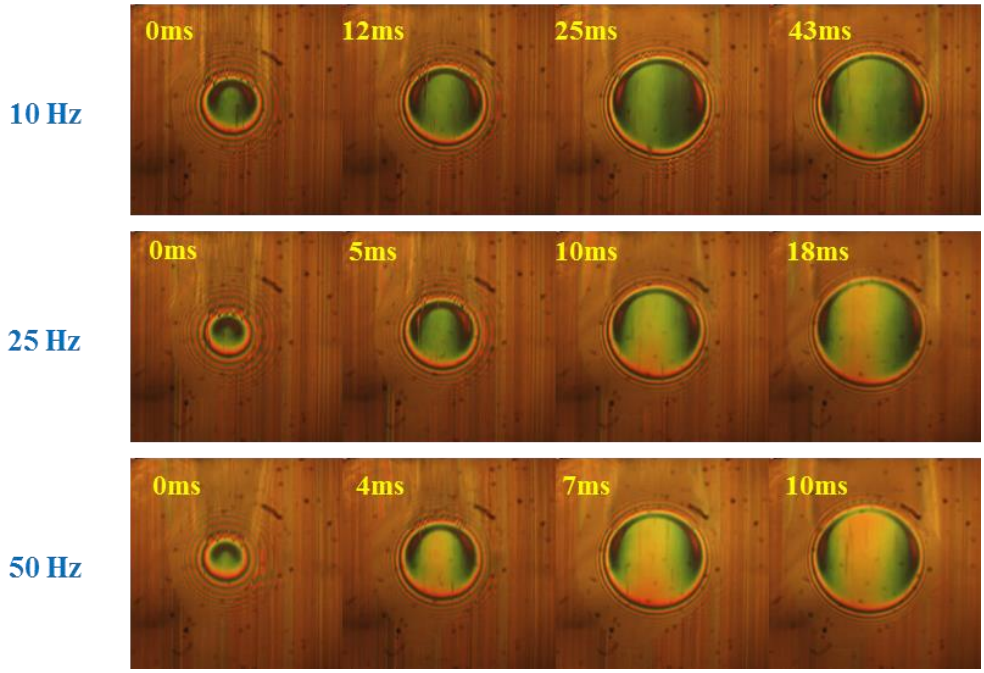

Figure 7.55: Images of contacts under low lubricant supply condition, subjected to vibrations at different frequencies

The first observation extracted from these images is that the film thickness is more uniform over the whole contact area, unlike the steady state case. This may lead to the conclusion that vibrations of the contact have a general effect of levelling somehow the quantity of lubricant in the contact inlet region. To better view and discuss this effect, film thickness profiles in the loading phase of each vibration cycle (in figure 7.55) are extracted and shown in figures 7.56 to 7.58.

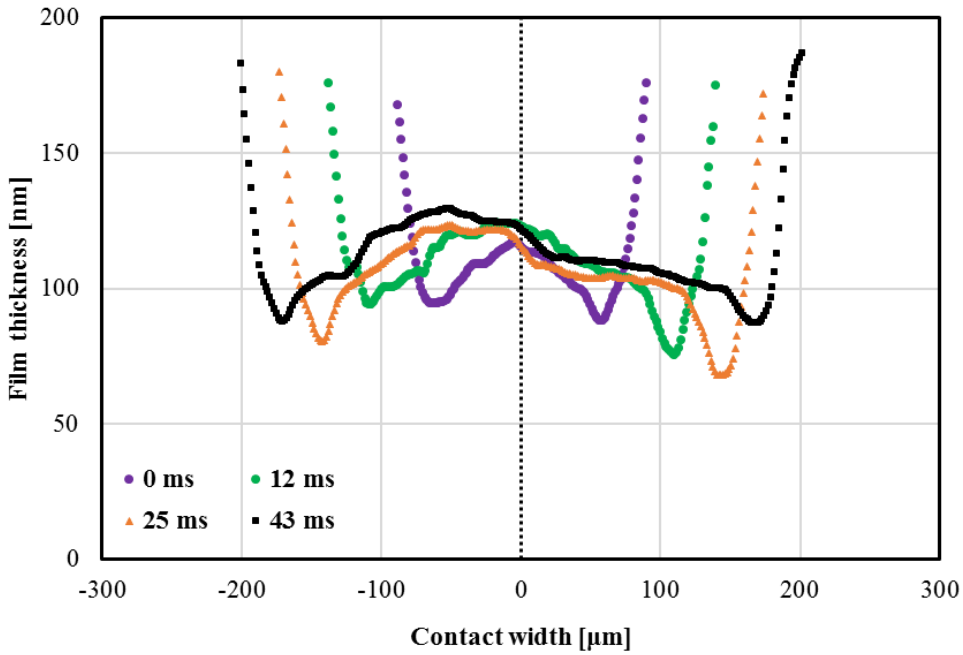

Figure 7.56: Film thickness profiles in loading phase of vibration cycle, **10 Hz**, 0.1 m/s.

As the entrainment speed, lubricant viscosity and amplitude of vibration are fixed, the only parameter which may play a role on levelling the lubricant quantity in the contact inlet is the frequency of the load variation.

As seen the plotted film profiles in figure 7.56, central film thickness increases from 116 nm to 129nm in the loading phase of the 10 Hz vibration cycle. Typical film thickness profiles in the loading phase of vibration cycle at higher frequencies of 25 Hz and 50 Hz are presented in figures 7.57 to 7.58. It can be seen that the film thickness increases in the loading phase for both vibration cycles. At 25 Hz, the film thickness in the central part of the contact increases from 118 nm to about 150 nm while for 50 Hz case it increases from 120 nm to about 172 nm. Although the lubricant flow is controlled by placing wipers in front of the ball and the disc, it is thought that two mechanisms are at play here, which help replenish the inlet zone of the contact. During the loading phase, the contact edge moves rapidly against the entrainment speed thus increasing the later and consequently the film thickness. In the load decreasing phase, a suction action takes place which brings more lubricant in the contact inlet.

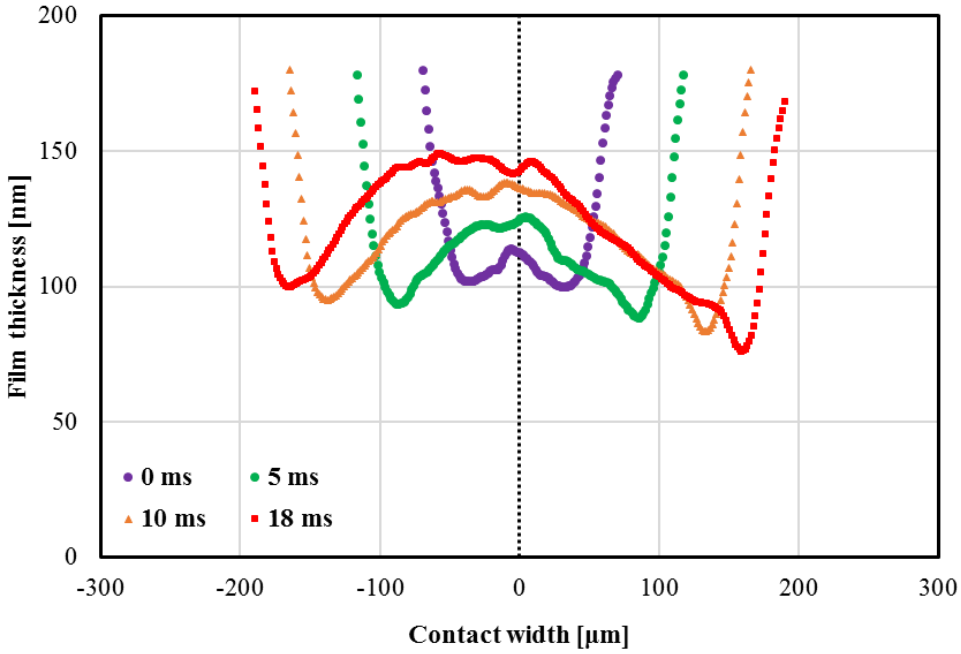

Figure 7.57: Film thickness profiles in loading phase of vibration cycle, **25 Hz**, 0.1 m/s.

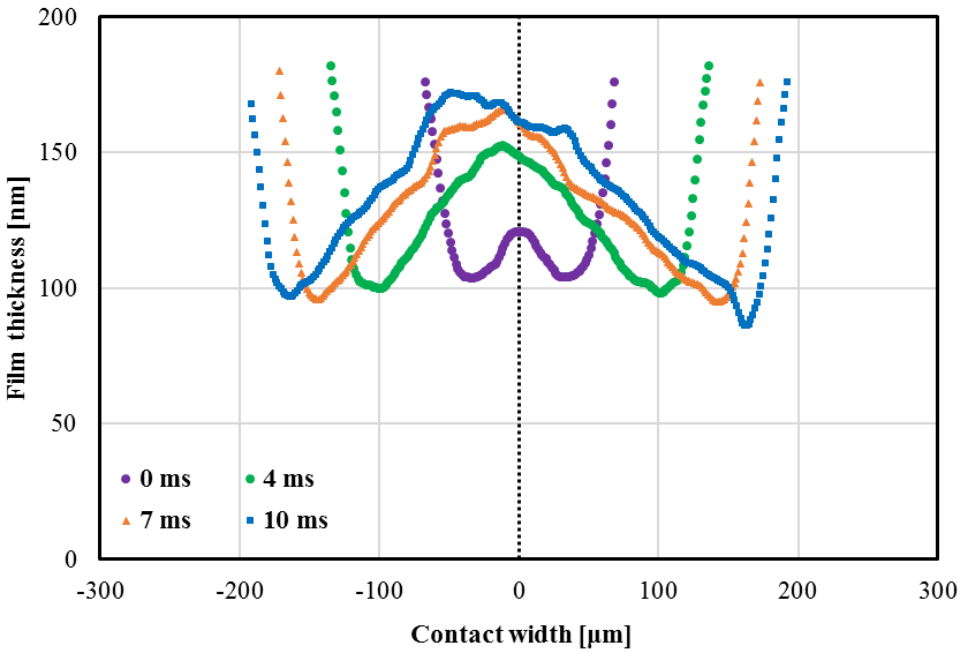

Figure 7.58: Film thickness profiles in loading phase of vibration cycle, **50 Hz**, 0.1 m/s.

Figure 7.59 compares the image of the steady state with those under vibration at peak load within the cycle.

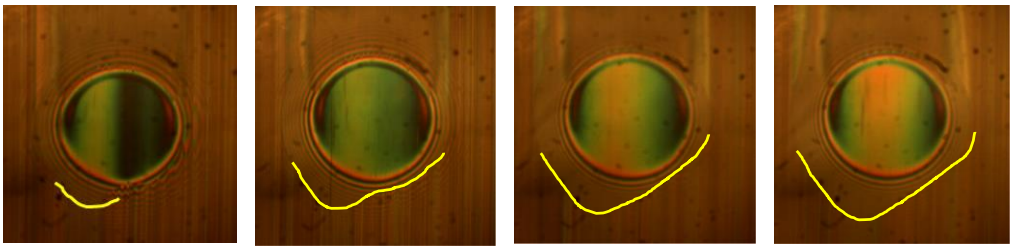

Figure 7.59: Inlet meniscus for steady state, 10 Hz, 25Hz, 50 Hz at peak load.

These images indeed show that the inlet of the contact is better covered by the inlet meniscus at larger frequencies. Compared with the steady state inlet meniscus, it is clear that vibrations have a beneficial effect upon the inlet replenishment mechanism in limited oil supply conditions. Following this trend, it can be speculated that at larger frequencies the inlet distance enhancement would be even stronger, however tests at frequencies larger than 50 Hz led to very rapid destruction of the silica layer before any meaningful images could have been recorded.

In order to summarise the conclusions of these tests, film thickness profiles extracted from the images of figure 7.59 are compared in figure 7.60. The trend of increasing the central film thickness with the frequency is obvious.

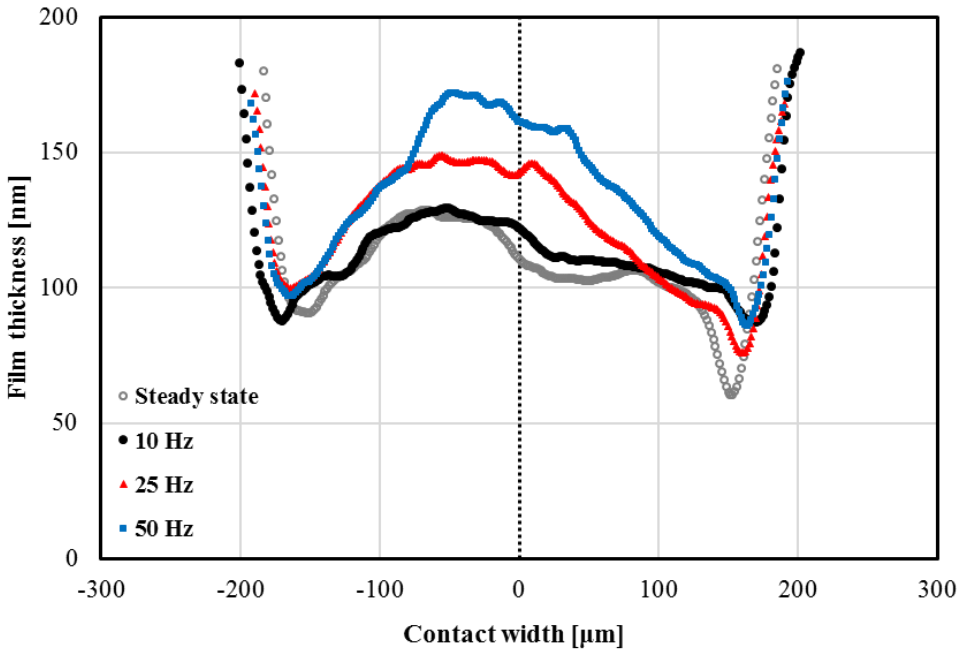

Figure 7.60: Film thickness profiles for different frequencies at peak load

The maximum film thickness is about 35 percent larger for 50 Hz than it is for the 10 Hz test. These results showed that vibrations have a beneficial role in the formation of the EHD film at low lubricant supply condition, helping the supply of the contact inlet, lowering the degree of starvation and resulting in larger film thickness.

7.10 Analysis of grease and base oil vibration results

Before discussing the experimental results of three types of greases studied one of the base oil results (SBM Base oil at 40°C) will be analysed first as reference. Due to low durability of the silica spacer layer in severe starved conditions typical to grease tests especially at higher frequency, 60 Hz is set as the maximum frequency for these tests. Lower frequencies test results with base oil can be referred to Chapter 6. In the light of the findings showed in earlier sections, only the results of 60 Hz at various entrainment speeds will be discussed further. The amplitudes during different tests may vary about ±5% due to hand adjusting the amplifier of dynamic shaker, however the minimum load applied to the contact is kept above zero, as seen in figure 7.61. This means that no impact loading occurred in these tests.

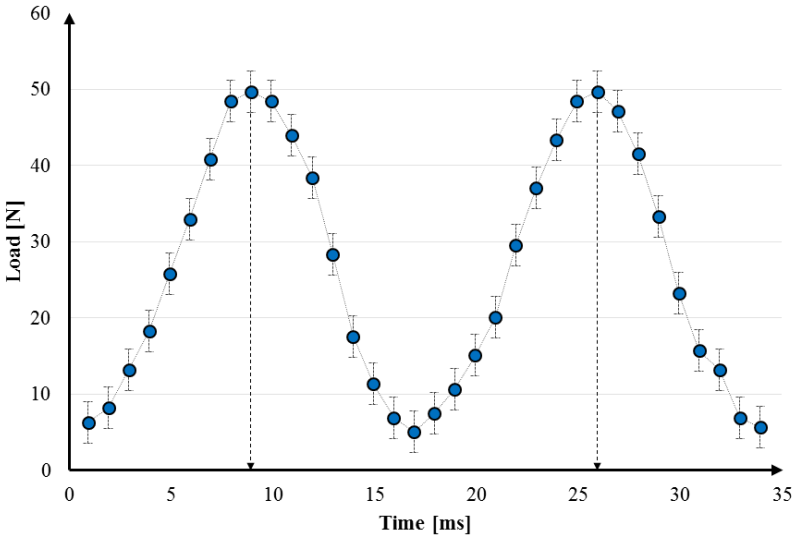

Figure 7.61: Typical load variation in 60 Hz vibration cycles of SBM base oil tests

Figures 7.62 to 7.66 show the analysed film thickness profiles of selected coloured interferograms in a complete loading-unloading vibration cycle with an entrainment speed range from 0.1 m/s to 0.9 m/s. Entrainment speeds larger than those employed in previous sections were chosen in these tests for two reasons: they are more relevant to practical applications, for example rolling bearings which are mainly grease lubricated, and in the present tests the effect of vibrations upon contact replenishment was sought rather than the generation of film perturbations.

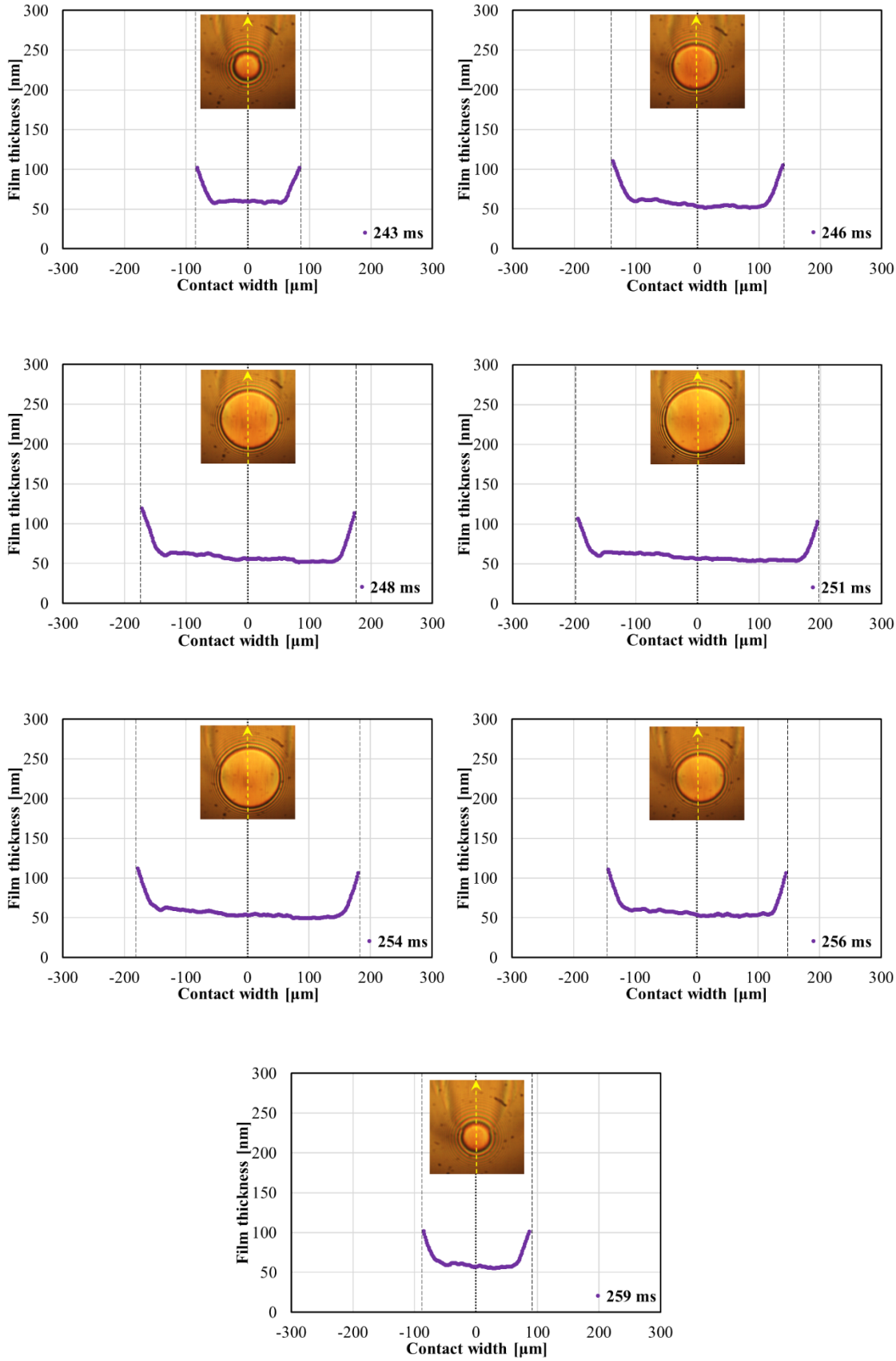

Figure 7.62: Coloured interferometry images and film thickness profile longitudinal to the entraining motion, SBM Base oil at 40°C, 60 Hz, 0.1 m/s.

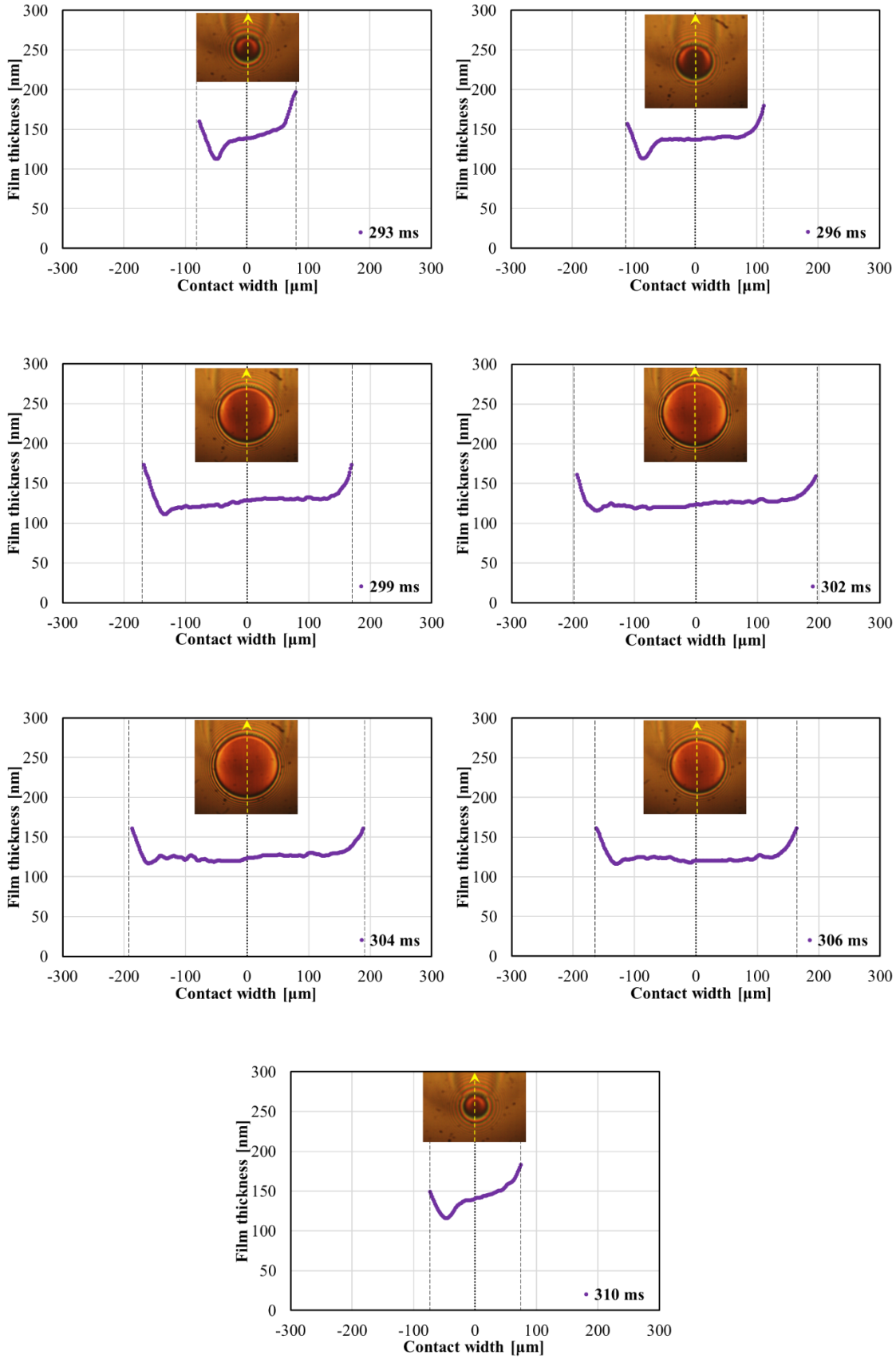

Figure 7.63: Coloured interferometry images and film thickness profile longitudinal to the entraining motion, SBM Base oil at 40°C, 60 Hz, 0.3 m/s.

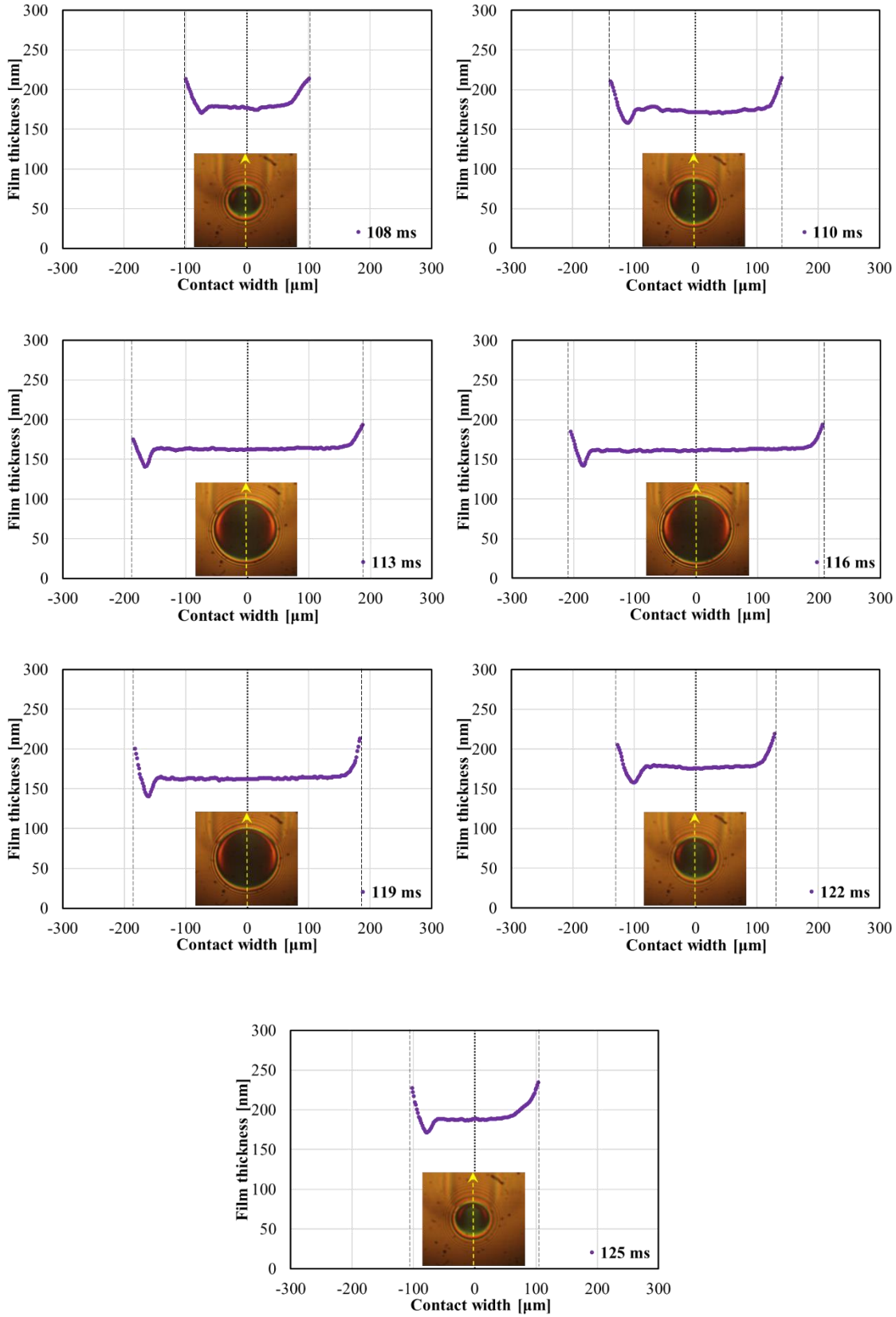

Figure 7.64: Coloured interferometry images and film thickness profile longitudinal to the entraining motion, SBM Base oil at 40℃, 60 Hz, 0.5 m/s.

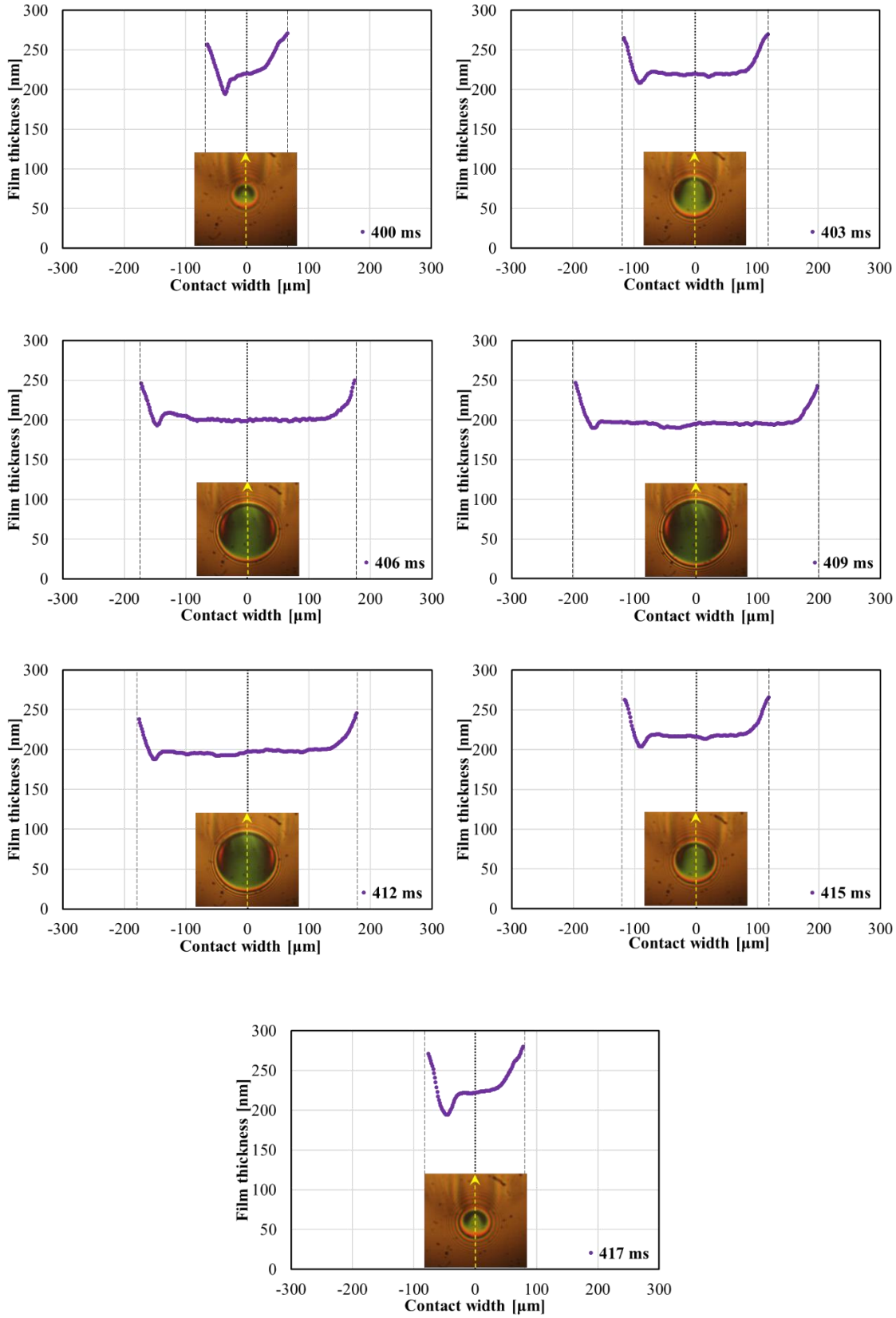

Figure 7.65: Coloured interferometry images and film thickness profile longitudinal to the entraining motion, SBM Base oil at 40°C, 60 Hz, 0.7 m/s.

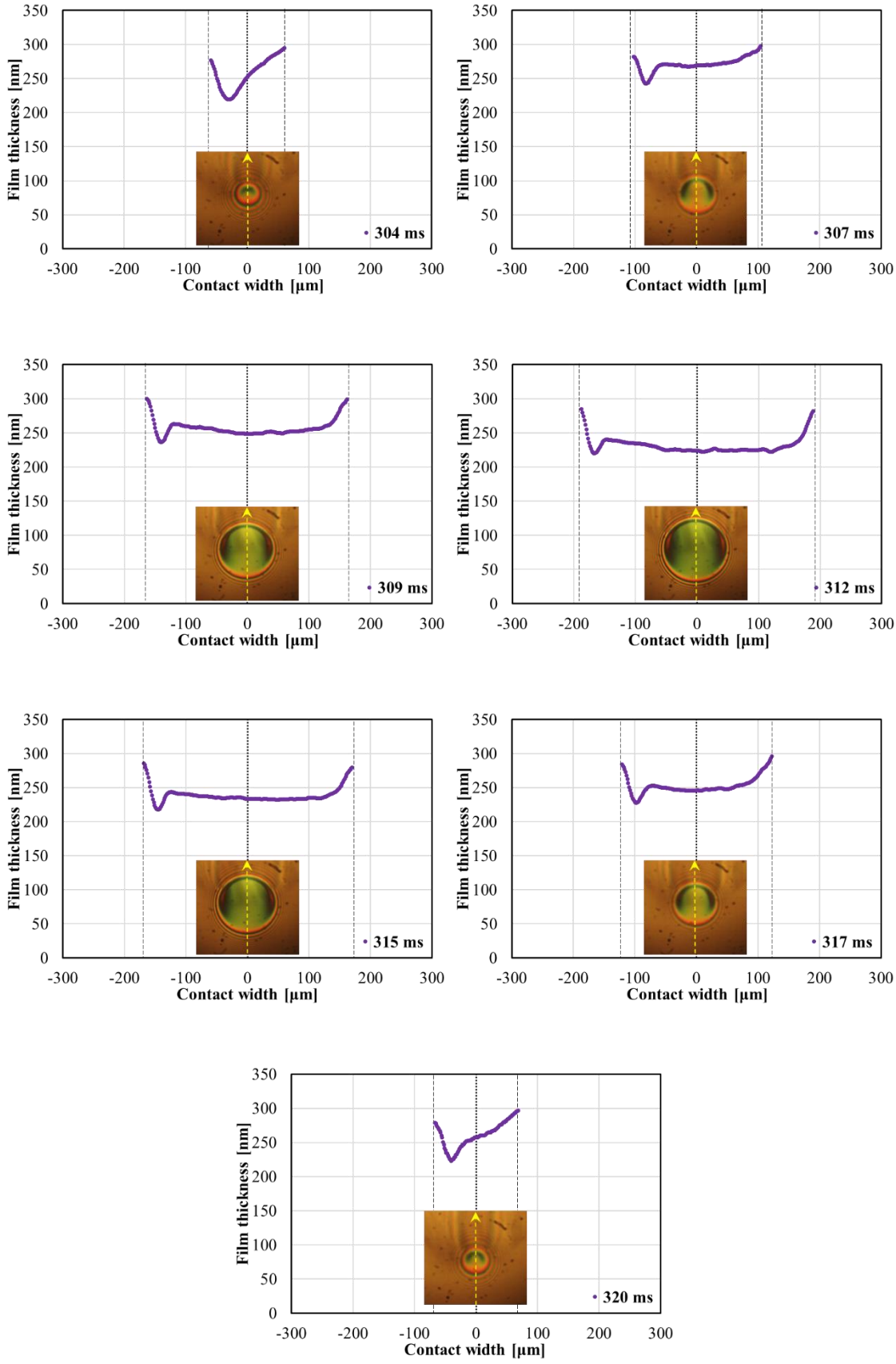

Figure 7.66: Coloured interferometry images and film thickness profile longitudinal to the entraining motion, SBM Base oil at 40°C, 60 Hz, 0.9 m/s.

It is well known and mentioned before EHD film thickness is established by the conditions in the inlet region of the contact. A sudden increase of load at the beginning of the load variation cycle will rapidly expand the contact size. Thus, the region where film thickness is formed moves towards larger separation between surfaces and a film perturbation is generated and subsequently passes through the contact at average speed of surfaces. Overviewing of the interferograms and their analysed film thickness profiles longitudinal to the direction of entraining motion in figure 7.62 to 7.66, it shows no film thickness perturbation phenomenon for the entire range of entrainment speed studied. In terms of the findings showed in previous discussion sections, the oil film perturbation generated is mainly dependent on two parameters, entrainment speed and frequency. The reason for unnoticeable film thickness perturbation is the fact that the time of lubricant transit through the contact is much smaller than the period of the oscillatory motion. For example, the load increases from valley to peak values in about 8.3 milliseconds for the 60 Hz tests, while the time of lubricant transit changes from about 1 milliseconds to 3.2 milliseconds. According to the proposed ratio between the average lubricant transit time in half period t_{av} and half period of oscillation *T/2* in previous section, τ is equal to 2.95 at the entrainment speed of 0.1 m/s thus significantly larger than the threshold value of 2 which is the limit at where film perturbations were produced. As the entrainment speed increases, this parameter will be continuously greater than 2 thus no film thickness perturbations are expected to be observed. Thereby, the results showed so far are in complete agreement with the findings from previous discussion sections.

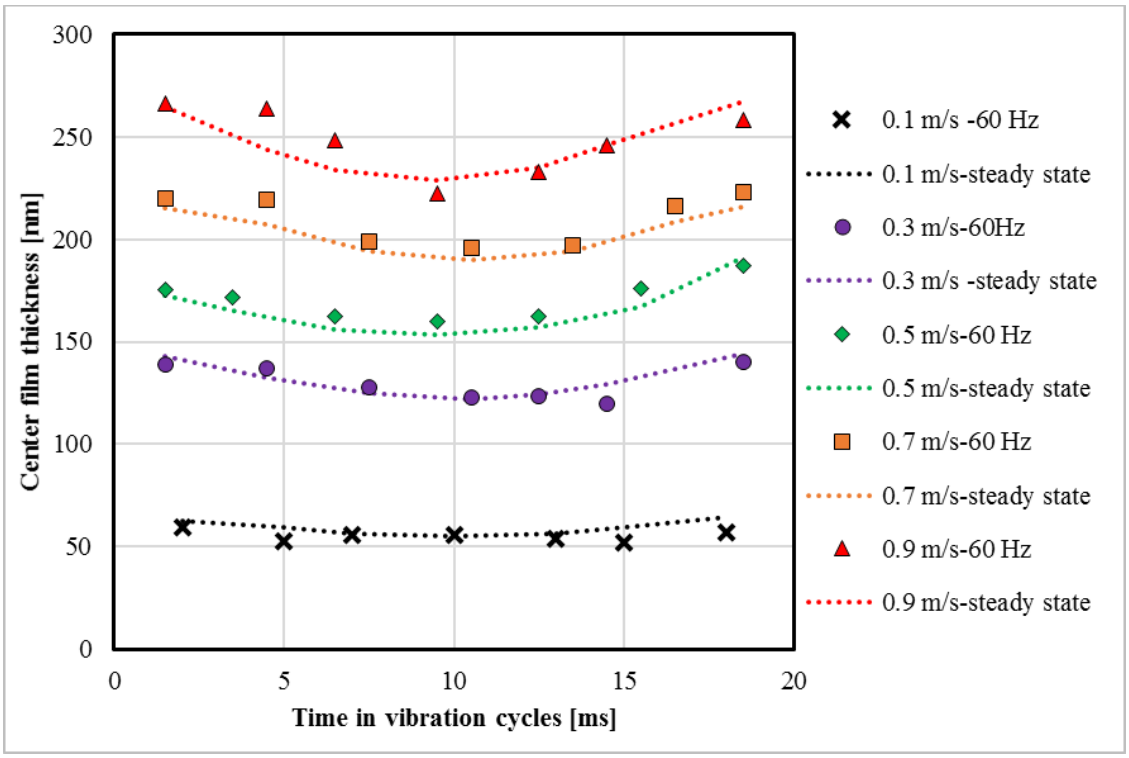

Figure 7.67: Comparison of transient and steady state film thickness in 60 Hz vibration cycles

A comparison of central film thickness at various entrainment speeds for SBM base oil is shown in figure 7.67. Except for the lowest speed of 0.1 m/s where the deviation from the steady state values is obvious, albeit not too large, at all the other values of the entrainment speed the transient film thickness follows the steady state predictions, within the error of the method. This is in complete agreement with the discussion detailed in previous sections.

7.11 Starved grease lubricated contact under vibration

7.11.1 Transition from fully flooded to starved grease lubrication

Steady state test results for the three tested greases and their base oils have been shown in the previous chapter. As the current section is concerned with the contact replenishment after starvation, the conditions of occurrence of starvation for all greases were analysed first. Film thickness as a function of rolling speed for all three tested greases is compared in figure 7.68.

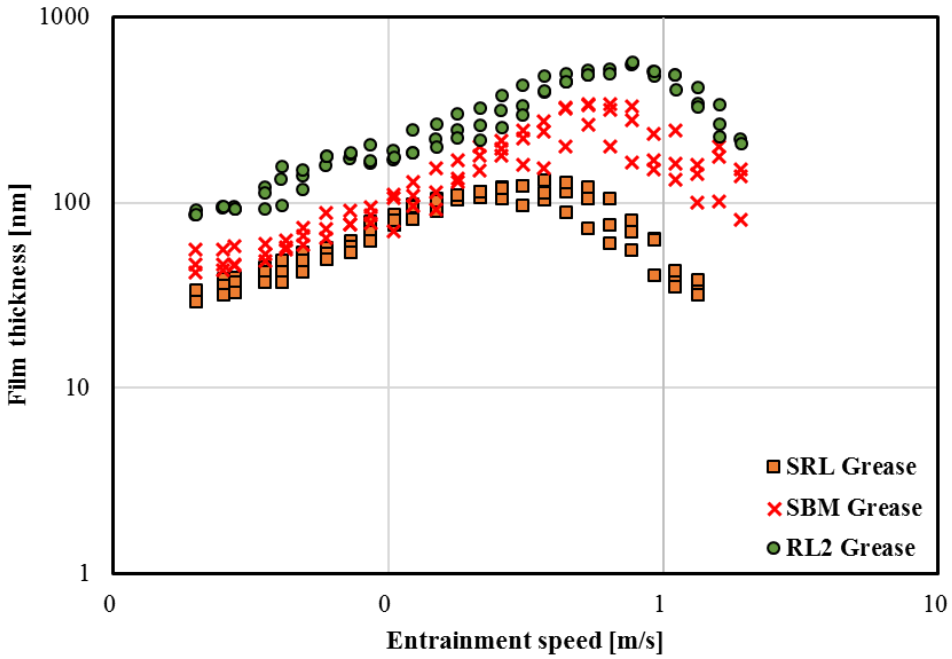

Figure 7.68: Comparison of film thickness of three tested greases in steady state conditions

Figure 7.68 allows the evaluation of the speed for the onset of starvation for **SRL**, **SBM** and **RL2** greases: 0.38 m/s, 0.55 m/s and 0.77 m/s respectively. As shown previously by other authors, the transition between fully flooded and starved contact depends on lubricant composition. Figures 7.69 to 7.71 show the film thickness profiles during fully flooded and starved conditions of the three tested greases. As seen, the film thickness has dropped nearly 95 percent of its fully flooded value for all three greases at their constant starved entrainment speed after different time intervals of pure rolling.

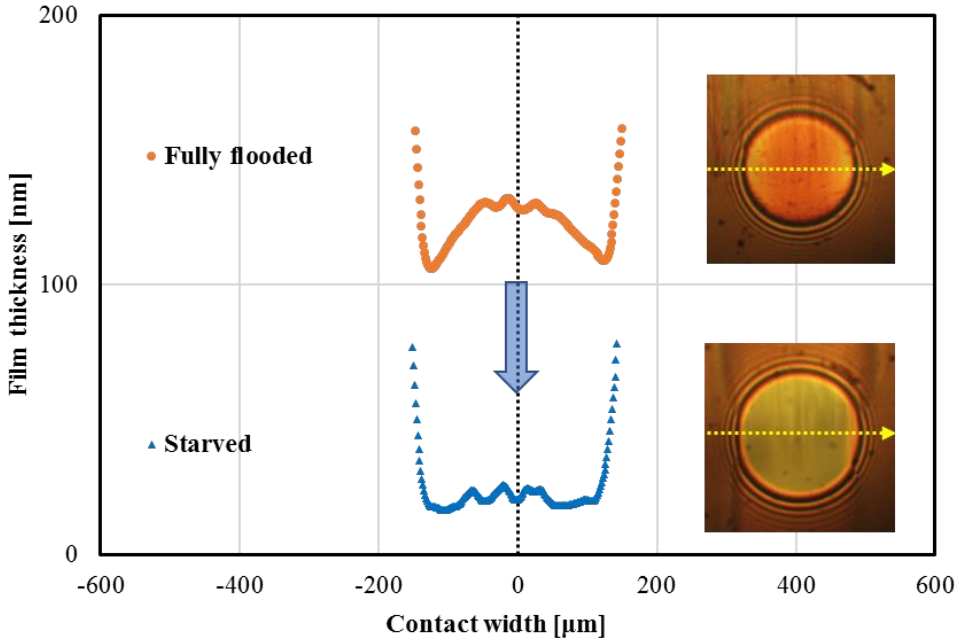

Figure 7.69: The transition from fully flooded to starved condition for **SRL** grease

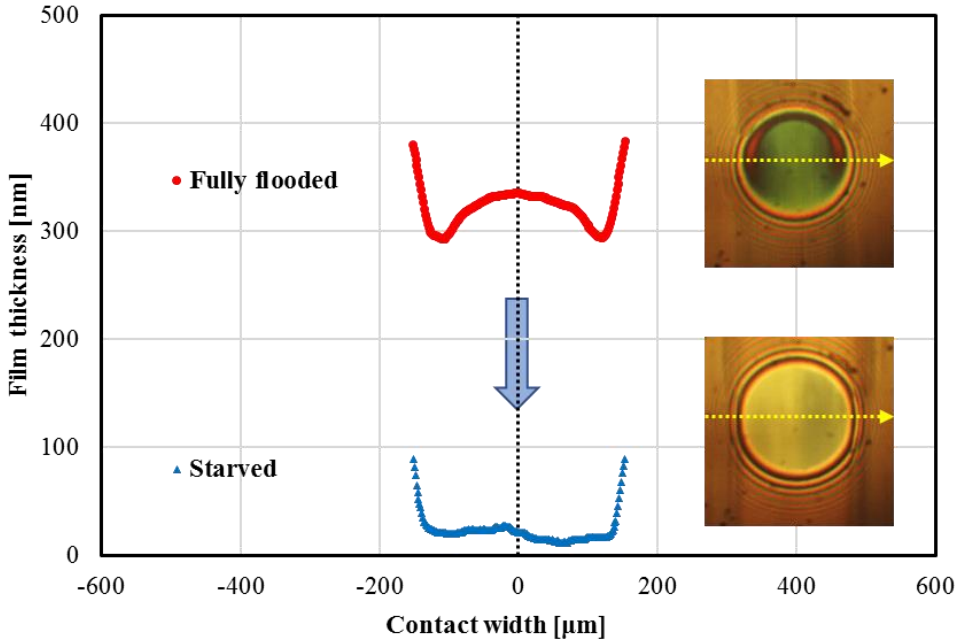

Figure 7.70: The transition from fully flooded to starved condition for **SBM** grease

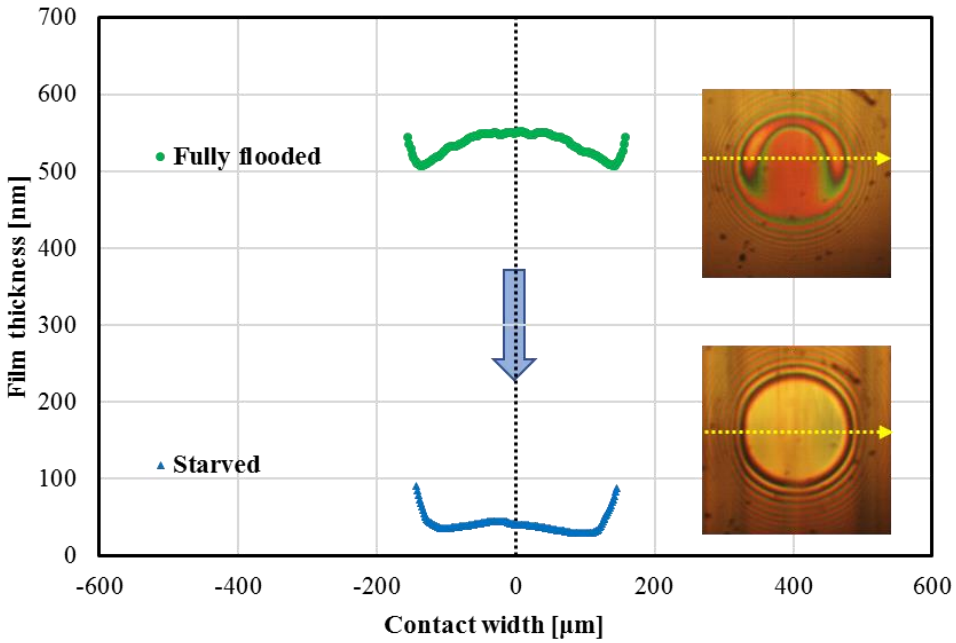

Figure 7.71: The transition from fully flooded to starved condition for **RL2** grease

Film thickness profiles are calculated in the direction transversal to the entraining motion. The ridges formed by grease at the sides of the contact can also be observed. This film thickness in starved condition is not constant but changes by about ± 15 nm during all the steady tests. It is also not uniform over the contact area, although visual inspection of the images captured show a dominant light blue colour which is very close to the colour of the bare silica layer. Thus, it will be easier to compare the behaviour of the contact and film thickness recovery process for different greases under the subsequent forced sinusoidal vibrations. This analysis is carried out in the next section.

7.11.2 The behaviour of starved grease lubricated contacts under vibration

It is well documented and showed in the previous section that in steady state conditions grease – lubricated EHD contacts eventually become starved after a number of revolutions at a certain speed. The question which this section tries to answer is to which extent vibrations applied to the contact helps recovery of the film thickness.

As shown in the results chapter, the grease lubricated contacts were rolling at the speed where starvation started to occur for certain time until starvation fully settled in, then forced sinusoidal vibrations were applied to the EHD contact. Images of the contact started to be recorded every 5 minutes' interval and were further recorded up to 20 minutes. Typical interferometry images and film thickness profiles transversal to the direction of entraining motion, in 60 Hz vibration cycle after five minutes' vibration period can be seen in figures 7.72 to 7.74.

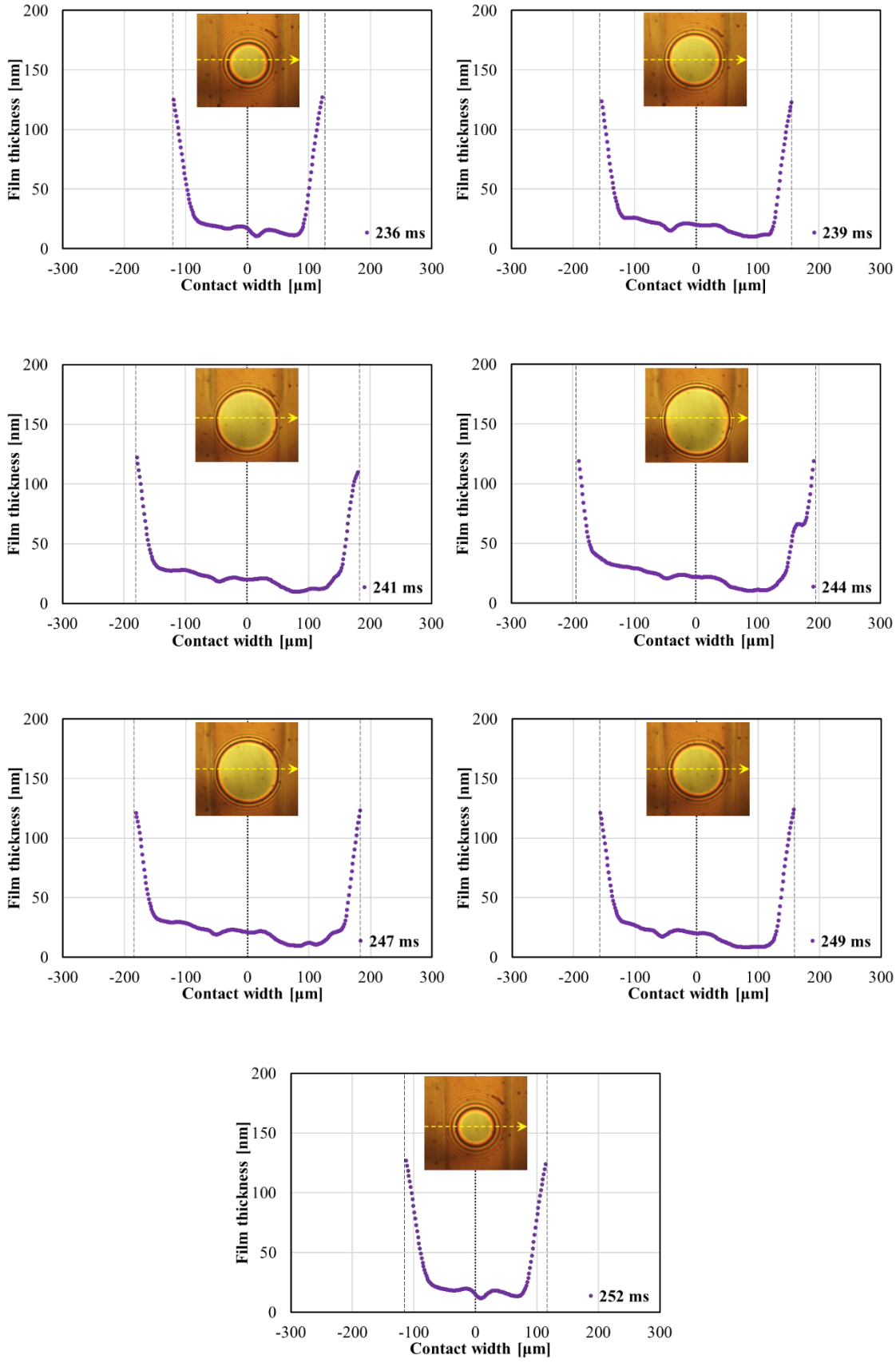

Figure 7.72: SRL grease after 5 minutes under 60 Hz vibration

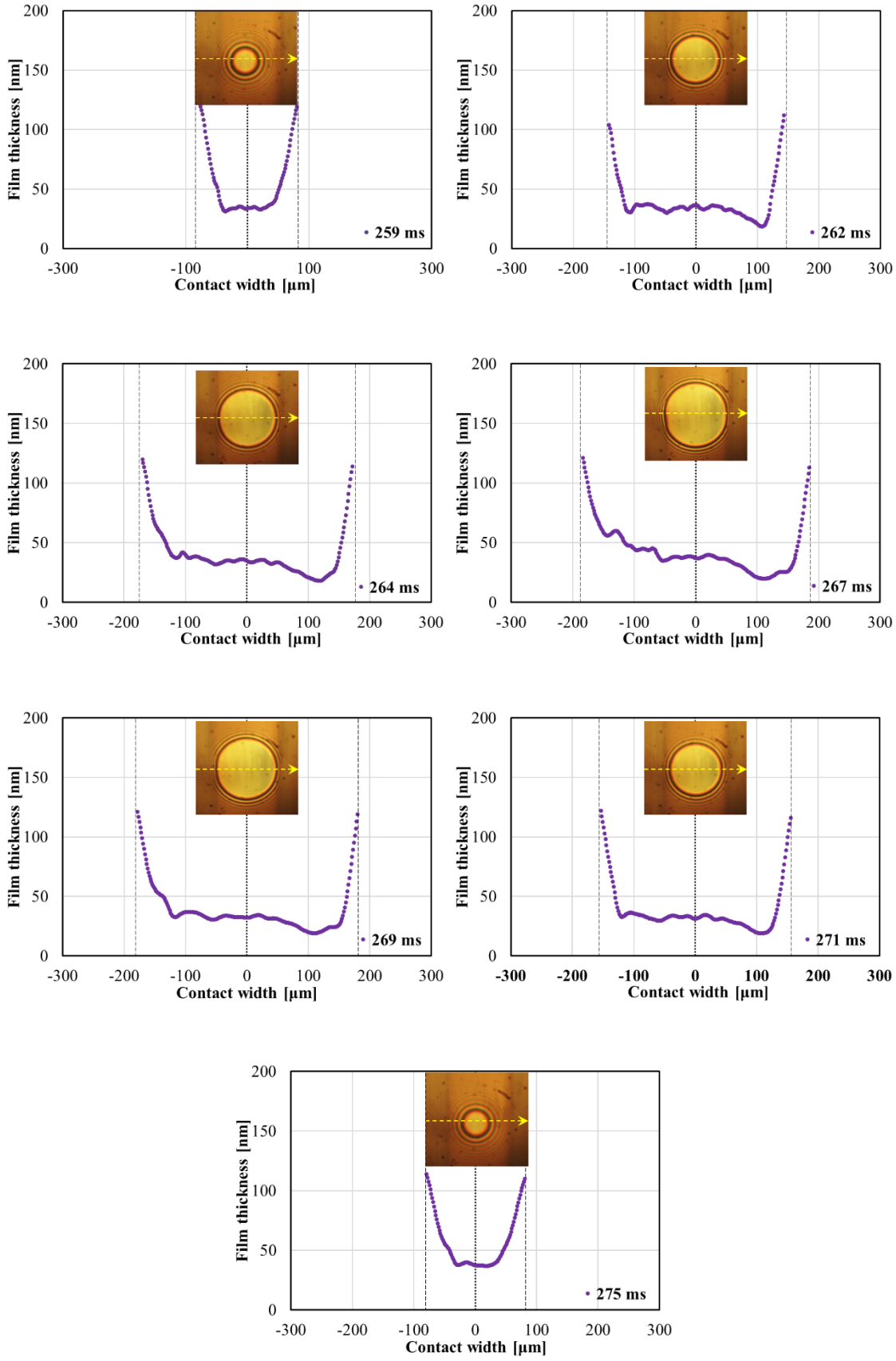

Figure 7.73: **SBM** grease after 5 minutes under 60 Hz vibration

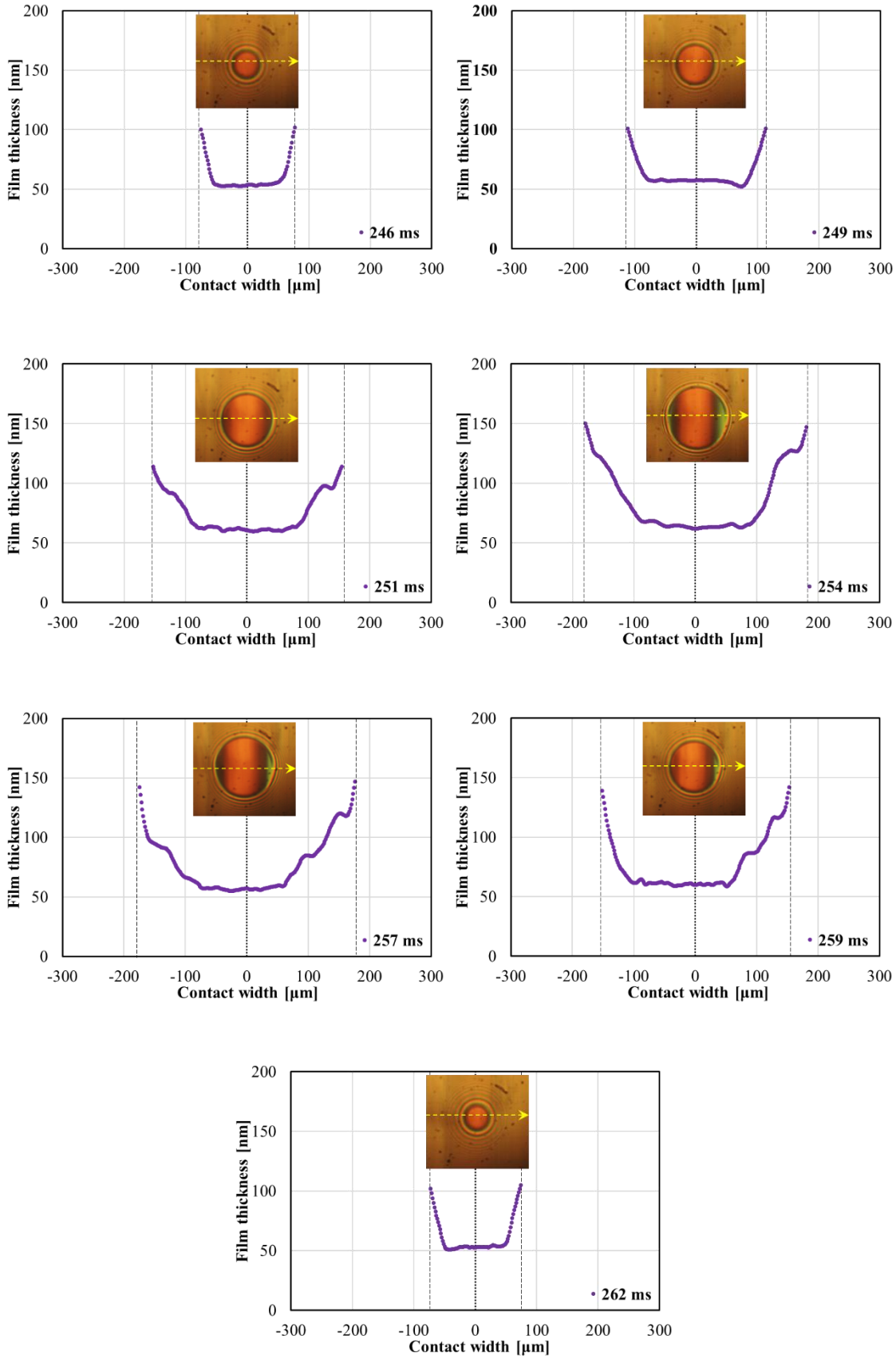

Figure 7.74: **RL2** grease after 5 minutes under 60 Hz vibration

Cann and Lubrecht [64] have found that cyclic loading and unloading, of grease – lubricated, starved contacts, helped track replenishment and film recovery. In their conditions, the lubricant film thickness recovered to up to 75 percent of the initial fully flooded thickness. In the current experimental conditions, and for the greases tested, this kind of strong film thickness recovery was not found. It can be observed that the inlet of the contact still to be depleted of lubricant and more or less as it was in the steady state conditions, shown in the previous section.

On the other hand, it can be seen that vibrations provide a mechanism for replenishing the contact from the side ridges of the contact. It is however noticed that the oil replenished form the side does not significantly change the value of the film thickness in the centre of the contact. As the loading – unloading cycle takes place, the oil bled from the side ridges is pushed sideways sixty times in a second, thus it does not have time to spread towards to central part of the contact, where the contact pressure is large.

In real applications in rolling element bearings, there is a combination of more than one mechanism for replenishing the contact: according to the research in the field, surface tension, centrifugal forces, forced or self – induced vibrations and lateral oscillations of the contact all contribute to track replenishment. Chiu [19] found that surface tension replenishes the contact only up to the point where oil layer at track edges is thicker enough to be retained against centrifugal force. Obviously, this is not the case for the current study.

Under the conditions of the current tests, analysis of film profiles under vibration indicate that sinusoidal variation of the load does not significantly reduce the severity of starvation of grease lubricated contact even at the largest frequency (60 Hz) tested. It helps nevertheless the film recovery to levels, which may prove important in applications where surface asperities are very small, like in rolling element bearings. In order to support this statement, the following figures compare the central film thickness, under vibrations at different frequencies, that is 10 Hz, 20 Hz, 40 Hz and 60 Hz.

Figures 7.75 compare central film thickness of SRL grease lubricated contact under steady state and vibration conditions. The central film thickness is averaged over the whole contact area and at different intervals of vibration that is 5 minutes, 10 minutes, 15 minutes and 20 minutes. Error bars of ±5% are also included in the transient results. In comparison to steady state conditions, a small film thickness recovery can only be observed at 10 minutes and 15 minutes period vibration, at 20 Hz. For these tests, the film thickness is about 12 percent and 22 percent of its fully flooded value respectively. This may be explained by the fact that the rate of pushing the oil towards the periphery of the contact is lower at smaller frequencies, which allows capillary flow of tiny amount of base oil back onto the track. At higher frequencies, SRL grease central film thickness does not show a change under vibration.

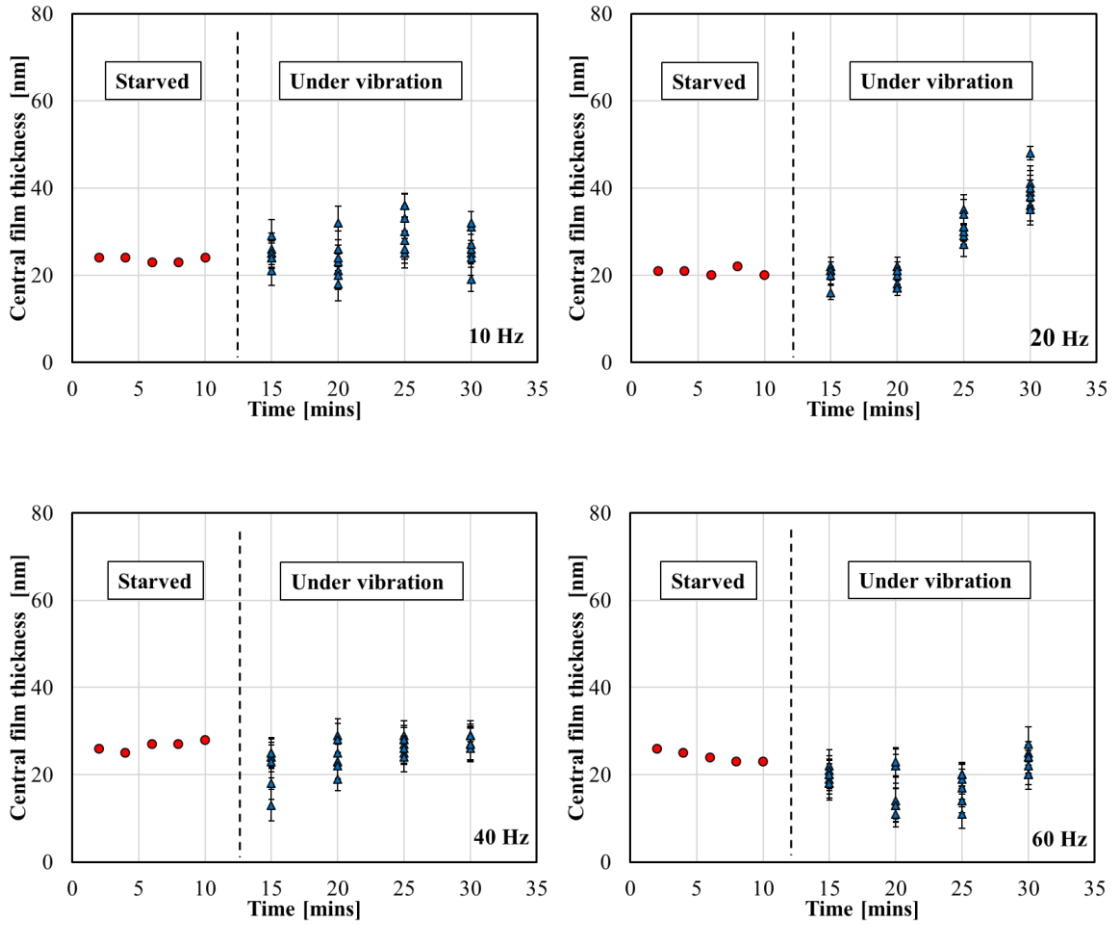

Figure 7.75: **SRL** grease central film thickness under steady state and vibration conditions

Figures 7.76 compare central film thickness of SBM grease lubricated contact under steady state and vibration conditions. Unlike the previous case, for the SBM grease, the strongest recovery is observed at the highest frequency tested and it is about 9 percent of the fully flooded condition. For the lowest frequency tested, no film recovery is observed. Although not very strong the recovery seems in this case to increase with the frequency of the load variation.

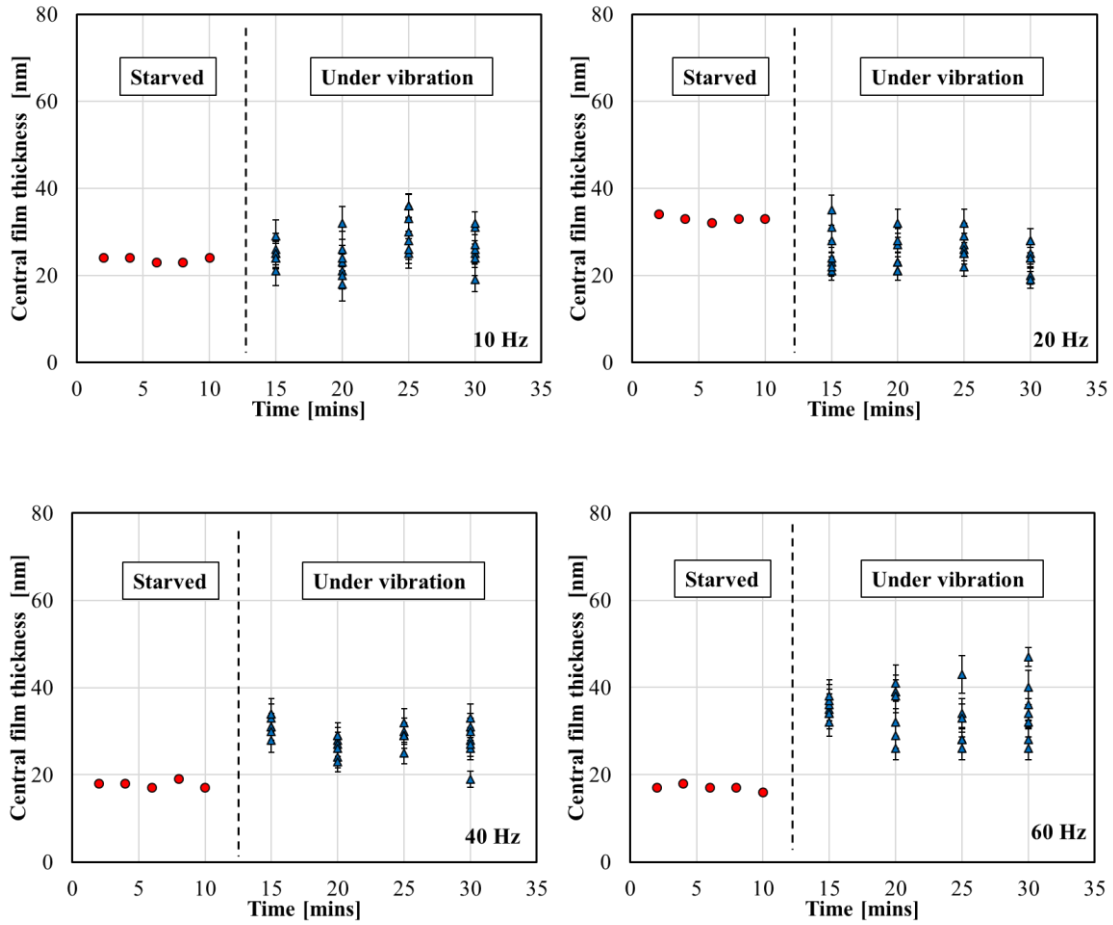

Figure 7.76: **SBM** grease central film thickness under steady state and vibration conditions

Finally, figures 7.77 compares central film thickness in steady state and transient conditions for the RL2 grease. The strongest recovery is observed again at the highest frequency and it is about 11 percent of the fully flooded condition.

It is believed that, over a long period under vibrations, an equilibrium is reached between the mechanisms of surface tension, centrifugal force, and the suction action during the unloading phase of the vibration cycle consequently the film thickness in the centre does increases slightly.

After a longer period, the equilibrium film thickness is a relatively small fraction of the fully flooded film thickness and is dependent of the composition and physical properties of the corresponding base oil.

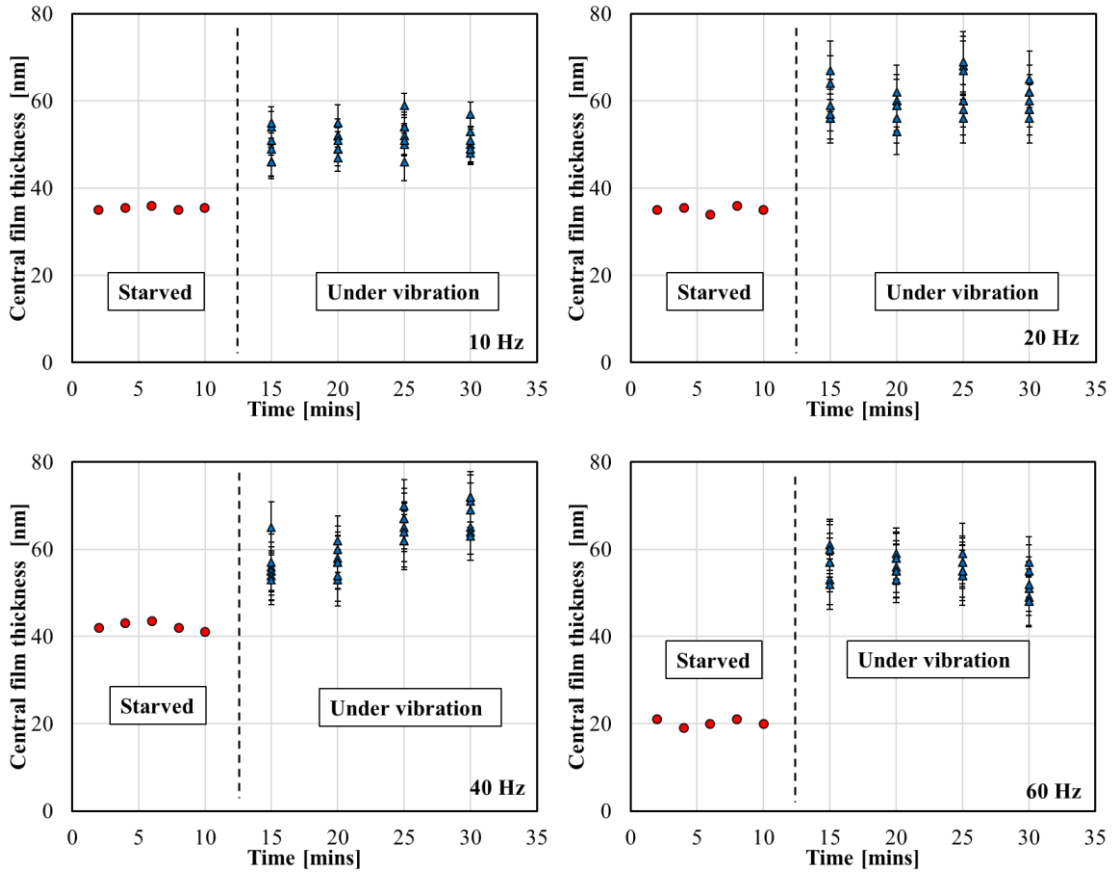

Figure 7.77: **RL2** grease central film thickness under steady state and vibration conditions

7.12 Conclusions

The analysis of the results of the EHD films subjected to harmonic variation of load has shown that the film behaves differently whether the two solid bodies separate or not during vibration. When they do separate, that is the case when the mean cyclic load is larger than the amplitude, a film perturbation (also called dimple or entrapment in other studies) forms in the centre of the contact at the beginning of the impact. Film perturbations would normally travel through the contact at the average speed of the surfaces (entrainment speed) however in the case of rapid increase of the load, the perturbation formed in the centre of the contact appear to travel slower until they exit the contact. This due to the fact that contact dimensions expand during the load increasing phase thus the effective velocity is smaller than the steady state velocity of the surfaces. These experiments have shown that the perturbation moves at an effective entrainment speed equal to the difference between the average speed of the surfaces and the speed of change of contact radius. As the contact expands the effective entrainment velocity in the inlet is the sum of these two components, thus a thicker film is formed. This thicker film moves in the direction of entrainment generating ripples through the film thickness.

In the case when the two solids, disc and ball in these experiments, do not separate no fluid entrapment is formed in the centre of the contact. Instead, the entrainment speed enhanced by rapid contact expansion generates in the inlet a film thicker than that corresponding to steady state conditions. This enhanced film also appears as a perturbation which, like in the previous case, travels through the contact at a velocity equal to the effective entrainment speed defined earlier.

Tests carried out at increasingly larger entrainment velocity have shown that the film perturbation decreases for larger values of this parameter and disappears completely when the steady entrainment speed is two times the peak of change of the contact radius.

An increase of the steady entrainment speed is equivalent, from the point of view of the film behaviour to a decrease of the frequency of the load variation.

In all conditions of frequency, load and entrainment speed, the film thickness during the load decreasing phase is smaller than the theoretical, steady state film thickness, although it is to be noted that there is a time lag between the theoretical and measured values due to the squeeze effect and the time of passage of the lubricant through the contact.

In the case of the mean load larger than the amplitude of the load variation, as a general guideline (for the conditions employed in these experiments at least), film thickness perturbations occur when the ratio between half the load cycle period and the average time of transit of the lubricant through the contact in the loading phase of vibration cycle is less than 2.

For oil lubricated contacts working with limited supply of lubricant harmonic vibrations have a beneficial effect upon inlet replenishment and film thickness recovery. This is believed to be the results of repeated entrainment in all sides of the EHD contact, which obviously enhances the film thickness, and the squeeze effect which does not allow the film to completely collapse during the load decreasing phase. Grease lubricated contacts which have already been working in severe starved conditions, experience an increase of the film thickness, but not as pronounced as the oil lubricated contacts. For the conditions of these tests it is believed that repetitive expansion of the contact dimensions push the side ridges sideways and the surface tension forces are not large enough to replenish the inlet.

Chapter 8: Conclusions and Suggestions for Future Work

The research described in this thesis tries to fill the gaps in our understanding of the behaviour of EHD films subjected to vibrations. Experimental investigations on this topic have rarely been reported in literature in the field. This research has overcome many of the difficulties encountered from the experimental point of view such that lubricant film thickness has been successfully measured in a wide range of experimental conditions. This thesis is the first study to report on a systematic research of the behaviour of EHD films under forced, harmonic vibrations. The results reported here are relevant to practically any machine components working in this regime of lubrication but mainly to rolling element bearings and gears. In rolling bearings, it is known that the contacts between the rolling elements and raceways are cyclically loaded/unloaded as the former pass through the loaded zone of the bearing. While in gears, the very nature of these elements makes them prone to cyclic load variation, shock loading and vibrations. In many systems, the power element is an electric motor which most often runs at rotational speeds around 3000 rpm. The rotating shafts of various machines would thus most frequently run at speeds up to 6000 rpm. In road vehicles, the IC engine runs at its peak efficiency and performance at speeds between 2700 and 3000 rpm, while the wheels turn at speeds about ten times smaller. This means that loading/unloading cycles of shaft – supporting bearings as well as vibrations due to unbalanced masses have most often frequencies anywhere between 5 Hz and 100 Hz. The range of frequencies employed in this research between 10 Hz and 100 Hz has thus strong practical relevance. Obviously in practice there will be vibration modes at frequencies much larger than these values, however on one hand it would be difficult to measure the film thickness at frequencies larger than 100 Hz, and on the other hand it is thought that the trends observed in the current research would extend to larger frequencies and the behaviour of the EHD film can thus be predicted.

The method used for measuring the lubricant film thickness was optical interferometry, adapted for the specifics of this research. This method has advantages and disadvantages. The chief advantage is its precision and accuracy as it is able to measure film thickness down to 10 nanometres and to provide maps of the film thickness distribution over the contact area. The main disadvantage is the fact that one element must be transparent, in this case glass, which makes the pressure level reached lower than that routinely encountered in rolling element bearings. The method is laboratory – based which also makes it flexible and allows suitable range of various parameters to be chosen. This means that the limitation mentioned above is acceptable, as the trend of the behaviour of the oil film can be followed and general conclusions can be drawn. The experimental arrangement used in the present research is novel and placing the load cell underneath the ball carriage gave knowledge of the force applied directly to the contact. This in turn allowed the analytical modelling of the dynamic behaviour of the system.

Regarding the behaviour of the EHD film under variable loading the most important conclusions which were drawn from this research are:

- The EHD film behaves differently whether there is complete separation between the contacting solids or not.
- If there is complete separation, (this corresponds to a loading cycle with the mean load equal to or smaller than the amplitude) large film perturbation of the film thickness is formed during the load – increase phase of the vibration cycle. This is due to rapid increase of the pressure in the centre of the contact and the formation of a fluid entrapment, similar to that found in static conditions.
- The film thickness perturbation is directly related to the frequency and amplitude of the load variation and it appears at any value of the entrainment speed. It may exit the contact before the load has reached the peak value in the vibration cycle.
- For viscous lubricants, the film thickness perturbation is about 75 percent larger than the steady state thickness.
- For less viscous lubricants, the film perturbation was found to be up to 4.5 times larger than steady state value measured in similar conditions of speed and load.
- The film thickness perturbations appear to travel slower than the average speed of the surfaces. It is believed that this is due to the rapid increase of contact dimensions which makes the entrainment speed in the exit half of the contact lower than the steady state entrainment speed.
- Central film thickness during the load – decreasing phase is smaller than the thickness corresponding to the static application of the load, with the larger deviation at higher frequencies. As the lubricant film thickness is established by the conditions in the inlet of the contact, a rapid decrease of the contact dimensions means that the effective entrainment speed is equal to the difference between the steady entrainment speed and the speed of change of the contact radius at the inlet.
- If the speed of change is large enough such that the effective entrainment velocity falls to zero, a strong squeeze effect prevents the collapse of the film thickness over the central area of the contact.
- In the case of the mean load larger than the amplitude of the load variation, the film perturbation depends of the frequency of the load cycle, the entrainment speed of the lubricant and the overall lubricant film thickness; it also depends of the ratio between the mean load and the amplitude. In this case the film perturbation is formed not in the centre of the contact but at the leading edge due to the enhanced entrainment speed resulted from the rapid increase of the load. These perturbations are subsequently carried through the contact area producing fluctuations in the film thickness.
- It is thought that the film perturbations due to load variation generate pressure

fluctuations over the contact area which would influence upon the fatigue life of the contact

- It was found that film perturbations occur in contacts for which the ratio between half the load cycle period and the average time of transit of the lubricant through the contact in the loading phase of vibration cycle is less than 2.
- In case of oil – lubricated contacts running under limited lubricant supply conditions, vibrations (that is rapid variation of load) help the recovery of film thickness towards values corresponding to fully flooded conditions. This is believed to be the results of repeated entrainment in all sides of the EHD contact, which obviously enhances the film thickness, and the squeeze effect which does not allow the film to completely collapse during the load decreasing phase.
- Variable loading of grease – lubricated, starved EHD contacts do help recovery of the film thickness to values larger than the starved conditions film, however this recovery is much less than that reported in other studies; to be mentioned that in other studies the frequency of load variation was orders of magnitude smaller than that employed in the present research. For the conditions of these tests it is believed that repetitive expansion of the contact dimensions push the side ridges sideways and the surface tension forces are not large enough to replenish the inlet during the load decreasing phase

8.1 Achievements of the research programme

- An optical interferometry – based test rig was successfully modified and adapted for the measurement of lubricant film thickness subjected to vibrations (rapid variation of load).

- Lubricant film thickness was measured in systematically – designed tests where a wide range of lubricants and working parameters was employed.

- The trends of EHD film behaviour under variable loading were evaluated and maps of the likelihood of film thickness perturbation occurrence were drawn for the first time. In the case of the mean load larger than the amplitude of the load variation, as a general guideline (for the conditions employed in these experiments at least), film thickness perturbations occur when the ratio between half the load cycle period and the average time of transit of the lubricant through the contact in the loading phase of vibration cycle is less than 2; as far as the author is aware this is the first time when such finding was put forward in literature.

- Analytical modelling of the dynamic response of the system was carried out which opens

the door for further research into the evaluation of damping of EHD films.

- An analytical model of the lubricant film thickness variation during rapid variation of load was also devised and successfully compared to the experimental findings.

- The systematic study of the effect of vibrations upon EHD film recovery from starved condition was the first carried out and published.

- As far as the author is aware no studies on the effect of vibrations upon the response of grease – lubricated contacts were published before this thesis.

8.2 Suggestions for future work

The research described in this thesis has brought novel contributions to the understanding of the behaviour of EHD films. At the same time, it has opened some other directions of research which can be pursued in future studies. These directions are:

- Study of the damping constant of EHD films. As it was shown in Chapter 7, the actual experimental system is practically insensitive to a change of the damping constant, however, the theoretical analysis carried out shows that experimental investigation on the damping constant of the EHD films can be done.
  If the current experimental system was to be used, one condition was to make the support of the disc rigid. This will obviously reduce the degree of freedom of the system by one and increase the accuracy of the theoretical analysis. This will be achieved by placing a large, thrust bearing to support the disc from deflecting under loading.
  Another change is to make the shaft and the bearings supporting the ball more rigid. The increase of the diameter of the shaft from 4 mm to 10 mm and supporting it by needle bearings on both sides would make the shaft considerably more rigid and eliminate another spring from the system.
  The other change would be to enlarge the mass attached to the ball carriage. Changing the value of the ball carriage mass in the theoretical analysis to 13 kg shows that the natural frequency of the system is brought down to around 100 Hz which means that the damping constant can be extracted by comparing theoretical and experimental analyses.

- Study of the effect of combined, vibrations, normal to the plane of the contact and in the plane of contact upon EHD film behaviour. In real-life applications bearings may be subjected to vibrations in more than one direction. It would thus be useful to analyse the

behaviour of the lubricant film in these conditions.

- In the limited supply tests, the amount of lubricant available to the contact was not measured. A better comparison to the grease tests would be obtained if the quantity of lubricant onto the disc surface was accurately measured. This would allow the derivation of a relationship between the quantity of lubricant, vibration parameters and film thickness recovery.

- Study of the effect of grease distribution around the rolling bodies in contact and vibrations upon film thickness recovery. In rolling element bearings grease is attached not only to the rings but also to the cage, possibly providing an additional reservoir of lubricant. Such a study would allow an understanding of how the vibrations of the cage might help lubricant supply and avoid starvation of the contact.

References

1. H. Hertz, “The Contact of Elastic Solids”, Journal fur de reine unde angewandte Mathematik, 92,156-171, 1881.
2. K. L. Johnson, “Contact Mechanics”, Cambridge University Press, United Kingdom, 1985.
3. K. L. Johnson, “Regimes of Elastohydrodynamic Lubrication”, Journal of Mechanical Engineering Science, Vol 12, Issue 1, 1970
4. O. Reynolds, “On the Theory of Lubrication and its Application to Mr. Beauchamp Tower experiments including an experimental determination of the viscosity of olive oil”, *Phil Trans. R. Soc*., London, 177, 1886.
5. C. Barus, “Isothermals, Isopietics and Isometrics relative to Viscosity”, AM. J. of Science, 45, 87-96, 1893.
6. C. J. A. Roelands, “Correlational Aspects of the Viscosity-Temperature Pressure Relationship of Lurbicating Oils”, Druk, V. R. B., Groingen, Netherlands, 1966.
7. D. Dowson and G. R. Higginson, “Elastohydodynamic Lubrication, The fundamentals of Roller and Gear Lubrication”, Pergamon Press, Great Britain, 1966.
8. A. Cameron, “Principles of lubrication”, Longmans, 1966
9. A. Cameron, “Righting a 40 – year – old wrong”, Trib. Int., 18, comment, 92, 1985.
10. J. A., Greenwood, “An extension of the Grubin theory of lubrication”, J. Physics. D. Appl. Phys., 5, 2195-221, 1972.
11. J.F. Archard, and M. T. Kirk, “Lubrication of point contacts”, Proc. Roy. Soc. Series A, 261, 532 – 550, 1961.
12. R. Gohar and A. Cameron, “Theoretical and experimental studies of the oil film in lubricated point contact”, Proc. Roy. Soc., Series A, 291, 520-536, 1966.
13. B. J. Hamrock and D. Dowson, “Isothermal Elastohydrodynamic Lubrication of Point Contact, Part 3-Fully Flooded Results”, Transactions ASME, Journal of Lubrication Technology, 99, 264-276, 1977.
14. R. J. Chittenden, D. Dowson, J. E. Dunn and C. M. Taylor, “A theoretical analysis of the isothermal elastohydrodynamic lubrication of concentrated contacts I: direction of lubricant entrainment coincident with the major axis of the contact ellipse”, Proc. R. Soc. London, A397, 345-369, 1985.
15. M. T. Van Zoelen, “Thin layer in rolling element bearings”, Ph. D. thesis, University of Twente. Netherlands, 2009.
16. D. Kostal, P. Sperka and M. Hartl, “Controlling and Measuring Starvation Severity in EHL Contacts”, Engineering Mechanics, 21, 5, 321-328, 2014.
17. P. M. Cann, “Starved Grease Lubrication of Rolling Contacts”, Tribology Transactions, 42, 4, 867-873, 1999.

18. L. D. Wedeven, D. Evans and A. Cameron, “Optical Analysis of Ball Bearing Starvation”, ASME Journal of Lubrication Technology, 93, 3, 349-361, 1971.
19. Y. P. Chiu, “An Analysis and Prediction of Lubricant Film Starvation in Rolling Contact Systems”, ASLE Transactions, 17, 1, 22-35, 1973.
20. E. Kingsbury, “Cross Flow in a Starved EHD Contact”, ASLE Transactions, 16, 4, 276-280, 1973.
21. B. J. Hamrock and D. Dowson, “Isothermal Elastohydrodynamic Lubrication of Point Contacts, Part 4-Starvation Results”, ASME Journal of Lubrication Technology, 99, 1, 15-23, 1977.
22. P. M. Cann, B. Damiens and A. A. Lubrecht, “The Transition between Fully Flooded and Starved Regimes in EHL”, Tribology International, 37, 859-864, 2004.
23. Y. Nagata, K. Kalogiannis and R. P. Glovnea, “Track Replenishment by Lateral Vibrations in Grease-Lubricated EHD Contacts”, Tribology Transactions, 55, 91-98, 2012.
24. P. Svoboda, D. Kostal, I. Krupka and M. Hartl, “Experimental Study of Starved EHL Contacts based on Thickness of Oil Layer in the Contact Inlet”, Tribology International, 67, 140-145, 2013.
25. H. Liang, D. Guo and J. Luo, “Experimental Investigation of Lubrication Film Starvation of Polyalphaolefin Oil at High Speeds’, Tribology Lett, 56, 491-500, 2014.
26. R. P. Glovnea, “Transient Phenomenon in Elastohydrodynamic Lubrication”, Recent Developments in Wear Prevention, Friction and Lubrication, Ed. G. Nikas, Research Signpost, ISBN: 978-81-308-0377-7.
27. L. E. Scales, J. E. Rycroft, N. R. Horswill and B. P. Williamson, “Simulation and Observation of Transient Effects in Elastohydrodynamic Lubrication”, SAE Tech. Paper, 961143, 1996.
28. N. Ren, D. Zhu and S. Z. Wen, “Experimental method for quantitative analysis of transient EHL”, Tribol. Int, 24, 225-230, 1991.
29. H. C. Rutlin, R. S. Sayles and M. S. Starkey, “An optical EHD Study Using a Reciprocating Hertzian Contact Rig Designed to Simulate the Kinematics of Constant Velocity Joints”, in Proc. 23rd Leeds-Lyon Symp., Spet, Elsevier, 297-303, 1996.
30. H. Nishikawa, K. Handa and M. Kaneta, “Behavior of EHL Films in Reciprocating Motion”, JSME Int. J. Series C, 38, 558-567, 1995.
31. J. Sugimura, T. Okumura, Y. Yamamoto and H. A. Spikes, “Simple equation for elastohydrodynamic film thickness under acceleration”, Tribology International, 32, 117-123, 1999.
32. L. Chang, “A simple and accurate method to calculate transient EHL film thickness in machine components undergoing operation cycles”, *Trib. Trans*., 43, 1, 116-122, 2000.

33. R. P. Glovnea and H. A. Spikes, “The Influence of Lubricant Upon EHD Film Behavior During Sudden Halting of Motion”, Tribology Transactions, 43, 4, 731-739, 2000.

34. R. P. Glovnea and H. A. Spikes, “Elastohydrodynamic Film Collapse During Rapid Deceleration: Part 1-Experimental Results”, Trans. of ASME, J. Trib. 123, 254-261, 2001.

35. R. P. Glovnea and H. A. Spikes, “Elastohydrodynamic Film Collapse During Rapid Deceleration: Part 2-Theoretical Analysis and Comparison of Theory and Experiment”, Trans. of ASME, J. Trib. 123, 262-267, 2001.

36. R. P. Glovnea and H. A. Spikes, “Elastohydrodynamic film formation at the start-up of the motion”, Proc. I. Mech. Eng, Series J, 215, 125-138, 2001.

37. M. Holmes, H. P. Evans and R. W. Snidle, “Comparison of transient EHL calculations with start-up experiments”, Presented at: *29th Leeds-Lyon Symposium on Tribology*, Leeds, UK, 3-6 September 2002, *Tribological Research and Design for Engineering Systems: Proceedings of the 29th Leeds-Lyon Symposium on Tribology,* Tribology Series, 41, Elsevier, pp. 79-89. 10.1016/S0167-8922(03)80121-9, 2003.

38. M. Holmes, H. P. Evans and R. W. Snidle, “Comparison of transient EHL calculations with shut-down experiments”, Presented at: *29th Leeds-Lyon Symposium on Tribology*, Leeds, UK, 3-6 September 2002, *Tribological Research and Design for Engineering Systems: Proceedings of the 29th Leeds-Lyon Symposium on Tribology,* Tribology Series, 41, Elsevier, pp. 91-99. 10.1016/S0167-8922(03)80122-0, 2003.

39. G. Popovici, C. H. Venner and P. M. Lugt, “Effects of Load System Dynamics on the Film Thickness in EHL Contacts During Start Up”, Transactions of the ASME, 126, 258-266, 2004.

40. C. J. Hooke, “Minimum Film Thickness in Lubricated Point Contacts Operating in the Elastic Piezo-Viscous Regime”, Proc. I. MechE., C202, 73-84, 1988.

41. R. P. Glovnea and H. A. Spikes, “Behaviour of EHD Films During Reversal of Entrainment in cyclically accelerated/decelerated motion”, Tribology Trans., 45, 2, 177-184, 2002

42. H. Christensen, “The Oil Film in a Closing Gap”, Proc. R. Soc, London, Ser. A., 365, 312-328, 1962.

43. H. Christensen, “Elastohydrodynamic Theory of Spherical Bodies in Normal Approach”, ASME J. Lubr. Technol., 91, 1, 145-154, 1970.

44. K. Herrebrugh, “Elastohydrodynamic Squeeze Between Two Cylinders in Normal Approach”, ASME, J. Lubric. Technol., 92, 2, 292-302, 1970.

45. J. P. Vichard, “Transient Effects in the Lubrication of Hertzian Contacts”, J. Mech. Eng. Sci.,

13, 173-189, 1971.

46. K. W. Lee and H. S. Cheng, “The Pressure and Deformation Profiles Between Two Normally Approaching Lubricated Cylinders”, ASME J. Lubr. Technol., 95, 3, 308-320, 1973.
47. D. Dowson and D. A. Jones, “Lubricant Entrapment Between Approaching Elastic Solids”, Nature (London), 214, 5091, 947-8, 1967.
48. G. R. Paul and A. Cameron, “Absolute Optical Measurement of the Oil Entrapment in a Dropping Ball”, Proc Inst Mech Eng, C95, 69-74, 1972.
49. P. R. Yang and S. Z. Wen, “Pure squeeze action in an isothermal elastohydrodynamic lubricated spherical conjuction, Part 1: Theory and dynamic load results”, Wear, 142, 1-16, 1991.
50. P. R. Yang and S. Z. Wen, “Pure squeeze action in an isothermal elastohydrodynamic lubricated spherical conjuction, Part 2: Constant speed and constant load results”, Wear, 142, 17-30, 1991.
51. R. Larsson and E. Hoglund, “Elastohydrodynamic Lubrication at Impact Loading”, ASME J Tribology, 116, 770-776, 1994.
52. M. M. A. Safa and R. Gohar, “Pressure distribution under a ball impacting a thin lubricant layer”, ASME J Tribology, 108, 372-376, 1986.
53. R. Larsson and J. Lundberg, “Study of Lubricated Impact Using Optical Interferometry”, Wear, 190, 2, 184-189, 1995.
54. R. M. Carson and K. L. Johnson, “Surface Corrugations Spontaneously Generated in A Rolling Contact Disc Machine”, Wear, 17, 59-72, 1971.
55. P. Panganath Nayak, “Contact Vibrations”, Journal of Sound and Vibration, 22, 3, 297-322, 1972.
56. D. W. Dareing and K. L. Johnson, “Fluid film damping of rolling contact vibrations”, Journal of Mechanical Engineering Science, 17, 214-218, 1975.
57. A. G. D. Smith and A. Cameron, “Scuffing Under Cyclic Loading-Unexpected Effect of Frequency”, ASLE Transactions, 26, 2, 236-242, 1983.
58. H. Rahnejat and R. Gohar, “The Vibrations of Radial Ball Bearings”, Proc Instn Mech Engrs, 199, C3, 181-193, 1985.
59. H. Mehdigoli, H. Rahnejat and R. Gohar, “Vibration Response of Wavy Surfaced Disc in Elastohydrodynamic Rolling Contact”, Wear, 139, 1-15, 1990.
60. J. Sabot, P. Krempf and C. Janolin, “Non-linear Vibrations of a Sphere-Plane Contact Excited

by A Normal Load", Journal of Sound and Vibration, 214, 2, 359-375, 1998.

61. Y. H. Wijnant, C. H. Venner, R. Lassron and P. Eriksson, "Effects of Structural Vibrations on the Film Thickness in an EHL Circular Contact", Journal of Tribology, 121, 259-264, 1999.
62. Y. H. Wijnant, J. A. Wensing and G. C. Van Nijen, "The Influence of Lubrication on the Dynamic Behavior of Ball Bearings", Journal of Sound and Vibration, 222, 4, 579-596, 1999.
63. S. Ramamurthy, C. M.Krousgrill and F. Sadeghi, "Vibration in grease lubricated bearing systems", Tribology Transactions, 43, 3, 403-410, 2000.
64. P. M. Cann and A. A. Lubrecht, "The Effect of Transient Loading on Contact Replenishment with Lubricating Greases", *Transient Processes in Tribology*, Elsevier, 745-750, 2004.
65. E. Rigaud and J. Perret-Liaudet, "Experiments and numerical results on non-linear vibrations of an impacting Hertzian contact. Part 1: Harmonic excitation", Journal of Sound and Vibration, 265, pp. 289-307, 2003.
66. T. El Kilali, J. Perret-Liaudet and D. Mazuyer, "Experimental analysis of a high pressure lubricated contact under dynamic normal excitation force", Transient Processes in Tribology, 43, 409-418, 2004.
67. M. Sakamoto, H. Nishikawa and M. Kaneta, "Behavikaor of Point Contact EHL Films Under Pulsating Loads", Trans. Proc. Trib., Elsevier, 391-399, 2004.
68. F. Guo, H. Nushikawa, P. Yang and M. Kaneta, "EHL under cyclic squeeze motion", Trib. Int. 40, 1–9, 2007.
69. A. Felix-Quinonez and G. E. Morales-Espejel, "Film thickness fluctuations in time-varing normal loading of rolling elastohydrodynamically lubricated contacts", Proc. IMechE, 224, Part C: J, 2010.
70. F. Nonato and K. L. Cavalca, "On the non-linear dynamic behavior of elastohydrodynamic lubricated point contact", Journal of Sound and Vibration, 329, 4656-4671, 2010.
71. K. Kalogiannis, "Behaviour of Elastohydrodynamic Films Subjected to Oscillatory Motion", Ph. D. Thesis, University of Sussex, United Kingdom, 2013.
72. C. S. Sunnersjo, "Varying Compliance Vibrations of Rolling Bearings", Journal of Sound and Vibration, 58, 3, 363-373, 1978.
73. P. K. Gupta, "Dynamics of Rolling-Element Bearing. Part 1: Cylindrical Roller Bearing Analysis", Journal of Lubrication Technology, 101, 293-304, 1979.
74. P. K. Gupta, "Dynamics of Rolling-Element Bearing. Part 2: Cylindrical Roller Bearing Results", Journal of Lubrication Technology, 101, 305-311, 1979.

75. P. K. Gupta, "Dynamics of Rolling-Element Bearing. Part 3: Ball Bearing Analysis", Journal of Lubrication Technology, 101, 312-318, 1979.
76. P. K. Gupta, "Dynamics of Rolling-Element Bearing. Part 4: Ball Bearing Results", Journal of Lubrication Technology, 101, 319-326, 1979.
77. Y. H. Wijnant, "Contact Dynamics in the field of Elastohydrodynamic Lubrication", PhD thesis, University of Twente, Enschede, the Netherlands, ISBN: 90-36512239, 1998.
78. J. A. Wensing, "On the dynamics of ball bearings", PhD thesis, University of Twente, Enschede, the Netherlands, ISBN: 90-36512298, 1998.
79. G. Stachowiak and A. Batchelor, "Engineering Tribology", 4th edition, Butterworth-Heinemann, 2013.
80. P. M. Lugt, "Grease Lubrication in Rolling Bearings", 1st edition, John Wiley and Sons, 2013.
81. I. K. Loukas and E. J. Maginn, "Molecular Simulation of Poly- alpha-olefin Synthetic Lubricants: Impact of Molecular Architecture on Performance Properties", J. Phys. Chem. B, 103, 10781-10791, 1999.
82. National Lubricating Grease Institute (NLGI), Lubricating Grease Guide, 2nd ed, Kansas City, 1987.
83. W. H. Bauer, A. P. Finkelstein and S. E. Wiberley, "Flow Properties of Lithium Stearate-Oil Model Greases as a Function of Soap Concentration and Temperature," ASLE Transactions, 3, 215-224, 1960.
84. P. M. Lugt, "A Review on Grease Lubrication in Rolling Bearings", Tribology Transactions, 52, 470-480, 2009.
85. T. Cousseau, "Film thickness and friction in grease lubricated contacts: Application to rolling bearing torque loss", PhD Thesis, University of Porto, Portugal, 2013.
86. R. Mortier, M. Fox and S. Orszulik, "Chemistry and technology of lubricants", SpringerLink: Springer E-Books, Springer Netherlands, 2010.
87. J. J. Kauzlarich and J. A. Greenwood, "Elastohydrodynamic Luburication with Herschel-Bulkley Model Greases", ASLE Transactions, 15(4), 269-277, 1972.
88. G. Mullineux, "Non-linear Least Squares Fitting of Coefficients in the Herschel-Bulkley Model", Applied Mathematical Modelling", 32, 2538-2551, 2008.
89. W. Jonkisz and H. Krzeminski-Freda, "Pressure Distribution and Shape of an Elastohydrodynamic Grease Film", Wear, 55, 81-89, 1979.
90. W. Jonksiz and H. Krzeminski-Freda, "The Properties of Elastohydrodynamic Grease Films", Wear, 77, 277-285, 1982.
91. J. B. Accinelli, "Grease Lubrication of Ultra High Speed Rolling Contact Bearings", ASLE Transactions, 1:1, 10-16, 1958.
92. A.R. Wilson, "The relative thickness of grease and oil films in rolling bearings", *Proc. I. Mech.*

E., 193, 185-192, 1979.

93. H. C. Muennich and H. J. R. Gloeckner, “Elastohydrodynamic Lubrication of Grease-Lubricated Rolling Bearings”, ASLE Transactions, 23, 1, 45-52, 1978.
94. J. M. Palacios, A. Cameron and L. Arizmendi, “Film Thickness of Grease in Rolling Contacts”, ASLE Transactions, 24, 4, 474-478, 1980.
95. P. M. Cann, B. P. Willianson, R. C. Roy and H. A. Spikes, “The Behaviour of Greases in Elastohydrodynamic Contacts”, J Phys, 25, 124-132, 1992.
96. M. Kaneta, H. Nishikawa and M. Naka. “Effects of Transversely Oriented Defects and Thickener Lumps on Grease Elastohydrodynamic Lubrication Films”, Proc Instn Mech Engrs, 215, part J, 279-288, 2001.
97. I. Couronne, P. Vergne, D. Mazuyer, N. Truong-Dinh and D. Girodin, “Effects of Grease Composition and Structure on Film Thickness in Rolling Contact”, Tribology Transactions, 46, 1, 31-36, 2003.
98. P. M. Cann and A. A. Lubrecht, “Bearing performance limits with grease lubrication: the interaction of bearing design, operating conditions and grease properties”, J. Phys, 40, 5546-5451, 2007.
99. R. Gohar and A. Cameron, “The Mapping of Elastohydrodynamic Contacts”, ASLE Trans., 10, 215-225, 1967.
100. C. A. Foord, W. C. Hammann and A. Cameron, “Evaluation of Lubricants Using Optical Elastohydrodynamics’, ASLE Trans, 11, 31-43, 1968.
101. L. J. Wedeven, “Optical Measurements in Elastohydrodynamic Rolling Contact Bearings”, PhD. Dissertation, London University, London, 1970.
102. F. Rasteger and W. O. Winer, “On the Traction and Film Thickness Behavior of Grease in Concentrated Contact”, NIGI Spokesman, 50, 162-174, 1986.
103. M. Kaneta, T. Sakai and H. Nishikawa, “Effects of Surface Roughness on Point Contact EHL”, Trib Trans, 36, 605-612, 1993.
104. F. J. Westlake and A. Cameron, “A Study of Ultra-Thin Lubricant Films using an Optical Technique”, Proc. Instn Mech Engrs, 182, Part 3g, 75-78, 1967-1968.
105. G. J. Johnston, R. Wayte and H. A. Spikes, “The Measurement and Study of Very Thin Lubricant Films in Concentrated Contacts”, Tribology Transactions, 34, 2, 187-194, 1991.
106. P. M. Cann, H. A. Spikes and J. Hutchinson, “The development of a Spacer Layer Imaging Method (SLIM) for Mapping Elastohydrodynamic Contacts”, Tribology Transactions, 39, 4, 915-921, 1996.
107. O. Marklund and L. Gustafsson, “Interferometry-based Measurements of oil-film thickness”, Proc Instn Mech Engrs, 215, Part J, 243-259, 2001.
108. R. P. Glovnea, A. K. Forrest, A. V. Olver and H. A. Spikes, “Measurement of sub-nanometer lubricant films using ultra-thin film interferometry”, Tribology Letters, 15, 3, 217-230, 2003.

109. J. Luo, S. Wen and P. Huang, “Thin Film Lurbication. Part 1: Study on the Transition between EHL and Thin Film Lubrication using a Relative Optical Intensity Technique”, Wear, 194, 107-115, 1996.
110. L. Ma and C. Zhang, “Discussion on the Technique of Relative Optical Interference Intensity for the Measurement of Lubricant Film Thickness”, Tribology Letters, 36, 239-245, 2009.
111. M. Hartl, I. Krupka and M. Liska, “Differential Colorimetry: Tools for Evaluation of Chromatic Interference Patterns”, Opt. Eng, 36 1-8, 1997.
112. M. Hartl, I. Krupka, M. Liska, J. Molimard, M. Querry and P. Vergne, “Thin Film Colorimetric Interferomerty”, Tribology Transactions, 44, 2, 270-276, 2001.
113. M. Françon, “Optical Interferometry”, Academic Press, New York and London, 1966.
114. M.M.A., Safa and R. Gohar, “Squeeze Films in Elastohydrodynamic Lubrication”, 12th Lyon-Leeds Symp. on Surface Distress Phenomena, 1985.
115. R. Larsson and E. Hoglund, “Elastohydrodynamic Lubrication at Pure Squeeze Motion”, Wear, 179, 39-43,1994.
116. R. P. Glovnea and H. A. Spikes, “Oscillations Induced in EHD Films Thickness by a Step in Entrainment Speed”, Lubrication Science, 15-4, 15, 311-320, 2003.
117. M. Kaneta, S. Ozaki, H. Nishikawa and F. Guo, “Effects of Impact Loads on Point Contact Elastohydrodynamic Lubrication Films”, Proc. IMechE 221, Part J: Engineering Tribology, 271-278, 2006.
118. D. M. Sanborn and W. O. Winer, “Fluid Rheological Effects in Sliding Elastohydrodynamic Point Contacts with Transient Loading: 1- Film Thickness”, Transactions of the ASME, Journal of Lubrication Technology, 262-271, 1971.
119. J. Lundberg, “Lubrication of Machine Elements During Combined Squeeze and Sliding Motion”, Wear, 1993, 161-166, 1993.
120. G. E. Morales-Espejel, “Central Film Thickness in Time-varying Normal Approach of Rolling Elastohyrodynamically Lubricated Contacts”, Proc. IMechE. 222, Part C: J. Mechanical Engineering Science, 1271-1280, 2008.
121. P. Guay and A. Frikha, “Ball Bearing Stiffness. A New Approach Offering Analytical Expressions”, Proceedings of 16th European Space Mechanisms and Tribology Symposium, ESA SP-737, 2015.
122. R. Singh and T. C. Lim, “Vibration Transmission Through Rolling Element Bearings in Geared Rotor Bearings”, NASA Contractor Report 4334, 1990.
123. H. R. El-Sayed, “Stiffness of Deep-Groove Ball Bearings”, Wear, 63, 89-94, 1980.
124. S. S. Rao, “Mechanical Vibrations”, 6th Edition, Pearson, 2016.